DEFECT ENGINEERING OF POLYCRYSTALLINE TITANIUM DIOXIDE SYNTHESIZED BY ATOMIC LAYER DEPOSITION

BY

MEREDITH CLARE KRATZER SELLERS

DISSERTATION

Submitted in partial fulfillment of the requirements
for the degree of Doctor of Philosophy in Chemical Engineering
in the Graduate College of the
University of Illinois at Urbana-Champaign, 2011

Urbana, Illinois

Doctoral Committee:

Professor Edmund G Seebauer, Chair
Professor Paul J A Kenis
Assistant Professor Charles M Schroeder
Assistant Professor Xiuling Li

ABSTRACT

There is good reason to believe that the properties of semiconducting metal oxides for catalytic and integrated circuit applications can be improved when designed according to the principles of microelectronic devices. Defect engineering is used extensively in the semiconductor processing industry to produce devices with well-defined physical properties (e.g., electrical conductivity, switching frequency, power consumption). Polycrystalline TiO_2 is an attractive material for supported metal catalyst, photocatalyst, memory resistor, and spin-based transistor devices due to its photostability, low cost, and non-toxicity. Nevertheless, methods for characterization and manipulation of carrier concentration, near-surface and near-interface electric fields, and magnetic ordering are lacking.

The present work employs ALD as a film synthesis technique to allow precise control over TiO_2 microstructure, crystallinity, and composition. It outlines the application of a sound metrological method for the evaluation of charge carrier concentration to metal oxide semiconductors not amenable to standard characterization techniques such as four-point-probe or Hall effect. This science base permits elucidation of complex defect behavior in polycrystalline TiO_2, a system comprising native defects such as oxygen vacancies and titanium interstitials as well as grain boundaries and voids, all of which may be electrically active. An emphasis is placed on manipulating these defects to affect charge carrier concentration and decoupling trends observed in the literature as a function of film thickness, illumination, and synthesis method. Subsequently, doping is investigated with an aim at precisely controlling carrier concentration by judicious selection of n-type (Cr, Nb) and p-type (Mn) transition metal species. For the case of undoped TiO_2, photoreflectance, a type of modulation spectroscopy, is invoked to examine the degree of fixed charge buildup at buried

solid-solid interfaces in metal oxide thin film structures. Lastly, since the method of in-situ doping during ALD is unique in its ability to allow for decoupling of microstructure, defect composition, and doping level, the suitability of Mn-TiO_2 deposited in this fashion for novel integrated circuit devices is highlighted.

ACKNOWLEDGEMENTS

I would like to express my gratitude to the many individuals who aided and advised me throughout my graduate career.

Thanks go to my advisor, Dr. Edmund Seebauer, for his technical, professional, and interpersonal insights over the years. His guidance has allowed me to develop a deeper understanding of my capabilities and limitations as a scientist and as an individual.

I appreciate the assistance of current and former members of the Seebauer Group. In particular, I would like to recognize Dr. Yevgeniy Kondratenko for his invaluable technical expertise and never-ending enthusiasm about research and life. Thanks to Prashun Gorai and Kristine Pangan-Okimoto for their helpful feedback on experimental design and interpretation, as well as many enjoyable conversations.

This work was greatly aided by the talent and kindness of members of the UIUC scientific community. Thanks go to Dr. Rick Haasch and Dr. Mauro Sardela at the Center for Microanalysis of Materials for their scientific input and advice. Also, Dane Sievers for allowing us to perform electrical characterization and device processing in the ECE 444 Laboratory. Thanks to Edmond Chow at the Micro and Nanotechnology Laboratory for help with SEM. I appreciate the assistance of Jim Wentz, as well as the SCS electronics shop, machine shop, and glass shop, with equipment design and troubleshooting.

I would like to recognize the technical contributions of Faisal Nasim and Dr. Arshad Bhatti at the COMSATS Institute for Information Technology, particularly with respect to advancement of photoreflectance capabilities. Also, Brandon Fisher at Argonne National Laboratory for assistance with magnetic measurements.

I am grateful for the financial support provided by the National Science Foundation Graduate Research Fellowship and Harry G. Drickamer Fellowship programs.

Lastly, my family and friends have been a constant source of support and affection as I have worked toward completing my PhD. My husband, Zack Sellers, has helped and inspired me immeasurably during this learning experience; I am eternally thankful for his love and encouragement.

…Sunward I've climbed, and joined the tumbling mirth of sun-split clouds, – and done a hundred things you have not dreamed of – wheeled and soared and swung high in the sunlit silence…

TABLE OF CONTENTS

Chapter 1: Introduction

1.1 Motivation and challenges

There is good reason to believe that the properties of semiconducting metal oxides for catalytic and integrated circuit applications can be improved when designed according to the principles of microelectronic devices. Defect engineering is used extensively in the semiconductor processing industry to produce devices with well-defined physical properties (e.g., electrical conductivity, switching frequency, power consumption) [1, 2, 3]. For example, it is possible to change the electronic band structure of a material by eliminating or compensating charged native defects in the bulk and then inserting substitutional defects in the form of charged dopant atoms. Since semiconductors support space charge, surface electronic properties can also couple to bulk electronic properties. This type of bulk-surface coupling has been demonstrated in the Seebauer laboratory in the context of dopant ion implantation for transistor fabrication [4, 5].

Polycrystalline TiO_2 is an attractive material for supported metal catalyst, photocatalyst, memory resistor, and spin-based transistor devices due to its photostability, low cost, and non-toxicity. Nevertheless, researchers tend to gloss over the fundamental aspects of charge transfer, surface band bending, and magnetic ordering governing the performance of these systems.

In as-grown, undoped TiO_2, oxygen vacancies (V_O) and/or titanium interstitials (Ti_i) introduce large concentrations of shallow donor levels that result in n-type conduction at standard temperatures and pressures [6]. Control and manipulation of defects in single crystal TiO_2, the lattice structure of which is shown in Fig. 1.1(a), has been demonstrated via

mechanisms such as surface-bulk coupling and photostimulation [7]. Polycrystalline TiO_2 is a more complicated system due to the presence of grain boundaries that can alter the electrical properties of the film and serve as traps for charge carriers (see Fig. 1.1(b)). Similar intricacies were encountered optimizing polycrystalline Si for solar cell and integrated circuit applications [8, 9]. Since polycrystalline semiconductors contain defects caused by incomplete bonding between adjacent crystallites, disordered material in the boundary region results in trapping states, space charge regions, and local potential barriers [10, 11]. The extent to which these factors influence a particular semiconductor depends on crystallite size, preparation method, and the resulting intergrain properties.

In direct contrast to the way in which silicon is precisely doped for integrated circuit applications in order to optimize device performance, there is little nuanced understanding of the correlation between TiO_2 charge carrier concentration, doping type and level, surface/interface electronic properties, and the operation of TiO_2-based catalysts and microelectronics components. Strategies for successful defect engineering of polycrystalline TiO_2 are critical to improving the commercial viability and utility of this unique and interesting material.

1.2 Applications of defect engineered TiO_2

1.2.1 Supported metal catalysis

Defect engineering can be employed to improve the design of supported metal catalysts. It is well known that catalysts are influenced by support properties [12, 13]. Numerous reports of qualitative enhancement of reaction rate and yield on TiO_2-supported metals exist in the literature. For instance, TiO_2-supported Pt exhibits activity that varies

with doping for benzene and ethylacetate oxidation [14]. Pt on cerium-modified TiO_2 exhibits enhancement of activity and stability for the water-gas shift reaction over CeO_2- or TiO_2-supported Pt alone [15]. These behaviors arise due to the so-called "Schwab effect," the phenomenon wherein a metal support changes the properties of an overlying oxide semiconductor catalyst or, conversely, an oxide semiconductor support affects an overlying metal catalyst [16]. In both cases, charge transfer occurs between the metal and the semiconductor, leading to a modification of the catalyst surface charge density and hence its catalytic activity. These concepts are depicted schematically in Fig. 1.2, which illustrates how Pt metal activity can alter a reaction such as water-splitting and the manner in which bulk doping level might change surface electron density.

1.2.2 Photocatalysis

TiO_2 has been investigated extensively as a photocatalyst due to its wide band gap and charge carrier trapping dynamics [17, 18]. For such applications, it is necessary to control electric fields near the surface of the semiconductor in order to manipulate the flow of photogenerated charge carriers. When photons of sufficient energy strike a photocatalyst, carriers are excited into the conduction band leading to electron/electron-hole pair separation. As additional free electrons are driven to the surface of the semiconductor, they are able participate in chemical reactions. The direction and magnitude of the near-surface electric field within the space charge region can be adjusted by bulk doping which, in turn, affects the flow of photogenerated charge carriers toward the surface. This is depicted schematically in Fig. 1.3, where bulk doping type is seen to affect the direction of the electric field ε; for n-type TiO_2, ε points towards the surface, while for p-type TiO_2, ε points into the bulk.

1.2.3 Novel integrated circuit devices

TiO_2 is one of the more attractive material options for next-generation non-volatile memory. Current charge-based memories will soon be prohibitive at the length scales targeted by integrated circuit manufacturers. Also, a fundamental minimum energy (and amount of time) is required to switch a charge-based device on and off. An ideal, non-charge-based alternative will be not only denser and faster, but also less energy-consuming. TiO_2 has been studied in the context of two novel devices which will be discussed in additional detail: memory resistors and spin transport based transistors.

Since the 1970s, the existence of a fundamental, two-terminal circuit element complementary to the resistor, conductor, and capacitor has been postulated. The missing memory resistor (or memristor) was found in 2008 by physicists at HP Labs [19]. Conceptually, it is a two-terminal device whose resistance depends on the magnitude and polarity of the voltage applied to it and the length of time that the voltage has been applied [20]. Functioning devices have been fabricated as multi-layer stacks incorporating Si, SiO_2, Pt, and TiO_2 (Fig. 1.4(a)). Understanding the physical mechanism behind the fast resistive switching in TiO_2-based memristors is critical to device optimization. Preliminary studies suggest close coupling between the built-in electric field at the TiO_2-Pt interface and memristor switching speed [21].

Spintronics, or "spin transport electronics," is a solid-state device technology that exploits not only the fundamental electronic charge of an electron, but also its intrinsic spin and associated magnetic moment [22]. Candidate materials are primarily diluted magnetic semiconductors, nonmagnetic semiconductors such as TiO_2, ZnO, etc. modified by the addition of small atomic percentages of transition metal (TM) dopants, that exhibit room

temperature ferromagnetism (RTFM). Indeed, RTFM has been reported for TiO_2 doped with Cr [23], Mn [24], as well as other TM elements. The relative importance of intrinsic versus extrinsic ferromagnetism (Fig. 1.4(b)) in TM-doped TiO_2 is still under investigation. Native point defects, grain boundaries, and dislocations play a key role, however. Upon Mn doping, in particular, the close coupling between ferromagnetism, film preparation conditions, and microstructure suggests opportunity for further optimization and control of TiO_2 magnetic properties via a precision synthesis method.

1.3 Atomic layer deposition for thin film synthesis

Atomic layer deposition (ALD), a pulsed-precursor vapor phase deposition method related to chemical vapor deposition (CVD), is an attractive technique for the fabrication of thin films with precise thickness and compositional control on large-area substrates. The self-limiting nature of the technique affords precise layer-by-layer deposition, typically accomplished by alternating pulses of precursor and oxidant comprising a single ALD "cycle" (Fig. 1.5(a) through (d)). The thickness and surface smoothness of the resulting film can be tuned by adjusting pulse and purge times, as well as other deposition parameters.

Undoped TiO_2 synthesized by ALD has been studied extensively [25, 26]; relatively little is known about the microstructure and electrical characteristics of doped TiO_2 synthesized by ALD, however. In comparison to alternative film synthesis methods, ALD avoids the complications related to solvent/byproduct removal and calcination-induced shrinkage [27] encountered with sol-gel processing and dip coating. Other deposition techniques such as pulsed laser deposition (PLD) and plasma-assisted molecular beam deposition (PAMBE) used to deposit TiO_2 thin films are less suited to the high throughput

requirements of commercial manufacturing. In addition, PLD can result in high particulate composition and uneven coverage, while PAMBE films suffer from thickness-dependent morphologies. ALD avoids such problems.

1.4 Significance of the present work for defect engineering of TiO_2

The present work employs ALD as a film synthesis method to allow precise control over film microstructure, crystallinity, and composition. ALD is preferred over CVD due to enhanced conformal coverage and film quality. The chemistry of TiO_2 synthesis using TTIP as an ALD precursor is well-known: slow, controllable deposition is achievable at moderate temperatures. The addition of an oxidant such as H_2O speeds the rate of TiO_2 deposition and reduces the amount of organic contamination in the bulk to near-negligible levels. The way in which ALD allows for modular switching of specific gaseous, liquid, and solid dopant precursors is also advantageous. For example, early studies of candidate metalorganics for n- and p-type doping suggested that $(Nb(OCH_2CH_3)_5$ permitted successful Nb doping while $NbCl_5$ did not [28].

This thesis outlines the application of a sound metrological method for the evaluation of charge carrier concentration to metal oxide semiconductors not amenable to standard characterization techniques such as four-point-probe or Hall effect. This science base permits elucidation of complex defect behavior in polycrystalline TiO_2, a system comprising native defects such as oxygen vacancies and titanium interstitials as well as grain boundaries and voids, all of which may be electrically active. An emphasis is placed on manipulating these defects to affect charge carrier concentration and decoupling trends observed in the literature as a function of film thickness, illumination, and synthesis method. Subsequently,

doping is investigated with an aim at precisely controlling carrier concentration by judicious selection of n-type (Cr, Nb) and p-type (Mn) transition metal species. For the case of undoped TiO_2, photoreflectance, a type of modulation spectroscopy, is invoked to examine surface and interface charge transfer and band bending. Lastly, since the method of in-situ doping during ALD is unique in its ability to allow for decoupling of microstructure, defect composition, and doping level, the suitability of Mn-TiO_2 deposited in this fashion for novel integrated circuit devices is highlighted.

1.5 Figures

Fig. 1.1 (a) Anatase TiO_2 unit cell from [29] where titanium ions are shown as hashed spheres and oxygen ions as large, light gray spheres. Dopant atoms, shown as the small gray spheres, can be added to change bulk carrier concentration. (b) Imaginary sketch of grain and grain boundary distribution in polycrystalline TiO_2.

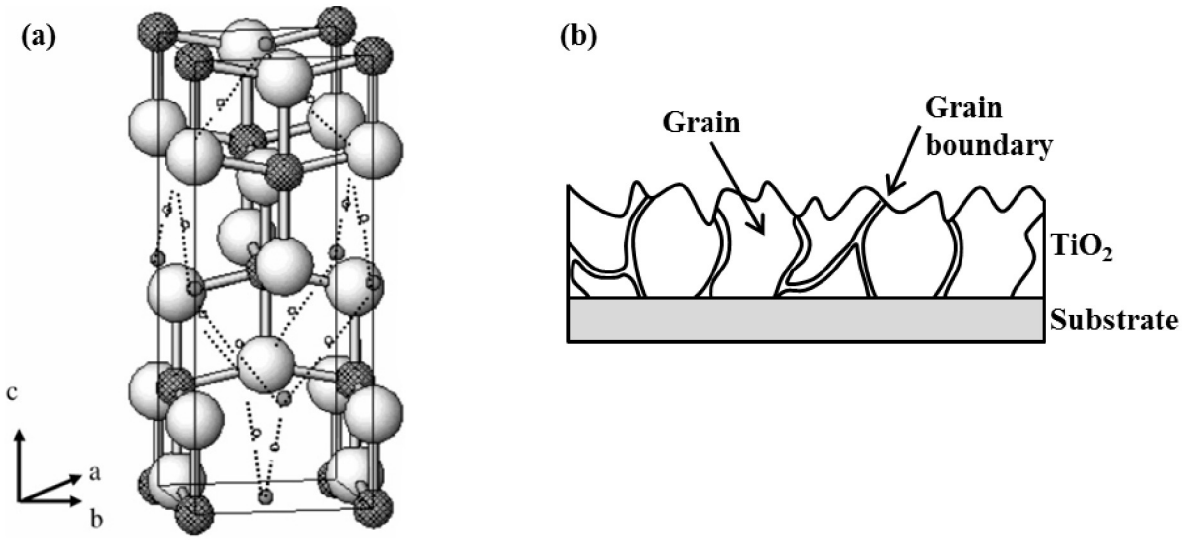

Fig. 1.2 Diagrams illustrating how (a) surface charge density can affect a reaction such as water-splitting and (b) bulk electron density induced by doping translates through to surface electron density.

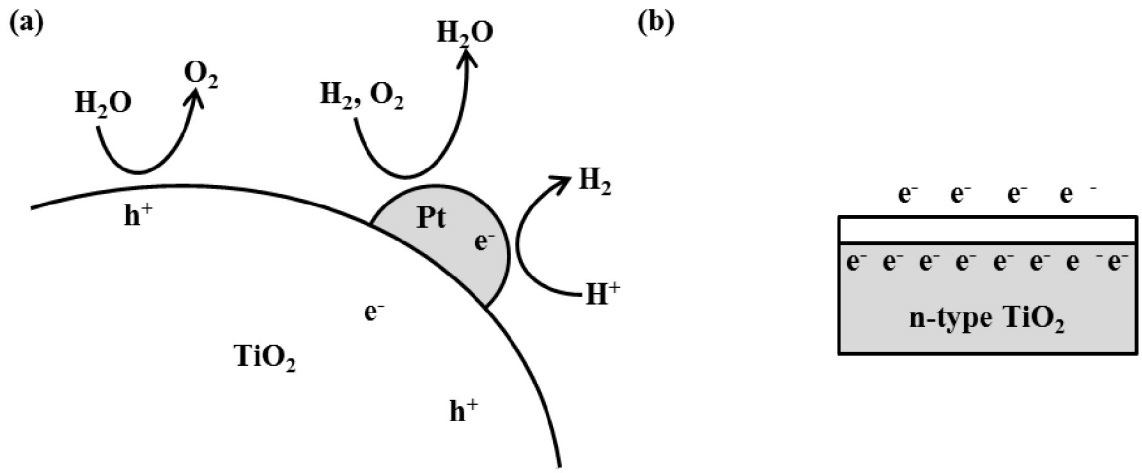

Fig. 1.3 Electronic band diagrams showing electron (n-type) and electron-hole (p-type) accumulation near a solid-gas interface and the resulting change in built-in electric field.

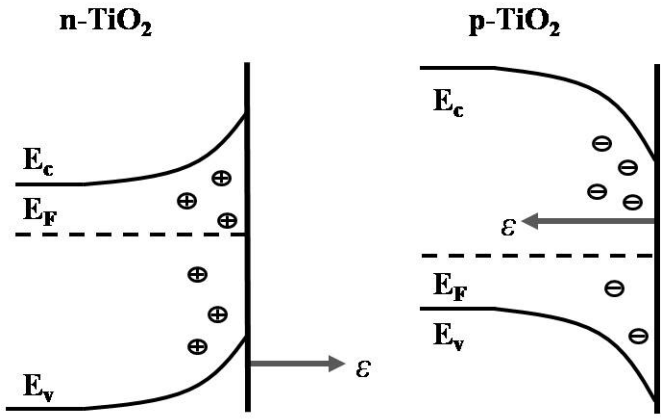

Fig. 1.4 (a) Schematic of a TiO_2-based memristor structure from [30] and (b) possible mechanisms for ferromagnetism in doped TiO_2 – intrinsic ferromagnetism results from coupling of unpaired electron spins on individual atoms while extrinsic ferromagnetism is typically caused by formation of secondary phases.

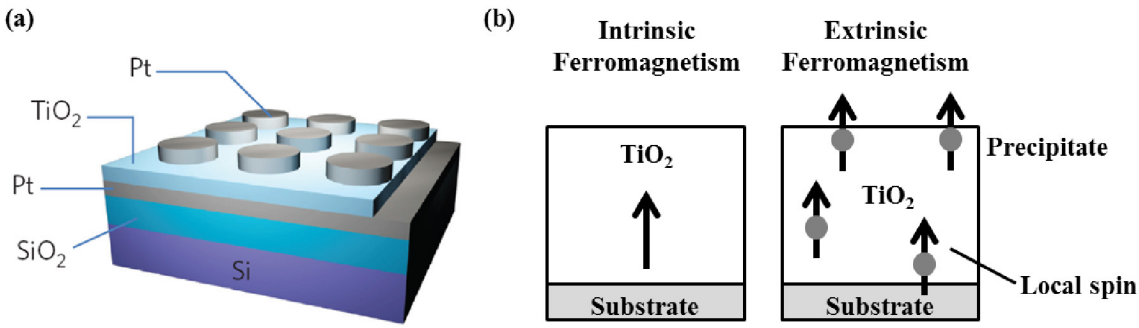

Fig. 1.5 Schematic depicting sequence of exposure and purge steps comprising a single ALD cycle. For the case of TiO_2, common precursors include $Ti(OCH(CH_3)_2)_4$ and $TiCl_4$; H_2O and H_2O_2 are used extensively as oxidants.

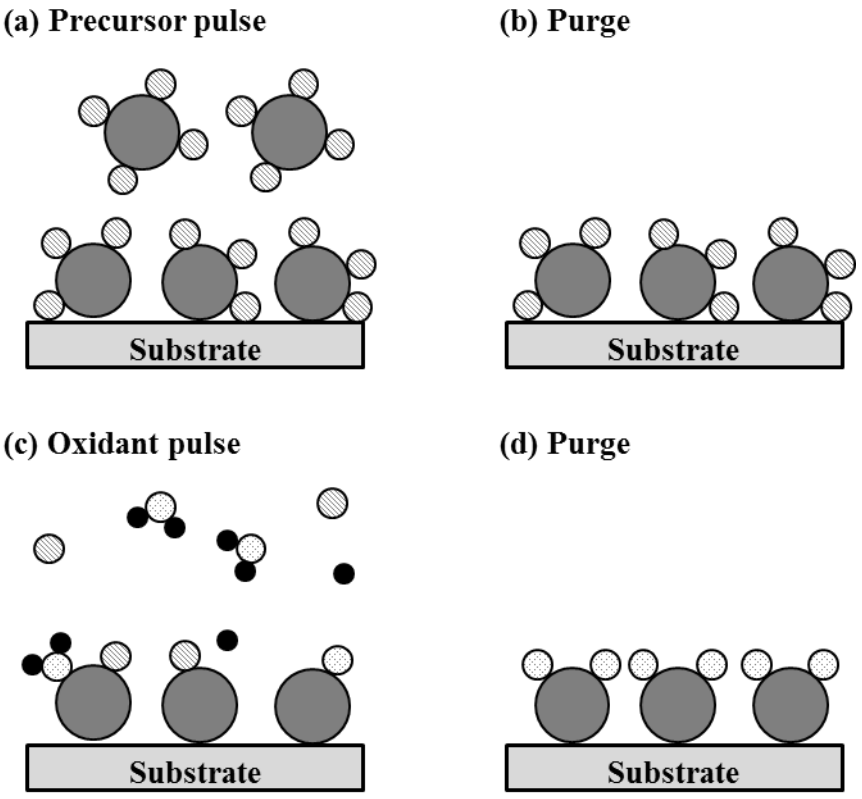

1.6 References

[1] H. J. Queisser and E. E. Haller, *"Defects in Semiconductors: Some Fatal, Some Vital,"* Science **281,** 945-950 (1998).

[2] E. G. Seebauer and M. C. Kratzer, *Charged Semiconductor Defects: Structure, Thermodynamics, and Diffusion* (Springer-Verlag, London, 2009).

[3] E. G. Seebauer and K. W. Noh, *"Trends in semiconductor defect engineering at the nanoscale,"* Mater. Sci. Eng., R **70,** 151-168 (2010).

[4] K. Dev, M. Y. L. Jung, R. Gunawan, R. D. Braatz, and E. G. Seebauer, *"Mechanism for coupling between properties of interfaces and bulk semiconductors,"* Phys. Rev. B: Condens. Matter **68,** 195311 (2003).

[5] K. Dev and E. G. Seebauer, *"Band bending at the Si(111)-SiO_2 interface induced by low-energy ion bombardment,"* Surf. Sci. **550,** 185-191 (2004).

[6] M. K. Nowotny, T. Bak, and J. Nowotny, *"Electrical properties and defect chemistry of TiO_2 single crystal. I. Electrical conductivity,"* J. Phys. Chem. B **110,** 16270-16282 (2006).

[7] A. G. Holllister, PhD Thesis, University of Illinois at Urbana-Champaign, Urbana, 2010.

[8] C. H. Seager, *"Grain boundaries in polycrystalline silicon,"* Annu. Rev. Mater. Sci. **15,** 271-302 (1985).

[9] Z.-J. Wang, S. Tsurekawa, K. Ikeda, T. Sekiguchi, and T. Watanabe, *"Relationship between Electrical Activity and Grain Boundary Structural Configuration in Polycrystalline Silicon,"* Interface Sci. **7,** 197-205 (1999).

[10] C. R. M. Grovenor, *"Grain boundaries in semiconductors,"* J. Phys. C **18,** 4079-4119 (1985).

[11] H. F. Matare, *"Carrier transport at grain boundaries in semiconductors,"* J. Appl. Phys. **56,** 2605-2631 (1984).

[12] G. M. Schwab and G. Mutzbauer, *"Mixed catalysts with doped carriers,"* Naturwissenschaften **46,** 13-14 (1959).

[13] G. M. Schwab and K. Koller, *"Combined action of metal and semiconductor catalysts,"* J. Am. Chem. Soc. **90,** 3078-3080 (1968).

[14] P. Papaefthimiou, T. Ioannides, and X. E. Verykios, *"Performance of doped Pt/TiO_2 (W^{6+}) catalysts for combustion of volatile organic compounds (VOCS),"* Appl. Catal., B **15,** 75-92 (1998).

[15] I. D. Gonzalez, R. M. Navarro, W. Wen, N. Marinkovic, J. A. Rodriguez, F. Rosa, and J. L. G. Fierro, *"A comparative study of the water gas shift reaction over platinum catalysts supported on CeO_2, TiO_2 and Ce-modified TiO_2,"* Catal. Today **149,** 372-379 (2010).

[16] M. Boudart and G. Djega-Mariadassou, *Kinetics of Heterogeneous Catalytic Reactions* (Princeton University Press, Princeton, New Jersey, 1984).

[17] A. L. Linsebigler, G. Lu, and J. T. Yates, Jr., *"Photocatalysis on TiO_2 surfaces. Principles, mechanisms, and selected results,"* Chem. Rev. **95,** 735-735 (1995).

[18] K. Hashimoto, H. Irie, and A. Fujishima, *"TiO_2 Photocatalysis: A Historical overview and future prospects,"* Jpn. J. Appl. Phys. **44,** 8269-8285 (2005).

[19] D. B. Strukov, G. S. Snider, D. R. Stewart, and R. S. Williams, *"The missing memristor found,"* Nature **453,** 80-83 (2008).

[20] S. Williams, *"How we found the missing memristor,"* IEEE Spectrum 29-35 (2008).

[21] S.-G. Park, B. Magyari-Kope, and Y. Nishi, *"Impact of oxygen vacancy ordering on the formation of a conductive filament in TiO_2 for resistive switching memory,"* IEEE Electron. Device Lett. **32,** 197-199 (2011).

[22] S. A. Wolf, D. D. Awschalom, R. A. Buhrman, J. M. Daughton, S. von Molnar, M. L. Roukes, A. Y. Chtchelkanova, and D. M. Treger, *"Spintronics: A Spin-Based Electronics Vision for the Future,"* Science **294,** 1488-1495 (2001).

[23] T. Droubay, S. M. Heald, V. Shutthanandan, S. Thevuthasan, S. A. Chambers, and J. Osterwalder, *"Cr-doped TiO_2 anatase: a ferromagnetic insulator,"* J. Appl. Phys. **97,** 046103 (2005).

[24] Z. Wang, J. Tang, Y. Chen, L. Spinu, W. Zhou, and L. D. Tung, *"Room-temperature ferromagnetism in manganese doped reduced rutile titanium dioxide thin films,"* J. Appl. Phys. **95,** 7384-7386 (2004).

[25] J. Aarik, A. Aidla, T. Uustare, and V. Sammelselg, *"Morphology and structure of TiO_2 thin films grown by atomic layer deposition,"* J. Cryst. Growth **148,** 268-275 (1995).

[26] V. Pore, A. Rahtu, M. Leskelä, M. Ritala, T. Sajavaara, and J. Keinonen, *"Atomic Layer Deposition of Photocatalytic TiO_2 Thin Films from Titanium Tetramethoxide and Water,"* Chem. Vap. Deposition **10,** 143-148 (2004).

[27] C. B. Carter and M. G. Norton, *Ceramic Materials: Science and Engineering* (Springer, New York, 2007).

[28] M. C. Kratzer, MS Thesis, University of Illinois at Urbana-Champaign, Urbana, 2008.

[29] C. L. Olson, J. Nelson, and M. S. Islam, *"Defect chemistry, surface structures, and lithium insertion in anatase TiO_2,"* J. Phys. Chem. B **110,** 9995-10001 (2006).

[30] D.-H. Kwon, K. M. Kim, J. H. Jang, J. M. Jeon, M. H. Lee, G. H. Kim, X.-S. Li, G.-S. Park, B. Lee, S. Han, M. J. Kim, and C. S. Huang, *"Atomic structure of conducting nanofilaments in TiO_2 resistive switching memory,"* Nature Nanotech. **5,** 148-153 (2010).

Chapter 2: Methods for Atomic Layer Deposition and Electrical Characterization of Polycrystalline TiO_2[*]

2.1 Introduction

Attempts to characterize and manipulate the electronic properties of polycrystalline TiO_2 are confounded by the accuracy of the available metrology tools for measuring carrier concentration. Commonly used methods such as four-point-probe or Hall effect measurements require ohmic contacts to the oxides, yet real contacts to wide-bandgap semiconductors usually create Schottky barriers that act like diodes. Both problems probably contribute to the wide variance of n-type carrier concentrations (N_d) found in the literature in the case of anatase TiO_2, ranging from approximately 1 x 10^{16} cm^{-3} to 1 x 10^{20} cm^{-3} [1, 2]. Such variations complicate attempts to perform defect engineering in TiO_2 [3].

This study highlights a metrology technique – in particular, the use of "Schottky diode" test structures for determining the carrier concentrations of anatase TiO_2 thin films synthesized by atomic layer deposition (ALD) based upon capacitance-voltage (*C*-*V*) measurements [4]. Related studies have been reported elsewhere for anatase TiO_2 deposited using alternative methods, as well as other metal oxides such as ZnO [5], but vital electrical characteristics of the diode structures are not always described or characterized adequately. In some instances, necessary current-voltage (*I*-*V*) data are not shown [6] or even collected [2, 7]. Sometimes both *I*-*V and C*-*V* data are missing [8], which is problematic for such nontrivial measurements. Similar problems afflict literature for single crystal rutile TiO_2 [9, 10].

[*] Part of this work has been published: M.C.K. Sellers and E.G. Seebauer, *"Measurement method for carrier concentration in TiO_2 via the Mott-Schottky approach,"* Thin Solid Films **519,** 2103-2110 (2011).

The evaluation of metal oxide carrier concentration in this manner is an attractive alternative to conventional four-point-probe or Hall effect measurements for several reasons. Given the 3.9 eV work function of TiO_2 [11], a characterization method that precludes forming an Ohmic contact to the TiO_2 surface is preferable. Additionally, Ohmic contact recipes that entail an annealing step (e.g., Al to n-type Si wherein the Al-Si eutectic region formed under the Al contact is critical) are out of the question, since high-temperature processing irreversibly alters the stoichiometry and thus carrier concentration of metal oxides. Lastly, the *C-V* method circumvents the need to form multiple contacts to the semiconductor surface. The cloverleaf, square, or rectangular four contact geometries necessary for Hall effect measurements may be restrictive with respect to sample size or preparation method. Since these geometries assume a laterally homogeneous metal oxide film, it is also not possible to probe spatial variations in carrier concentration as a result of gradients in thickness or doping level.

There is no single "correct" carrier concentration for undoped polycrystalline TiO_2 due to the fact that native defects including charged oxygen vacancies and titanium interstitials influence the concentration of electronic charge carriers in the bulk depending on their degree of ionization [3]. That being said, metrology inaccuracies certainly contribute to the broad range of donor carrier concentration values found in the literature for undoped anatase TiO_2. As seen in Table 2.1, the numbers range over four orders of magnitude. The synthesis and metrology methods vary considerably among these reports, so it is difficult to immediately ascribe the wide range of results to either factor. Film crystallinity (anatase versus rutile) has no obvious correspondence with N_d. Films thicker than ~250 nm account for the majority of carrier concentration values in the $10^{18} – 10^{19}$ cm^{-3} range.

A rigorous and accurate metrology protocol for determination of N_d is needed in order to decouple legitimate versus spurious contributions to bulk carrier concentration. For instance, surprisingly large values of N_d may be explained by the fact that $N_{d,measured} > N_{d,actual}$ for diode structures with large series resistance R_s. Failure to evaluate and/or ensure that R_s is below a certain threshold (depending on measurement frequency) will result in overestimation of TiO_2 carrier concentration. Electrochemical measurements require an ohmic contact be formed to the TiO_2 "working electrode" (although it is critical for the aqueous solution to act as the Schottky junction with the semiconductor) [12]. It is not always clear if an ohmic contact has been applied to the TiO_2 film [1] or if the chosen contact (e.g., silver paste and copper wire [13]) exhibits linear *I-V* behavior. Similarly, N_d values on the order of 10^{18} to 10^{19} cm^{-3} for films evaluated using Hall effect measurements may suffer from inaccuracies due to formation of Schottky versus ohmic contact between the probe and the semiconducting metal oxide. If a rectifying barrier arises at a Hall electrode, the experimentally determined Hall voltage that is manipulated to obtain N_d will include contributions from additional, unwanted floating potentials that can lead to overestimation of carrier concentration [14].

The present work outlines a rigorous methodology for the determination of free carrier concentration for metal oxide semiconductors such as TiO_2 that are not amenable to standard metrology protocols. Thorough "device-like" characterization of TiO_2 Schottky diodes is carried out to justify the subsequent extraction of carrier concentration values from capacitance-voltage (*C-V*) measurements using the Mott-Schottky approach. The influence of factors such as substrate type, contact metal type, and surface and interface preparation are examined.

2.2 Methods and procedures

2.2.1 Atomic layer deposition of TiO_2

Thin film polycrystalline anatase TiO_2 was synthesized by ALD in a 3L stainless steel vacuum chamber evacuated with a mechanical pump to a base pressure of about 50 mTorr. The substrates were mounted on a resistively heated chuck whose temperature was maintained at 200°C during deposition and monitored with a chromel-alumel (type K) thermocouple. For reference, the chuck is capable of depositing at temperatures up to about 450°C. A schematic of the low-pressure vacuum chamber is shown in Fig. 2.1.

Substrates of dimensions 2 cm x 2 cm were cut from commercial Si(100) wafers doped n-type in two different ways: Sb (0.013 Ω·cm resistivity) and P (15 Ω·cm resistivity). In almost all cases, Si substrates were etched with 49% HF (1 min) following by rinsing with deionized water (1 min) immediately prior to insertion in the vacuum chamber to minimize native oxide formation at the TiO_2/Si interface. Gaseous precursors were introduced into the chamber through a delivery tube placed approximately 5 cm from the substrate. The precursors included $Ti(OCH(CH_3)_2)_4$ (TTIP, Strem Chemicals Inc., 98%) and H_2O (DI, no further purification), with N_2 (SJ Smith, 99.999%) serving as the carrier gas. The temperatures of the TTIP and H_2O bubbler sources were maintained at 65°C and 23°C, respectively, and the carrier gas flow rates were set to 60 SCCM with mass flow controllers. Total chamber pressure during growth was typically 400 mTorr. A full ALD cycle consisted of a $Ti(OCH(CH_3)_2)_4$ pulse, N_2 purge, H_2O pulse, and another N_2 purge. A pulse time of 8 seconds and a purge time of 10 seconds yielded self-limiting growth. At 200°C, 27 cycles were typically required to obtain 100 nm thick undoped TiO_2.

2.2.2 Annealing

Following film deposition, thermal annealing was carried out in a Barnstead Thermolyne F79300 tube furnace equipped with an eight stage Eurotherm 2416 programmable controller. All annealing was performed under ambient atmosphere with no supplementary O_2, N_2, or H_2O vapor. Samples were cleaned with acetone and dried with compressed air before being loaded into the cool quartz furnace process tube. The standard process ramp rate and annealing temperature were 20°C/min and 550°, respectively. For initial electrical characterization studies, samples were kept at this temperature for 24 hrs.

2.2.3 Preparation of TiO_2 Schottky diodes

A schematic of the TiO_2 Schottky diode designed to yield information about carrier type and concentration is shown in Fig. 2.2(a). 200 nm thick metal contacts of well-defined area (2.0×10^{-3} cm^2) were formed to the TiO_2 surface by photolithographic patterning followed by metal sputtering (Al) or evaporation (Au) and photoresist lift-off. High purity (99.999%) Al was sputtered in a Cooke Dual-Gun Sputter System with base pressure of 3×10^{-6} Torr, and Au contacts were formed using a CHA SEC-600 E-Beam Evaporator with base pressure of 5×10^{-7} Torr. Subsequently, the n-Si substrate was prepared for application of the ohmic contact by either manual abrasion with sandpaper or a two-step protocol involving a CF_4/O_2 capacitively coupled plasma and 49% HF wet etch (to prevent rapid removal of the entire TiO_2 film during wet etching). The contact to bare Si was then formed by the application of InGa metal eutectic (Aldrich, 99.99%) using a metal 26s-gauge needle affixed to a 10 μl syringe [15].

2.2.4 Electrical characterization

I-V and *C-V* measurements were performed using a probe station consisting of a vacuum chuck for holding the wafer mounted on a *x-y* stage, a fiber optic illuminator, a probe platform with *z* adjustment for holding micromanipulators, four Signatone S-725 micropositioners, and a switch plate for connecting the probes to the instruments. Each micropositioner was equipped with a SE-T tungsten probe tip with a tip diameter of 5.0 μm, shank diameter of 25 mil, and length of 1.25".

I-V and *C-V* data were collected using an Agilent 4155C Semiconductor Parameter Analyzer (SPA) and Agilent 4284A Precision LCR Meter. The instruments were both controlled using Metrics ICS, a PC-based interface for semiconductor test instruments. The test instruments were connected as follows for TiO_2 Schottky diode measurements:

1) 4155C "SMU1" → probe station triax connector labeled "Probe 1"
2) 4155C "SMU3" → probe station triax connector labeled "Probe 3"
3) 4284A "H (cur and pot)" → probe station coax connector labeled "Probe 1" and InGa contact to n-Si
4) 4284A "L (cur and pot)" → probe station coax connector labeled "Probe 3" and Al contact to TiO_2

To obtain *I-V* data for the ohmic behavior of the metal to n-Si junction, "Probe 1" and "Probe 3" were both contacted to the metal/n-Si.

The *C–V* measurements were done at a frequency of 1 MHz; the range of the applied bias voltage was −1.2 to 0.2 V.

2.3 Diode qualification

A diode exhibiting Mott-Schottky behavior obeys the following relation between capacitance C and applied voltage V:

$$\frac{1}{C^2} = \left(\frac{2}{q\varepsilon_s \varepsilon_0 N_d A^2} \right) \left(V - V_{bi} - \frac{kT}{q} \right) \tag{2.1}$$

when the film under examination exhibits n-type conductivity. In this expression, N_d is the donor carrier concentration, ε_s denotes the dielectric constant of the semiconductor, ε_0 the permittivity of free space, and V_{bi} the built-in voltage. The quantities q, k, and T represent the electronic charge, Boltzmann's constant, and temperature in K, respectively. The dielectric constant of anatase TiO_2 equals 55 [1]. Eq. (2.1) indicates that the slope of C^{-2} vs. V in the depletion region is inversely proportional to the desired quantity: the net ionized donor concentration, N_d. The relation is equally suitable for determination of acceptor concentration in p-type material, N_a. In practice, a reversal in conductivity manifests itself as a sign change for the slope of C^{-2} vs. V.

To justify the use of Eq. (2.1), the diode structure must undergo several steps of qualification to ensure that the assumptions underlying the Mott-Schottky equation are satisfied. In particular, the diode structure must exhibit the following characteristics:

1) The region of the device associated with the metal-Si contact must (a) show ohmic behavior and (b) contribute minimally to the series resistance of the diode.
2) The region of the device associated with the metal-TiO_2 contact must (a) show rectifying behavior, (b) have an ideality factor n such that $1 < n < 2$, and (c) contribute minimally to the series resistance of the diode.
3) The Si-TiO_2 interface must contribute minimally to the series resistance of the diode.

The following sections show that each of these seven conditions is satisfied for the structure and materials used here.

2.3.1 Diode series resistance

Each condition specifies the need to minimize the overall series resistance of the Schottky diode. In brief, this is crucial as R_s interferes with carrier concentration determination. The extent to which R_s affects the value of N_d extracted from *C-V* measurements depends on the measurement frequency:

$$N_{d,\,measured} = \frac{N_{d,actual}}{1-\left(\omega R_s C\right)^4} \tag{2.2},$$

where ω is frequency in Hz [4]. Thus, fulfillment of condition 1(b), 2(c), and 3 is equivalent to ensuring that $(\omega R_s C)^4$ is small compared to unity. For the frequency utilized in this study (1 MHz) and the observed capacitances ($< 10^{-8}$ F), values of R_s smaller than 1 kΩ will have no significant effect (<1%) on the calculated carrier concentration.

The overall series resistance R_s of the Schottky device can be broken down into three distinct contributions:

$$R_s = R_{s,Si} + R_{s,\,TiO_2} + R_{s,interface} \tag{2.3},$$

the series resistance $R_{s,Si}$ associated with the Si and its contact through the ohmic metal to the external probe, the series resistance $R_{s,TiO2}$ associated with the TiO_2 layer and its contact through the Schottky metal to the external probe, and the series resistance $R_{s,interface}$ associated with the Si-TiO_2 interface. These are labeled on the equivalent lumped-element circuit of the Schottky diode in Fig. 2.2(b). The resistance describing the metal-Si portion of the TiO_2 Schottky diode $R_{s,Si}$ can be obtained directly via *I-V* measurements. The individual

contributions of $R_{s,TiO2}$ and $R_{s,interface}$ cannot be determined experimentally in this manner. Instead, trends in $R_{s,TiO2}$ and $R_{s,interface}$ as a function of TiO_2 bulk and Si-TiO_2 interface properties are assessed by examining changes in overall series resistance.

2.3.2 Metal-Si contact

A metal–semiconductor contact is defined as either ohmic or rectifying. If the contact is ohmic in nature, its *I-V* characteristics will appear linear and symmetrical with respect to $V = 0$. If it rectifying, the *I-V* characteristics will instead be asymmetrical, with current scaling exponentially with voltage for $V > 0$. The behavior of the metal-Si contact of the TiO_2 Schottky diode can be examined by passing a current through the modified test structure shown in Fig. 2.3(a) and measuring the voltage across the two contacts. Fig. 2.4 shows the *I-V* characteristics for the InGa-Si junction as a function of Si resistivity and substrate preparation method. The curves are linear in all cases, which confirms the InGa contact with n-type Si is ohmic, thereby satisfying condition 1(a).

The *I-V* curves also yield useful information about the extent to which the metal-Si contact contributes to R_s. The slope of each *I-V* curve at $V = 0$ corresponds to a total resistance R_T:

$$R_T = \left\{ \frac{\partial V}{\partial I} \right\}_{V=0} \tag{2.4}.$$

For a lateral two-terminal contact resistance structure with both contacts on the top surface as employed in the modified test structure, R_T is given by:

$$R_T = 2R_c + 2R_{sp} + 2R_p \tag{2.5},$$

where R_c denotes the contact resistance, R_{sp} the spreading resistance in the semiconductor directly under the contact, and R_p the probe resistance (see Fig. 2.3(b)) [4]. Comparison of

Figs. 2.2(a) and 2.3(a) indicates that the resistance describing the metal-Si portion of the TiO_2 Schottky diode, $R_{s,Si}$, is simply the sum of R_c, R_{sp}, and R_p:

$$R_{s,\,Si} = R_c + R_{sp} + R_p \tag{2.6}$$

Consequently, minimizing R_c serves to minimize R_s. Since the thickness of the Si substrate is much greater than the contact radius, the spreading resistance of each contact can be expressed as:

$$R_{sp} = \frac{\rho}{4r} \tag{2.7}$$

where ρ and r are respectively the resistivity of the underlying semiconductor and the radius of the metal contact [4]. Here, the numerical values of R_{sp} typically fell between 0.03 and 40 Ω. The empirical value of R_p for the SE-T tungsten probe tips used in this study is 9.3×10^{-5} Ω.

Fig. 2.4 includes the values of R_c obtained via application of Eqs. (2.4), (2.5), and (2.7) to the *I-V* data. For the 0.013 Ω·cm substrate, Si conditioning by abrasion and etching yielded contact resistance values of 5.6 Ω and 13 Ω, respectively. Values for the 15 Ω·cm substrate were more than ten times larger in both cases. The value of 5.6 Ω best fulfills condition 1(b) in that the contribution of the ohmic contact resistance to the overall diode series resistance is minimized. The 0.013 Ω·cm substrate and abrasion surface preparation method were used for all diode structures intended for *C-V* measurements.

2.3.3 Metal–TiO_2 contact

The thermionic current-voltage relationship of a Schottky barrier diode is given by [16]:

$$I = I_s\left[\exp\left(\frac{q\left(V - IR_s\right)}{nkT}\right) - 1\right] \quad (2.8),$$

where I_s denotes the saturation current and n the ideality factor. I_s is defined as:

$$I_s = AA^{**}T^2 \exp\left(-\frac{q\Phi_B}{kT}\right) \quad (2.9),$$

where A represents the diode area, A^{**} the effective Richardson constant for TiO_2 (6.71 x 10^6 A m^{-2} K^{-2} [17]), and Φ_B the effective barrier height. Eq. (2.8) indicates that the current through the diode varies exponentially with applied voltage in the forward bias case and is very small in the reverse bias case – a variation that represents the classic signature of rectifying behavior for condition 2(a).

Fig. 2.5 shows the forward and reserve bias *I-V* characteristics for two diodes with differing metal contacts: Al/TiO_2/n-Si/InGa and Au/TiO_2/n-Si/InGa. In both cases, an asymmetric, Schottky-barrier response is observed, thereby fulfilling condition 2(a).

However, diodes exhibiting rectifying behavior may yet be unsuitable for *C-V* measurements of carrier concentration [18]. Such measurements presuppose that current transport through the device is limited by the diffusion and/or electric-field-driven drift of majority carriers within the depletion region of the semiconductor adjacent to the metal interface. In some devices, current may be limited by other factors such as image force lowering of the Schottky barrier height, quantum mechanical tunneling, current leakage, or the presence of an insulating layer between the metal and the semiconductor. Such devices exhibit $n > 2$ in Eq. (2.8) for *I-V* measurements [19], and *C-V* determinations of carrier concentration are not appropriate because of additional, unwanted contributions to the capacitance. However, some non-idealities are tolerable. For example, a fraction of majority carriers may recombine with minority carriers within the depletion region of the

semiconductor. In such cases, $1 < n < 2$ (condition 2(b)), and *C-V* measurements remain appropriate for determinations of carrier concentration.

The present work employed the Cheung method [20] to obtain n for the metal-TiO_2 contacts. In this method, n is obtained from a plot of $dV/d\ln J$ vs. J where J is current density in units of A/cm^2:

$$\frac{dV}{d\ln J} = R_s AJ + n\left(\frac{kT}{q}\right) \tag{2.10}$$

As shown in Fig. 2.6(a), application of this equation to the data of Fig. 2.5 yields ideality factors for the Al-based and Au-based TiO_2 diodes of 1.6 and 3.5, respectively. Thus, only the diode with Al contact meets condition 2(b).

R_s was also determined by the Cheung method, which prescribes plotting an auxiliary function $H(J)$ versus current density:

$$H(J) = V - \left(\frac{nkT}{q}\right)\ln\left(\frac{J}{AA^{**}T^2}\right) = n\Phi_B + R_s J \tag{2.11}$$

With n known from Eq. (2.10), both R_s and Φ_B can be determined. As seen in Fig. 2.6(b), R_s values are 0.90 kΩ for the Al contact and 1.2 kΩ for the Au contact, so that condition 2(c) was fulfilled in both cases. The corresponding values of Φ_B were 0.57 and 0.39 eV, although these values do not directly affect any of the required conditions for accurate *C-V* measurements.

2.3.4 Si-TiO_2 interface

It remains to minimize the contribution of $R_{s,interface}$ to the overall series resistance of the diode as specified in condition 3 to avoid interfering with accurate N_d determination. There is no direct way to measure $R_{s,interface}$ for the TiO_2 Schottky diode, nor is its exact

magnitude critical, since the goal is merely to minimize R_s. However, it is possible to obtain a qualitative understanding of how surface preparation protocols affect the series resistance associated with the Si-TiO_2 interface and advise upon which of these surface preparation protocols must be undertaken to avoid spurious contributions to N_d. The TiO_2 film and Schottky diode preparation were carried out as described in Sections 2.2.1 and 2.2.3 except that Si substrates were prepared in one of three ways prior to TiO_2 deposition: no HF etching, HF etching, or growth of a thick (200 nm) layer of thermal SiO_2. In the presence of native or thermal oxide, high values of series resistance (> 1 x 10^5 Ω·cm) are obtained from *I-V* data for the Al/TiO_2/Si/InGa Schottky diodes. In contrast, HF etching results in a Si-TiO_2 interface that contributes minimally to diode R_s.

It is well known that if the interfacial layer is sufficiently thick, it will contribute significantly to the overall capacitance of the diode and prohibit accurate extraction of N_d [21]. For example, a layer of SiO_2 wedged between the Si and TiO_2 would serve as an additional capacitor connected in series with the capacitance associated with the depletion layer (the equivalent circuit diagram in Fig. 2.2(b) would no longer be accurate); the total capacitance would then be lower than that of a diode without an interfacial layer. This artifact would propagate through into a higher, or overestimated, value of N_d. The native oxide result is more remarkable since the equivalent circuit diagram remains valid. Even a thin (~5 Å) native oxide layer left on the Si substrate prior to TiO_2 film deposition leads to an undesirably high value of R_s.

2.4 Determination of TiO_2 carrier concentration

Fig. 2.7(a) shows an example *C-V* curve for a fully characterized TiO_2 Schottky diode structure. In this instance, the film is 100 nm thick, undoped anatase TiO_2 subjected to 24 hrs of post-deposition annealing. Values for n, R_s, and Φ_B of 1.6, 0.90 kΩ, and 0.60 eV are obtained, in that order. The capacitance increases with decreasing positive voltage until reaching a maximum in the accumulation region, which is labeled in the figure. Fig. 2.7(b) shows the same data in conventional Mott-Schottky format (C^{-2} vs. V). Carrier concentration can be extracted from the electrical data since the assumptions underlying the Mott-Schottky equation are all satisfied. For this TiO_2 film, N_d equals $8.3 \pm 0.2 \times 10^{16}$ cm^{-3}. The estimate of standard error is obtained by computation of a least squares curve fit to C^{-2} vs. V in the linear depletion region.

2.5 Conclusion

Defect engineering of metal oxide semiconductors such as TiO_2 is hardly straightforward. Spurious contributions to experimentally determined carrier concentration values must be eliminated in order to tune polycrystalline TiO_2 for catalysis and integrated circuit applications. *C-V* measurements can be used to obtain accurate values of carrier concentration in n- and p-type metal oxide semiconductors, although thorough device-like characterization of Schottky diode test structures and judicious selection of contact metals and surface/interface preparation methods are necessary. Especially for polycrystalline TiO_2, the body of literature pertaining to *C-V* characterization of polycrystalline Si and Ge [22, 23] should be leveraged to better understand the challenges of defect engineering polycrystalline TiO_2 films synthesized by assorted deposition methods.

2.6 Tables and figures

Table 2.1 Literature values of undoped anatase TiO_2 carrier concentration.

Reported N_d (cm^{-3})	Synthesis Method	Thickness (nm)	Metrology Method	Reference
~1 x 10^{16}	Spray pyrolysis (12hr anneal at 450°C)	100 ± 20	Impedence spectroscopy	[1]
4.1 x 10^{16}	E-beam evaporation	120	*C-V*	[24]
7.7 x 10^{16}	PAMBE	100	Hall effect	[25]
7.9 x 10^{16}	E-beam evaporation	80	*C-V*	[24]
2.9 x 10^{17}	E-beam evaporation	40	*C-V*	[24]
3.2 x 10^{17}	Spray pyrolysis (6hr anneal at 450°C)	100 ± 20	Impedence spectroscopy	[1]
2.1 x 10^{18}	CVD	250	*C-V*	[26]
5.0 x 10^{18}	PLD	200	Hall effect	[27]
5.6 x 10^{18}	CVD	250	*C-V*	[8]
9.7 x 10^{18}	MBE	~ 30	Hall effect	[28]
9.0 x 10^{18}, 2.0 x 10^{19}	Sputtering	1000	Hall effect	[29]
1.5 x 10^{19}	Spray pyrolysis (as-deposited)	100 ± 20	Impedence spectroscopy	[1]
1.7 x 10^{19}	Sol-gel	~ 1300	Photo-electrochemical measurements	[13]
2 x 10^{19} to 9 x 10^{19}	Galvanostatic technique	62 and 83	Impedence spectroscopy	[2]
3.4 x 10^{19}	Hydrothermal processing	10,000	*C-V*	[30]

Fig. 2.1 Schematic depicting the low-pressure vacuum chamber for ALD of undoped TiO_2.

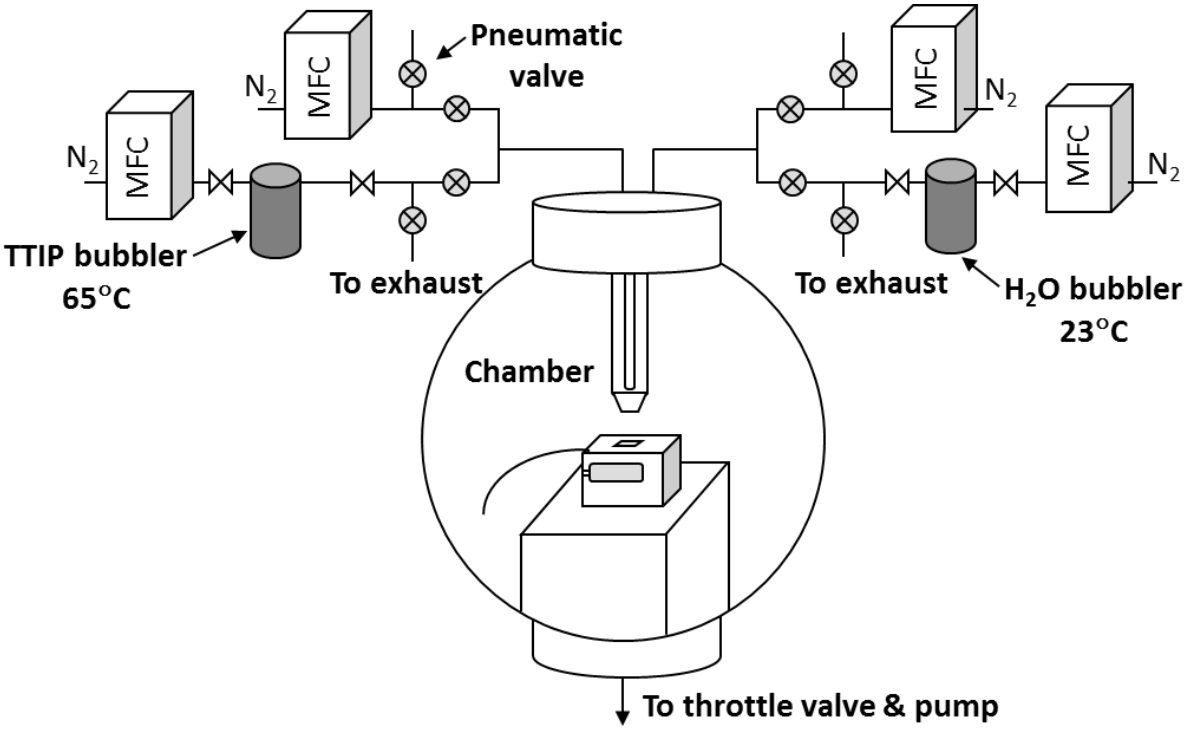

Fig. 2.2 Schematic of (a) TiO_2 Schottky diode structure with key features labeled and (b) equivalent lumped element circuit for TiO_2 Schottky diode.

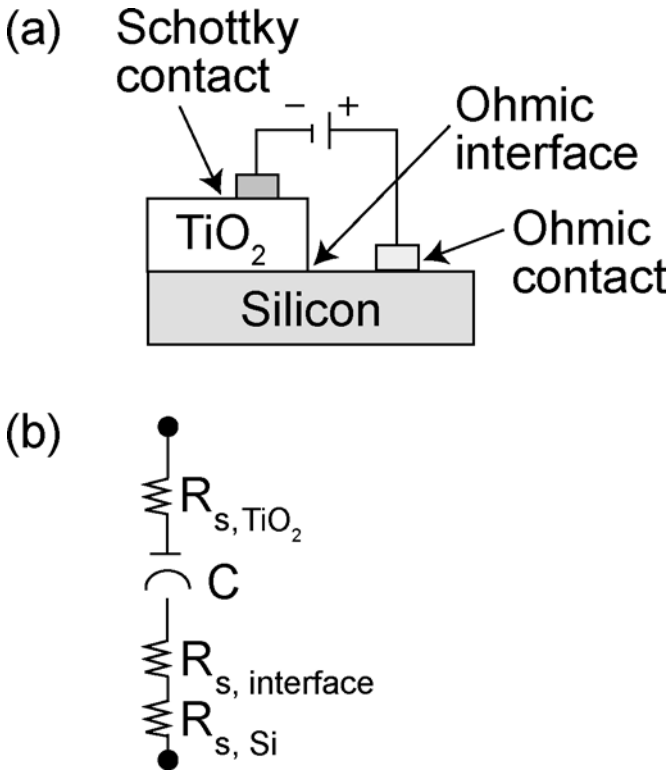

Fig. 2.3 Schematic of (a) test structure for determining metal-Si R_c and (c) resistance contributions to R_T for metal-Si R_c test structure.

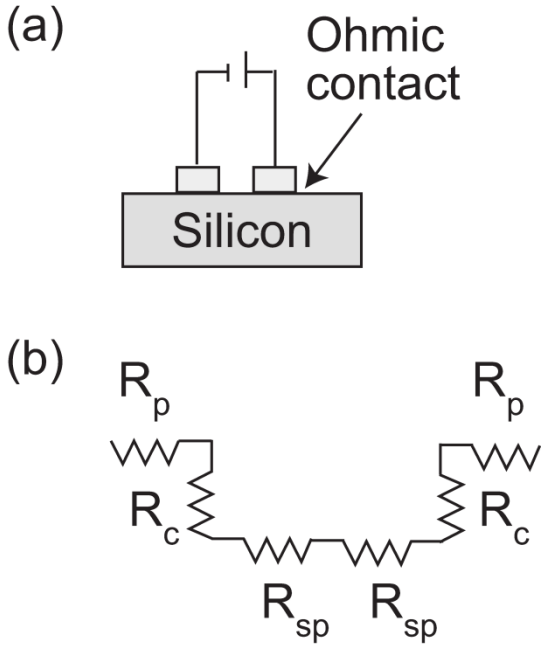

Fig. 2.4 Current-voltage characteristics for InGa-Si contacts in the test structure of Fig. 2.3(a) as a function of Si substrate resistivity and surface preparation method. "A" indicates abraded and "E" indicates etched. All curves are linear, indicating ohmic behavior, and corresponding contact resistances are shown.

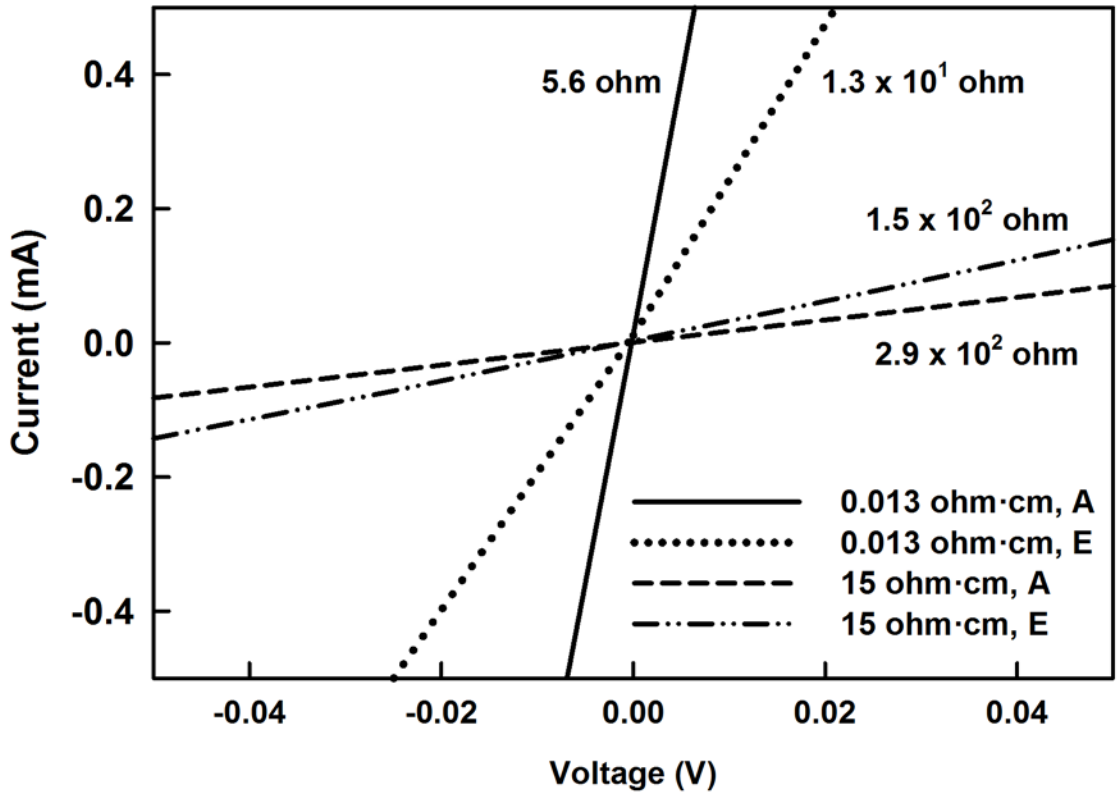

Fig. 2.5 Current-voltage characteristics for comparison of Au and Al contacts to diodes fabricated with undoped TiO_2. Contact area is 2.0×10^{-3} cm^2.

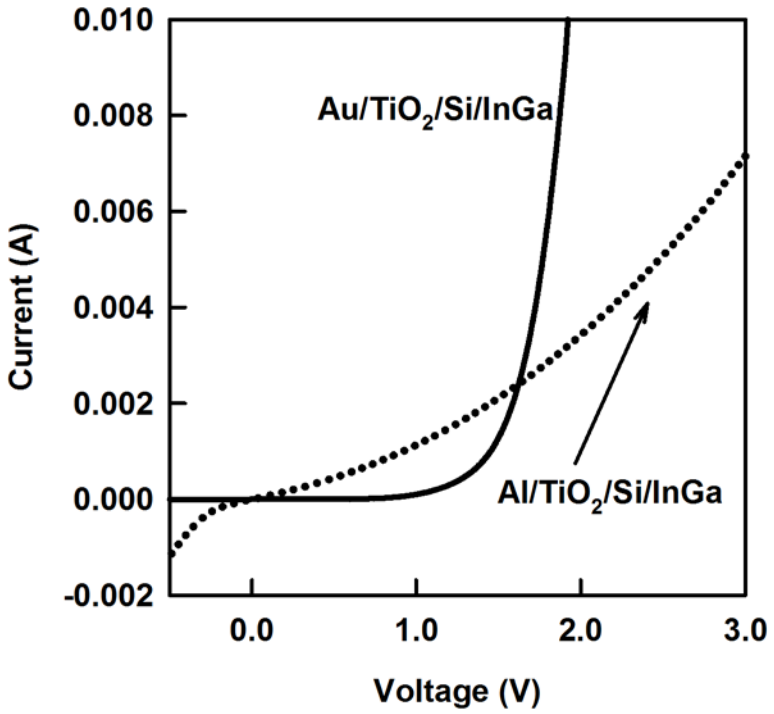

Fig. 2.6 Plots of (a) d(*V*)/d(ln*I*) vs. *I* and (b) *H*(*I*) vs. *I* utilized to calculate *n*, R_s, and Φ_B according to the Cheung method.

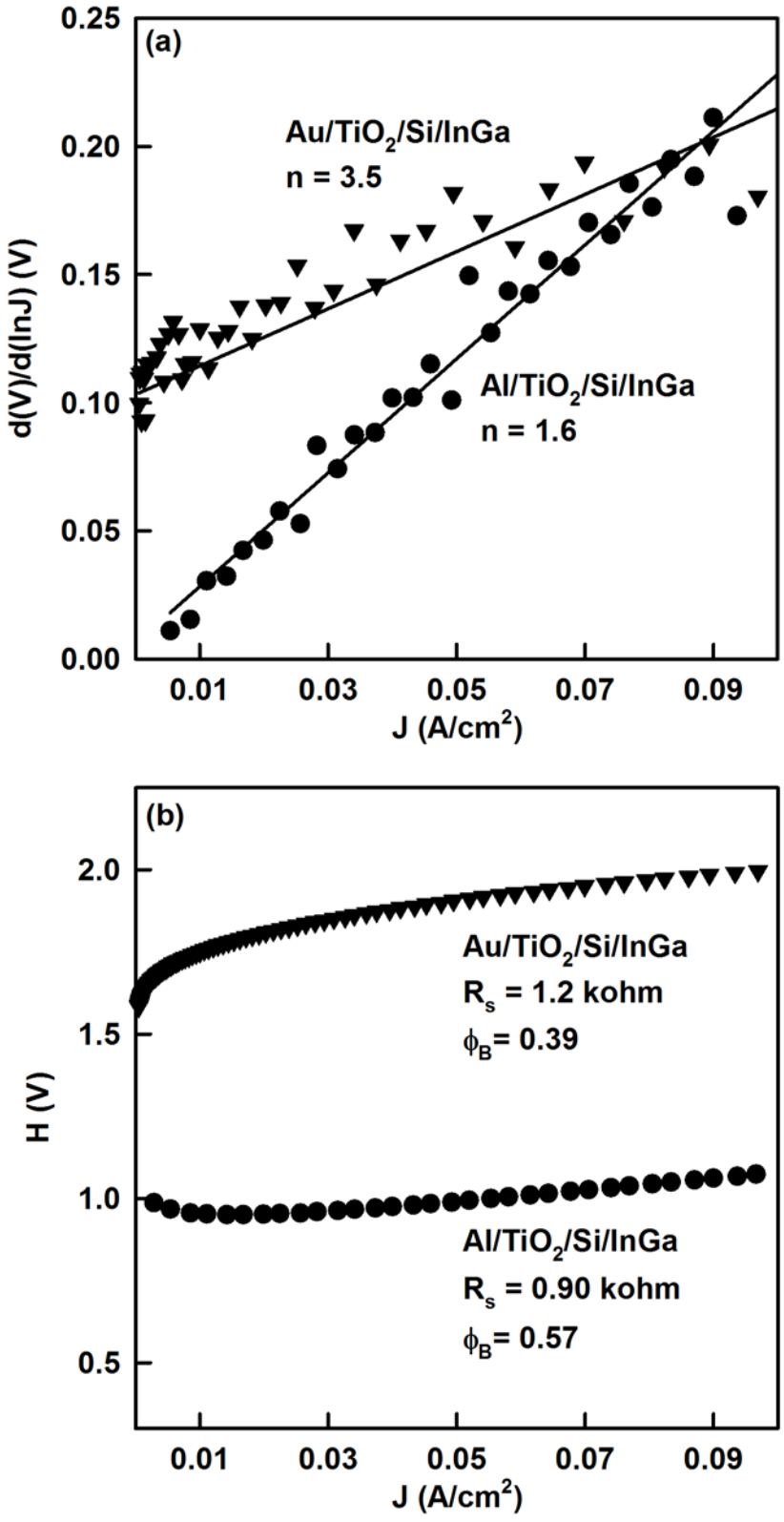

Fig. 2.7 (a) Dependence of capacitance upon voltage for undoped anatase TiO_2 (100 nm, 24 hr anneal). Voltage ranges leading to accumulation, depletion, and inversion at the TiO_2-metal contact are shown. Only the data taken under the depletion condition are useful for calculating carrier concentration. (b) The data in (a) plotted in conventional Mott-Schottky form. The plots are recorded at 1 MHz. For the bias voltage polarity used with this diode structure, a positive slope indicates n-type behavior.

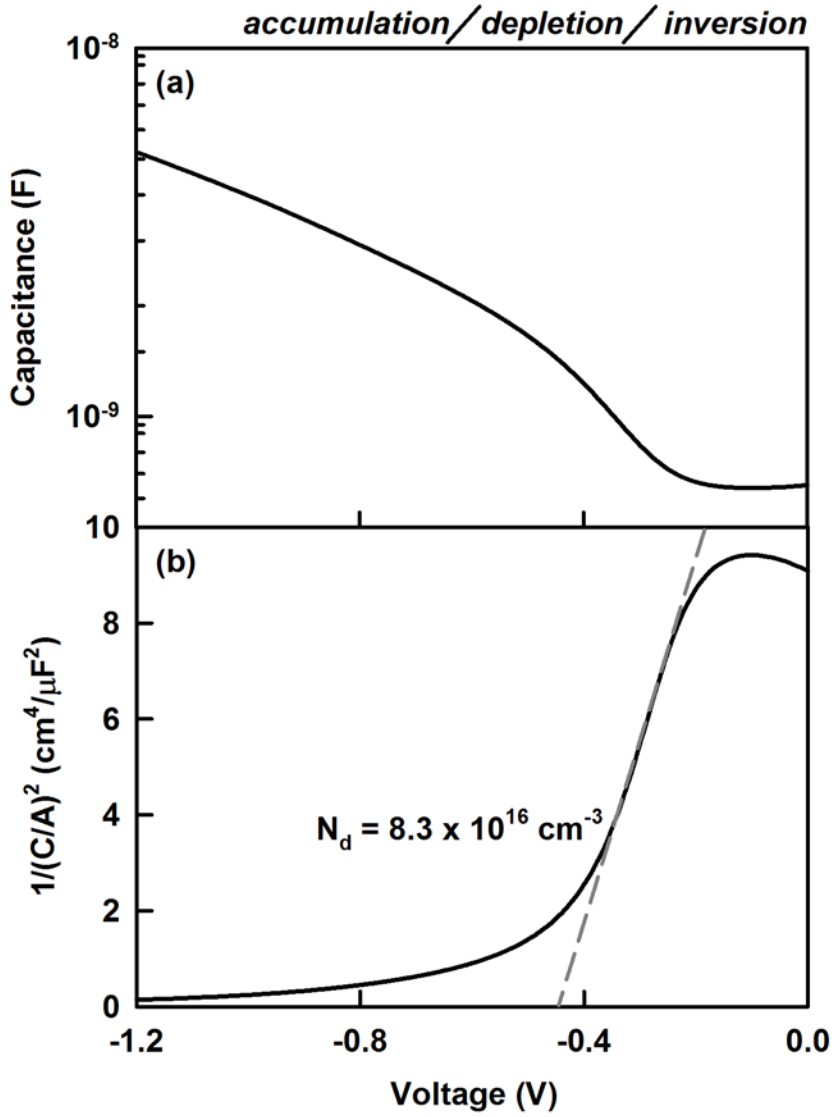

2.7 References

[1] C. S. Enache, J. Schoonman, and R. Van De Krol, *"The photoresponse of iron- and carbon-doped TiO_2 (anatase) photoelectrodes,"* J. Electroceram. 13, 177-182 (2004).

[2] E.-J. Lee and S.-I. Pyun, *"Analysis of nonlinear Mott-Schottky plots obtained form anodically passivating amorphous and polycrystalline TiO_2 films,"* J. Appl. Electrochem. 22, 156-160 (1992).

[3] M. K. Nowotny, L. R. Sheppard, T. Bak, and J. Nowotny, *"Defect chemistry of titanium dioxide. Application of defect engineering in processing of TiO_2-based photocatalysts,"* J. Phys. Chem. C 112, 5275-5300 (2008).

[4] D. K. Schroder, *Semiconductor Material and Device Characterization* (John Wiley & Sons, Inc., Hoboken, New Jersey, 2006).

[5] C. F. Windisch and G. J. Exarhos, *"Mott-Schottky analysis of thin ZnO films,"* J. Vac. Sci. Technol. A 18, 1677-1680 (2000).

[6] R. O'Hayre, M. Nanu, J. Schoonman, and A. Goossens, *"Mott-Schottky and charge-transport analysis of nanoporous titanium dioxide films in air,"* J. Phys. Chem. C 111, 4809-4814 (2007).

[7] J. Yan, D. C. Gilmer, S. A. Campbell, W. L. Gladfelter, and P. G. Schmid, *"Structural and electrical characterization of TiO_2 grown from titanium tetrakis-isopropoxide (TTIP) and TTIP/H_2O ambients,"* J. Vac. Sci. Technol. B 14, 1706-1711 (1996).

[8] T. Miyagi, M. Kamei, E. Sakaguchi, T. Mitsuhashi, and A. Yamazaki, *"Photocatalytic property and deep levels of Nb-doped anatase TiO_2 film grown by metalorganic chemical vapor deposition,"* Jpn. J. Appl. Phys. 43, 775-776 (2004).

[9] K. Kobayashi, M. Takata, Y. Fujimura, and S. Okamoto, *"Investigation of trapping states in a Nb-doped rutile by admittance spectroscopy,"* J. Appl. Phys. 60, 4191-4196 (1986).

[10] N. Szydlo and R. Poirier, *"I-V and C-V characteristics of Au/TiO_2 Schottky diodes,"* J. Appl. Phys. 51, 3310-3312 (1980).

[11] R. Konenkamp, *"Carrier transport in nanoporous TiO_2 films,"* Phys. Rev. B: Condens. Matter 61, 11057-11064 (2000).

[12] A. Da Silva Filho and N. C. Frateschi, *"Optimized electrolyte for electrochemical capacitance-voltage profiling of carrier concentration in $In_{0.49}Ga_{0.51}P$,"* J. Electron. Mater. 28, 1428-1432 (1999).

[13] A. P. Singh, S. Kumari, R. Shrivastav, S. Dass, and V. R. Satsangi, *"Iron doped nanostructured TiO_2 for photoelectrochemical generation of hydrogen,"* Int. J. Hydrogen Energy 33, 5363-5368 (2008).

[14] P. C. Banbury, H. K. Henisch, and A. Many, *"On the theory of the isothermal Hall effect in semiconductors,"* Proc. Phys. Soc. A 66, 753-758 (1953).

[15] R. C. Chiechi, E. A. Weiss, M. D. Dickey, and G. M. Whitesides, *"Eutectic gallium-indium (EGaIn): A moldable liquid metal for electrical characterization of self-assembled monolayers,"* Agnew. Chem. 120, 148-150 (2008).

[16] S. M. Sze, *Physics of Semiconductor Devices* (John Wiley & Sons, New York, 1969).

[17] M. Ni, M. K. H. Leung, D. Y. C. Leung, and K. Sumathy, *"Theoretical modeling of TiO_2/TCO interfacial effect on dye-sensitized solar cell performance,"* Sol. Energy Mater. Sol. Cells 90, 2000-2009 (2006).

[18] S. A. Bashar, PhD Thesis, King's College London, England, 1998.

[19] S. I. Shah, Y. Li, T. Gessmann, and E. F. Schubert, *"Experimental analysis and a new theoretical model for anomalously high ideality factors (n>>2.0) in GaN-based p-n junction diodes,"* Mat. Res. Soc. Symp. Proc. 798, Y7.11.11-16 (2004).

[20] S. K. Cheung and N. W. Cheung, *"Extraction of Schottky diode parameters from forward current-voltage characteristics,"* Appl. Phys. Lett. 49, 85-87 (1986).

[21] A. T. R. Briggs and J. P. Stagg, *"Series resistance effects in electrochemical carrier concentration profiling,"* Semicond. Sci. Technol. 3, 469-476 (1988).

[22] J. A. von Windheim, V. Venkatesan, D. M. Malta, and K. Das, *"Comparison of the electric properties of single-crystal and polycrystalline diamond by hall effect and capacitance-voltage measurements,"* Diamond Relat. Mater. 2, 841-846 (1993).

[23] J. H. Werner, *"Schottky barrier and pn-junction I/V plots - small signal evaluation,"* Appl. Phys. A 47, 291-300 (1988).

[24] R. van de Krol, A. Goossens, and J. Schoonman, *"Mott-Schottky analysis of nanometer-scale thin-film anatase TiO_2,"* J. Electrochem. Soc. 144, 1723-1727 (1997).

[25] X. Li, S. Wu, P. Hu, X. Xing, Y. Liu, Y. Yu, M. Yang, J. Lu, S. Li, and W. Liu, *"Structures and magnetic properties of p-type Mn:TiO_2 dilute magnetic semiconductor thin films,"* J. Appl. Phys. 106, 043913 (2009).

[26] T. Miyagi, T. Ogawa, M. Kamei, Y. Wada, T. Mitsuhashi, A. Yamazaki, E. Ohta, and T. Sato, *"Deep level transient spectroscopy analysis of an anatase epitaxial film grown by metal organic chemical vapor deposition,"* Jpn. J. Appl. Phys., Part 2 40, 404-406 (2001).

[27] H. Matsui, H. Tabata, N. Hasuike, H. Harima, and B. Mizobuchi, *"Epitaxial growth and characteristics of N-doped anatase TiO_2 films grown using a free-radical nitrogen oxide source,"* J. Appl. Phys. 97, 1-8 (2005).

[28] T. Fukumura, Y. Yamada, K. Tamura, K. Nakajima, T. Aoyama, A. Tsukazaki, M. Sumiya, S. Fuke, Y. Segawa, T. Chikyow, T. Hasegawa, H. Koinuma, and M. Kawasaki, *"Magneto-optical spectroscopy of anatase TiO_2 doped with Co,"* Jpn. J. Appl. Phys., Part 2 42, 105-107 (2003).

[29] H. Tang, K. Prasad, R. Sanjines, P. E. Schmid, and F. Levy, *"Electrical and optical properties of TiO_2 anatase thin films,"* J. Appl. Phys. 75, 2042-2047 (1994).

[30] K.-P. Wang and H. Teng, *"Zinc-doping in TiO_2 films to enhance electron transport in dye-sensitized solar cells under low-intensity illumination,"* Phys. Chem. Chem. Phys. 11, 9489-9496 (2009).

Chapter 3: Manipulation of Charged Defects in Undoped Polycrystalline TiO_2

3.1 Abstract

Defect engineering of polycrystalline TiO_2 is complicated by charged point defects and grain boundaries that alter bulk carrier concentration in a manner that depends on synthesis and post-treatment protocols. These influences are hard to decouple with standard electrical characterization methods, which are not well-suited to metal oxides like TiO_2. Here, TiO_2 donor carrier concentration (N_d) is investigated as a function of film thickness, annealing time, and illumination using a rigorous Schottky diode-based electrical characterization approach. N_d scales inversely with film thickness due to a reduction in the concentration of electrically active grain boundaries in the bulk. Annealing of polycrystalline TiO_2 at 550°C induces film densification that reduces the void volume surface area available for charge trapping. Low-level photostimulation drives N_d toward a bulk-like value of 1.2×10^{17} cm^{-3} irrespective of film microstructure; this suggests either a reduction in grain boundary potential barrier height or surface state-induced Fermi level pinning. Strategies for defect engineering polycrystalline metal oxides must focus on tuning electrical activity of grain boundaries and intergranular voids for successful control and manipulation of N_d.

3.2 Introduction

Many metal oxide semiconductors with wide bandgaps (> 3 eV) possess electronic properties that, in combination with chemical stability and modest cost, suit them well for

important applications such as photocatalysis [1, 2], dye-sensitized solar cells (DSSCs) [3], and gas sensing for environmental pollutants [4], combustion products [5], and explosives [6]. Such applications would benefit greatly from the same precision in controlling charge carrier concentration that is presently possible for conventional microelectronic devices based on silicon and III-V semiconductors. In photocatalysts and DSSCs, for example, such control would permit manipulation of near-surface or near-interface electric fields to optimize the flow of photogenerated charge carriers [7]. In gas sensors based on electrical conductivity, such control would improve the sensitivity, which depends upon background charge carrier concentration [8].

Defect engineering is used extensively in the semiconductor processing industry to produce devices with well-defined physical properties (e.g., electrical conductivity, switching frequency, power consumption) [9]. In as-grown, undoped TiO_2, oxygen vacancies (V_O) and/or titanium interstitials (Ti_i) introduce large concentrations of shallow donor levels that result in n-type conduction at standard temperatures and pressures [10]. Control and manipulation of defects in single crystal TiO_2 has been demonstrated via mechanisms such as surface-bulk coupling and photostimulation [11].

Polycrystalline TiO_2 is a more complicated system due to the presence of grain boundaries that can alter the electrical properties of the film and serve as traps for charge carriers. Similar intricacies were encountered optimizing polycrystalline Si for solar cell and integrated circuit applications [12, 13]. Since polycrystalline semiconductors contain defects caused by incomplete bonding between adjacent crystallites, disordered material in the boundary region results in trapping states, space charge regions, and local potential barriers

[14, 15]. The extent to which these factors influence a particular semiconductor depends on crystallite size, preparation method, and the resulting intergrain properties [16].

Film thickness serves as a useful control for studying the interplay between microstructure and carrier concentration. For instance, N_d of Sb-doped SnO_2 decreases with film thickness in a manner that depends on substrate selection and, consequently, grain size, crystallinity, and morphology [17]. Windisch *et al.* noted a reduction in N_d of sputtered ZnO from 1.31 x 10^{17} cm^{-3} to 7.94 x 10^{16} cm^{-3} as film thickness was increased from 50 nm to 200 nm [18]. Generally, grain size is expected to increase with film thickness [19]. In materials like Cu_2O where smaller grains form to compensate for the additional stress in thicker films [20], N_d may track independently from either grain size or lattice constant. One report of TiO_2 carrier concentration for 40 nm, 80 nm, and 120 nm films prepared by e-beam evaporation exists [21]; no explanation is given for the observed drop in N_d with increasing film thickness. Certainly, a comprehensive study of N_d vs. film thickness for a range of thicknesses more suitable for practical applications is lacking.

In polycrystalline metal oxide films, there is also evidence to suggest that illumination influences carrier concentration. For n-type SnO_2 thin films, O_2^- ions adsorbed at grain boundaries create local potential barriers between adjacent grains [22]. Under moderate UV light irradiation (13 mW/cm^2), adsorbed oxygen ions are removed and the grain boundary potential barrier is reduced. Since grain boundary barrier height scales inversely with donor carrier concentration, this causes an increase in N_d. Over the course of ~16 hr, carrier concentration grows from 6 x 10^{18} cm^{-3} to 2.2 x 10^{19} cm^{-3}. The conductivity of ZnO is likewise affected when nonequilibrium holes are captured by surface oxygen states upon illumination with white light (2 W/cm^2) [23]. An oxygen adsorption-desorption

process creates slow photoconductivity transients that continue to decay even ~27 hr after termination of light exposure. A sole report exists to describe the effect of photostimulation on polycrystalline TiO_2 donor carrier concentration. Wang *et al.* examined changes in N_d for 70 nm TiO_2 grown by chemical vapor deposition (CVD) and illuminated with light (of unknown intensity) in the 320 to 390 range [24]. The authors saw a twofold increase in N_d (initially 10^{17} cm^{-3}) after two hours of illumination. A quantitative correlation between N_d and illumination time is difficult to tease out of this study and no explanation was provided for the observed trend. Further investigation of illumination-induced changes in polycrystalline TiO_2 donor carrier concentration is merited.

3.3 Methods and procedures

Undoped TiO_2 was deposited at 200°C as described in Chapter 2. Substrates of dimensions 2 cm x 2 cm were cut from commercial n-type Si(100) (Sb, 0.013 Ω·cm resistivity) and etched with dilute aqueous HF immediately prior to insertion in the vacuum chamber. All processing parameters including TTIP and H_2O temperatures, carrier gas flow rates, and ALD cycle timing were unchanged. After deposition and post-treatment, TiO_2 diode preparation and electrical characterization were performed as described in Chapter 2. Schottky diode structures fulfilling all criteria for accurate *C-V* measurements of carrier concentration were fabricated with InGa ohmic contacts to abraded n-Si and Al Schottky contacts to the TiO_2 surface. Additional details pertinent to the studies in this chapter will be discussed in brief.

3.3.1 Annealing

Following film deposition, thermal annealing was carried out as required in the Barnstead Thermolyne F79300 tube furnace introduced in Chapter 2. The standard process ramp rate was 20°C/min; here, ramp rates of 40°C/min and 60°C/min were also investigated. The annealing temperature was 550°C in all cases. Samples were kept at this temperature for 20 min, 1 hr, 2 hr, 3 hr, 7 hr, 11 hr, or 24 hr, depending on the experiment.

3.3.2 Illumination

For illumination studies, samples were cleaved in two and stored either in the dark or under a compact fluorescent lamp (2.3 mW/cm^2). The installed bulb was a Lights of America 9024B fluorescent linear quad bulb rated at 1800 lumens. Light intensity was measured with a digital SLR camera set to ISO of 100 and aperture of *f*/5.6 [25]. The light bulb was considered as a point source of light radiating equally in all directions. Dividing the light bulb's power output by the effective area at the bulb to sample distance allowed for determination of light intensity in W/m^2. Since there was no spectral filtering of the light, it is presumed that the light flux included a small fraction of super-bandgap radiation.

Illuminated samples were subjected to the incident light for 24 hr/day; the light source and samples were shrouded and enclosed with black aluminum foil to maintain constant intensity from day-to-night. In one case, an electrically characterized and cleaved 100 nm TiO_2 sample was immersed in a shallow petri dish of H_2O (DI, no further purification). The H_2O level was checked every two days and topped up as necessary. In all other cases, the TiO_2 samples were placed face up in opened plastic sample cases, all of which were situated directly under the light source.

3.3.3 Physical characterization

Film thickness was measured prior to annealing using a Rudolph Technologies AutoEL III single wavelength ellipsometer. The instrument was programmed to measure film thickness assuming a fixed value of refractive index for TiO_2 (2.458 [26]). The AutoEL III has a detection limit of approximately 10Å, an accuracy of ± 3 Å, and 1% repeatability.

X-ray photoelectron spectroscopy (XPS) data were obtained with a Kratos AXIS Ultra utilizing a pass energy of 40 eV, with excitation by monochromatized Al Kα radiation. Samples were mounted to the stainless steel sample holder with copper tape. Care was taken to minimize the amount of exposed tape to prevent inaccurate estimation of surface and bulk chemical composition. The angle between the incident beam and the sample is variable on this tool; an angle-resolved XPS study (θ = 90, 45, 30, and 10°) was performed to investigate the origin of the multiple contributions to the O *1s* spectra for TiO_2. An angle of 90° corresponds to the beam being perpendicular to the sample. For reference, the default angle between the incident beam and the substrate is 90°.

XPS data processing and analysis was accomplished with CasaXPS software. The binding energy (BE) scale was referenced to the C *1s* line of aliphatic carbon, set at 285.0 eV. Spectral regions were fit with either a linear or Shirley background. Components were added to the spectra using Casa's automatic peak fitting feature. Estimates of peak binding energy and area were obtained by fitting an individual region (i.e. C *1s*). Percentage atomic concentrations were obtained by comparing the relative intensities of the peaks in the survey spectra.

TiO_2 morphology was examined using a Hitachi Model S4800 scanning electron microscope (SEM). It features a maximum resolution of 1.0 nm and a variable acceleration

voltage of 0.5 to 30 kV. Images were collected an at acceleration voltage of 15 kV. Samples for cross-sectional visualization were cleaved immediately prior to insertion in the vacuum chamber. In order to obtain well-resolved cross-sectional images, the sample stage was rotated by 180° and tilted by 10°.

X-ray diffraction (XRD) and all x-ray reflectivity (XRR) patterns were obtained at room temperature with a high-resolution Philips X'Pert diffractometer (λ = 0.15406 nm) operated at 45 kV and 40 mA with a Cu Kα1 primary x-ray beam from a hybrid monochromator consisting of a parabolic x-ray mirror and a 2-reflection Ge(220) monochromator (aka "X'Pert 2"). The secondary optics consisted of a high-speed PIXcel line detector using 255 channels.

For temperature-programmed XRD, a different Phillips X'Pert instrument (aka "X'Pert 1") was utilized. All settings were the same except for the presence of a (1) crossed-slit collimator for point focus applications, (2) Ni filter, and (3) parallel plate collimator with slit size of 0.1 mm x 10 mm.

MDI JADE software was used for XRD pattern analysis and phase identification. Anatase TiO_2 spectra were fit to JCPDS card No. 21-1272 (tetragonal, a = 3.7852, c = 9.5139). Data were cross-referenced with patterns for rutile (JCPDS card No. 21-1276) and brookite (JCPDS card No. 29-1360) TiO_2. JADE invokes Scherrer's formula to determine crystallite size:

$$D = \frac{0.9\lambda}{\beta \cos\theta} \qquad (3.1),$$

where λ = 0.15406 nm. The parameter $\beta = B - b$, where B is the observed FWHM and b is the instrument function determined from the broadening of the monocrystalline silicon diffraction line. For the analysis described here, it was assumed that peak broadening was

due to crystallite size only (i.e., contributions from microstrain or temperature variation were neglected).

In some instances, XRR data were fit using PANalytical X-ray reflectivity software to attain estimates for bulk density, roughness, and thickness. The program allows automatic fitting of simulated to experimental specular XRR curves. A sample stack of specific composition (e.g. Si/TiO_2) is defined by the user along with appropriate thickness and roughness ranges for each stack layer. Sample parameters can be obtained by segmented fitting, genetic algorithm routine, or combined fitting mode. The films synthesized in this work were modeled using a four layer stack ($Si/SiO_2/TiO_2/CH$) in the manner of [27, 28], with the combined fitting mode providing the best fit to the experimental data.

As the XRR fitting procedure is time consuming, bulk density can also be obtained in a more direct fashion. The experimentally determined critical angle of total external reflection, θ_c, is related to the bulk density of the film ρ according to:

$$\frac{\theta_c^2}{\rho} = \frac{r_e \lambda^2 Z N_A}{\pi A} = F \qquad (3.2),$$

where r_e is the classical electron radius (2.82×10^{-15} m), λ the x-ray wavelength, Z the atomic number, N_A Avogadro's number, and A the mass number [29]. Thus, F is a constant for a given material and irradiating beam. θ_c is obtained from the angle at which the XRR spectral intensity is half of the plateau value [30]. After θ_c has been extracted from the XRR curve, ρ is calculated directly from Eq. (3.2).

If desired, bulk density can be converted to porosity P via the simple expression

$$P(\%) = (1 - \rho / \rho_0) \times 100 \qquad (3.3),$$

where ρ_0 is the bulk density of single crystal anatase TiO_2 (3.89 g/cm^3). In this context, porosity should result from two sources: intragranular porosity and intergranular porosity. When grain growth rate is rapid, pores can be left behind as grain boundaries evolve; this causes pores trapped inside grains [31]. Intergranular pore shape and size is affected by the shape, size, and packing of bounding grains [32].

3.4 Results

3.4.1 Chemical composition

The chemical composition of TiO_2 grown by ALD was investigated to confirm the absence of unintentional "dopants" (e.g., carbon, metallic impurities from film precursors) and evaluate elemental states.

An example XPS survey spectrum for undoped TiO_2 deposited at 200°C and annealed at 550°C for 24 hr is shown in Fig. 3.1(a). Strong peaks corresponding to Ti *2p*, O *1s*, and C *1s* are observed. Previous studies in the Seebauer group have revealed that C is adsorbed to the vapor phase deposited TiO_2 surface and exists only minimally in the bulk after Ar ion sputtering [33]. To confirm this, the C *1s* peak was studied before and after depth profiling/film removal. The "surface" trace in Fig. 3.1(b) shows the C *1s* feature obtained prior to Ar ion sputtering. This translates to approximately 20% C on the film surface. The "bulk" trace in the same figure illustrates the substantial drop in C *1s* signal after the top 10 nm of the film are removed. As evidenced by the inability to curve fit the C feature after sputtering, there is less than 0.2 at% carbon in the bulk.

Multiplex scans were performed to inspect the Ti *2p* and O *1s* XPS features in more detail. Ti $2p_{3/2}$ and Ti $2p_{1/2}$ peaks are situated at 458.6 and 464.3 eV for undoped TiO_2 (Fig.

3.2(a)). The change in BE of the Ti *2p* peaks relative to those of metallic Ti and 5.7 eV line separation between Ti $2p_{3/2}$ and Ti $2p_{1/2}$ indicates that Ti atoms are in the +4 oxidation state [34]. The pronounced peak at ~529.5 eV in Fig. 3.2(b) corresponds to lattice oxygen, where the "90 deg" spectrum compliments the Ti *2p* spectrum described above.

A variety of interpretations exist to describe the features found in O *1s* spectra for metal oxide semiconductors. Perron *et al.* report contributions from bulk oxygen, "bridging" oxygen, and "top" oxygen for the O *1s* spectrum of rutile (110) single crystal TiO_2 where "bridging" atoms are two-fold coordinated and "top" are single-fold coordinated [35]. On the other hand, for polycrystalline anatase TiO_2, Lin and coworkers suggest a correlation between a small feature at ~532 eV and the concentration of oxygen vacancies in the bulk [36]. This link was reported earlier for Co-doped ZnO [37] and Co_3O_4 [38]. Given the multiple interpretations for the O *1s* signal, several of which relate to native defect concentration, angle-resolved XPS measurements were also performed.

Fig. 3.2(b) shows the change in O *1s* signal as a function of take-off angle ranging from 15 to 90°. A reduction in take-off angle translates to a reduction in the depth from which the XPS information is obtained. Consequently, data obtained at 15° is more sensitive to surface species. Fitting the spectra with two components, a high BE component at ~531.5 eV and a low BE component at ~529.5 eV, allows for comparison of the two peak areas. As seen in the inset of Fig. 3.2(b), the contribution of the high BE peak decreases substantially as take-off angle is increased from 15 to 90°. This suggests that the O *1s* feature at 531.5 eV originates from surface species, most likely hydroxyl groups [39, 40]. As such, the area of the high BE peak provides minimal insight into bulk or near-surface defect concentration.

Furthermore, it must be neglected in order to obtain an accurate estimate of surface elemental composition for undoped (and doped) TiO_2.

3.4.2 Morphology and crystallinity

Application of XRD, XRR, and SEM to the evaluation of TiO_2 microstructure permits investigation of crystallite size, bulk density, and crystallite shape as a function of film thickness and annealing time.

TiO_2 morphology and crystallinity for three permutations of film thickness and annealing time are shown in Fig. 3.3, where (a), (b), and (c) correspond to 100 nm/20 min, 100 nm/24 hr, and 300 nm/20 min, in that order. All films are polycrystalline anatase with preferential (101) orientation (JCPDS card No. 21-1272). An increase in peak intensity is observed for the 300 nm film, suggesting improved crystallinity. Annealing time has no effect on peak intensity. Film strain was estimated by comparing the *c*-axis lattice constant to that of bulk anatase TiO_2 (9.5139 Å); the variation was minimal (less than ± 0.3%) for all films. Cross-sectional SEM images indicate 100 nm TiO_2 comprises round (20 min – Fig. 3.3(a)) and oblong (24 hr – Fig. 3.3(b)) agglomerates with distinguishable crystallite boundaries but no obvious cracks or voids. The 300 nm film (Fig. 3.3(c)) exhibits more homogeneous texturing with little definition between adjacent crystallites.

To probe the dynamics of TiO_2 crystallization, temperature-programmed XRD (TPXRD) was carried out, selected results of which are shown in Fig. 3.4. Prior to annealing, no peaks are discernable (data not shown). By the time the sample temperature is ramped to 550°C at a rate of 45°C/min and the first data collection routine begun, peaks corresponding to the (101), (112), (200), and (211) orientations are clearly visible. Indeed,

little further change is observed with time. There is no enhancement in crystallinity for extended annealing as previously reported for TiO_2 synthesized by sol-gel [41] and CVD [42]. The conclusions obtained from TPXRD are consistent with the room temperature data in Fig. 3.3(a) and (b), however, which show minimal change in peak intensity for 20 min vs. 24 hr annealing time. In all likelihood, for the annealing temperature in this study, crystallization is probably complete by the time 550°C is even reached. For example, Kirsch and co-workers anneal 280 nm TiO_2 films synthesized by dip coating at temperatures of 400°C, 425°C, and 450°C [43]. Maximum XRD peak areas are reached at 12.5 min, 6.3 min, and 4 min for these annealing temperatures, respectively. Since high-resolution XRD spectra for even narrow 2-theta ranges require ~5 min to complete, a different temperature ramping and annealing strategy would have to be adopted to further probe in-situ crystallization of TiO_2 synthesized by ALD.

Room temperature XRD peak profiles were analyzed using Scherrer's formula to obtain average crystallite size in the film growth direction for TiO_2 films of varying thickness and subjected to assorted post-deposition annealing times. As depicted in Figs. 3.5(a) and (b), crystallite size remains ~40 to 50 nm for the film thicknesses and annealing times in this study. Annealing ramp rate was found to have no effect on crystallite size (data not shown).

It is important to highlight the physical significance of "crystallite size" obtained in this manner. First, a crystallite is a unit lattice in which atoms are arranged in a specific position; in contrast, a grain may comprise a collection of crystallites arranged in a single direction. While grain size typically scales with crystallite size [44], the latter cannot be manipulated to obtain a quantitative value such as "grain boundary surface area per unit volume," for example. Second, in a system such as polycrystalline TiO_2, crystallites are

tightly packed thus precluding charged defect states or facile atomic diffusion between individual crystallites. It is also worth mentioning that subtleties in evolution of crystallite size may be obscured by the fact that this method of XRD analysis yields size in the film growth direction *only*. For example, crystallites may evolve laterally in shape and size in a manner not captured by the above characterization method. In-plane XRD measurements to probe lateral variations in crystallite size were attempted, but peak intensities were too weak to obtain information of any value.

XRR spectra fitting shows a slight decrease in TiO_2 bulk density from 3.64 g/cm^3 to 3.48 g/cm^3 as film thickness increases from 100 to 300 nm (Fig. 3.5(c) and (e)). Conversely, annealing at 550°C causes a significant density increase of ~0.3 g/cm^3 for long (24 hr) anneal times (Fig. 3.5(d)). For comparison, the bulk density of single crystal anatase is 3.89 g/cm^3.

3.4.3 Influence of film thickness on carrier concentration

Values of TiO_2 donor carrier concentration versus film thickness for samples stored in the dark are shown in Fig. 3.6. Phenomenological curves have been included as a guide to the eye. Each N_d value represents the average of three distinct data sets acquired one week apart. Consequently, error bars represent week-to-week variation in measured carrier concentration. The uncertainties in the linear fits of the Mott-Schottky plots are not displayed since they lead to <2% error in the determined carrier concentration. For TiO_2 films annealed for 20 min at 550°C (Fig. 3.6(a)), there is a steady decrease in N_d from approximately 6.2 x 10^{17} cm^{-3} to 2.8 x 10^{16} cm^{-3} as film thickness is increased from ~50 nm to ~300 nm. Samples annealed for 24 hr exhibit a similar decrease in N_d from 2.0 x 10^{17} cm^{-3} to 4.0 x 10^{15} cm^{-3} with increasing film thickness. As evidenced in Fig. 3.6(b), the range of

carrier concentration variation is comparatively larger for films annealed for 24 hr. Additionally, the concavity of the N_d versus thickness trend is inverted.

While the donor carrier concentration of undoped TiO_2 has been determined for films of varying thickness (refer back to Table 2.1), a rigorous empirical correlation between N_d and film thickness has not existed up until now. Van de Krol and co-workers used *C-V* measurements to determine N_d for 40 nm, 80 nm, and 120 nm polycrystalline anatase TiO_2 on ITO produced by e-beam evaporation [21]. Their results are amended to, and in close agreement with, those in Fig. 3.6(b). In fact, after deposition, their samples were annealed at 450°C in air for 10 hr in order to induce crystallization. They obtain a crystallite size of 310 nm from analysis of XRD data for the 120 nm film using Scherrer's equation. In all likelihood, this estimate is inaccurate due to improper application of the 0.9 constant in Eq. (3.1), which assumes spherical crystals. While Lee and Pyun [45] report values for N_d of 62 nm and 83 nm polycrystalline anatase TiO_2 prepared by galvanostatic method, they implement a numerical analysis procedure to obtain "instantaneous" N_d as a function of applied voltage. Consequently, it is only possible to infer "average" values of 6.0×10^{19} cm^{-3} and 2.5×10^{19} cm^{-3} for the 62 nm and 83 nm films. It should be noted, however, that N_d decreases with increasing thickness for both of these existing reports.

3.4.4 Influence of annealing time on carrier concentration

The influence of annealing time on N_d was systematically studied. Fig. 3.7 reveals a gradual decrease in N_d for 100 nm thick TiO_2 from 4.7×10^{17} cm^{-3} to 7.9×10^{16} cm^{-3} as annealing time is increased from 20 min to 24 hr. As a reminder, these values correspond to a dramatic rise in bulk density (Fig. 3.5(d)) but a minimal change in crystallite size (Fig.

3.5(b)). Film thickness was re-measured after annealing to assess the extent (if any) of film compaction. The post-annealing thickness of the sample annealed for 24 hr was 95% of its original value. Samples annealed for intermediate time between 20 min and 24 hr exhibited compaction ranging from 1 to 4%.

3.4.5 Influence of illumination on carrier concentration

It was clear that N_d varied little with time when samples were stored in dark (Fig. 3.6(a)). Samples prepared with either 20 min or 24 hr post-deposition annealing exhibited minimal week-to-week variation in N_d. In contrast, Fig. 3.8(a) displays N_d as a function of thickness at t = 0, 1 week, and 2 weeks for samples annealed for 20 min and exposed to fluorescent light. The carrier concentration varies significantly for some thicknesses, sometimes by as much as a factor of five. Since the lamp is unfiltered, it is assumed that the incident light comprises some UV as well as visible components. Upon illumination, donor carrier concentration becomes relatively independent of film thickness and converges to ~1.2 x 10^{17} cm^{-3}. Fig. 3.8(b) presents change in N_d from t = 0 plotted to better illustrate magnitude and direction of carrier concentration change. Depending upon the initial value of the carrier concentration, illumination can stimulate either an increase or a decrease in N_d. By the one week point, a steady-state value of N_d is reached for all films thicker than 100 nm.

3.4.6 Influence of aqueous environment on carrier concentration

TiO_2 is chemically stable in aqueous environments, but little is known about the influence of extended exposure to H_2O *and* visible light on N_d in polycrystalline anatase films. The evolution of a steady state N_d value for 20 min annealed, illuminated TiO_2 as

described in Section 3.4.5 prompted a "reversibility study" of sorts. In considering the possible mechanisms for this change in N_d, the out-diffusion of electrically active hydrogen was considered as a potential cause. By extension, exposing a steady-state sample to illumination in a H-rich environment could prompt N_d to rise. 100 nm TiO_2 annealed for 24 hr was prepared and cleaved in half. One fragment was placed in H_2O and illuminated; the other fragment was stored in the dark. After a period of two weeks, the carrier concentrations of both samples were measured. There was no obvious degradation in the quality of the film following H_2O exposure as assessed by visual inspection. N_d for the H_2O, illuminated sample was 4.6 x 10^{16} cm^{-3}; N_d for the reference fragment was 7.9 x 10^{16} cm^{-3}. This difference is slightly outside the expected run-to-run variation (± 0.5 x 10^{16} cm^{-3}) in donor carrier concentration obtained by *C-V* measurements, but is otherwise unremarkable.

3.5 Discussion

Several physical phenomena should be considered in the context of the observed carrier concentration trends. Some or all of these entities may contribute to the behaviors observed for undoped TiO_2. These include:

1) Intragranular voids i.e., voids that may exist within grains, which can support electrically active defects but are unreachable by gas-phase diffusion. In principle, these could disappear upon sufficient annealing and compaction.
2) Intergranular voids i.e., voids that may exist between grains, which can support electrically active defects (probably with geometries similar to above) and are possibly reachable by gas phase diffusion. In principle, these could also disappear upon sufficient annealing and compaction.

3) Interfaces between grains i.e., grain boundaries, which can support electrically active defects (with different geometries than above) and are unreachable by gas-phase diffusion. These interfaces do not disappear even with essentially 100% compaction.

The schematic in Fig. 3.9 clarifies the terminology outlined in this list. Intragrain voids are only reachable by a bulk diffusion process, usually coupled with grain boundary diffusion. In common parlance, a grain boundary is defined as both a solid-solid interface as well as a boundary between two grains with associated void volume. Here, it is useful to distinguish between these two configurations. For grains separated by a solid-solid interface, the bond strains, dangling bonds, and atomic arrangements near charged defects take on certain characteristics. In contrast, a void volume surface (or grain boundary with a certain amount of porosity) likely resembles a standard free surface in terms of dangling bonds, atomic arrangements, etc. The two configurations also differ with respect to their reactivity in catalysis. Chemical reactants can typically reach voids between grains via gas-phase or liquid-phase diffusion through a network of pores and voids. The efficiency of such diffusion can be quantified by parameters such as a catalyst effectiveness factor and Thiele modulus. However, reactants typically reach the solid-solid interfaces between grains much more slowly by thermally activated site-hopping diffusion. These interfaces are normally considered inaccessible in catalysis applications.

Within this conceptual framework, changes in donor carrier concentration can be related to variations in charge trapped at grain boundaries. In polycrystalline materials, the dominant mechanism affecting current flow is grain boundary scattering; lattice scattering governs current flow in undoped single crystal material. Grain boundary potential barriers

are formed in polycrystalline semiconductors when the grain boundary regions have a lower chemical potential for majority carriers than the grains themselves. Integration of Poisson's equation yields an expression for barrier height (Φ_B) at the grain boundary [46]:

$$\Phi_B = \frac{eN_d}{2\varepsilon_s\varepsilon_0} w^2 \quad (3.4),$$

where ε_s and ε_0 are the dielectric constant of the semiconductor and permittivity of free space, in that order, and w is the thickness of the depleted grain boundary region. Electroneutrality stipulates that there exists electric charge Q trapped at the grain boundary:

$$Q = \frac{2N_d}{w} \quad (3.5).$$

Rearrangement of Eqs. (3.4) and (3.5) yields an expression for N_d in terms of grain boundary barrier height:

$$N_d = \frac{eQ^2}{8\varepsilon_s\varepsilon_0\Phi_B} \quad (3.6).$$

The significance of this equation is twofold. First, if the potential barrier at the grain boundary increases, N_d decreases. Second, in terms of control mechanisms, N_d is clearly reduced by removing charge trapped at the grain boundary. This has been remarked upon for polycrystalline ZnO; films with large carrier concentrations have low potential barriers at grain boundaries [47].

3.5.1 Effects of film thickness and annealing time on carrier concentration

Results of extensive experimentation showed that both annealing time and film thickness exerted strong effects on carrier concentration. The fact that annealing time should affect carrier concentration was not surprising, as an extensive literature base shows that

point defects, extended defects, and film microstructure vary upon heating. However, the strong effects of film thickness were less expected *a priori*.

This study indicates that N_d of polycrystalline TiO_2 decreases with increasing film thickness due to a reduction in concentration of electrically active grain boundaries. Grain boundaries serve as unintentional donor defects [48] by annihilating or trapping charge carriers. Furthermore, it is energetically favorable for native donor defects such as V_O and Ti_i to aggregate at grain boundaries and cause an increase in n-type conductivity [49]. Despite the minimal change in crystallite size with increasing film thickness noted in Fig. 3.5(a), *crystallite* size is not a proxy for *grain* size and does not insinuate constant grain size with increasing film thickness. Since in-plane crystallite size was unable to be determined, crystallite size could be changing in any direction other than the film growth direction. Furthermore, for a system like polycrystalline TiO_2, attributing XRD peak broadening to changes in crystallite size alone (Section 3.3.3) may be less than ideal. XRD line broadening can also arise due to strain, which is minimal for the films examined here, or changes in the density of crystallite defects such as stacking faults and twins [50].

To this end, since the intensities of the (101), (112), (200), and (211) anatase TiO_2 XRD peaks increase with film thickness (see Fig. 3.3), thicker films are more crystalline i.e., possess additional long-range ordering. This increase is shown graphically in Fig. 3.10(a), where the intensities of three different anatase TiO_2 (*hkl*) orientations are plotted vs. film thickness. Recasting the data of Fig. 3.6(a) as a function of peak intensity instead of film thickness reveals a well-behaved linear dependence (Fig. 3.10(b)); N_d decreases as film crystallinity is enhanced. In studies that obtain grain size by a suitable method like transmission electron microscopy (TEM), an increase in XRD peak intensity scales with an

increase in grain size [51]. In such cases, it is also acknowledged that crystallite size ascertained by XRD and grain size measured by TEM differ substantially

At the same time, the slight decrease in bulk density noted in Fig. 3.5(c) may arise due to the appearance of electrically inactive porous features such as extended defects or cracks. Further investigation of film microstructure by TEM or with a higher resolution SEM instrument would help confirm this conceptualization.

Annealing of polycrystalline anatase at 550°C induces film densification that decreases TiO_2 donor carrier concentration. Heating for extended time causes film compaction and a drop in overall porosity, where porosity stems from voids in between (as well as perhaps within) grains. Regardless, a reduction in total void volume minimizes the void volume surface area available for capture of electrically active donor defects such as V_O and Ti_i. Assuming that some fraction of grain boundaries within the bulk are not just solid-solid interfaces but rather boundaries with associated void volumes, annealing removes trapped charge and, per Eq. 3.6, reduces N_d.

XRR data analysis revealed negligible change in bulk density after approximately seven hours of annealing (Fig. 3.5(d)). Indeed, for annealing times after this, N_d remained fairly constant. A correlation between porosity and donor carrier concentration has been observed for anatase TiO_2 prepared by sol-gel synthesis [52]. For films of unknown thickness subjected to 700°C post-annealing, N_d dropped from 1.97×10^{19} cm^{-3} to 9.0×10^{17} cm^{-3} as post-annealing time was increased from 22 min (27% porosity) to 54 min (22% porosity). The trend was not explained. The order of magnitude change in N_d versus percent variation in porosity is similar to that found here.

3.5.2 Effects of illumination on carrier concentration

Illumination affords another means of affecting charge trapped at grain boundary defects and N_d in polycrystalline TiO_2. As mentioned in Section 3.2, low-level illumination provides a route for altering the potential barriers in other metal oxide semiconductors such as ZnO [23] and SnO_2 [22]. Fig. 3.8(a) showed N_d converging toward a common value regardless of thickness. Critically, this points to crystallinity and grain boundary concentration *no longer* influencing N_d. It is important to point out that the ~1.2 x 10^{17} cm^{-3} carrier concentration arrived at upon illumination is only coincidentally equal to the steady state N_d arrived at upon extended annealing. There is no implication of a shared rationale behind the two data sets.

Interestingly, conduction in solar illuminated polycrystalline Si approaches that in monocrystalline material and is no longer affected by grain boundary size or density [53]. This could be attributed to a change in the dominant mechanism affecting current flow in the bulk. If grain boundary scattering no longer governs conduction, N_d will no longer scale with the charge trapped at grain boundaries. One could envision a scenario wherein illumination reduces Φ_B to zero via passivation of electrically active defects and dangling bonds at grain boundaries; N_d then reflects an *inter*granular free carrier concentration more so than an *intra*granular free carrier concentration. Alternatively, illumination could create film or grain boundary surface states that pin the Fermi level [54]. The decrease in N_d for thin films and increase in N_d for thick films is consistent with both of these explanations. If a fundamentally different mechanism is responsible for conduction (or lack thereof) in illuminated TiO_2, the magnitude of N_d can be set/pinned anywhere within the band gap. For TiO_2 grown by CVD, Wang and co-workers saw N_d increase from approximately 10^{17} cm^{-3} to

10^{18} cm^{-3} upon illumination with light (of unknown intensity, ~3 hr) in the 320 to 390 nm range [24]. Assuming this illumination intensity and duration permitted N_d to reach steady-state, ~10^{18} cm^{-3} reflects the concentration of lattice defects and/or surface energy states for their particular CVD film.

3.5.3 Possible influence of electrically active hydrogen

Given the H_2O-based chemistry used for film synthesis, it is within the realm of possibility that hydrogen acts as a shallow donor in polycrystalline TiO_2 and contributes discernably to N_d under certain conditions (presumably, for short annealing times) where electrically active hydrogen remains within the material. Here, hydrogen content or evolution was not explicitly probed; some indirect evidence is obtained from the available materials characterization techniques.

Since crystallization of as-synthesized amorphous material occurs rapidly at 550°C, excess hydroxyls from the TTIP/H_2O ALD process [55] could remain in the thin film upon only brief heat treatment. Fig. 3.11 shows an intriguing implication of the O *1s* signal interpretation outlined in Section 3.4.1. When 100 nm TiO_2 (20 min anneal) is stored at ambient conditions, repeated XPS characterization over time suggests a substantial increase in the ratio of surface hydroxyl species to lattice oxygen atoms. At the same time, bulk film composition (Ti:O) remains unchanged. In theory, these trends could arise from dangling bonds on the film surface trapping mobile H as it exits the bulk. That being said, per Fig. 3.8(a), minimal week-to-week variation was noted in N_d of ~100 nm TiO_2 stored in the dark (for which similar XPS ratio information has not been obtained). This could point to the

mechanism of H evolution being irrelevant as a whole, or simply irrelevant for samples stored in the dark.

Furthermore, there is no indication of whether hydroxyl species should reside within grains or at grain boundaries *or* if these species would even be electrically active. Deuterium-enhanced SIMS profiles together with infrared measurements confirm that N_d of 40 nm thick polycrystalline ZnO increases upon exposure to H_2 plasma due to incorporation of electrically active H into the film [56]. Annealing of H-injected (0001) ZnO at 600°C leads to a reduction in N_d [57]. The water-based TiO_2 ALD process does not involve energetic "insertion" of H like these studies. That being said, it cannot be ruled out that annealing of ALD TiO_2 at 550°C induces analogous removal of H out of configurations where it can serve as a shallow donor, either via in-situ passivation or out-diffusion.

3.5.4 Possible coupling between synthesis method and carrier concentration

Application of the rigorous Schottky diode metrology protocols outlined in Chapter 2 to the determination of undoped TiO_2 carrier concentration reveals that N_d is closely coupled to film properties such as morphology and microstructure. Since the TiO_2 atomic layer deposition methods and post-treatment strategies reviewed here allow substantial control and manipulation of N_d, there is reason to believe N_d may vary in a meaningful fashion with other film synthesis techniques. While the accuracies of the n-type carrier concentrations found in the literature for anatase TiO_2 are uncertain due to metrology complications, gross trends should be apparent. For ease of evaluation, synthesis methods are grouped into four categories: physical vapor deposition (PVD) including sputtering, evaporation, and pulsed

laser deposition (PLD); molecular beam epitaxy (MBE); CVD; and solution-based including sol-gel and dip coating.

Fig. 3.12(a) summarizes the literature values for N_d of undoped TiO_2 averaged and arranged by film synthesis method. In the same manner, Fig. 3.12(b) correlates available values for bulk density of undoped TiO_2 to synthesis method (also available in Table 3.1). For both graphics, the large error bars are indicative of the substantial spread in N_d and ρ for certain techniques. Since variations in crystallinity and film thickness are disregarded for the purpose of this analysis, the take-home message is primarily qualitative. For PVD techniques such as sputtering and evaporation, processing parameters including oxygen flow rate and chamber pressure dramatically affect bulk density [58, 59]. For solution-based methods like sol-gel, the choice of acid, base, or polymeric solution alters density by a comparable amount. Neglecting MBE due to the lack of available data for bulk density, Fig. 3.12(c) synthesizes the available literature data for N_d and ρ to evaluate a possible correlation. On the whole, there is reason to believe that the wide variance of n-type carrier concentration values found in the literature in the case of polycrystalline TiO_2 reflects, in part, differences in film porosity as a function of synthesis method. Denser films should contain less void volume surface area available for capture of electrically active donor defects; N_d values are closer to 10^{19} cm^{-3} for techniques that tend to produce more porous films.

Couched in a different fashion, it may be possible to interpret trends in N_d as a function of synthesis method in terms of variations in kinetic energy of atoms arriving at the substrate. The conductivity of diamond has been correlated to substrate temperature and thermal diffusivity in a manner that suggests particle kinetic energy during film deposition

and surface accommodation determine the physical properties of the resulting film [60]. Deposition techniques can be separated into three thermal regimes:

1) Thermal (0 – 0.3 eV): chemical vapor deposition, thermal evaporation, electrodeposition
2) Intermediate (1 – 100 eV): ion beam sputtering, cathodic arc, laser vaporization
3) Implantation (> 100 eV): high energy ion implantation

A relative low energy deposition process like CVD resulting in direct synthesis of polycrystalline material provides comparatively less opportunity for adatoms to move across the film surface. Since ALD is designed to minimize transport limitations, competition between deposition and surface diffusion is reduced. In both processes, however, the microstructure of the as-deposited film should be more porous. In a process involving intermediate energies, ionized gas atoms are being accelerated toward the surface with a substantial kinetic energy. This should cause film densification. At the same time, it should also lead to removal of some atoms and increased film disorder (i.e., defect concentration) unless significant substrate heating during deposition is permitted.

3.6 Conclusion

The present work provides the most rigorous examination to date of undoped TiO_2 donor carrier concentration as a function of film properties and external stimuli (heating, light). A correlation between film thickness and N_d is fleshed out for thicknesses of interest to photocatalysis, DSSCs, and gas sensors. Physical characterization helps elucidate trends in N_d as a function of preparation protocol; grain boundaries and intergranular void surface area couple strongly to film electrical properties. Certain synthesis methods may “lock-in”

the range of attainable carrier concentrations due to process kinetic energy, ambient gas composition and pressure, and inherent microstructure and porosity. Additional effort must be devoted to understanding the effects of electrically active grain boundaries on carrier concentration [45]; polycrystalline metal oxide semiconductors often hold the most promise for catalysis and sensing applications. The body of literature pertaining to *C-V* characterization of polycrystalline Si and Ge [61, 62] should be leveraged to better understand the challenges of defect engineering polycrystalline TiO_2 films synthesized via sputtering, sol-gel, and vacuum deposition methods. Further manipulation of undoped TiO_2 N_d may be possible with annealing temperatures less than 550°C or ramp rates less than 20°C/min that promote gradual crystallization and reduction of structural defects. The effect of illumination on polycrystalline TiO_2 carrier concentration should be probed in more detail, particularly with respect to time- and intensity-dependence.

3.7 Tables and figures

Table 3.1 Available values for undoped TiO_2 bulk density with corresponding film synthesis details.

Bulk Density (g/cm^3)	**Synthesis Method**	**Thickness (nm)**	**Crystallinity**	**Reference**
3.68 ± 0.03	Sputtering	~232	Not given	[63]
3.67 – 4.46	Sputtering	~40	Amorphous, anatase, rutile	[59]
3.06	Evaporation	56	Not given	[63]
3.57	Evaporation	117	Not given	[64]
3.62 ± 0.2	CVD	220	Anatase	[65]
3.85 ± 0.2	PECVD	220	Mixed anatase/rutile	[65]
3.45	PECVD	137	Not given	[63]
3.38	Spin-coating (acid)	246	Anatase	[66]
3.17	Spin-coating (base)	229	Anatase	[66]
3.83	Sol-gel (acid)	62 ± 0.5	Anatase	[67]
3.0	Sol-gel (polymer)	90 ± 0.5	Anatase	[67]
2.6 ± 0.2	Sol-gel	110 ± 10	Anatase	[68]
2.9 ± 0.1	Dip coating	Not given	Anatase	[69]
3.25 ± 0.05	Dip coating (100% EtOH)	150	Anatase	[70]
3.5 ± 0.05	Dip coating (90% EtOH)	Not given	Anatase	[70]
3.45 ± 0.05	Dip coating (80% EtOH)	110	Anatase	[70]

Fig. 3.1 (a) XPS survey spectrum of undoped TiO_2 acquired with the Kratos AXIS Ultra with Ti, O, C, and substrate peaks labeled and (b) comparison between C *1s* peak prior to and after Ar ion sputtering using the PHI 5400 instrument.

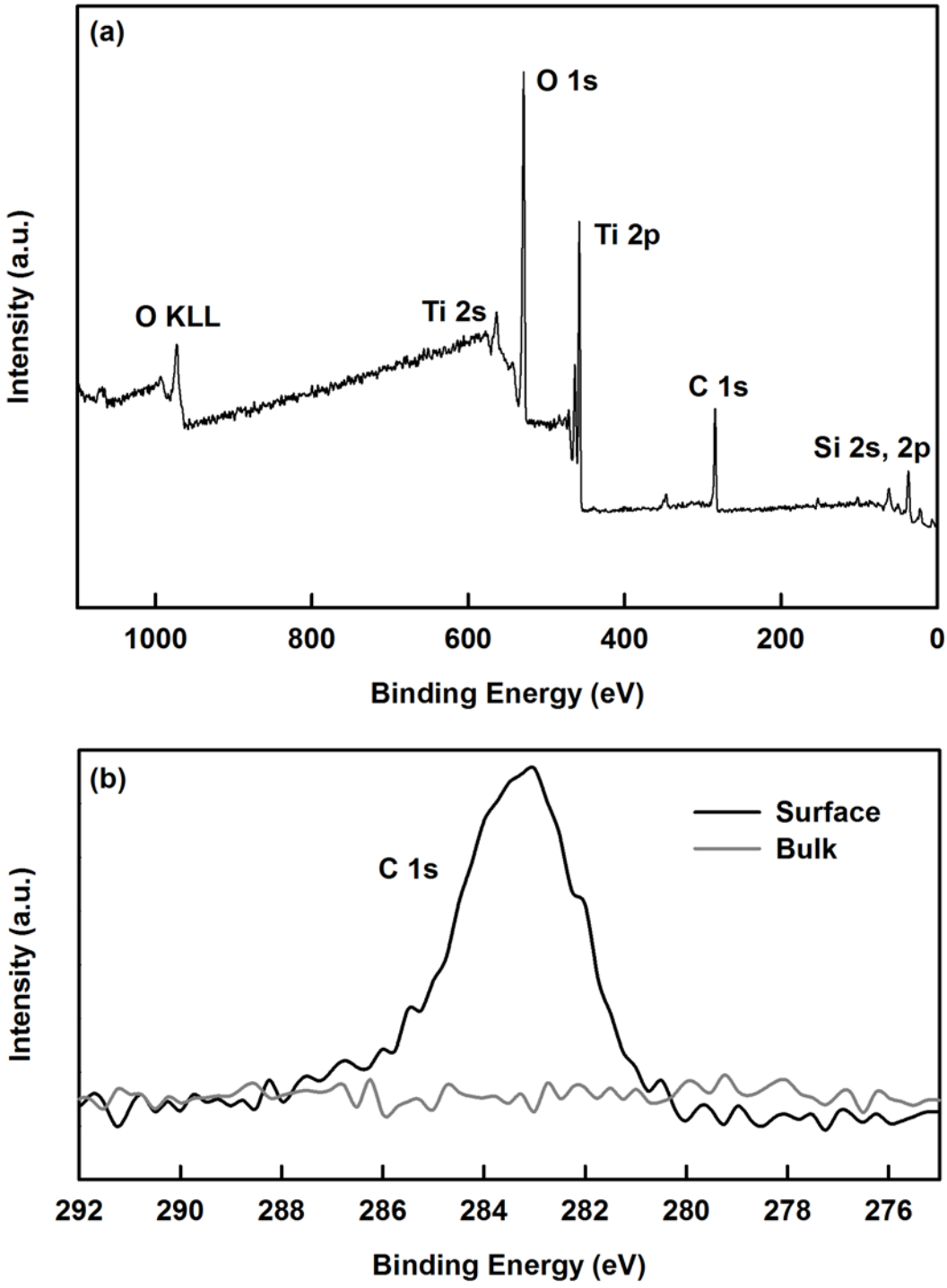

Fig. 3.2 (a) XPS spectrum of Ti *2p* in undoped TiO_2 and (b) angle-resolved XPS O *1s* spectra for undoped TiO_2 obtained at 90, 45, 30, and 15° take-off angle. The relative area of the high BE peak (surface OH) to the low BE peak (lattice O) as a function of take-off angle is shown in the inset. For reference, 90° is defined as the beam being perpendicular to the sample. Data obtained with the Kratos AXIS Ultra.

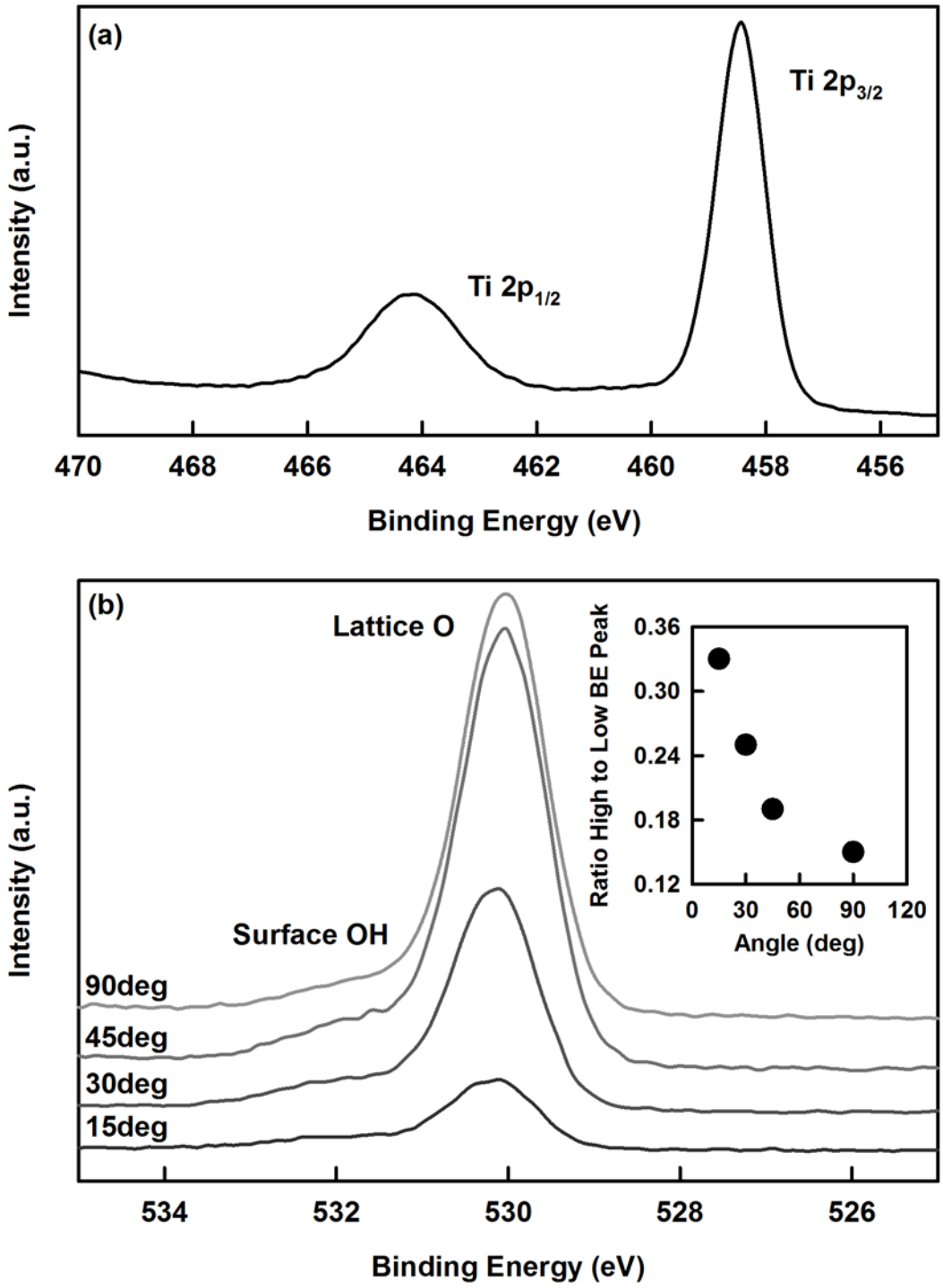

Fig. 3.3 XRD patterns of (a) 100 nm TiO_2/20 min anneal, (b) 100 nm TiO_2/24 hr anneal, and (c) 300 nm TiO_2/20 min anneal with corresponding cross-sectional SEM images.

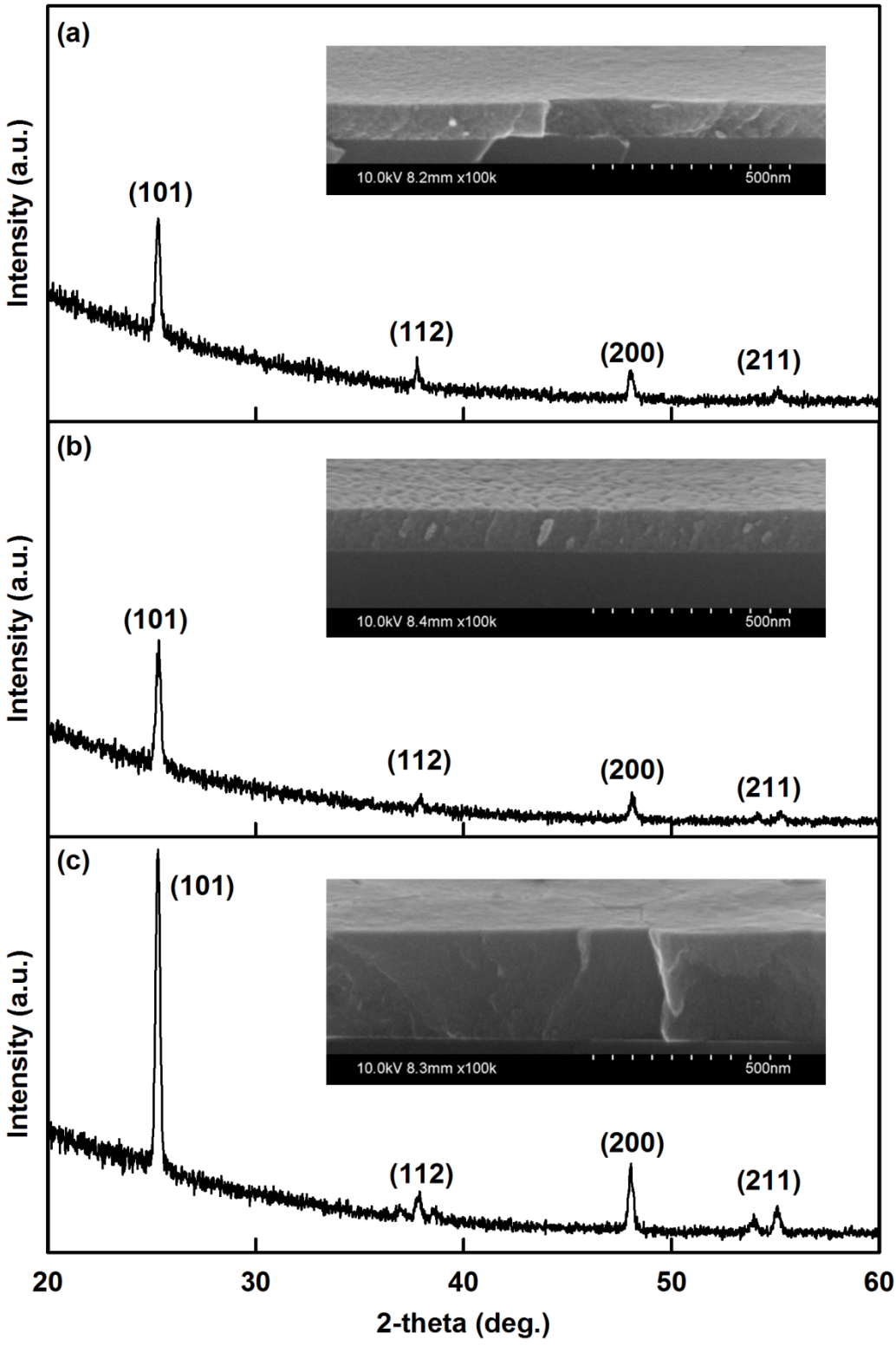

Fig. 3.4 Temperature programmed XRD for 100 nm, undoped TiO_2 where a scan was acquired instantaneously after ramping to 550°C (45°C/min) and then once per hour while at 550°C (1 hr, 19 hr shown here). Crystallization is basically complete by the time the instantaneous scan is collected.

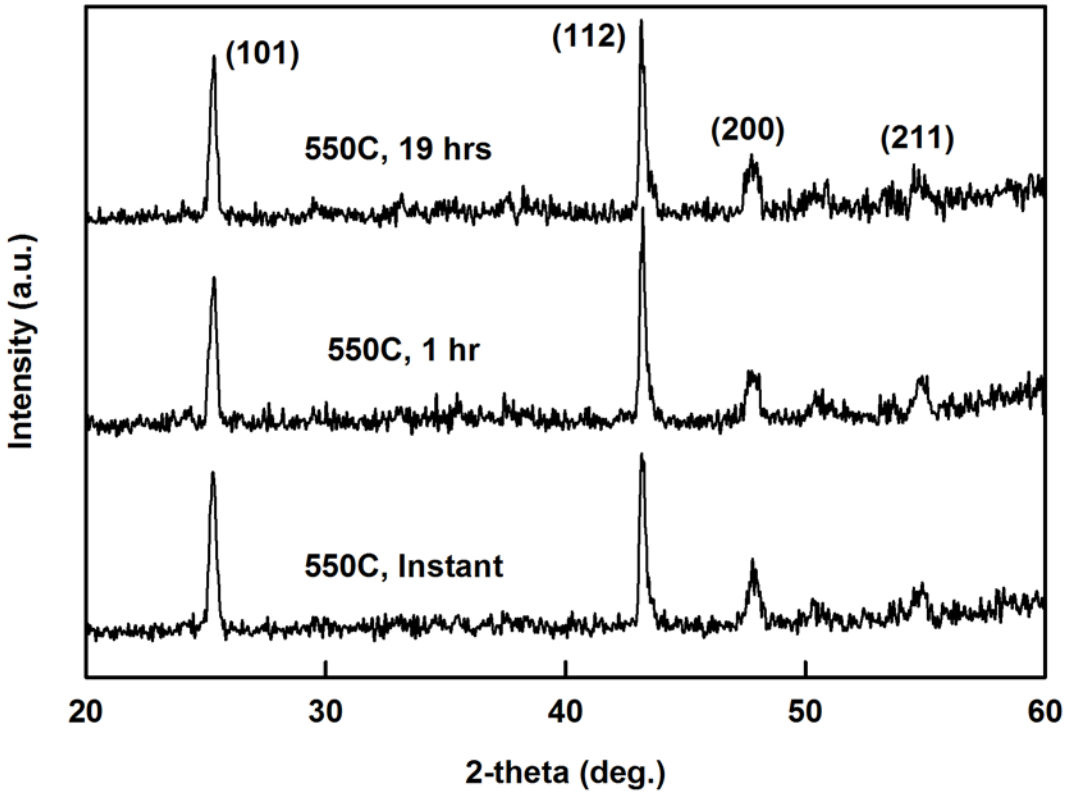

Fig. 3.5 Average crystallite size obtained by XRD peak fitting vs. (a) film thickness and (b) annealing time and bulk density obtained from XRR spectra fitting vs. (c) film thickness for 20 min annealing time, (d) annealing time, and (e) film thickness for 24 hr annealing time.

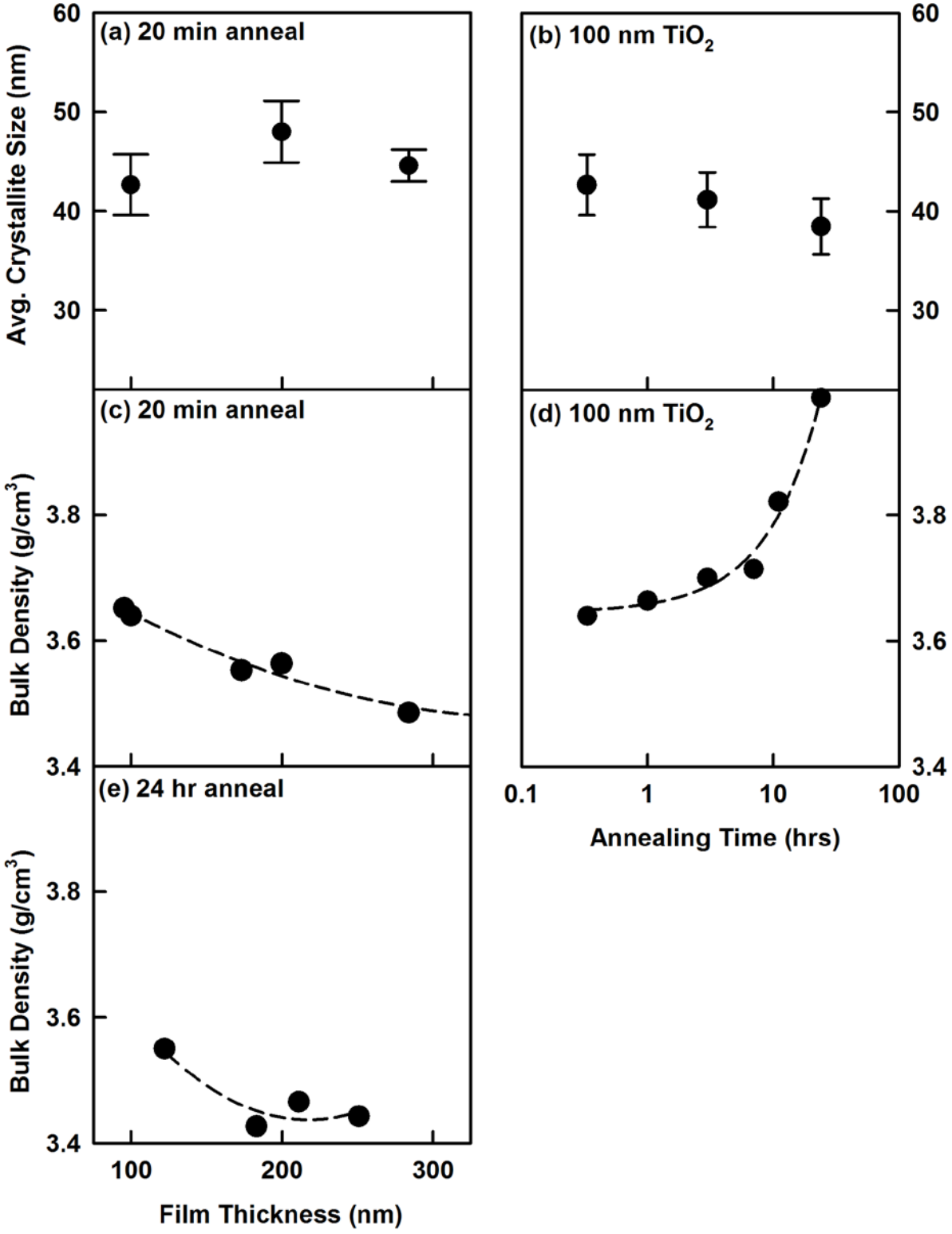

Fig. 3.6 N_d vs. film thickness for (a) anatase TiO_2 annealed at 550°C for 20 min and (b) anatase TiO_2 annealed at 550°C for 24 hr. Data for e-beam evaporated anatase TiO_2 [21] are shown in (b) for purposes of comparison. N_d values and corresponding error bars were obtained by averaging three distinct data sets acquired one week apart. All samples were stored in dark.

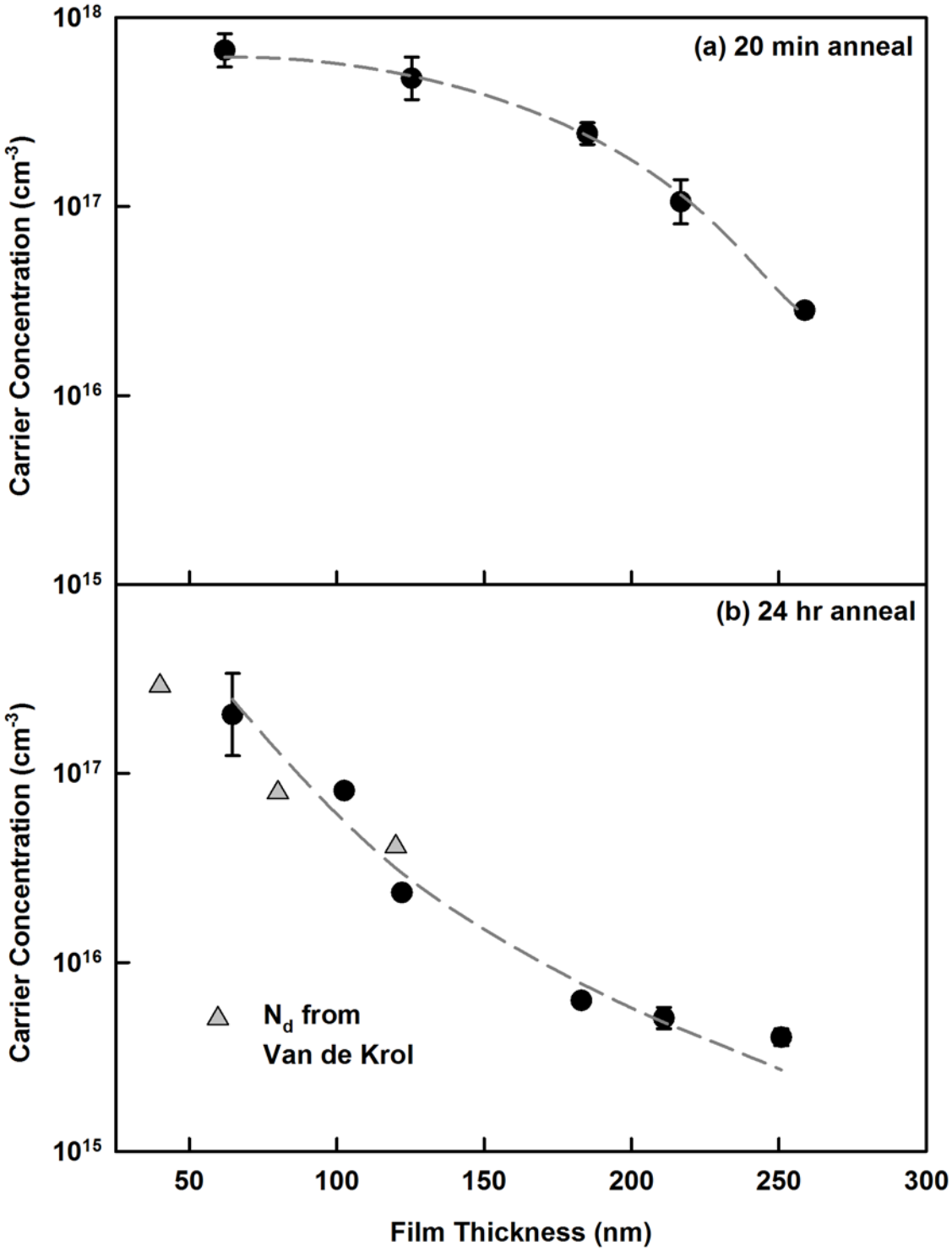

Fig. 3.7 N_d vs. annealing time for 100 nm anatase TiO_2. N_d values and corresponding error bars were obtained by averaging two distinct data sets acquired one week apart. All samples were stored in dark.

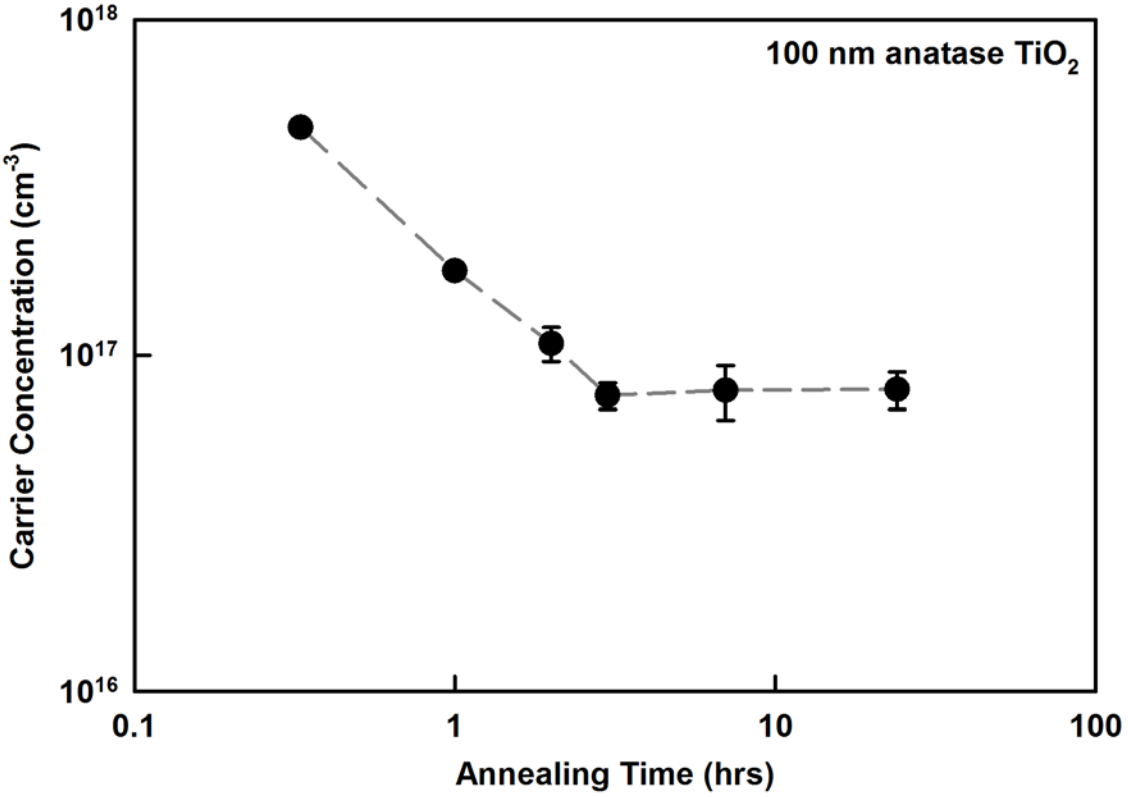

Fig. 3.8 (a) N_d vs. film thickness measured at t = 0, 1 week, and 2 weeks for 20 min anneal samples stored under fluorescent illumination and (b) change in N_d from t = 0 plotted to better illustrate magnitude and direction of carrier concentration change. Full-range on the y-axis scale corresponds to two orders of magnitude (i.e. 10^{16} to 10^{18} cm^{-3}).

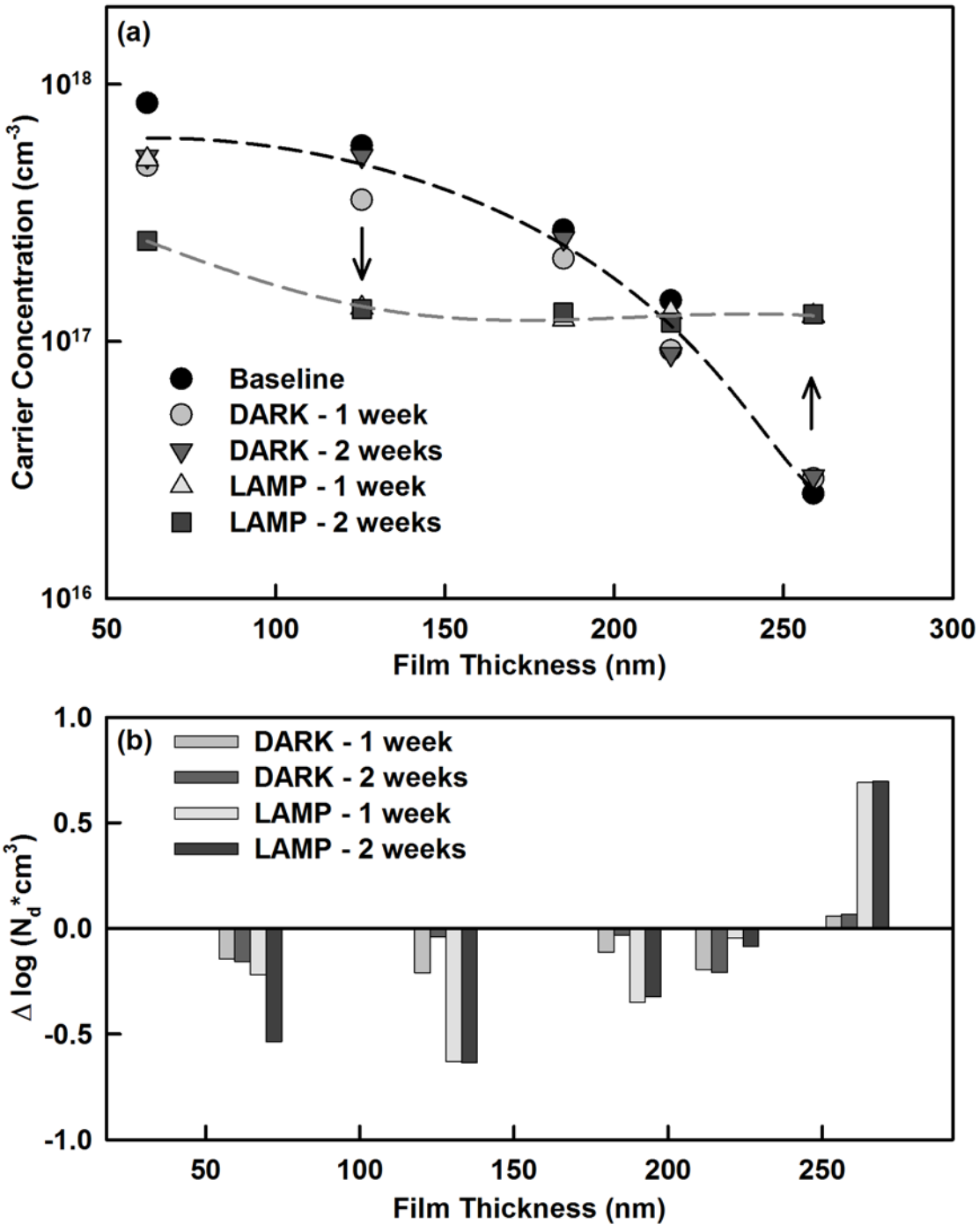

Fig. 3.9 Schematic of proposed polycrystalline TiO_2 microstructure containing differently oriented grains. The interfaces between grains are referred to as grain boundaries. In some cases, intergranular voids may exist at grain boundaries. These voids are bounded by grains and have an associated surface area. Voids may also exist within individual grains; these are referred to as intragranular voids.

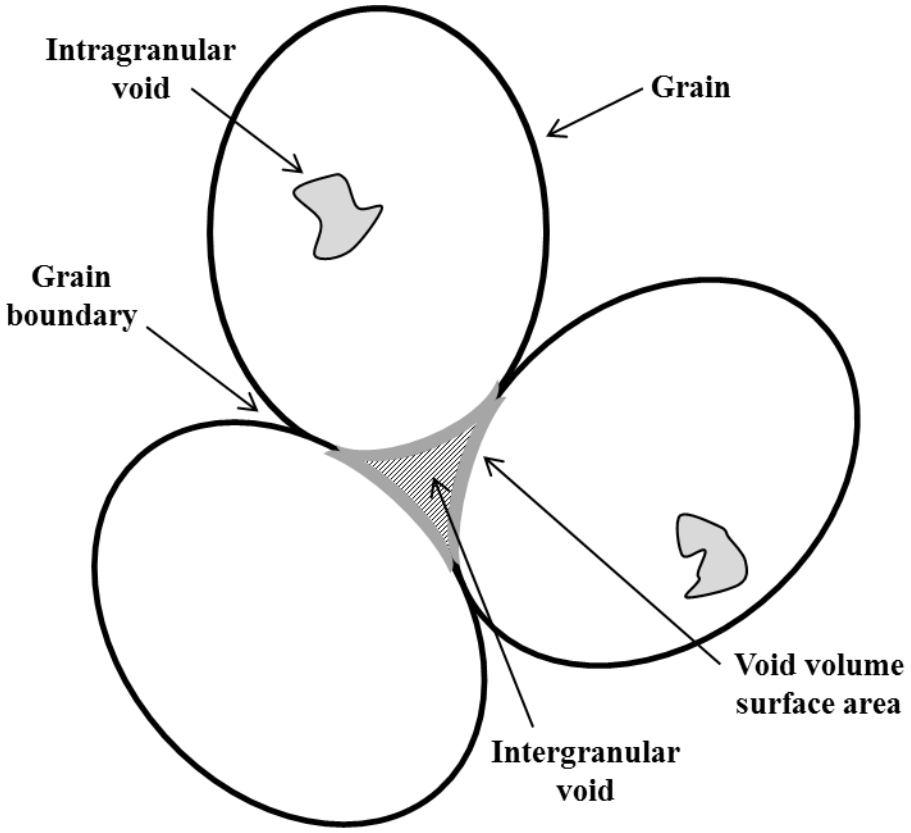

Fig. 3.10 (a) XRD peak intensity for (101), (200), and (211) reflections of anatase TiO_2 annealed for 20 min at 550°C vs. film thickness and (b) the N_d values from Fig. 3.6(a) recast as a function of (101), (200), and (211) peak height.

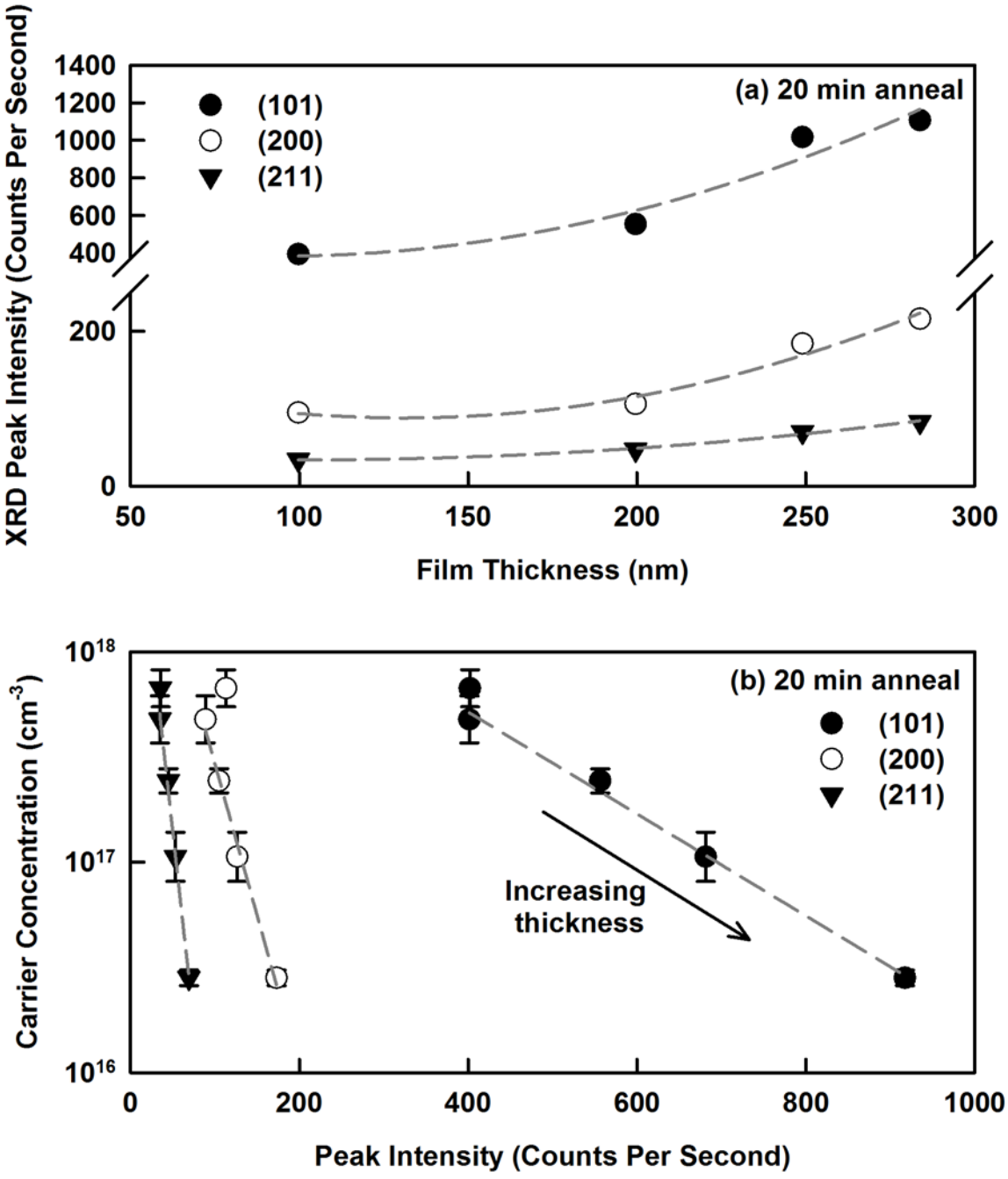

Fig. 3.11 XPS-derived ratio of surface OH species to lattice O as a function of days between TiO_2 deposition and XPS examination (top) as well as the ratio of lattice O to Ti (bottom). Sample was annealed for 20 min at 550°C and stored under ambient conditions.

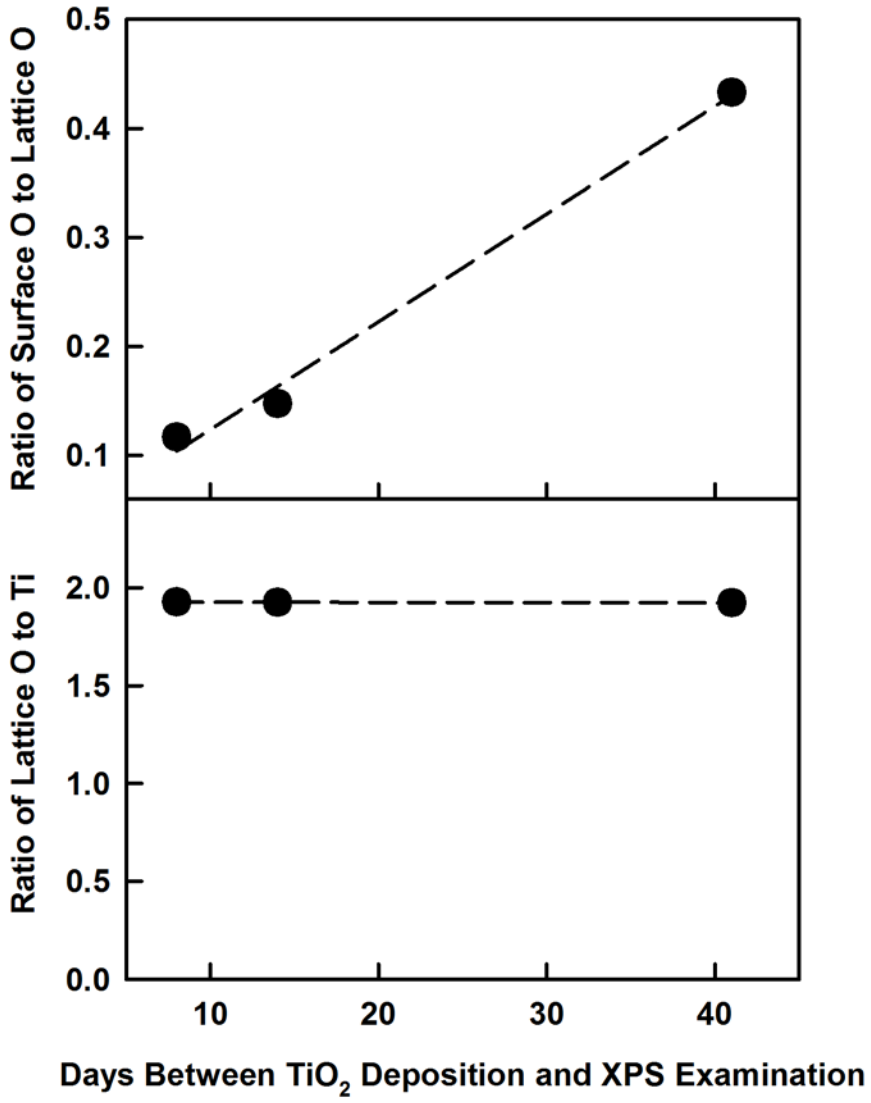

Fig. 3.12 (a) Literature values for N_d of undoped TiO_2 averaged and arranged by film synthesis method, (b) available measurements of undoped TiO_2 bulk density as a function of film synthesis method, and (c) proposed correlation between N_d and bulk density based on the available literature data.

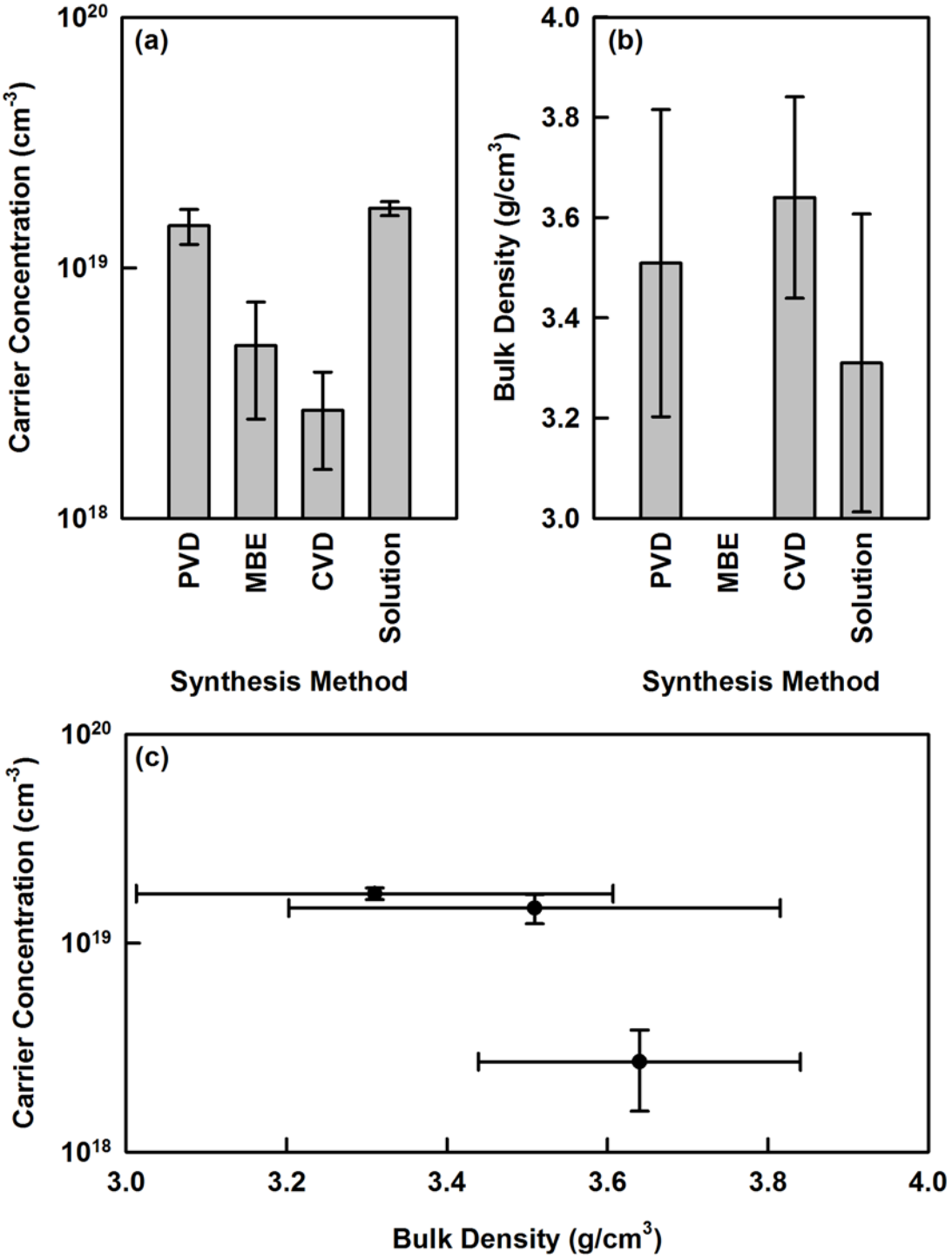

3.8 References

[1] K. Hashimoto, H. Irie, and A. Fujishima, *"TiO_2 Photocatalysis: A Historical overview and future prospects,"* Jpn. J. Appl. Phys. **44,** 8269-8285 (2005).

[2] A. L. Linsebigler, G. Lu, and J. T. Yates, Jr., *"Photocatalysis on TiO_2 surfaces. Principles, mechanisms, and selected results,"* Chem. Rev. **95,** 735-735 (1995).

[3] B. O'Regan and M. Gratzel, *"A low-cost, high-efficiency solar cell based on dye-sensitized colloidal TiO_2 films,"* Nature **353,** 737-740 (1991).

[4] A. Vaseashta, M. Vaclavikova, S. Vaseashta, G. Gallios, P. Roy, and O. Pummakarnchana, *"Nanostructures in environmental pollution detection, monitoring, and remediation,"* Sci. Technol. Adv. Mater. **8,** 47-59 (2007).

[5] N. O. Savage, S. A. Akbar, and P. K. Dutta, *"Titanium dioxide based high temperature carbon monoxide selective sensor,"* Sens. Actuators, B **72,** 239-248 (2001).

[6] S. Banerjee, S. K. Mohapatra, M. Misra, and I. B. Mishra, *"The detection of improvised nonmilitary peroxide based explosives using a titania nanotube array sensor,"* Nanotechnology **20,** 075502 (2009).

[7] M. Takahashi, K. Tsukigi, T. Uchino, and T. Yoko, *"Enhanced photocurrent in thin film TiO_2 electrodes prepared by sol-gel method,"* Thin Solid Films **388,** 231-236 (2001).

[8] D. Morris and R. G. Egdell, *"Application of V-doped TiO_2 as a sensor for detection of SO_2,"* J. Mater. Chem. **11,** 3207-3210 (2001).

[9] E. G. Seebauer and K. W. Noh, *"Trends in semiconductor defect engineering at the nanoscale,"* Mater. Sci. Eng., R **70,** 151-168 (2010).

[10] M. K. Nowotny, T. Bak, and J. Nowotny, *"Electrical properties and defect chemistry of TiO_2 single crystal. I. Electrical conductivity,"* J. Phys. Chem. B **110,** 16270-16282 (2006).

[11] A. G. Holllister, PhD Thesis, University of Illinois at Urbana-Champaign, Urbana, 2010.

[12] C. H. Seager, *"Grain boundaries in polycrystalline silicon,"* Annu. Rev. Mater. Sci. **15,** 271-302 (1985).

[13] Z.-J. Wang, S. Tsurekawa, K. Ikeda, T. Sekiguchi, and T. Watanabe, *"Relationship between Electrical Activity and Grain Boundary Structural Configuration in Polycrystalline Silicon,"* Interface Sci. **7,** 197-205 (1999).

[14] C. R. M. Grovenor, *"Grain boundaries in semiconductors,"* J. Phys. C **18,** 4079-4119 (1985).

[15] H. F. Matare, *"Carrier transport at grain boundaries in semiconductors,"* J. Appl. Phys. **56,** 2605-2631 (1984).

[16] L. L. Kazmerski, *"Micro- to nano-characterization of semiconductor grain boundaries,"* Surf. Sci. Rep. **19,** 169-189 (1993).

[17] H. Kaneko and K. Miyake, *"Physical properties of antimony-doped tin oxide thick films,"* J. Appl. Phys. **53,** 3629-3633 (1982).

[18] C. F. Windisch and G. J. Exarhos, *"Mott-Schottky analysis of thin ZnO films,"* J. Vac. Sci. Technol. A **18,** 1677-1680 (2000).

[19] M. Bender, N. Katsarakis, E. Gagaoudakis, E. Hourdakis, E. Douloufakis, V. Cimalla, and G. Kiriakidis, *"Dependence of the photoreduction and oxidation behavior of indium oxide films on substrate temperature and film thickness,"* J. Appl. Phys. **90,** 5382-5387 (2001).

[20] S. Jeong and E. S. Aydil, *"Structural and electrical properties of Cu_2O thin films deposited on ZnO by metal organic chemical vapor deposition,"* J. Vac. Sci. Technol. A **28,** 1338-1343 (2010).

[21] R. van de Krol, A. Goossens, and J. Schoonman, *"Mott-Schottky analysis of nanometer-scale thin-film anatase TiO_2,"* J. Electrochem. Soc. **144,** 1723-1727 (1997).

[22] Y. Muraoka, N. Takubo, and Z. Hiroi, *"Photoinduced conductivity in tin dioxide thin films,"* J. Appl. Phys. **105,** 103702 (2009).

[23] S. A. Studenikin, N. Golego, and M. Cocivera, *"Carrier mobility and density contributions to photoconductivity transients in polycrystalline ZnO films,"* J. Appl. Phys. **87,** 2413-2421 (2000).

[24] F. Wang, N. G. Kubala, and C. A. Wolden, *"Photoelectrochemical performance of anatase TiO_2 thin films deposited by self-limiting growth technique,"* J. Electrochem. Soc. **157,** D432-D436 (2010).

[25] "Measuring Light Intensity with your Camera's Meter." from http://www.firstrays.com/measurelight.htm.

[26] F. Gracia, F. Yubero, J. P. Holgado, J. P. Espinos, A. R. Gonzalez-Elipe, and T. Girardeau, *"SiO_2/TiO_2 thin films with variable refractive index prepared by ion beam induced and plasma enhanced chemical vapor deposition,"* Thin Solid Films **500,** 19-26 (2006).

[27] P. Colombi, E. Bontempi, L. E. Depero, Y. Azuma, and T. Fujimoto, *"X-ray reflectivity and total reflection x-ray fluorescence study of surface oxide evolution in a GaAs/AlAs multilayer system,"* J. Appl. Phys. **105,** 014307 (2009).

[28] K.-P. Wang and H. Teng, *"Zinc-doping in TiO_2 films to enhance electron transport in dye-sensitized solar cells under low-intensity illumination,"* Phys. Chem. Chem. Phys. **11,** 9489-9496 (2009).

[29] V. Holy, U. Pietsch, and T. Baumbach, *High Resolution X-ray Scattering from Thin Films and Multilayers* (Springer, New York, 1999).

[30] P. Bergese, E. Bontempi, and L. E. Depero, *"A simple solution to systematic errors in density determination by X-ray reflectivity: The XRR-density evaluation (XRR-DE) method,"* Appl. Surf. Sci. **253,** 28-32 (2006).

[31] A. K. M. Akther Hossain, M. A. Rahman, S. F. U. Farhad, B. Vilquin, and H. Tanaka, *"Effect of Li substitution on the magnetic properties of $LixMg_{0.40}Ni_{0.60-2x}Fe_{2+x}O_4$ ferrites,"* Physica B, In Press (2011).

[32] J. A. Kupecz, J. G. Gluyas, and S. Bloch, *Reservoir Quality Prediction in Sandstones and Carbonates* (American Association of Petroleum Geologists, 1997).

[33] R. Vaidyanathan, PhD Thesis, University of Illinois at Urbana-Champaign, Urbana, 2007.

[34] J. T. Mayer, U. Diebold, T. E. Madey, and E. Garfunkel, *"Titanium and reduced titania overlayers on titanium dioxide(110),"* J. Electron. Spectrosc. Relat. Phenom. **73,** 1-11 (1995).

[35] H. Perron, J. Vandenborre, C. Domain, R. Drot, J. Roques, E. Simoni, J. J. Ehrhardt, and H. Catalette, *"Combined investigation of water sorption on TiO_2 rutile (1 1 0) single crystal face: XPS vs. periodic DFT,"* Surf. Sci. **601,** 518-527 (2007).

[36] Y. B. Lin, Y. M. Yang, B. Zhuang, S. L. Huant, L. P. Wu, Z. G. Huang, F. M. Zhang, and Y. W. Du, *"Ferromagnetism of Co-doped TiO_2 films prepared by plasma enhanced chemical vapour deposition (PECVD) method,"* J. Phys. D: Appl. Phys. **41,** 195007 (2008).

[37] M. Naeem, S. K. Hasanain, M. Kobayashi, Y. Ishida, A. Fujimori, S. Buzby, and S. Ismat Shah, *"Effect of reducing atmosphere on the magnetism of $Zn_{1-x}Co_xO$ nanoparticles,"* Nanotechnology **17,** 1675-2680 (2006).

[38] G. Tyuliev and S. Angelov, *"The nature of excess oxygen in Co_3O_{4+x},"* Appl. Surf. Sci. **32,** 381-391 (1988).

[39] B. Erdem, R. A. Hunsicker, G. W. Simmons, E. D. Sudol, V. L. Dimonie, and M. S. El-Aasser, *"XPS and FTIR surface characterization of TiO_2 particles used in polymer encapsulation,"* Langmuir **17,** 2664-2669 (2001).

[40] H. Jensen, A. Soloviev, Z. Li, and E. G. Sgaard, *"XPS and FTIR investigation of the surface properties of different prepared titania nano-powders,"* Appl. Surf. Sci. **246,** 239-249 (2005).

[41] Y. Zhu, L. Zhang, W. Yao, and L. Cao, *"The chemical states and properties of doped TiO_2 film photocatalyst prepared using the Sol-Gel method with $TiCl_4$ as a precursor,"* Appl. Surf. Sci. **158,** 32-37 (2000).

[42] X. H. Xu, M. Wang, Y. Hou, S. R. Zhao, H. Wang, D. Wang, and S. X. Shang, *"Effect of Thermal Annealing on Structural Properties, Morphologies and Electrical Properties of TiO_2 Thin Films Grown by MOCVD,"* Cryst. Res. Technol. **37,** 431-439 (2002).

[43] B. L. Kirsch, E. K. Richman, A. E. Riley, and S. H. Tolbert, *"In-situ x-ray diffraction study of the crystallization kinetics of mesoporous titania films,"* J. Phys. Chem. B **108,** 12698-12706 (2004).

[44] J. R. Ares, A. Pascual, I. J. Ferrer, and C. Sánchez, *"Grain and crystallite size in polycrystalline pyrite thin films,"* Thin Solid Films **480-481,** 477-481 (2005).

[45] E.-J. Lee and S.-I. Pyun, *"Analysis of nonlinear Mott-Schottky plots obtained form anodically passivating amorphous and polycrystalline TiO_2 films,"* J. Appl. Electrochem. **22,** 156-160 (1992).

[46] C. H. Seager and T. G. Castner, *"Zero-bias resistance of grain boundaries in neutron-transmutation-doped polycrystalline silicon,"* J. Appl. Phys. **49,** 3879-3889 (1978).

[47] T. Tsurumi, S. Nishizawa, N. Ohashi, and T. Ohgaki, *"Electric properties of zinc oxide epitaxial films grown by ion-beam sputtering with oxygen-radical irradiation,"* Jpn. J. Appl. Phys. **38,** 3682-3688 (1999).

[48] H. Lu, W. J. Schaff, and L. F. Eastman, *"Growth of Thick InN by Molecular Beam Epitaxy,"* Mat. Res. Soc. Symp. Proc. **743,** L4.10.11 (2003).

[49] J. Nowotny, T. Bak, T. Burg, M. K. Nowotny, and L. R. Sheppard, *"Effect of grain boundaries on semiconducting properties of TiO_2 at elevated temperatures,"* J. Phys. Chem. C **111,** 9769-9778 (2007).

[50] B. E. Warren, *X-Ray Diffraction* (Dover, New York, 1969).

[51] A. H. Mahan, B. Roy, J. R. C. Reedy, D. W. Readey, and D. S. Ginley, *"Rapid thermal annealing of hot wire chemical-vapor-deposited a-Si:H films: The effect of the film hydrogen content on the crystallization kinetics, surface morphology, and grain growth,"* J. Appl. Phys. **99,** 023507-023509 (2006).

[52] G. Zhao, S. Utsumi, H. Kozuka, and T. Yoku, *"Photoelectrochemical properties of sol-gel derived anatase and rutile TiO_2 films,"* J. Mater. Sci. **33,** 3655-3659 (1998).

[53] C. A. Dimitriadis, *"The mobility of polycrystalline semiconductors under optical illumination,"* J. Phys. D: Appl. Phys. **18,** 2241-2246 (1985).

[54] J. Hofhuis, J. Schoonman, and A. Goossens, *"Time-of-flight studies on TiO_2/$CuInS_2$ heterojunctions,"* J. Appl. Phys. **103,** 014503 (2008).

[55] J. Aarik, A. Aidla, T. Uustare, M. Ritala, and M. Leskela, *"Titanium isopropoxide as a precursor for atomic layer deposition: characterization of titanium dioxide growth process,"* Appl. Surf. Sci. **161,** 385-395 (2000).

[56] C. A. Wolden, T. M. Barnes, J. B. Baxter, and E. S. Aydil, *"Infrared detection of hydrogen-generated free carriers in polycrystalline ZnO thin films,"* J. Appl. Phys. **97,** 043522 (2005).

[57] K. Ip, M. E. Overberg, Y. W. Heo, D. P. Norton, S. J. Pearton, C. E. Stutz, B. Luo, F. Ren, D. C. Look, and J. M. Zavada, *"Hydrogen incorporation and diffusivity in plasma-exposed bulk ZnO,"* Appl. Phys. Lett. **82,** 385-387 (2003).

[58] D. Mergel, D. Buschendorf, S. Eggert, R. Grammes, and B. Samset, *"Density and refractive index of TiO_2 films prepared by reactive evaporation,"* Thin Solid Films **371,** 218-224 (2000).

[59] S. H. Mohamed, O. Kappertz, T. P. L. Pedersen, R. Drese, and M. Wuttig, *"Properties of TiO_x coatings prepared by dc magnetron sputtering,"* Phys. Status Solidi A **198,** 224-237 (2003).

[60] J. J. Cuomo, D. L. Pappas, J. Bruley, J. P. Doyle, and K. L. Saenger, *"Vapor deposition processes for amorphous carbon films with sp3 fractions approaching diamond,"* J. Appl. Phys. **70,** 1706-1711 (1991).

[61] J. A. von Windheim, V. Venkatesan, D. M. Malta, and K. Das, *"Comparison of the electric properties of single-crystal and polycrystalline diamond by hall effect and capacitance-voltage measurements,"* Diamond Relat. Mater. **2,** 841-846 (1993).

[62] J. H. Werner, *"Schottky barrier and pn-junction I/V plots - small signal evaluation,"* Appl. Phys. A **47,** 291-300 (1988).

[63] M. Laube, F. Rauch, C. Ottermann, O. Anderson, and K. Bange, *"Density of thin TiO_2 films,"* Nucl. Instrum. Methods B **113,** 288-292 (1996).

[64] M. Hüppauff, K. Bange, and B. Lengeler, *"Density, thickness and interface roughness of SiO_2, TiO_2 and Ta_2O_5 films on BK-7 glasses analyzed by x-ray reflection,"* Thin Solid Films **230,** 191-198 (1993).

[65] T. Busani and R. A. B. Devine, *"Dielectric and infrared properties of TiO_2 films containing anatase and rutile,"* Semicond. Sci. Technol. **20,** 870-875 (2005).

[66] K. Jiang, A. Zakutayev, J. Stowers, M. D. Anderson, J. Tate, D. H. McIntyre, D. C. Johnson, and D. A. Keszler, *"Low-temperature, solution processing of TiO_2 thin films and fabrication of multilayer dielectric optical elements,"* Solid State Sci. **11,** 1692-1699 (2009).

[67] M. C. Ferrara, L. Pilloni, S. Mazzarelli, and L. Tapfer, *"Hydrophilic and optical properties of nanostructured titania prepared by sol-gel dip coating,"* J. Phys. D: Appl. Phys. **43,** 095301 (2010).

[68] M. Morozova, P. Kluson, J. Krysa, C. Gwenin, and O. Solcova, *"Oxalic acid sensors based on sol–gel nanostructured TiO_2 films,"* J. Sol-Gel Sci. Technol., In Press (2011).

[69] A. Kleiman, A. Márquez, M. L. Vera, J. M. Meichtry, and M. I. Litter, *"Photocatalytic activity of TiO_2 thin films deposited by cathodic arc,"* Appl. Catal., B **101,** 676-681 (2011).

[70] M. Bockmeyer and P. Löbmann, *"Crack formation in TiO_2 films prepared by sol-gel processing: Quantification and characterization,"* Thin Solid Films **515,** 5212-5219 (2007).

Chapter 4: Doping of Polycrystalline TiO_2 for Manipulation of Carrier Concentration*

4.1 Abstract

In direct contrast to the way in which silicon is precisely doped for integrated circuit applications in order to optimize device performance, there is little nuanced understanding of the correlation between TiO_2 doping level, charge carrier concentration, and the operation of TiO_2-based photocatalysts, dye-sensitized solar cells, and sensors. The present work applies a rigorous methodology to the determination of free carrier concentration for doped TiO_2 that is not amenable to standard metrology methods. Cr-, Mn-, and Nb-doped polycrystalline anatase TiO_2 are synthesized by atomic layer deposition (ALD) using $Ti(OCH(CH_3)_2)_4$, H_2O, $Cr(C_5H_7O_2)_3$, $Mn(DPM)_3$ (DPM = 2,2,6,6-tetramethyl-3, 5-heptanedionato), and $Nb(OCH_2CH_3)_5$ as the source materials for Ti, O, Cr, Mn, and Nb, respectively. Chemical composition and crystallinity are investigated. Measurements of donor carrier concentration are obtained for Cr-, Mn-, and Nb-doped TiO_2 synthesized by ALD. Possible causes for the obtained carrier concentrations are discussed.

4.2 Introduction

There is a substantial body of literature on the doping of metal oxide semiconductors such as TiO_2 [1, 2, 3, 4, 5, 6]. Historically, transition metals have been employed for altering bulk carrier concentration while non-metals such as N, C, and S are appealing candidates for

* Part of this work has been published: M.C.K. Sellers and E.G. Seebauer, *"Measurement method for carrier concentration in TiO_2 via the Mott-Schottky approach,"* Thin Solid Films **519,** 2103-2110 (2011).

narrowing the fundamental bandgap of TiO_2 [7, 8, 9]. Unfortunately, doping for precise control of donor/acceptor carrier concentration (N_d/N_a) is notoriously difficult due to the lack of readily available dopants providing shallow donor and acceptor levels [10]. Furthermore, as discussed in Chapter 3, TiO_2 contains oxygen vacancies (V_O) and/or titanium interstitials (Ti_i) that result in n-type conduction at standard temperatures and pressures. A successful doping strategy must compensate for native defects present as a function of TiO_2 preparation method and heat treatment history.

The relative merits of doping with metallic cations versus non-metal anions have been studied elsewhere. Experimental work in the mid-1990s showed that metal cation doping of TiO_2 significantly influenced photoactivity as well as charge carrier recombination and interfacial electron transfer rates [11]. Such manipulation is advantageous for supported metal catalysis and photocatalysis. Non-metal doping garnered increased interest around the same time due to concerns over thermal stability and carrier recombination centers in metal-doped TiO_2 [5]. When TiO_2 is doped with an anion such as N, the band gap is narrowed and the material's ability to absorb visible light increased [6]. For the applications of interest in this study, it is advantageous to introduce energy levels within the band gap and alter donor carrier concentration; non-metals are not ideal for this purpose.

As researchers continue to develop more advanced doping techniques, many fundamental questions remain unanswered. Reports that determine N_d/N_a of doped TiO_2 remain difficult to compare side-by-side in even a semi-quantitative fashion; the synthesis methods and film thicknesses in these studies vary substantially. At the same time, co-doping, or the addition of more than one extrinsic atom into the TiO_2 crystal lattice, is being undertaken with increasing frequency [12, 13, 14]. Rare earth atoms have been explored as

dopants due to their unique *4f* electron configuration [15, 16]. Yet as these more complicated doping protocols are adopted, the majority of catalytic studies still continue to correlate acetone [17] or methylene blue [18] photodecomposition rates to dopant atomic fractions.

When it comes to transition metal doping of TiO_2, there is evidence to suggest that di- and trivalent impurities such as Cr, Mn, Al, and Fe act as acceptors, while pentavalent impurities including Nb and V act as donors. This is analogous to the way in which silicon can be doped p- and n-type via the addition of group III and group V elements. In photocatalysts and dye-sensitized solar cells fabricated from TiO_2, carrier concentration alters near-surface and/or near-interface electric fields and thus the flow of photogenerated charge carriers [19]. Similar principles underlie photocatalytic processes employing suspensions of TiO_2 nanoparticles in aqueous environments. Likewise, gas sensor detection capabilities depend upon background carrier concentration [20].

It may be possible to infer the impact of a given dopant on TiO_2 carrier concentration *a priori* from photoreactivity studies, for example. Significantly enhanced visible-light photocatalytic activity is observed for TiO_2 doped with 0.1 to 1.0 at% Cr prepared via sol-gel synthesis [21]. Chen *et al.* examined TiO_2 nanoparticles doped with Cr, Mn, Fe, and V [22]; their report belies the importance of precise tuning of dopant composition. In some cases, a "sweet spot" in the range of 0.0002 at% to 0.2 at% resulted in optimal discoloring of methyl orange. Trends in dopant effectiveness are certainly identifiable; rarely does the addition of Fe improve the degradation of a chemical reactant upon UV exposure [23, 24]. Nb is a more interesting case, however, since it has been shown to increase N_d in TiO_2 to approximately 10^{21} cm^{-3} [25]. For the most part, inferior photo-induced decomposition rates are observed for Nb-doped TiO_2 [26, 17]. This ties in with preliminary predictions correlating

photocurrent to TiO_2 doping level [27]. A reduction in free electron concentration i.e., a decrease in N_d, is hypothesized to enhance the photodecomposition of 2-propanol.

Considerations pertaining to dopant solubility should also play into the decision-making process. Matsumoto and co-workers examined the solubility of Cr, Mn, Fe, V, and several other transition metal ions in anatase and rutile TiO_2 [28]. Iron has a very low solubility in TiO_2, and may not be suitable for compensating native donor defects despite being trivalent [29]. In reviewing n-type dopants, there is evidence to suggest that Nb incorporates readily into the TiO_2 lattice, in part due to proximity in size to Ti^{4+} [30].

The present work applies a rigorous methodology to the determination of free carrier concentration for doped TiO_2 that is not amenable to standard metrology methods. Measurements of donor carrier concentration are obtained for Cr-, Mn-, and Nb-doped TiO_2 synthesized by ALD. Possible causes for the obtained carrier concentrations are discussed.

4.3 Methods and procedures

TiO_2 deposition, diode preparation, and electrical characterization were performed as described in Chapter 2. Schottky diode structures fulfilling all criteria for accurate *C-V* measurements of carrier concentration were fabricated with InGa ohmic contacts to abraded 0.013 Ω·cm n-Si and Al Schottky contacts to the TiO_2 surface. Details pertaining specifically to the deposition and characterization of doped films will be reviewed in brief.

4.3.1 Atomic layer deposition of doped TiO_2

Thin film polycrystalline anatase TiO_2 was synthesized by ALD and in some cases doped to ~2 at% with transition metals such as Cr, Mn, and Nb. All substrates were mounted

on a resistively heated chuck whose temperature was maintained at 200°C during deposition and monitored with a chromel-alumel (type K) thermocouple. Undoped TiO_2 was deposited with a total of 27 cycles in order to obtain 100 nm thick films for comparison with doped films.

Dopants were introduced from the vapor phase during deposition as follows. $Cr(C_5H_7O_2)_3$ (Sigma Aldrich, 99.99%), $Mn(DPM)_3$ where (DPM) is 2,2,6,6-tetramethyl-3, 5-heptanedionato (Strem Chemicals Inc., 99%), and $Nb(OCH_2CH_3)_5$ (Sigma Aldrich, 99.95%) served as the source materials for Cr, Mn, and Nb, respectively. $Cr(C_5H_7O_2)_3$ and $Mn(DPM)_3$ are solids at room temperature, with respective melting points of 210°C and 154°C. These precursors were evaporated from a porous filter enclosure placed adjacent to the TTIP/H_2O delivery tube within the vacuum chamber. The enclosure resembles a refillable pouch; the inert pocket-like pouch, fabricated from thin, high porosity paper derived from Abaca fiber, was loaded with the solid precursor as necessary. The supply rate of the dopant source was controlled by changing the distance between the enclosure and the heated substrate chuck. $Nb(OCH_2CH_3)_5$, a liquid at room temperature, was placed in a quartz crucible with a vented lid; the vapor pressure was also controlled by proximity to the heated chuck. These source configurations are shown in Fig. 4.1. Furthermore, the vapor pressures of $Cr(C_5H_7O_2)_3$ [31], $Mn(DPM)_3$ [32], and $Nb(OCH_2CH_3)_5$ [33] as a function of temperature are shown in Fig. 4.2.

Thirty to forty ALD cycles were typically necessary to deposit 100 nm thick Cr-, Mn-, and Nb-doped films. This increase in the number of cycles can be attributed to a change in the gas velocity profile when the porous filter enclosure is affixed to the delivery

tube (Cr, Mn) and a reduction in the number of sites available for Ti, O precursor adsorption due to adsorption of dopant species (Cr, Mn, Nb).

Following growth, all films were thermally annealed at 550°C under an ambient atmosphere for 24 hrs.

4.3.2 Physical characterization

Film thickness, surface chemical composition and elemental state information, SEM images, as well as XRD and XRR spectra were acquired as outlined in Chapter 3. CasaXPS and PANalytical X-ray reflectivity software were used for XPS data processing and analysis and XRR data fitting, in that order.

For doped TiO_2 films, XPS depth profiling was accomplished with a PHI 5400 with excitation by monochromatized Al Kα radiation. The instrument is equipped with an Ar ion sputtering gun capable of operating in the range of 0.5 to 5 keV. The tool was calibrated for TiO_2 sputtering at 3 keV. At this setting, approximately 1.7 nm of TiO_2 were etched per minute of sputtering. A typical depth profiling routine involved two sweeps prior to sputtering, two minutes of sputtering, a sweep after the sputtering cycle, two minutes of sputtering, etc.

4.4 Results and discussion

4.4.1 Chemical composition

XPS confirmed introduction of the metal dopants into the films and provided an estimate of surface elemental composition. Fig. 4.3 shows the XPS spectra for the Cr *2p*, Mn *2p*, and Nb 3*d* core-levels. The binding energy (BE) scale has been referenced to the C *1s*

peak at 285 eV. Quantitative analysis indicates that Cr, Mn, and Nb doping levels of approximately 2 at% were obtained.

Peaks corresponding to Cr $2p_{3/2}$ and $2p_{1/2}$ appear at 576.8 eV and 585.9 eV in Fig. 4.3(a). These BE values suggest that Cr is present as Cr^{3+} [34]. There is no evidence of hexavalent or tetravalent Cr; others who have identified these ions may have neglected to account for the O *1s* satellite peak in the ~570 eV range. In Fig. 4.3(b), the peaks at ~641.5 eV and ~653.4 eV correspond to the Mn $2p_{3/2}$ and $2p_{1/2}$ core-levels, respectively. As with similar films synthesized by plasma-assisted molecular beam epitaxy (PAMBE) [35], the satellite structure observed at a BE ~5 eV higher than the $2p_{3/2}$ peak suggests the presence of divalent Mn ions. The Mn $2p_{3/2}$ BE values themselves indicate that Mn may also be present as Mn^{3+}; a similar mixture of Mn^{2+} and Mn^{3+} ions has been proposed for Mn-doped TiO_2 fabricated via sol-gel processing [36]. The Nb $3d_{5/2}$ and $3d_{3/2}$ core-level features are located at 207.4 eV and 210.0 eV, as shown in Fig. 4.3(c). The locations of the *3d* peaks suggest that Nb is present as Nb^{5+} [37, 38]. Furthermore, there is no evidence for Nb^{4+} in the form of a small shoulder structure at ~206.5 eV. This minor component has been identified in Nb-doped TiO_2 synthesized via pulsed laser deposition (PLD) [39].

As seen in Fig. 4.4, Ti $2p_{3/2}$ and Ti $2p_{1/2}$ peaks are situated at 458.6 and 464.3 eV for undoped TiO_2 and shift by ~0.3 eV in all doped films. The change in BE of the Ti *2p* peaks relative to those of metallic Ti and 5.7 eV line separation between Ti $2p_{3/2}$ and Ti $2p_{1/2}$ indicates that Ti atoms are in the +4 oxidation state [40]. The shift towards lower BE and slight peak broadening in the doped films is caused by Ti^{4+} ions releasing extra electrons in order to reestablish charge equilibrium following dopant incorporation [34].

Since the dopants are incorporated into the TiO_2 during the film deposition process, it is important to examine their composition not only on the surface but also in the bulk. For this purpose, XPS depth profiling was carried out. Shown in Fig. 4.5 are 3-D area plots of Cr *2p* in Cr-doped TiO_2, Mn *2p* in Mn-doped TiO_2, and Nb *3d* in Nb-doped TiO_2, respectively. Two full sweeps were carried out prior to sputtering (labeled "surface"); these are comparable to the spectra presented in Fig. 4.3, although of weaker intensity due to the different instrumentation used for data collection. Spectra were then acquired sequentially after consecutive two minute sputtering cycles (for a total of 8 cycles per sample). For Cr-doped TiO_2, sputtering reduces the intensity of the $2p_{1/2}$ peak as seen in Fig. 4.5(a); the entire spectrum also shifts toward lower BE. The Mn *2p* spectrum changes in a similar fashion (Fig. 4.5(b)). The shift in BE is attributed to local reduction of TiO_2 via preferential sputtering of oxygen with the Ar ion beam [41]. In Fig. 4.5(c), the shape of the Nb *3d* doublet changes substantially upon sputtering. Reduction prompts the evolution of a peak corresponding to pure Nb metal [42]. Most importantly, however, after initial changes in all spectral features due to sputtering, there is little change in the intensity of the constituent peaks from sputtering cycle to sputtering cycle. This indicates that dopant composition remains relatively unvarying from the TiO_2 free surface to the TiO_2/Si interface.

4.4.2 Morphology and crystallinity

Fig. 4.6 shows cross-sectional SEM micrographs of undoped, Cr-doped, Mn-doped, and Nb-doped TiO_2 as deposited. The underlying Si substrate can be distinguished by slightly darker coloration. The micrographs show that the undoped TiO_2 film (Fig. 4.6(a)) is densely packed with extremely small granular features on the order of 5 nm and a mostly

indiscernible void volume. In contrast, the Cr- and Mn-doped TiO_2 films (Figs. 4.6(b) and 4.6(c)) are composed of easily identifiable, round crystallites with an average size of ~20 to 40 nm. Doping clearly increases the number of visible grain boundaries and induces slight surface roughening. The morphology of the Nb-doped TiO_2 film (Fig. 4.6(d)) comprises vaguely columnar, merged crystallites with a reduced visible void fraction and merging in the lateral direction.

Fig. 4.7(a) shows XRD patterns for undoped, Cr-, Mn-, and Nb-doped TiO_2. The undoped pattern corresponds to polycrystalline anatase with slight preferential (101) crystallographic orientation (JCPDS card No. 21-1272). Doped films are still anatase in structure and no secondary phases are discernable. A slight downward shift in the position of the (101) diffraction peak is observed in each case. Since the positions of diffraction peaks are governed by the spacing between planes of atoms, a shift in peak position suggests a change in interplanar spacing i.e., lattice parameter. In the case of doped material, Vegard's law can be invoked. Simply, it argues that unit cell parameters should vary linearly with composition for a continuous substitutional solid solution in which atoms or ions that substitute for each other are randomly distributed. In Fig. 4.7(b), *c*-axis lattice parameter is plotted as a function of Ti (undoped material) or dopant (doped material) ionic radius where the radii for Ti^{4+}, Cr^{3+}, Mn^{3+}, and Nb^{5+} are 0.61, 0.62, 0.58, and 0.64 Å, in that order [43]. The linear correlation suggests that dopant atoms are most likely incorporated at lattice Ti^{4+} sites. The comparatively larger (smaller) ionic radii cause an expansion (contraction) of the crystal lattice and concordant shift in the TiO_2 (101) diffraction peak to a smaller (larger) angle.

Fig. 4.8 shows XRR curves for the same films. All curves show fringes characteristic of a well correlated upper and lower surface. Fringe period and amplitude depend on film thickness and surface and interface roughness, respectively. A decrease in the fringe amplitude indicates an increase in roughness; qualitatively, the roughness increases according to undoped TiO_2 > Nb-doped TiO_2 > Mn-doped TiO_2 > Cr-doped TiO_2.

Analysis of XRD peak profiles using a size-only fitting model yields an average crystallite size in the film growth direction of 20 – 45 nm. As indicated in Fig. 4.9, Cr and Mn doping cause a reduction in crystallite size of ~15 nm in comparison to undoped material. Nb doping, on the other hand, results in a slight rise in crystallite size to approximately 45 nm. XRR spectra fitting shows an increase in TiO_2 bulk density (initially 3.64 g/cm^3) upon doping. For comparison, the bulk density of single crystal anatase is 3.89 g/cm^3. To some extent, the trend in density as a function of dopant mirrors that of crystallite size. This suggests, somewhat intuitively, that smaller crystallites allow for closer packing and a reduction in film void volume. It is important to consider the implications of this result in the context of defect engineering via doping. While dopants can introduce donor/acceptor energy levels in the band gap that alter bulk electronic properties, other distinct effects on carrier concentration can arise that are difficult to deconvolve. These include dopant-induced changes in electrically active defects at grain boundaries or void volumes, as well as changes in the structure or concentrations of charges residing in extended defects such as crystallographic shear planes.

4.4.3 Influence of doping on carrier concentration

Fig. 4.10(a) shows *C*-*V* curves for undoped, Cr-, Mn-, and Nb-doped TiO_2 Schottky diode structures. In all cases, the capacitance increases with decreasing positive voltage until reaching a maximum in the accumulation region, which is labeled in the figure. Fig. 4.10(b) shows the same data in conventional Mott-Schottky format (C^{-2} vs. V). Table 4.1 gives the calculated donor carrier concentration values for the diodes along with the corresponding values of n, R_s, and Φ_B. As reported in Chapter 2, N_d equals $8.3 \pm 0.2 \times 10^{16}$ cm^{-3} for the undoped TiO_2 film; the donor carrier concentrations for the Cr-, Mn-, and Nb-doped TiO_2 are $3.2 \pm 0.1 \times 10^{17}$ cm^{-3}, $1.9 \pm 0.1 \times 10^{16}$ cm^{-3}, and $7.3 \pm 0.2 \times 10^{16}$ cm^{-3}, respectively. Estimates of standard error are obtained by computation of least squares curve fits of C^{-2} vs. V in the linear depletion region.

To better illustrate the scope of carrier concentration manipulation made possible by doping of 100 nm TiO_2, these N_d values are compared to those of undoped TiO_2 (~60 nm to 280 nm) in Fig. 4.11. Cr and Mn raise and lower N_d by about half an order of magnitude, respectively. The carrier concentration in Nb-doped TiO_2 changes only minimally. Carrier concentration measurements have not been made for undoped TiO_2 films thinner than 60 nm; it is unlikely, however, that further reduction in film thickness would increase N_d to the 3.2×10^{17} cm^{-3} level of Cr-doped TiO_2. On the other hand, N_d for 100 nm Mn-doped TiO_2 is about equal to that of 130 nm undoped TiO_2.

Some attempt can be made to rationalize the carrier concentration values for doped TiO_2, although the existing literature base prohibits facile identification of trends in N_d (and N_a) as a function of dopant type and atomic fraction. Table 4.2 summarizes carrier concentration values found in the literature for anatase TiO_2 doped with Cr and Mn.

Comparable data for Nb-doped TiO_2 appears in Table 4.3. It is difficult to comment on the accuracy of these respective measurements given the available metrology protocol details, although the order of magnitude differences in carrier concentration apparent for Nb-doped TiO_2 probably correspond to real differences in dopant electrical activation. Ideally, a substitutional dopant in the TiO_2 crystal lattice donates free electrons or holes that change the overall conductance of the TiO_2; this type of dopant is referred to as "electrically active." Electrical inactivity, or a negligible change in conductance despite donor/acceptor doping, may arise from clustering of dopant atoms at grain boundaries, within bulk crystallites as with interstitial clusters of B in Si [44], or compensation by charged native defects [45].

Here, in-situ Cr-doping at the 2 at% level results in a slight increase in carrier concentration from the undoped case. A donor carrier concentration of $1.5 – 1.75 \times 10^{19}$ cm^{-3} was reported for 45 nm, 8 at% Cr-doped TiO_2 synthesized via PAMBE [46]; the same study does not provide a value of N_d for undoped material. Radecka and co-workers report N_d values of ~1.8×10^{19} cm^{-3}, 3×10^{18} cm^{-3}, and 1.3×10^{18} cm^{-3} for 300 – 350 nm TiO_2 deposited by sputtering with 2.8, 4.4, and 7.6 at% Cr, in that order [47]. The donor carrier concentration of their undoped material prepared in a similar fashion was 5.5×10^{18} cm^{-3}. Fig. 4.12(a) presents these literature values for N_d of Cr-doped TiO_2 as a function of film thickness. The presence of the Cr^{3+} ion in the anatase TiO_2 lattice certainly does not induce p-type conductivity, as might be expected for a trivalent dopant atom. However, recent total energy calculations employing the local density approximation identify Cr_{Ti} as a deep donor in anatase TiO_2 with an ionization level ~0.31 eV below the conduction band minimum (CBM) [48].

For the material synthesized in this study, N_d drops by almost an order of magnitude upon ~2 at% Mn doping, although n-type conductivity persists. TiO_2 grown by PAMBE and doped with 7 at% Mn exhibits p-type (N_a = 1.24 x 10^{17} cm^{-3}) rather than n-type behavior according to Li *et al*. [35], who also determined the carrier concentration of undoped TiO_2 via Hall effect measurements (N_d = 7.7 x 10^{16} cm^{-3}). Mn-doped rutile TiO_2 synthesized by sol-gel method is p-type with a carrier concentration of ~10^{19} cm^{-3} for 2.5 to 8.3 at% Mn; an undoped film synthesized identically was n-type with N_d equal to 3 x 10^{18} cm^{-3} [49]. Indeed, a density functional theory (DFT) study reports defect levels at E_v + 0.16 eV, E_v + 0.28 eV, and E_v + 0.52 eV for a structural model incorporating Mn_{Ti} [50]; the proximity of these levels to the valence band maximum agrees with substitutional Mn acting as an acceptor defect. The literature-derived acceptor carrier concentrations for Mn-doped TiO_2 are shown in Fig. 4.12(b) as a function of film thickness.

In this study, lack of p-type conductivity in ALD films could occur due to Mn_{Ti} compensation by native donor defects or segregation of electrically active Mn^{3+} to voids between or within crystallites. Consequently, the incorporation of additional Mn during film synthesis might further reduce N_d or, possibly, lead to p-type conductivity. Interestingly, however, for both of the experimental studies described above, Mn-doped TiO_2 was subjected to a reducing treatment. Li and co-workers [35] thermally annealed the PAMBE film at 600°C and 2 x 10^{-8} Torr for 30 minutes while Kim *et al.* [49] subjected the sol-gel films to 4 hours of annealing at 600°C and a pressure of 10^{-3} Torr. Little is known about the defect chemistry of Mn-doped TiO_2. It is worth considering the possibility that reduction increases the concentration of V_O or Ti_i available for complexing with Mn ions; perhaps p-type conductivity arises due to point defects other than Mn_{Ti}.

ALD synthesis results in minimal change in N_d of TiO_2 with Nb doping. Of all the dopants considered here, Nb has been studied most frequently. Fig. 4.13 includes literature values for N_d of Nb-doped TiO_2 as a function of film thickness. For the purposes of this analysis, the influence of atomic fraction of Nb is neglected. In all cases, however, it is less than 6 at%. The vast majority of the data points correspond to films synthesized by physical vapor deposition (PVD) techniques such as PLD or sputtering. Furubayashi *et al.*, [25], Hitosugi *et al.* [38], and Dabney *et al.* [51] are just a few of the laboratories who synthesize Nb-doped TiO_2 using PVD and report high carrier concentration values on the order of 10^{20} cm^{-3} to 10^{21} cm^{-3}. In contrast, the isolated N_d values for Nb-doped TiO_2 grown by chemical vapor deposition (CVD) [52] and sol-gel [53] are in the 10^{17} cm^{-3} to 10^{18} cm^{-3} range.

The processing parameters that cause N_d for undoped, polycrystalline TiO_2 synthesized by PVD to vary widely have already been discussed in Chapter 3. For doped films produced by PVD, oxygen flow rate and partial pressure during growth will similarly affect both the bulk density and the concentration of native defects. When Nb^{5+} ions are added to the TiO_2 crystal lattice, Nb should readily substitute for Ti atoms due to is comparable ionic radius and act as a donor defect. DFT calculations reveal that a Nb_{Ti}-V_O complex is relatively stable and also a donor defect in the bulk [54]. Each Nb_{Ti}-V_O complex emits one electron and introduces an impurity state below the CBM, the exact location of which is unclear. Experimental evidence of this structure exists in the form of Nb *3d* XPS spectra with contributions from both Nb^{5+} and Nb^{4+} ions [39]. The Nb_{Ti}-V_O complex converts the charge state of Nb from 5+ to 4+ while the number of emitted electrons remains the same. Both Nb_{Ti} and Nb_{Ti}-V_O donor defects exist in Nb-doped TiO_2 synthesized by PVD,

although the number of carriers contributed by the Nb atoms should be the same regardless of which form the Nb assumes.

In the case that a highly n-type Nb-doped film is annealed in O_2 ambient, N_d drops by approximately two orders of magnitude as oxygen from the gas phase annihilates O vacancies. This annihilation reduces the concentration of the Nb_{Ti}-V_O complex, leaving behind isolated Nb_{Ti}. This causes Nb^{4+} ions to disappear. The change is induced by oxygen interstitial formation [55]; these acceptor-type defects annihilate bulk oxygen vacancies. In Fig. 4.3(c), no evidence of Nb^{4+} is found. Thus, in the present material, Nb_{Ti}-V_O is not expected to contribute substantially to conduction in the bulk. Since the 550°C annealing performed here is carried out under ambient conditions, it is unlikely that oxygen interstitials compensate for Nb_{Ti} to any sizeable extent. Although it is worth noting that oxygen interstitials exist in rutile TiO_2 at pressures as high as 10^{-5} Torr [45]. Rather, as reinforced by the data in Fig. 4.13, Nb may be electrically inactive in ALD-synthesized material due to inherent film porosity and the tendency for dopant atoms to segregate to internal voids. Extended defects incorporating multiple electrically active Nb atoms are also a possibility, although it is not clear why such defects should form in material grown by ALD vs. other synthesis methods that lead to high carrier concentrations.

4.5 Conclusion

The doping science of metal oxide semiconductors such as TiO_2 is hardly straightforward. As a consequence, TiO_2 "device" performance is typically correlated to atomic percentage of dopant in the bulk [56, 57]. For the first time, the influence of transition metal doping on the carrier concentration of TiO_2 synthesized by ALD has been

examined. The addition of Cr and Mn afford an order of magnitude variation in N_d over that of undoped TiO_2. That being said, the prospect of further tuning the carrier concentration of TiO_2 prepared by ALD seems remote due to compensation by native donor defects and complications arising from voids and grain boundaries in the bulk. There is still much to be learned about the energy levels of impurity atoms [10] and the exact way in which these species alter the electrical properties of TiO_2 possessing complex microstructure and native donor defects. Electrical activation of dopants incorporated during ALD has been studied only recently for ZnO [58, 59, 60]; no other reports of this nature exist for TiO_2. With respect to metrology for determination of carrier concentration, Schottky diode contact metals and preparation protocols must be compatible with changes in bulk Fermi level due to n- and p-type doping. *C-V* measurements can be used to obtain accurate values of carrier concentration in n- and p-type metal oxide semiconductors, although, as shown in Chapter 2, thorough device-like characterization of Schottky diode test structures and judicious selection of contact metals and surface/interface preparation methods are necessary.

4.6 Tables and figures

Table 4.1 Doping dependence of TiO_2 carrier concentration and diode parameters.

Dopant	N_d **(cm^{-3})**	***n***	R_s **(kΩ)**	Φ_B **(eV)**
(Undoped)	$8.3 \pm 0.2 \times 10^{16}$	1.6	0.90	0.60
Cr	$3.2 \pm 0.1 \times 10^{17}$	1.7	0.87	0.71
Mn	$1.9 \pm 0.1 \times 10^{16}$	1.6	0.90	0.79
Nb	$7.3 \pm 0.2 \times 10^{16}$	1.7	0.92	1.0

Table 4.2 Literature values of Cr- and Mn-doped TiO_2 carrier concentration. Unless indicated, film is n-type and donor carrier concentration N_d is reported.

Reported N_d/N_a (cm^{-3})	**Dopant, At%**	**Synthesis Method**	**Thickness (nm)**	**Metrology Method**	**Reference**
3×10^{18}	Cr, 4.4 at%	Sputtering	~325	*C-V*	[47]
1.3×10^{19}	Cr, 7.6 at%	Sputtering	~325	*C-V*	[47]
1.5×10^{19} to 1.75×10^{19}	Cr, 8 at%	PAMBE	45	Hall effect	[46]
1.89×10^{19}	Cr, 2.8 at%	Sputtering	~325	*C-V*	[47]
1.24×10^{17} (p-type)	Mn, 7 at%	PAMBE	100	Hall effect	[35]
7.0×10^{18} (p-type)	Mn, 2.5 at%	Sol-gel	1000	Hall effect	[49]
7.0×10^{18} (p-type)	Mn, 8.3 at%	Sol-gel	1000	Hall effect	[49]
9.0×10^{18} (p-type)	Mn, 5.6 at%	Sol-gel	1000	Hall effect	[49]
1.0×10^{19} 2.0 (p-type)	Mn, 3.9 at%	Sol-gel	1000	Hall effect	[49]

Table 4.3 Literature values of Nb-doped TiO_2 carrier concentration.

Reported N_d (cm^{-3})	Nb At%	Synthesis Method	Thickness (nm)	Metrology Method	Reference
2.3×10^{17}	6 at%	Sol-gel	150	Hall Effect	[53]
1.6×10^{18}	5 at%	CVD	250	*C-V*	[52]
2×10^{18} to 7×10^{18}	5 at%	PLD	110	Hall Effect	[51]
1.12×10^{19}	0.22 at%	PLD	40	Hall Effect	[25]
6.5×10^{19}	6 at%	PLD	15	Probe station	[61]
8.13×10^{19}	0.55 at%	PLD	40	Hall Effect	[25]
9.0×10^{19}	6 at%	PLD	18	Probe station	[61]
1.5×10^{20}	6 at%	PLD	22	Probe station	[61]
2.35×10^{20}	1.2 at%	PLD	40	Hall Effect	[25]
2.4×10^{20}	3 at%	Sputtering	150	Hall Effect	[62]
5.0×10^{20}	2 at%	PLD	150	Hall Effect	[63]
5×10^{20} to 1×10^{21}	5 at%	PLD	110	Hall Effect	[51]
7.96×10^{20}	3.3 at%	PLD	40	Hall Effect	[25]
1.0×10^{21}	6 at%	PLD	32	Probe station	[61]
1.21×10^{21}	5 at%	PLD	60	Hall Effect	[30]
1.3×10^{21}	6.4 at%	Sputtering	400	Hall Effect	[64]
1.5×10^{21}	6 at%	PLD	100	Hall Effect	[38]
1.64×10^{21}	6.6 at%	PLD	40	Hall Effect	[25]
1.7×10^{21}	6 at%	Sputtering	135	van der Pauw method, HE	[65]
2.0×10^{21}	6 at%	PLD	38	Probe station	[61]
2.17×10^{21}	11 at%	PLD	40	Hall Effect	[25]
3.24×10^{21}	18 at%	PLD	40	Hall Effect	[25]
4.56×10^{21}	37 at%	PLD	40	Hall Effect	[25]

Fig. 4.1 Schematic depicting the low-pressure vacuum chamber for ALD of doped TiO_2.

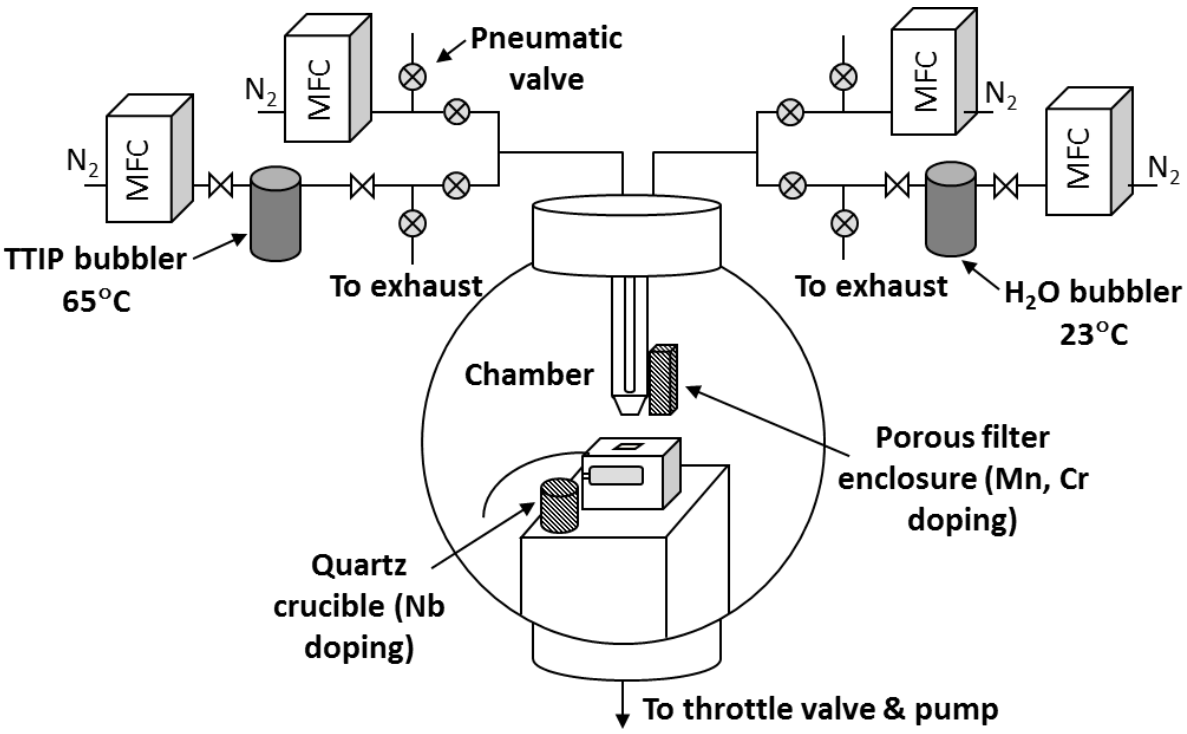

Fig. 4.2 Vapor pressure of Cr, Mn, and Nb precursors as a function of temperature.

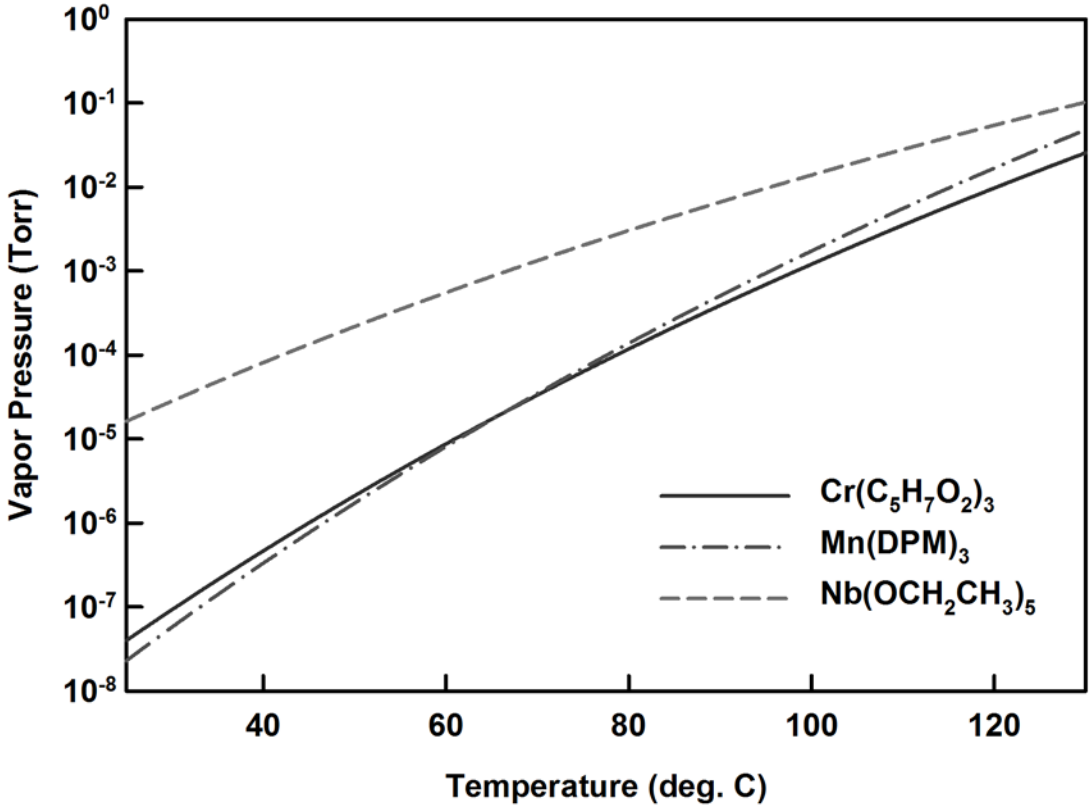

Fig. 4.3 XPS spectra of TM-doped TiO_2 films obtained with the Kratos AXIS Ultra: (a) Cr *2p* in Cr-doped TiO_2, (b) Mn *2p* in Mn-doped TiO_2, and (c) Nb *3d* in Nb-doped TiO_2.

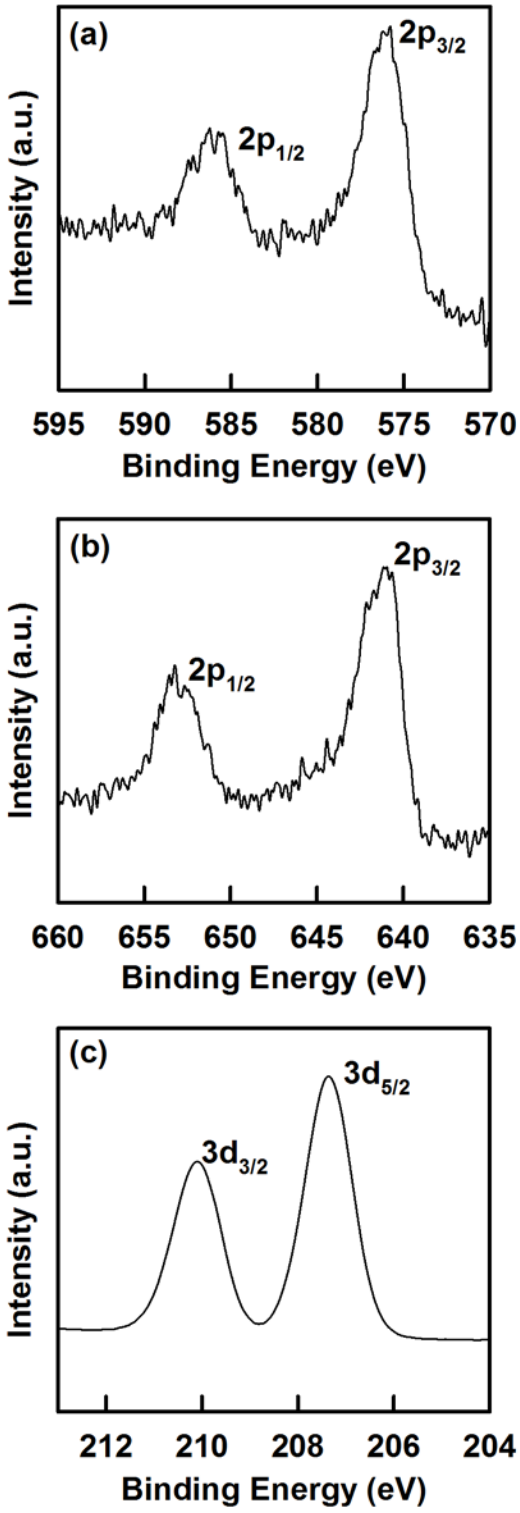

Fig. 4.4 XPS spectra showing Ti $2p_{3/2}$ and Ti $2p_{1/2}$ core-levels situated at 458.6 and 464.3 eV for undoped TiO_2 and shifting by ~0.3 eV in all doped films. Data also obtained with the Kratos AXIS Ultra.

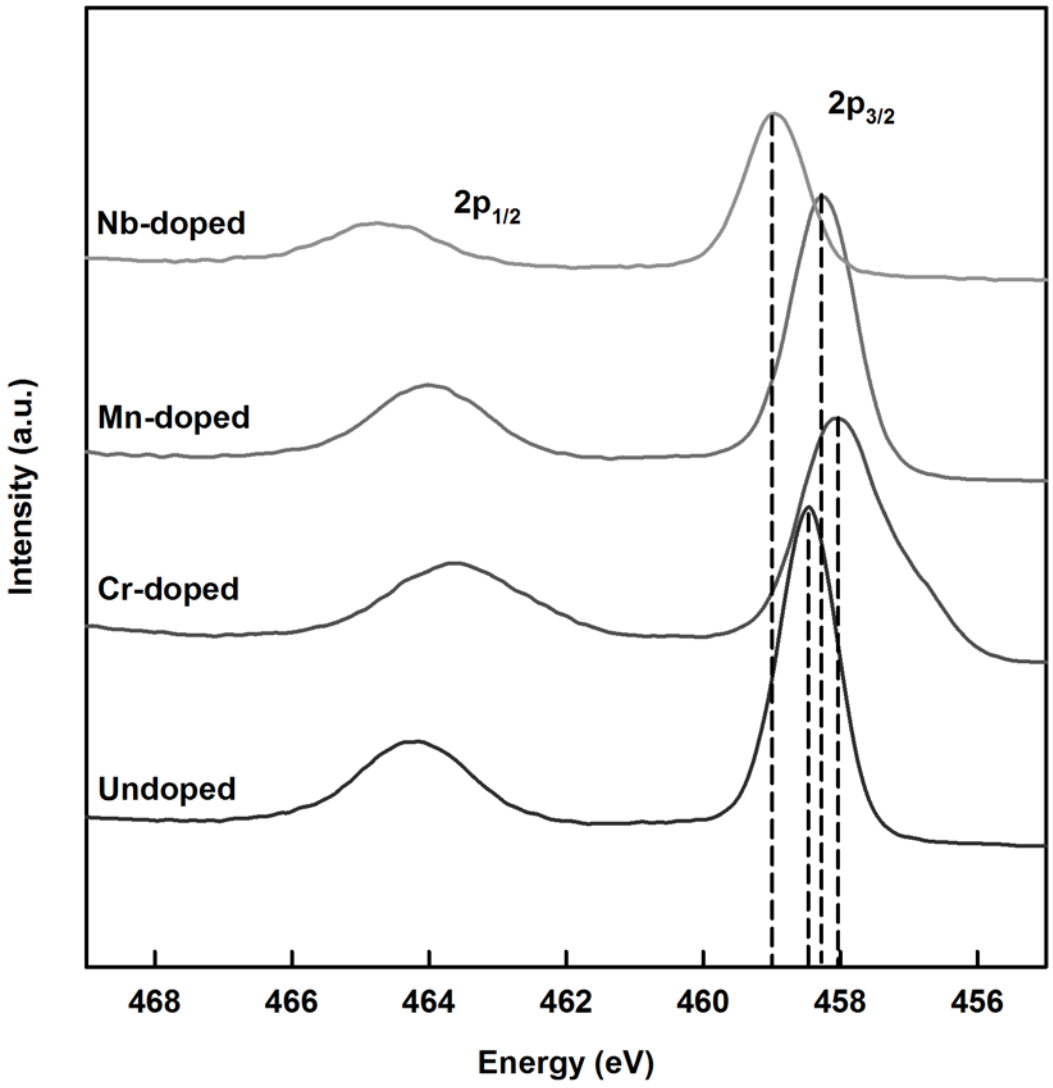

Fig. 4.5 XPS depth profiles of doped TiO_2 films obtained with the PHI 5400: (a) Cr *2p* in Cr-doped TiO_2, (b) Mn *2p* in Mn-doped TiO_2, and (c) Nb *3d* in Nb-doped TiO_2.

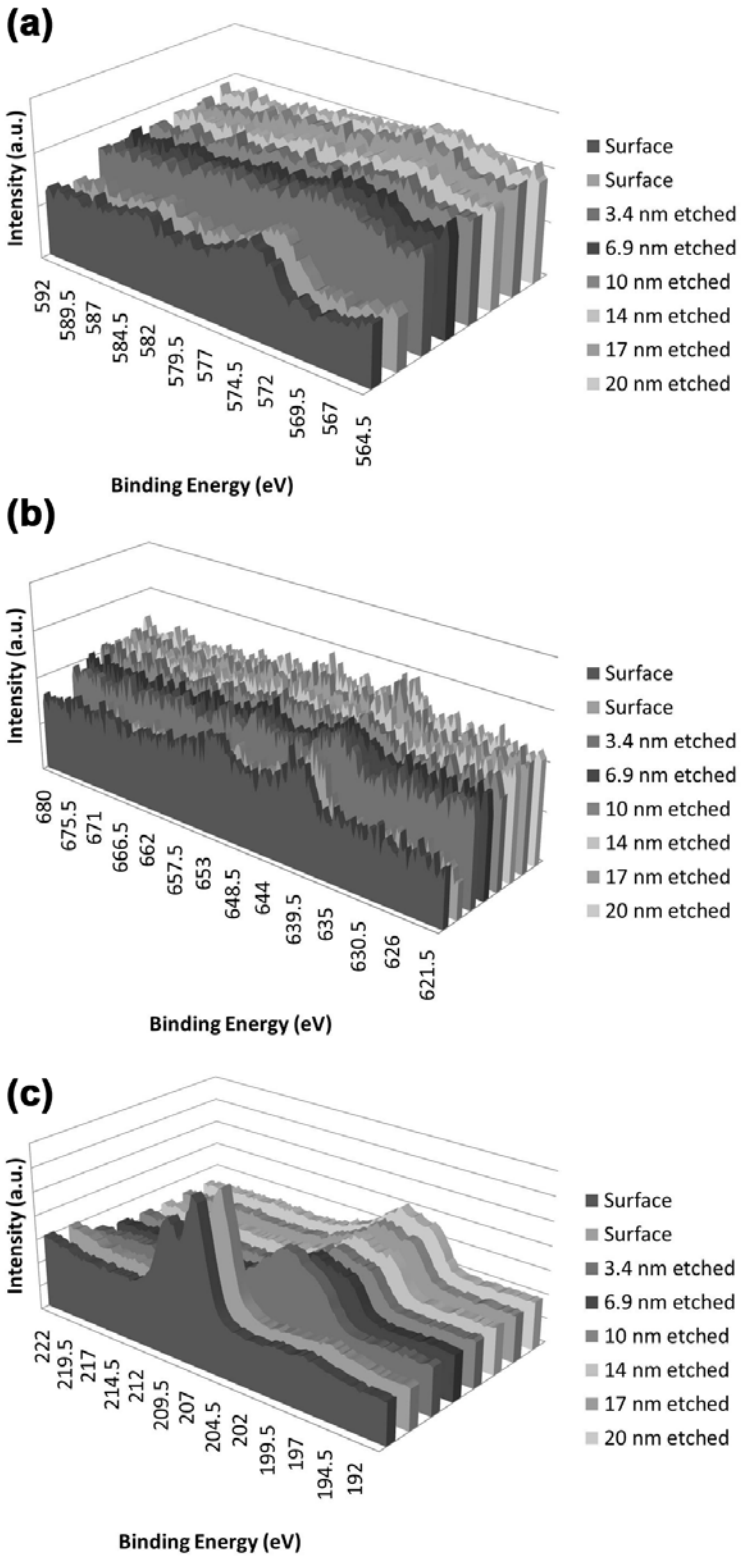

Fig. 4.6 SEM images of (a) undoped, (b) Cr-, (c) Mn-, and (d) Nb-doped TiO_2 films exhibiting variations in morphology and void fraction.

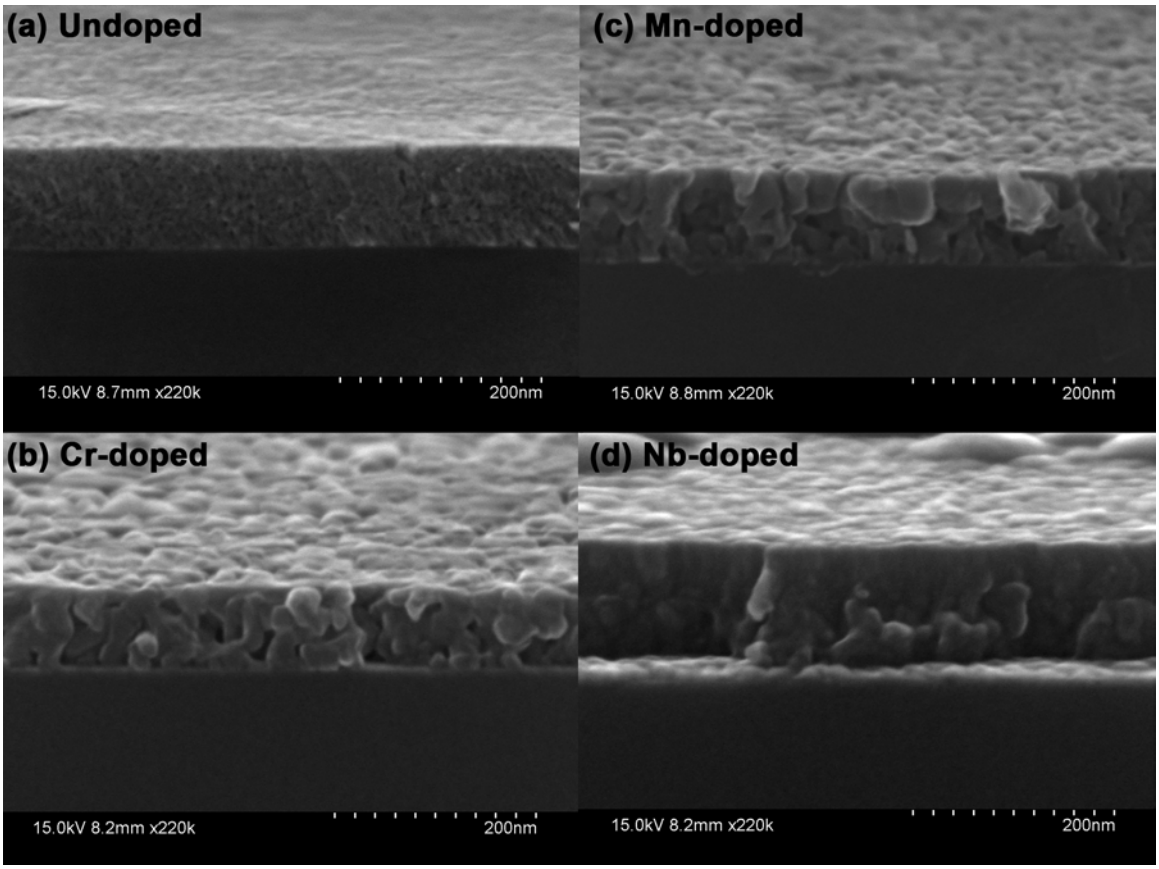

Fig. 4.7 (a) XRD patterns of undoped, Cr-, Mn-, and Nb-doped TiO_2 films showing anatase structure with (101), (112), and (200) reflections and (b) *c*-axis lattice constant versus dopant ionic radius demonstrating adherence to Vegard's law.

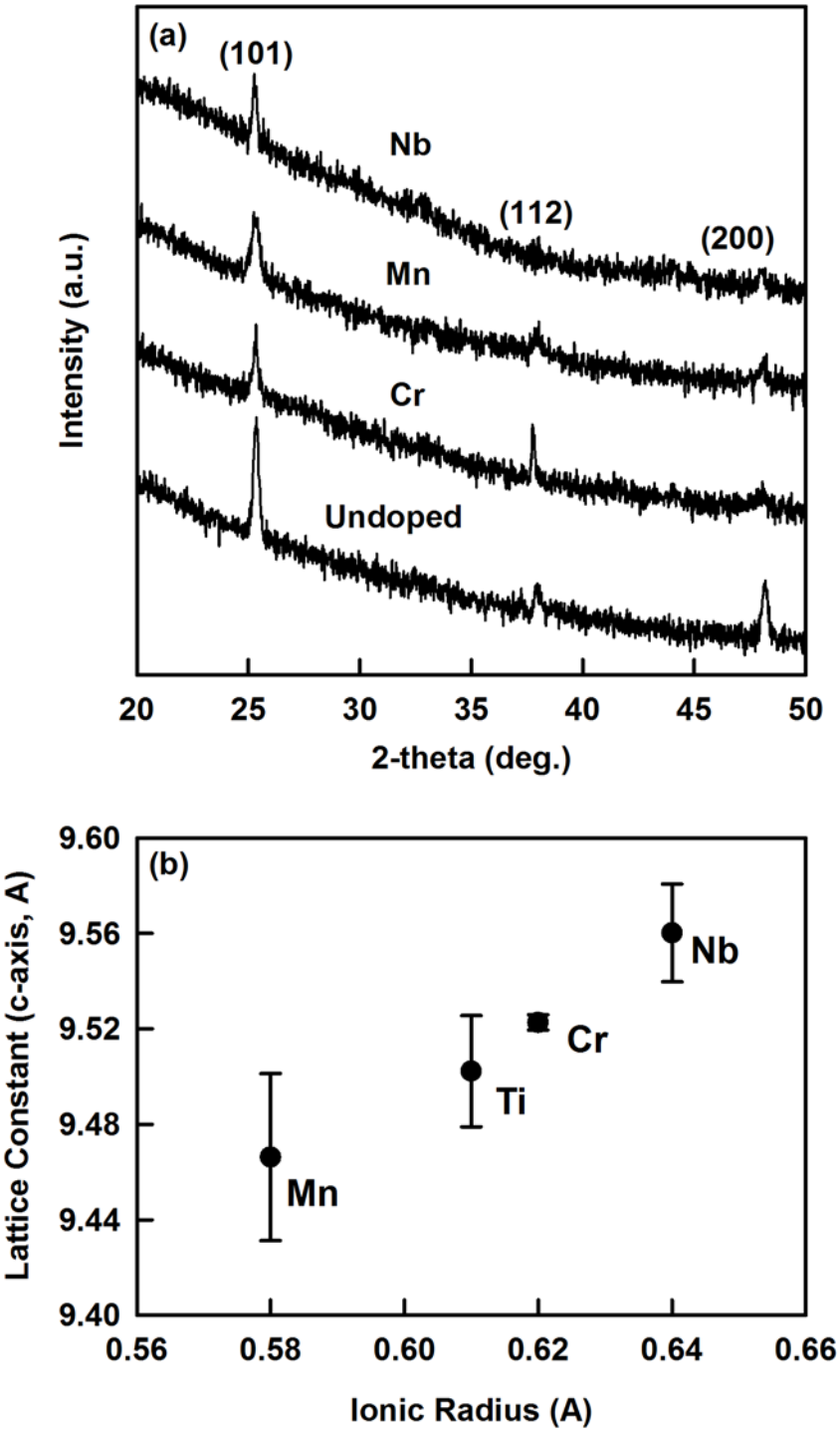

Fig. 4.8 XRR data for the undoped, Cr-, Mn-, and Nb-doped TiO_2 films exhibiting well-defined fringes.

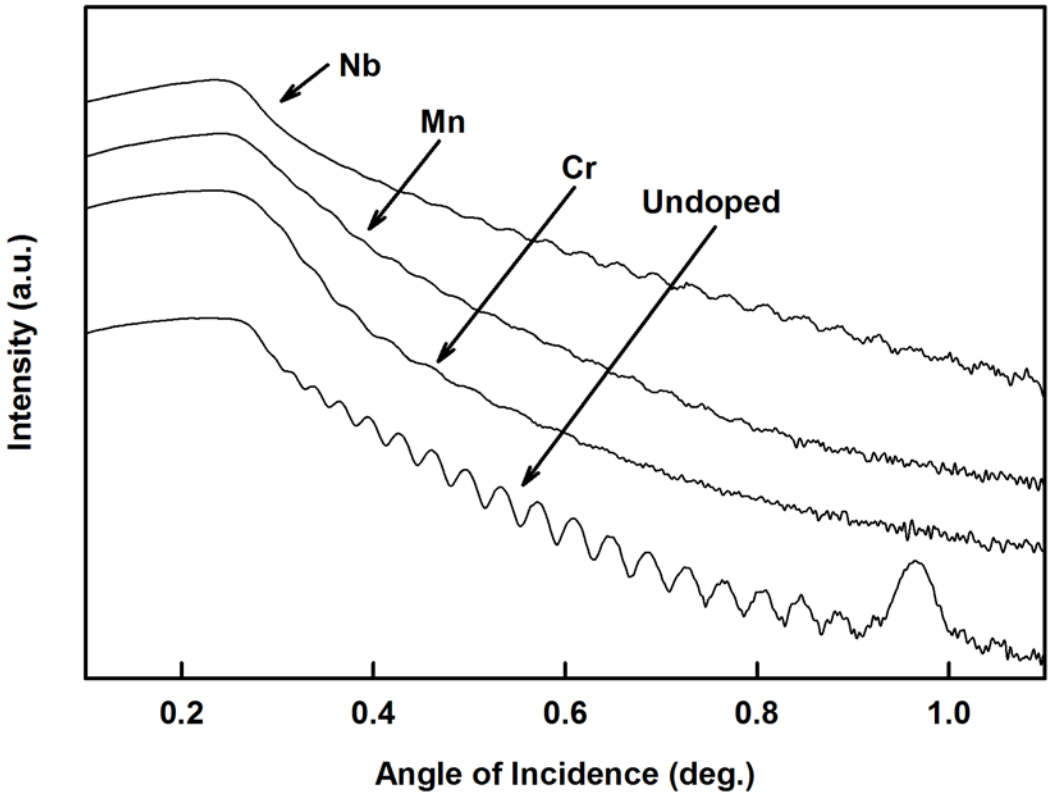

Fig. 4.9 Average crystallite size obtained by XRD peak fitting (left axis, scatter plot) and bulk density obtained from XRR spectra fitting (right axis, bar graph) for undoped, Cr-, Mn-, and Nb-doped TiO_2.

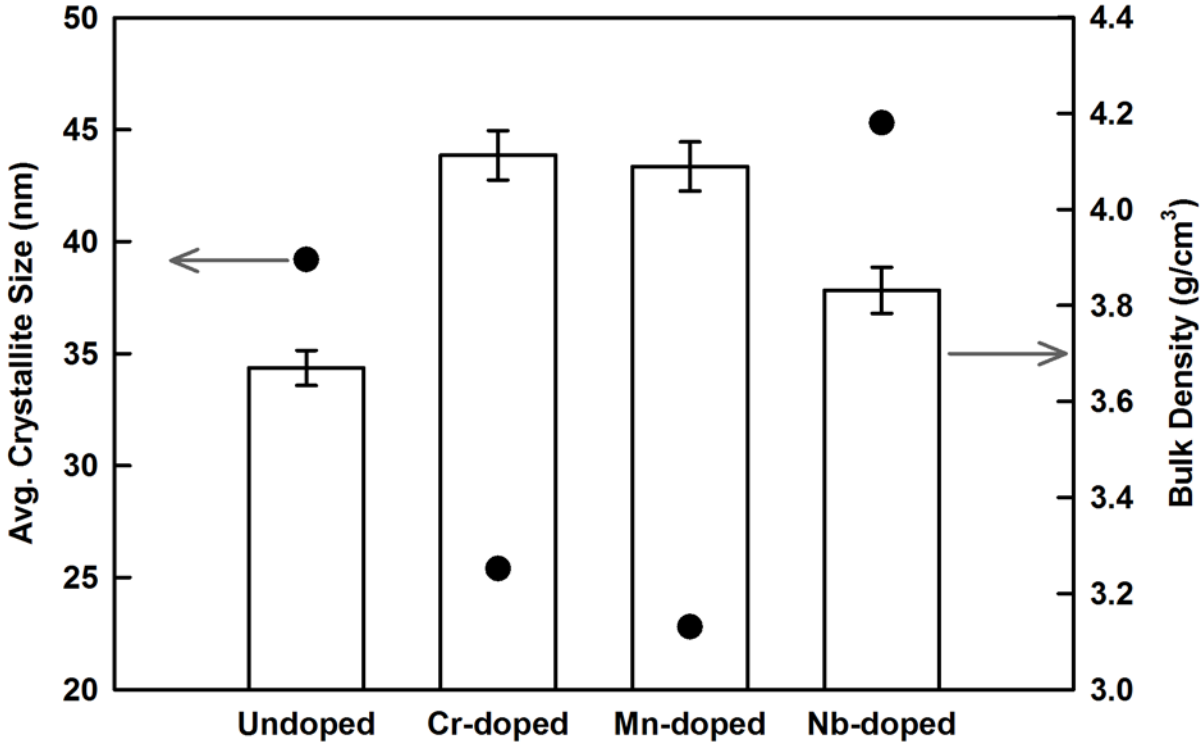

Fig. 4.10 (a) Dependence of capacitance upon voltage for various doping types. Voltage ranges leading to accumulation, depletion, and inversion at the TiO_2-metal contact are shown. Only the data taken under the depletion condition are useful for calculating carrier concentration. (b) The data in (a) plotted in conventional Mott-Schottky form. The plots are recorded at 1 MHz. For the bias voltage polarity used with these diode structures, a positive slope indicates n-type behavior.

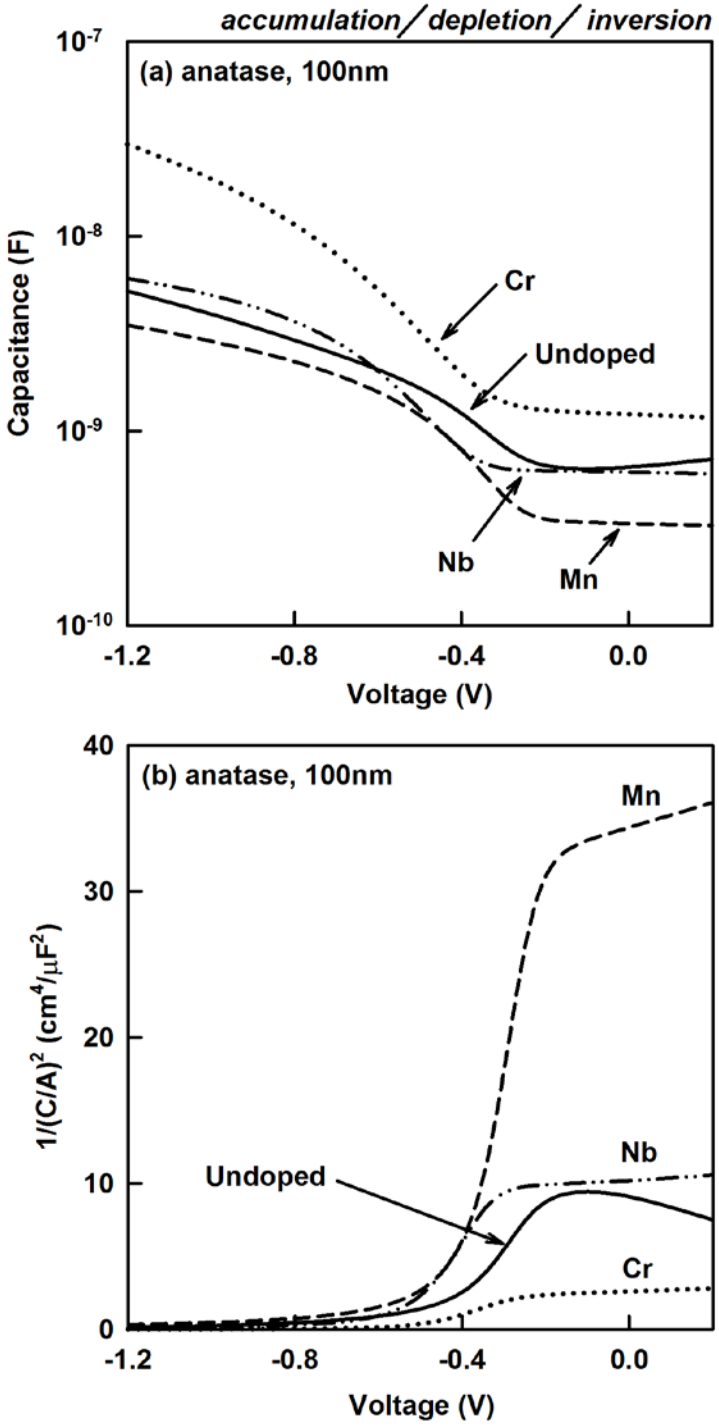

Fig. 4.11 Comparison between N_d values for undoped TiO_2 of varying thickness (550°C anneal, 24 hr) with N_d values of ~100 nm Cr-, Mn-, and Nb-doped TiO_2.

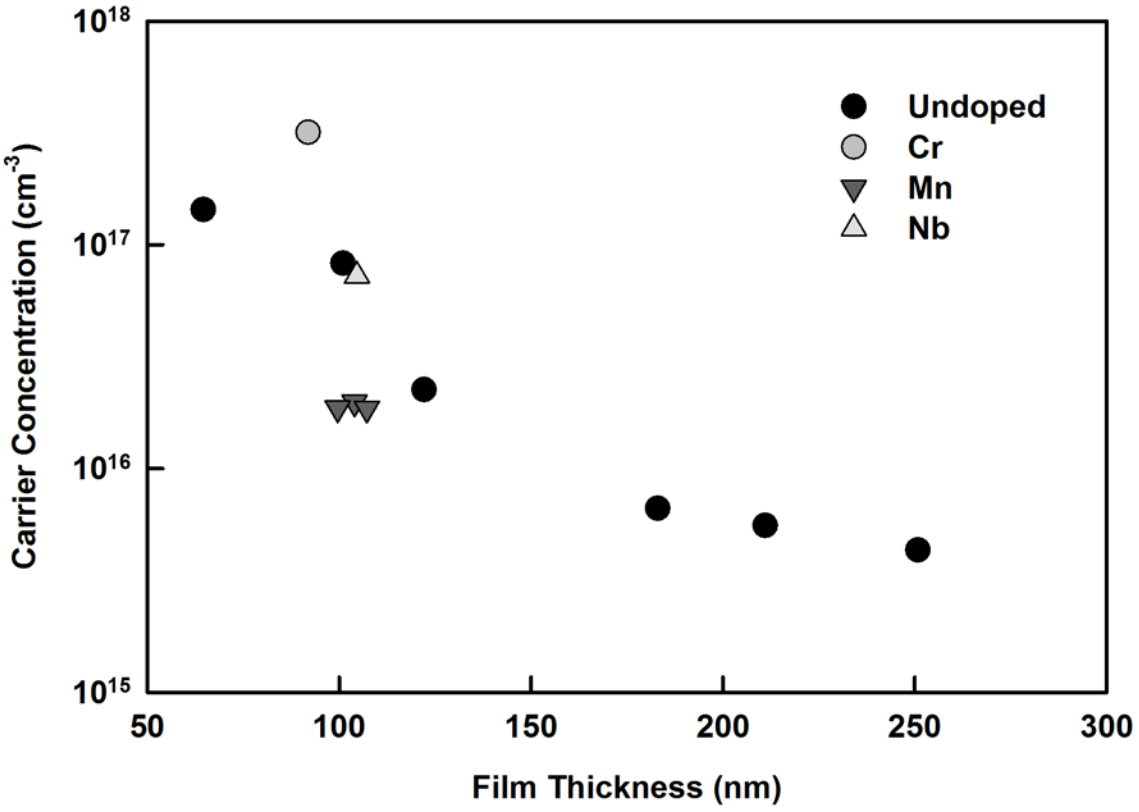

Fig. 4.12 Literature values for (a) N_d of Cr-doped and (b) N_a of Mn-doped TiO_2 plotted against film thickness. At% Cr is labeled on the figure; Mn doping fraction varies from 2.5 to 8.3 at%.

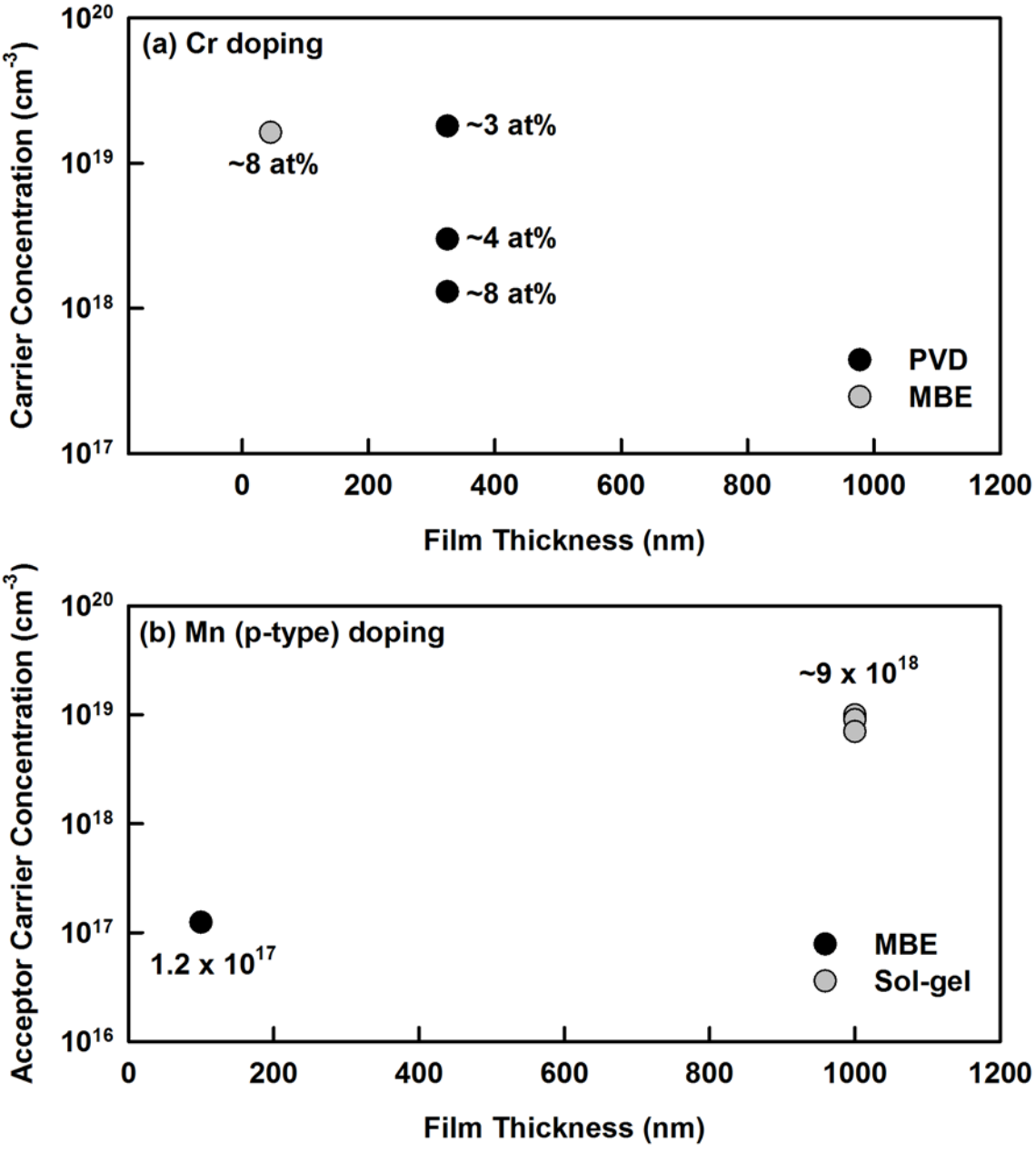

Fig. 4.13 Literature values for N_d of Nb-doped TiO_2 plotted against film thickness. In this graph, report-to-report variations in at% Nb are neglected; all films contain less than 6 at% Nb, however. The CVD and sol-gel data points come from [52] and [53], in that order.

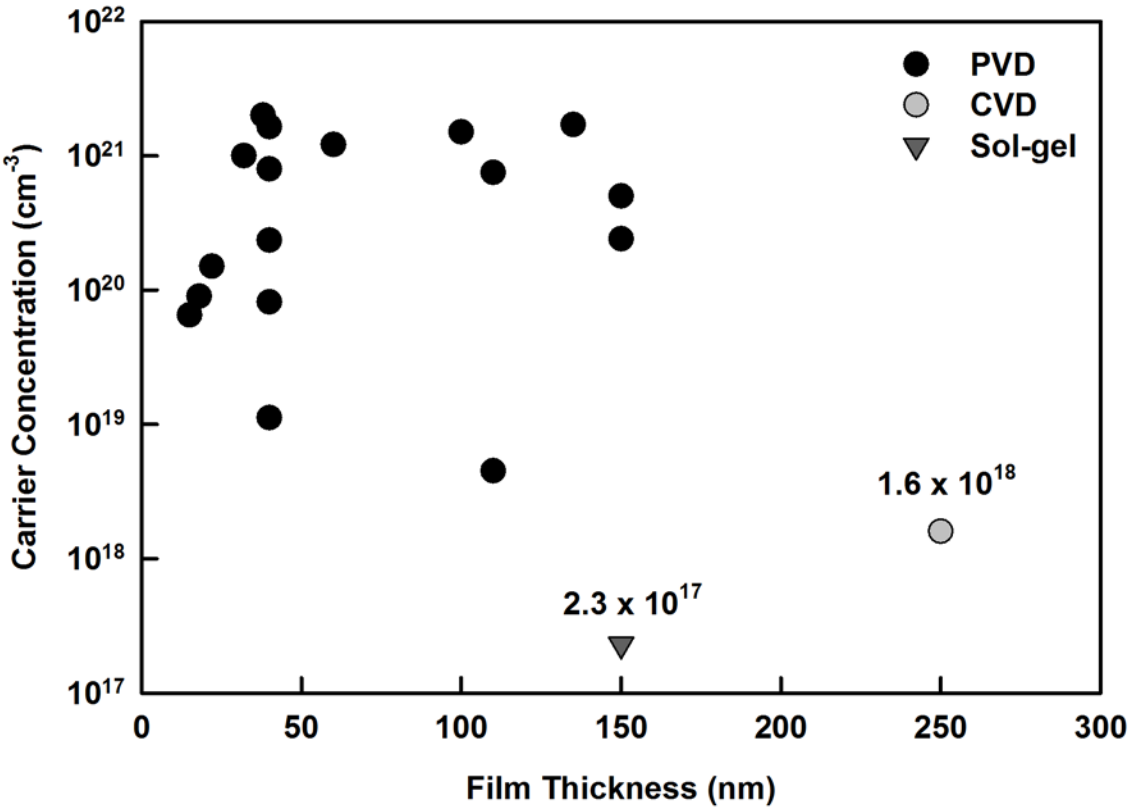

4.7 References

[1] M. A. Malati and W. K. Wong, *"Doping TiO_2 for solar energy applications,"* Surf. Technol. **22,** 305-322 (1984).

[2] V. Brezova, A. Blazkova, L. Karpinsky, and J. Groskova, *"Phenol decomposition using M^{n+}/TiO_2 photocatalysts supported by the sol-gel technique on glass fibres,"* J. Photoch. Photobio. A **109,** 177-177 (1997).

[3] R. Janisch, P. Gopal, and N. A. Spaldin, *"Transition metal-doped TiO_2 and ZnO - present status of the field,"* J. Phys.: Condens. Matter **17,** R657-689 (2005).

[4] M. K. Nowotny, L. R. Sheppard, T. Bak, and J. Nowotny, *"Defect chemistry of titanium dioxide. Application of defect engineering in processing of TiO_2-based photocatalysts,"* J. Phys. Chem. C **112,** 5275-5300 (2008).

[5] Y. Cui, H. Du, and L. Wen, *"Doped-TiO_2 photocatalysts and synthesis methods to prepare TiO_2 films,"* J. Mater. Sci. Technol. **24,** 675-689 (2008).

[6] A. Zaleska, *"Doped-TiO_2: A Review,"* Rec. Pat. Eng. **2,** 157-164 (2008).

[7] R. Asahi, T. Morikawa, T. Ohwaki, K. Aoki, and Y. Taga, *"Visible-light photocatalysis in nitrogen-doped titanium oxides,"* Science **293,** 269-271 (2001).

[8] Y. Mizukoshi, N. Ohtsu, S. Semboshi, and N. Masahashi, *"Visible light responses of sulfur-doped rutile titanium dioxide photocatalysts fabricated by anodic oxidation,"* Appl. Catal., B **91,** 152-156 (2009).

[9] D. Wang, Y. Zou, S. Wen, and D. Fan, *"A passivated codoping approach to tailor the band edges of TiO_2 for efficient photocatalytic degradation of organic pollutants,"* Appl. Phys. Lett. **95,** 012106 (2009).

[10] E. G. Seebauer and M. C. Kratzer, *Charged Semiconductor Defects: Structure, Thermodynamics, and Diffusion* (Springer-Verlag, London, 2009).

[11] W. Choi, A. Termin, and M. R. Hoffmann, *"The Role of Metal Ion Dopants in Quantum-Sized TiO_2: Correlation between Photoreactivity and Charge Carrier Recombination Dynamics,"* J. Phys. Chem. **98,** 13669-13679 (1994).

[12] L. F. Fu, N. D. Browning, S. X. Zhang, S. B. Ogale, D. C. Kundaliya, and T. Venkatesan, *"Defects in Co-doped and (Co, Nb)-doped TiO_2 ferromagnetic thin films,"* J. Appl. Phys. **100,** 123910 (2006).

[13] C. Silva, M. M. Cruz, R. C. da Silva, L. C. Alves, and M. Godinho, *"Iron and cobalt co-doping of single crystalline titanium dioxide,"* J. Phys.: Conf. Ser. **200,** 062028 (2010).

[14] Q. Xiao and L. Ouyang, *"Photocatalytic photodegradation of xanthate over C, N, S-tridoped TiO_2 nanotubes under visible light irradiation,"* J. Phys. Chem. Solids **72,** 39-44 (2011).

[15] Q. Xiao, Z. Si, Z. Yu, and G. Qiu, *"Characterization and photocatalytic activity of Sm^{3+}-doped TiO_2 nanocrystalline prepared by low temperature combustion method,"* J. Alloys Compd. **450,** 426-431 (2008).

[16] L. Jinhuan, Y. Xia, Y. Xiaodan, X. Leilei, K. Wanli, Y. Wenhua, G. Hongfeng, L. Zhonghe, and G. Yihang, *"Rare earth oxide-doped titania nanocomposites with enhanced photocatalytic activity towards the degradation of partially hydrolysis polyacrylamide,"* Appl. Surf. Sci. **255,** 3731-3738 (2009).

[17] A. Mattsson, M. Leideborg, L. Persson, G. Westin, and L. Osterlund, *"Oxygen diffusion and photon-induced decomposition of acetone on Zr- and Nb-doped TiO_2 nanoparticles,"* J. Phys. Chem. C **113,** 3810-3818 (2009).

[18] C.-C. Yen, D.-Y. Wang, M.-H. Shih, L.-S. Chang, and H. C. Shih, *"A combined experimental and theoretical analysis of Fe-implanted TiO_2 modified by metal plasma ion implantation,"* Appl. Surf. Sci. **256,** 6865-6870 (2010).

[19] M. Takahashi, K. Tsukigi, T. Uchino, and T. Yoko, *"Enhanced photocurrent in thin film TiO_2 electrodes prepared by sol-gel method,"* Thin Solid Films **388,** 231-236 (2001).

[20] D. Morris and R. G. Egdell, *"Application of V-doped TiO_2 as a sensor for detection of SO_2,"* J. Mater. Chem. **11,** 3207-3210 (2001).

[21] J. Choi, H. Park, and M. R. Hoffmann, *"Effects of single metal-ion doping on the visible-light photoreactivity of TiO_2,"* J. Phys. Chem. C **114,** 783-792 (2010).

[22] J. Chen, M. Yao, and X. Wang, *"Investigation of transition metal ion doping behaviors on TiO_2 nanoparticles,"* J. Nanopart. Res. **10,** 163-171 (2008).

[23] K. Nagaveni, M. S. Hegde, and G. Madras, *"Structure and photocatalytic activity of $Ti_{1-x}M_xO_2$ (M=W, V, Ce, Zr, Fe, and Cu) synthesized by solution combustion method,"* J. Phys. Chem. B **108,** 20204-20212 (2004).

[24] S. I. Shah, W. Li, C.-P. Huang, O. Jung, and C. Ni, *"Study of Nd^{3+}, Pd^{2+}, Pt^{4+}, and Fe^{3+} dopant effect on photoreactivity of TiO_2 nanoparticles "* P. Natl. Acad. Sci. **99,** 6482-6486 (2002).

[25] Y. Furubayashi, N. Yamada, Y. Hirose, Y. Yamamoto, M. Otani, T. Hitosugi, T. Shimada, and T. Hasegawa, *"Transport properties of d-electron-based transparent conducting oxide: Anatase $Ti_{1-x}Nb_xO_2$,"* J. Appl. Phys. **101,** 093705 (2007).

[26] A. V. Emeline, Y. Furubayashi, X. Zhang, M. Jin, T. Murakami, and A. Fujishima, *"Photoelectrochemical behavior of Nb-doped TiO_2 electrodes,"* J. Phys. Chem. B **109,** 24441-24444 (2005).

[27] S. W. D. Ong (2009). Design of Band Engineered Photo-Catalysts using Titanium Dioxide. Urbana, IL, University of Illinois at Urbana-Champaign.

[28] Y. Matsumoto, M. Murakami, T. Hasegawa, T. Fukumura, M. Kawasaki, P. Ahmet, K. Nakajima, T. Chikyow, and H. Koinuma, *"Structural control and combinatorial doping of titanium dioxide thin films by laser molecular beam epitaxy,"* Appl. Surf. Sci. **189,** 344-348 (2002).

[29] A. P. Singh, S. Kumari, R. Shrivastav, S. Dass, and V. R. Satsangi, *"Iron doped nanostructured TiO_2 for photoelectrochemical generation of hydrogen,"* Int. J. Hydrogen Energy **33,** 5363-5368 (2008).

[30] S. Zhang, PhD Thesis, University of Maryland, College Park, MD, 2007.

[31] P. P. Semyannikov, I. K. Igumenov, S. V. Trubin, T. P. Chusova, and Z. I. Semenova, *"Thermodynamics of chromium acetylacetonate sublimation,"* Thermochim. Acta **432,** 91-98 (2005).

[32] M. A. Siddiqi, R. A. Siddiqui, and B. Atakan, *"Thermal Stability, Vapor Pressures, and Diffusion Coefficients of Some Metal 2,2,6,6-Tetramethyl-3,5-heptandionate $[M(tmhd)_n]$ Compounds,"* J. Chem. Eng. Data **55,** 2149-2154 (2010).

[33] D. Saulys, V. Joshkin, M. Khoudiakov, T. F. Keuch, A. B. Ellis, S. R. Oktyabrsky, and L. McCaughan, *"An examination of the surface decomposition chemistry of lithium niobate precursors under high vacuum conditions,"* J. Cryst. Growth **217,** 287-301 (2000).

[34] J. Zhu, Z. Deng, F. Chen, J. Zhang, H. Chen, M. Anpo, J. Huang, and L. Zhang, *"Hydrothermal doping method for preparation of Cr^{3+}-TiO_2 photocatalysts with concentration gradient distribution of Cr^{3+},"* Appl. Catal. B **62,** 329-335 (2006).

[35] X. Li, S. Wu, P. Hu, X. Xing, Y. Liu, Y. Yu, M. Yang, J. Lu, S. Li, and W. Liu, *"Structures and magnetic properties of p-type Mn:TiO_2 dilute magnetic semiconductor thin films,"* J. Appl. Phys. **106,** 043913 (2009).

[36] Y. Xu, B. Lei, L. Guo, W. Zhou, and Y. Liu, *"Preparation, characterization and photocatalytic activity of manganese doped TiO_2 immobilized on silica gel,"* J. Hazard. Mater. **160,** 78-82 (2008).

[37] S. A. Chambers, Y. Gao, and Y. J. Kim, *"Valence Band and Core-level Photoemission and Photoelectron Diffraction in Epitaxial Nb-Doped TiO_2 (110),"* Surf. Sci. Spectra **5,** 211-218 (1998).

[38] T. Hitosugi, H. Kamisaka, K. Yamashita, H. Nogawa, Y. Furubayashi, S. Nakao, N. Yamada, A. Chikamatsu, H. Kumigashira, M. Oshima, Y. Hirose, T. Shimada, and T. Hasegawa, *"Electronic band structure of transparent conductor: Nb-doped anatase TiO_2,"* Appl. Phys. Express **1,** 111203 (111203 pp.) (2008).

[39] H. Nogowa, T. Hitosugi, A. Chikamatsu, S. Nakao, Y. Hirose, T. Shimada, H. Kumigashira, M. Oshima, and T. Hasegawa, *"Carrier compensation by excess oxygen atoms in anatase $Ti_{0.94}Nb_{0.06}O_{2+\chi}$ epitaxial thin films,"* Jpn. J. Appl. Phys. **49,** 041102 (2010).

[40] J. T. Mayer, U. Diebold, T. E. Madey, and E. Garfunkel, *"Titanium and reduced titania overlayers on titanium dioxide(110),"* J. Electron. Spectrosc. Relat. Phenom. **73,** 1-11 (1995).

[41] M. Kwoka, L. Ottaviano, M. Passacantando, S. Santucci, and J. Szuber, *"XPS depth profiling studies of L-CVD SnO_2 thin films,"* Appl. Surf. Sci. **252,** 7730-7733 (2006).

[42] J. Jouve, Y. Belkacem, and C. Severac, *"X-ray photoelectron spectroscopy study of phosphorus incorporation in anodic oxide films on niobium,"* Thin Solid Films **139,** 67-75 (1986).

[43] *CRC Handbook of Chemistry and Physics* (CRC Press, Boca Raton, FL, 2003).

[44] C. T. M. Kwok, R. D. Braatz, S. Paul, W. Lerch, and E. G. Seebauer, *"An improved model for boron diffusion and activation in silicon,"* AlChE J. **56,** 515-521 (2010).

[45] A. G. Holllister, PhD Thesis, University of Illinois at Urbana-Champaign, Urbana, 2010.

[46] T. C. Kaspar, T. Droubay, V. Shutthanandan, S. M. Heald, C. M. Wang, D. E. McCready, S. Thevuthasan, J. D. Bryan, D. R. Gamelin, A. J. Kellock, M. F. Toney, X. Hong, C. H. Ahn, and S. A. Chambers, *"Ferromagnetism and structure of epitaxial Cr-doped anatase TiO_2 thin films,"* Phys. Rev. B: Condens. Matter **73,** 155327-155321 (2006).

[47] M. Radecka, M. Wierzbicka, S. Komornicki, and M. Rekas, *"Influence of Cr on photoelectrochemical properties of TiO_2 thin films,"* Physica B **348,** 160-168 (2004).

[48] Y. Gai, J. Li, S.-S. Li, J.-B. Xia, and S.-H. Wei, *"Design of narrow-gap TiO_2: a passivated codoping approach for enhanced photoelectrochemical activity,"* Phys. Rev. Lett. **102,** 036402 (2009).

[49] K. J. Kim, Y. R. Park, J. H. Lee, S.-L. Choi, H. J. Lee, C. S. Kim, and J. Y. Park, *"Room-temperature ferromagnetic properties in Mn-doped rutile TiO_2 thin films,"* J. Magn. Magn. Mater. **316,** 215-218 (2007).

[50] G. Shao, *"Electronic structures of manganese-doped rutile TiO_2 from first principles,"* J. Phys. Chem. C **112,** 18677-18685 (2008).

[51] M. S. Dabney, M. F. A. van Hest, C. W. Teplin, S. P. Arenkiel, J. D. Perkins, and D. S. Ginley, *"Pulsed laser deposited Nb doped TiO_2 as a transparent conducting oxide,"* Thin Solid Films **516,** 4133-4138 (2008).

[52] T. Miyagi, M. Kamei, E. Sakaguchi, T. Mitsuhashi, and A. Yamazaki, *"Photocatalytic property and deep levels of Nb-doped anatase TiO_2 film grown by metalorganic chemical vapor deposition,"* Jpn. J. Appl. Phys. **43,** 775-776 (2004).

[53] L. Zhao, X. Zhao, J. Liu, A. Zhang, D. Wang, and B. Wei, *"Fabrications of Nb-doped TiO_2 (TNO) transparent conductive oxide polycrystalline films on glass substrates by sol-gel method,"* J. Sol-Gel Sci. Technol. **53,** 475-479 (2010).

[54] H. Kamisaka, T. Hitosugi, T. Suenaga, T. Hasegawa, and K. Yamashita, *"Density functional theory based first-principle calculation of Nb-doped anatase TiO_2 and its interactions with oxygen vacancies and interstitial oxygen,"* J. Chem. Phys. **131,** 034702 (2009).

[55] S. X. Zhang, S. Dhar, W. Yu, H. Xu, S. B. Ogale, and T. Venkatesan, *"Growth parameter-property phase diagram for pulsed laser deposited transparent oxide conductor anatase Nb:TiO_2,"* Appl. Phys. Lett. **91,** 112113 (2007).

[56] T. Ioannides, M. Tsapatsis, M. Koussathana, and X. E. Verykios, *"Influence of carrier doping on the interaction of benzene and toluene with supported rhodium,"* J. Catal. **152,** 331-340 (1995).

[57] A. Ruiz, A. Calleja, F. Espiell, A. Cornet, and J. R. Morante, *"Nanosized Nb-TiO_2 gas sensors derived from alkoxides hydrolization,"* IEEE Sens. J. **3,** 189-194 (2003).

[58] J.-S. Na, G. Scarel, and G. N. Parsons, *"In situ analysis of dopant incorporation, activation, and film growth during thin film ZnO and ZnO:Al atomic layer deposition,"* J. Phys. Chem. C **114,** 383-388 (2010).

[59] S. J. Lim, J.-M. Kim, D. Kim, S. Kwon, J.-S. Park, and H. Kim, *"Atomic Layer Deposition ZnO:N Thin Film Transistor: The Effects of N Concentration on the Device Properties,"* J. Electrochem. Soc. **157,** H214-H218 (2010).

[60] S.-Y. Pung, K.-L. Choy, X. Hou, and K. Dinsdale, *"In situ doping of ZnO nanowires using aerosol-assisted chemical vapour deposition,"* Nanotechnology **21,** 345602 (2010).

[61] J. Y. Yang, W. S. Li, H. Li, Y. Sun, R. F. Dou, C. M. Xiong, L. He, and J. C. Nie, *"Grain size dependence of electrical and optical properties in Nb-doped anatase TiO_2,"* Appl. Phys. Lett. **95,** 213105 (2009).

[62] B. Neumann, F. Bierau, B. Johnson, C. A. Kaufmann, K. Ellmer, and H. Tributsch, *"Niobium-doped TiO_2 films as window layer for chalcopyrite solar cells,"* Phys. Status Solidi B **245,** 1849-1857 (2008).

[63] D. Kurita, S. Ohta, K. Sugiura, H. Ohta, and K. Koumoto, *"Carrier generation and transport properties of heavily Nb-doped anatase TiO_2 epitaxial films at high temperatures,"* J. Appl. Phys. **100,** 096105 (2006).

[64] Y. Sato, H. Akizuki, T. Kamiyama, and Y. Shigesato, *"Transparent conductive Nb-doped TiO_2 films deposited by direct-current magnetron sputtering using a TiO_{2-x} target,"* Thin Solid Films **516,** 5758-5762 (2008).

[65] N. Yamada, T. Hitosugi, H. Ngoc Lam Huong, Y. Furubayashi, Y. Hirose, S. Konuma, T. Shimada, and T. Hasegawa, *"Structural, electrical and optical properties of sputter-deposited Nb-doped TiO_2 (TNO) polycrystalline films,"* Thin Solid Films **516,** 5754-5757 (2008).

Chapter 5: Transient Behavior of Defects at TiO_2 Interfaces

5.1 Abstract

Buried solid-solid interfaces of metal oxides in thin film structures are arising with increasing frequency in electronics applications such as memory resistors and dye-sensitized solar cells. Yet certain electrical properties of these interfaces, such as the degree of fixed charge buildup, can be difficult to characterize. This charge buildup can be very sample-dependent for some oxides, and depend on only a small fraction of the total surface sites ($< 1 \times 10^{-3}$). Photoreflectance (PR), a type of optical modulation spectroscopy, can be utilized to detect and sometimes quantify the presence of electric fields near solid-solid interfaces as long as the overlayer is transparent to the probe light. The present work describes the applicability of PR to characterizing metal oxide interfaces using thin film TiO_2 as an example metal oxide. The approach involves the synthesis of thin film polycrystalline anatase TiO_2 on Si(100) and quartz by atomic layer deposition (ALD) with $Ti(OCH(CH_3)_2)_4$ and H_2O as precursors. PR is utilized to examine the surface and interface electric fields as a function of substrate material and microstructure. Spectra reveal the existence of distinct transient effects evolving on several different time scales. A several week effect shows up as a decrease in overall PR signal amplitude and could arise from a change in bulk carrier concentration or chemical reaction at the solid interface. Faster temporal effects manifest as a sloping PR signal baseline and spectral phase change and are attributed to charge exchange between surface/interface/grain boundary states and the bulk bands.

5.2 Introduction

Conventional and photonic integrated circuits employ silicon in close proximity to functional silicon oxide and nitride layers. As device length scales shrink according to Moore's Law, interfaces between these sorts of disparate materials are growing ever-closer to bulk regions. Consequently, the performance of transistors and interconnect structures are increasingly influenced by defects and fixed charge at solid-solid interfaces. Non-traditional "devices" such as memory resistors [1] and dye-sensitized solar cells (DSSCs) [2] comprising metal oxide semiconductors like TiO_2 are similarly affected. Nevertheless, phenomena at metal oxide interfaces are comparatively less well-characterized. In order to further tune device performance, rates of bulk-interface charge exchange must be better characterized. Additionally, metrology challenges must be overcome to allow for real-time, contactless characterization of metal oxide-substrate and metal oxide-metal junctions.

TiO_2 is one of the more attractive material options for next-generation non-volatile memory. Current charge-based memories will soon be prohibitive at the length scales targeted by integrated circuit manufacturers. An ideal, non-charge-based alternative will be not only denser and faster, but also less energy-consuming. Since the 1970s, the existence of a fundamental, two-terminal circuit element complementary to the resistor, conductor, and capacitor, has been postulated. The missing memory resistor (or memristor) was found in 2008 by physicists at HP Labs [3]. Conceptually, it is a two-terminal device whose resistance depends on the magnitude and polarity of the voltage applied to it and the length of time that the voltage has been applied [1]. Functioning devices have been fabricated as multi-layer stacks incorporating Si, SiO_2, Pt, and TiO_2. Understanding the physical mechanism behind the fast resistive switching in TiO_2-based memristors is critical to device

optimization. Preliminary studies suggest that fast switching is accomplished by the formation of conductive nanofilaments within the TiO_2 layer that exists sandwiched between top and bottom Pt electrodes [4]. Transmission electron microscopy has been used to probe the formation and disruption of these unique Magneli phase filaments. In such a scenario, close coupling exists between the built-in electric field at the TiO_2-Pt interface and memristor switching speed. The formation of the conductive filaments themselves depends on an oxygen vacancy-assisted tunneling processes and the breakdown of interfacial oxide [5].

Metal oxide semiconductors are also appealing for integration into photovoltaics such as DSSCs. Nanocrystalline materials are substantially more economical than the silicon-based solid-state junction devices that have historically dominated the photovoltaic market. New systems replace the contacting phase to the semiconductor with an electrolyte, liquid, gel, or solid in order to form a photo-electrochemical cell [6]. Specifically, a DSSC consists of a wide-band gap polycrystalline semiconductor such as TiO_2 or ZnO decorated with a monolayer of dye. Upon photoexcitation, the dye injects an electron into the conduction band of the oxide. Equilibrium is re-established by charge transfer from the adjacent electrolyte. A constant regenerative process allows for the generation of electric power from incident light. It is important to realize that the TiO_2-dye interface is not the only interface that affects power generation. Modeling results suggest that a built-in electric field at the TiO_2-substrate interface significantly affects DSSC performance [7].

There is a limited cadre of techniques suitable for evaluating defects and fixed charge at solid-solid interfaces. Electron beam induced current (EBIC) is a scanning electron microscopy imaging mode that localizes regions of Fermi level transition. It is primarily used to identify buried diffusions and semiconductors defects [8] that produce local

variations in Fermi levels or built-in potentials [9]. These features can enhance or diminish recombination current and thus alter the collected EBIC signal. EBIC is not an ideal choice for studying surfaces and interfaces since it requires the formation of electrical contact to the sample. Additionally, an external scan control generator is required to convert the qualitative contrast image produced directly from the EBIC signal into quantitative results. The contactless second harmonic generation technique has also been proven sensitive to electric fields at deeply buried interfaces [10]. It exploits the tendency of asymmetrical surfaces and interfaces to generate light at a frequency twice that of the incident light. While it has been used to study silicon on interface (SOI) wafers [11], it is only suitable for bulk materials that are centrosymmetric and often requires several weeks to collect a single spectrum [12].

Photoreflectance (PR) is one of a class of modulation spectroscopies in which the temperature, applied stress, electric or magnetic field of a semiconductor sample is periodically perturbed, and the resulting small change in dielectric constant is detected by reflectance [13, 14]. Electroreflectance (ER) is another type of electromodulation wherein normalized reflectance changes result from electric field modulation accomplished by the application of voltage to contacts attached to the sample [15]. ER is capable of yielding information about the energy gap of semiconducting materials, as well as the energies of optical transitions. Unlike PR, this method is traditionally not contactless and requires a Schottky barrier or a semiconductor electrolyte junction [16]. A contactless ER method has been developed more recently [17, 18], but requires the use of a confined geometry that is not well-suited to UHV or heating [19].

The principle behind PR is shown in Fig. 5.1. The semiconductor sample is periodically perturbed with a chopped laser beam having $h\nu$ greater than the fundamental

bandgap energy E_g. Photogenerated minority charge carriers migrate to the interface and recombine with charge stored there. The resulting change in built-in electric field affects the surface reflectance R in narrow regions of wavelength corresponding to optical transitions of the material under examination. The small reflectance change $\Delta R/R$ exhibits a spectral dependence that is monitored with a weaker, independent probe beam using phase-sensitive detection. The presence of a nonzero PR spectrum demonstrates unequivocally the existence of surface band bending [20]. The amplitude of the spectrum increases as electric field increases. Thus, the degree of band bending can be inferred from trends in $\Delta R/R$ with respect to time, heat, or temperature. For instance, the decay in PR signal at the Si/SiO_2 interface upon 250°C annealing (Fig. 5.2) corresponds to the healing of charged defects present at the interface and a concurrent decrease in electric field. For spectra of suitable intensity and lineshape, fitting using the classical third-derivative functional form expected for electromodulation spectroscopies [21] yields quantitative information about surface potential.

Metal oxide semiconductor surfaces and interfaces have not been studied extensively with either photoreflectance or electroreflectance. For the case of ZnO, PR and ER investigations focus on bulk electronic band structure [22, 23, 24]. For instance, the Franz-Keldysh oscillations present in PR spectra of ZnO have not been studied to characterize the surface Fermi level, surface electric field, or density of surface states.

The only available TiO_2 modulation spectroscopy studies employ electrolyte electroreflectance; photoreflectance has not been demonstrated. Illuminated single crystal rutile TiO_2 (n-type, 10^{17} cm^{-3}) in contact with 0.5M Na_2SO_4 exhibits band unpinning for certain photocurrent values (< 2 $\mu A/cm^2$) [25]. Changes in flatband voltage are discussed in the context of local pH changes and hole trapping at surface states. Boschloo and co-workers

examined ~200 nm polycrystalline anatase TiO_2 deposited on indium tin oxide (ITO) using chemical vapor deposition (CVD) [26]. Their spectra were obtained at 80 Hz and 100 mV rms as a function of applied DC potential. At 0V bias, they found a critical point of 3.8 eV with a broadening factor of 0.2 eV that they ascribed to a direct optical transition of anatase TiO_2. In comparing these results to the dielectric-function spectra measured by Karunagaran *et al.* [27], the aforementioned critical point likely corresponds to the $E_1 + \Lambda_1$ critical point structure noted at 3.9 eV, which arises due to spin-orbit splitting of the valence band in the Λ-direction. Kulak *et al.* obtained ER spectra for 100 nm films of amorphous (300°C anneal), anatase (450°C anneal), and mixed anatase-rutile (700°C anneal) TiO_2 prepared by hydrolysis of poly(butyl titrate) [28]. Annealing induced an intense signal in the 2.4 to 3.0 eV range; the response was attributed to localized surface and grain boundary electronic states.

The present work describes the applicability of PR to characterizing metal oxide interfaces using thin film TiO_2 as an example metal oxide. The approach involves the synthesis of thin film polycrystalline anatase TiO_2 on Si(100) and quartz by ALD with $Ti(OCH(CH_3)_2)_4$ and H_2O as precursors. PR is utilized to examine surface and interface electric fields as a function of substrate material and microstructure.

5.3 Methods and procedures

A schematic diagram of the general experimental setup for photoreflectance is shown in Fig. 5.3. The apparatus has been described previously [29], and the details of the apparatus automation including stepper motor control and data collection remain the same.

The changes made to the experiment in order to successfully obtain and analyze spectra from TiO_2 will be discussed in more detail.

The apparatus was set up in "benchtop configuration;" experiments were not performed under vacuum as in [30] or [31]. PR scans were collected at room temperature. The signal acquired at room temperature was already relatively small and PR spectral amplitude should decrease rapidly with increasing temperature due to thermal free carrier generation.

5.3.1 Optics and lasers

When examining TiO_2, BK-7 optics were used for both the pump and probe beam optical trains; these act as filters for the pump beam photons to prevent saturation of the detector. UV grade fused-silica lenses afford far greater UV transmission and do not fluoresce under UV light (for wavelengths longer than 290 nm).

Monochromatic light was directed through two plano-convex lenses and focused on the sample at a 45º angle of incidence. The beam was expanded horizontally by a LUP-50.0-93.9-UV Melles Griot fused silica lens with focal length of 200.0 mm and diameter of 50 mm; vertical expansion was accomplished by a LUP-50.0-82.2-UV Melles Griot fused silica lens with focal length 175 mm and diameter of 50 mm. The illuminated area of the sample was approximately 1.7 cm x 1.7 cm after beam expansion.

An additional LUP-50.0-82.2-UV plano-convex lens was inserted after the sample mount to focus the reflected probe beam on the Si photodiode detector. A blue filter was also present inside the photodiode assembly at all times. When the light reflected back from the sample is focused on the detector, the entire assembly can be moved up/down and left/right

in order to optimize the collection of light/signal. Focusing is accomplished by moving the assembly forward and backward on the slide rail.

For all studies described here, a Hamamatsu S1336-44BK photodiode was utilized. Fig. 5.4(a) shows the wiring and connections for the photodiode assembly. The Hamamatsu photodiode is sufficient for use with wavelengths above 325 nm. For wavelengths below 325 nm, a UV enhanced photodiode Pacific Silicon Sensor PR33-2-TO8 with area of 5.5 mm x 6.1 mm is available. The UV enhanced photodiode has high sensitivity for wavelengths down to 190 nm.

Two lower-wavelength pump beams were investigated as replacements for the Uniphase 106-1 continuous wave 632.8 nm HeNe laser used for Si studies.

The first was a Aixiz Rkcstr Blu-Ray 405nm 120mA laser module (www.hightechdealz.com). A potentiometer and ammeter were placed in series with the voltage fed to the laser driver. The current was adjusted by using a “trimmer” mounted on the driver assembly. The laser was calibrated such that 34 mA = 10 mW and 42 mA = 20 mW.

The second was a NSPU510CS UV LED from Nichia Corporation. The LED was encased with a shroud fabricated from heat shrink wire casing. This helped to give shape to the beam as well as reduce stray photon emission from the sides of the LED. The circuit for operation of the UV LED is shown in Fig. 5.4(b). The voltage delivered to the LED should be kept less than 4.5 V; the power supply should be operated with the current limit knob set to maximum. The failure mechanism of the LED is that less UV output is obtained. However, the LED will continue to glow and the current draw will remain in the appropriate range (3 – 4 V). An additional component, a fused silica plano-convex lens of focal length

300 mm (LUP-50.0-140.9) was added to the optical train when this probe beam was used. The lens converged the light of the LED into a beam of approximately 5 mm in diameter.

5.3.2 Sample preparation and physical characterization

Experiments were performed using TiO_2 deposited by ALD onto either n-type Si(100) or glass slides as described previously. In almost all cases, Si substrates were etched with 49% HF (1 min) following by rinsing with deionized water (1 min) immediately prior to insertion in the vacuum chamber to minimize native oxide formation at the TiO_2/Si interface. Glass samples were degreased by successive 5 min rinsing cycles in electronic-grade trichloroethylene, acetone, and methanol. Here, films were deposited at 400°C as well as 200°C. Film thickness was varied between 100 and 500 nm as needed by manipulation of number of ALD cycles. Films deposited at 400°C are polycrystalline as synthesized and were not subjected to any post-deposition annealing. Films deposited at 200°C were subjected to 24 hr annealing under ambient conditions at 550°C.

As described in Chapters 3 and 4, TiO_2 morphology was examined using a Hitachi Model S4800 SEM. XRD and XRR patterns were obtained at room temperature with a high-resolution Philips X'Pert diffractometer (λ = 0.15406 nm) operated at 45 kV and 40 mA with a Cu Kα1 primary x-ray beam from a hybrid monochromator consisting of a parabolic x-ray mirror and a 2-reflection Ge(220) monochromator (aka "X'Pert 1").

All samples were stored under ambient conditions (i.e., they were neither kept in the dark nor illuminated). TiO_2 on Si samples were rinsed with acetone immediately prior to mounting on the PR sample mount. TiO_2 on glass samples were cleaned in a similar fashion.

5.3.3 Photoreflectance data collection

PR measurements were all acquired at room temperature using the Nichia UV LED and LabVIEW "virtual instrument" (VI) shown in Fig. 5.5. Wavelength was typically scanned over the range of 410 to 325 nm, or near the degenerate E_1 and E_0' optical transitions of Si and the fundamental band edge of anatase TiO_2. The monochromator was stepped at a rate of either 0.15 or 0.3 nm/min.

5.3.4 Photoreflectance data analysis

Historically, a Visual Basic program has been used to analyze collected photoreflectance spectra [30]. Here, LabVIEW was used to create a VI for analyzing photoreflectance data. The user interface of the VI can be seen in Fig. 5.6. The complete LabVIEW VI code can be found in Appendix B.

In brief, the VI prompts the user to enter the sensitivity, start wavelength, and scan speed used for collection of the spectrum in question. If data smoothing is desired, the "Data Smoothing" Boolean button can be selected. The standard weighting fraction of 0.05 will typically result in smoothed data that resembles the original raw data. Parameters can be extracted by selecting both the "Data Smoothing" and "Extract Parameters" Boolean buttons.

Once the software is run, data will be plotted on the "Unsmoothed PR Data" graph and "Data Smoothing" graph (if applicable). If the "Extract Parameters" Boolean button was selected, a preliminary fit will be plotted on the "Parameter Fitting" graph. Further refinement of fitting parameters can be performed by entering in a revised broadening parameter followed by selecting "Adjust Broad Fit." Subsequently, the phase factor can be tweaked by entering in a new phase factor and selecting the "Adjust Phase Fit" Boolean

button. Lastly, the amplitude factor can be varied by entering in a new amplitude factor and selecting “Adjust Amp Fit.”

At the conclusion of converting, smoothing, or fitting data, selecting the “Save Final Parameter Fit” Boolean button will save the pertinent data to file. If you only chose to convert data, the file will contain values of wavelength in eV and 1000*$\Delta R/R$. If you chose to smooth the data, the file will also contain the smoothed 1000*$\Delta R/R$ values. If you performed parameter fitting, the broadening parameter, amplitude factor, and phase factor will also be saved to file.

5.4 Results and discussion

5.4.1 Morphology and crystallinity

TiO_2 morphology and crystallinity for example 100 nm polycrystalline anatase films deposited at 200°C and 400°C are shown in Fig. 5.7. As discussed in Chapter 3, the 200°C film comprises oblong agglomerates with distinguishable crystallite boundaries but no obvious cracks or voids (Fig. 5.7(a)). In contrast, the 400°C film has high aspect ratio columnar rods ~20 nm in width with substantial spacing in between crystallites (Fig. 5.7 (b)).

The room temperature XRD spectra in Fig. 5.7(c) reveal that both films are polycrystalline anatase with slight preferential (101) orientation. Peak intensity is reduced for the 400°C film. Average crystallite size in the film growth direction changes significantly with deposition temperature. Values of 39.2 ± 2.0 nm and 27.9 ± 1.5 nm are obtained for the 200°C and 400°C films, in that order. Film strain was estimated by comparing the *c*-axis lattice constant to that of bulk anatase TiO_2 (9.5139 Å). The variation

was minimal (less than ± 0.3%) for the 200°C film, but approximately 1% for the 400°C film.

5.4.2 TiO_2 free surface

Fig. 5.8 shows room temperature PR spectra for polycrystalline anatase TiO_2 deposited on glass at 200°C (Fig. 5.8(a)) and 400°C (Fig. 5.8(b)). The lack of spectral features indicates negligible band bending at the TiO_2 free surface. This suggests that the Fermi level at the interface and within the near-interface bulk coincide, resulting in little or no electric field at the interface [31]. A lack of electric field would reduce the photoreflectance signal to zero.

The negligible surface electric field for both morphologies of polycrystalline anatase TiO_2 on glass is attributed to passivation of dangling bonds by ambient contamination such as water or hydroxyl species. Clearly, adsorbates affect surface band bending in a similar fashion regardless of variations in inter-crystallite spacing. On rutile TiO_2, H_2O molecules aggregate into clusters due to the high surface tension of H_2O arising from intermolecular hydrogen bonds [32]. This aggregation leads to a relaxation of free surface energy and stabilization of H_2O adsorption states. Intrinsic defects on the TiO_2 surface also act as active sites for chemisorption and/or decomposition of O_2, H_2, and CO [33]. Hydrogen atoms and oxygen vacancies diffuse rapidly even at room temperature. The latter act as chemisorption sites for H_2 and CO and prevent bulk TiO_2 properties from influencing the electrical potential at the free surface.

5.4.3 TiO_2/Si interface

In contrast, PR spectra obtained for TiO_2 on Si exhibit well-defined spectral features, the amplitudes of which decay gradually over time. Figs. 5.9(a) and (b) display average PR spectra for ~500 nm thick 200°C and 400°C films where data is collected one day and seven days after deposition and post-annealing (200°C sample only). At the one day mark, a clear spectral feature attributed to TiO_2 is noted in the 3.05 to 3.10 eV range. The amplitude of the PR signal decreases noticeably with time to roughly one third its original value. There is no evidence of a contribution from the underlying Si substrate, which would manifest as a signal at approximately 3.4 eV.

For extended time scales (~1 year), even thinner ~100 nm TiO_2 films exhibit a weak feature at comparable energy (Fig. 5.10). Note the substantial difference in *y*-axis $\Delta R/R$ scale.

For polycrystalline anatase TiO_2 deposited on Si by ALD, electric fields at the TiO_2-Si interface lead to non-negligible band bending in the vicinity of the E_0 optical transition for TiO_2. Alternative experimental techniques support this observation. Wei and co-workers performed transient photovoltage measurements of nanoporous TiO_2 films on fluorine-doped tin oxide (FTO) electrodes and semitransparent platinum substrates [34]. A thick layer of TiO_2 (15,000 nm) was prepared by sol-gel and annealed at 450°C to induce crystallization. At the interface between the TiO_2 film and the substrate, separation and transport of photo-induced charge carriers was controlled by a built-in electric field, the magnitude of which varied with the work function of the FTO vs. Pt substrate. Rothschild *et al.* used surface photovoltage spectroscopy to study ~200 nm TiO_2 on Si(100) subjected to 24 heat treatment in reducing (~7.5 x 10^{-8} Torr, 450°C) or oxidizing environment (atmosphere, 400°C) [35].

They noted surface and intergranular interface band bending in both cases; the degree of band bending was enhanced for the oxidized film. This behavior was attributed to the chemisorption of charged oxygen atoms during the atmospheric pressure annealing process. According to the authors, states at the crystallite surfaces as well as intergranular interfaces (i.e., grain boundaries) capture conduction band electrons, producing depletion layers in the adjacent regions and altering surface and intergranular potential barriers.

In this study, the reduction in TiO_2 PR signal amplitude suggests a decrease in interfacial electric field over time. The decay is independent of film microstructure; films deposited at 200°C and 400°C exhibit the same behavior. There are two possible explanations for this:

1) Change in bulk donor carrier concentration over time
2) Slow interfacial reaction leading to a change in interface band bending

These options will be evaluated in the context of the available TiO_2 physical and electrical characterization data.

As discussed at length in Chapter 3, the donor carrier concentration of polycrystalline TiO_2 changes with time for samples exposed to moderate illumination. After one week of illumination, N_d became relatively independent of film thickness and converged to ~1.2 x 10^{17} cm^{-3}. This was attributed to a change in charge trapped at grain boundary defects or the creation of surface states capable of pinning the Fermi level. In either of these scenarios, illumination intensity should influence the rate of carrier concentration change. Indeed, preliminary studies suggest that N_d varies with time even for samples stored under ambient conditions. In the context of the experimentally determined PR spectra, a reduction in N_d

would cause a widening of the space charge region and reduction in interface electric field even with constant band bending.

Alternatively, the reduction in PR signal over time could arise due to a slow chemical reaction at the anatase TiO_2-Si interface causing a decrease in band bending. If this were the case, one would expect to see an enhancement of Si spectral contribution. Indeed, Fig. 5.11 shows that the TiO_2 film is thin enough to observe a Si signal under some configurations. A small Si feature (Fig. 5.11(a)) is discernable for ~175 nm polycrystalline anatase on TiO_2 (200°C) on Si when native oxide is left on the Si surface prior to TiO_2 deposition. A substantial Si feature (Fig. 5.11(b)) is identified for ~450 nm amorphous TiO_2 (200°C, no annealing) on Si, also without HF etching prior to film deposition. Two conclusions can be gleaned from this data. First, despite the subtle differences in film preparation method, there is every reason to believe that the UV LED is capable of generating a Si signal. No such signal is identifiable in Fig. 5.9, regardless of deposition temperature and measurement acquisition interval. Second, failure to remove native SiO_2 at the Si substrate surface prior to TiO_2 deposition actually *increases* the degree of band bending at the interface.

By extension, it is more likely that a slow chemical reaction at the TiO_2-Si interface would lead to increased oxide formation and thus *increased* band bending. The TiO_2-Si interface for CVD films deposited at 300°C and 400°C consists of an interlayer on the order of 2 nm thick comprising SiO_x and $TiSiO_x$ [36]. High-resolution transmission electron microscopy images reveal a sharp boundary between the TiO_2 and the interlayer. A similar interlayer should exist for the films deposited at 200°C and 400°C in this study. If anything, post-deposition annealing should lead to the formation of additional SiO_2 at the TiO_2-Si

interface [37]. The decrease in PR signal observed here is uninfluenced by post-deposition annealing, however.

Additional transient time scales are identified in TiO_2 PR spectra. The individual photoreflectance scans contributing to the average presented in Fig. 5.9(b) (400°C, day 1) are shown in Fig. 5.12. The four runs were collected sequentially over the course of about one hour. Less than a minute passed in between the conclusion of one run and the commencement of another. No adjustments were made to the UV LED or lock-in amplifier over the data collection period. While the PR lineshape remains fairly constant from run-to run, it inverts in a fashion that suggests the optical signal is moving from in-phase with the reference phase to 90 degrees out of phase, to 180 degrees out of phase, etc. Furthermore, there is modest evolution in the absolute magnitude of the signal over the ~10 minutes required to collect a single spectrum.

The first phenomenon can be explained in terms of charge exchange between defects and optically generated charges. The spectral inversion implies a phase shift in the lock-in detection. With knowledge of the chopping frequency, the time constant of this process can be estimated. Since the chopping frequency is approximately 400 Hz, charge exchanges into defects at 1/400 Hz or about 2 ms.

The second phenomena, which manifests as a change in the absolute magnitude of the PR signal for intermediate time scales, may arise from either:

1) A change in the relative contributions of two separate, but spectrally unresolved, surface state and bulk features or

2) Discharging of a surface state feature. In this case, photostimulation is responsible for both the original charging of the surface state feature and the subsequent discharging of the same feature.

Evidence to this effect stems from electroreflectance spectra of hydrogen peroxide terminated n-type GaAs(100) single crystal in solution [38]. Koper and co-workers identified two distinct contributions to their ER spectra: one having to do with field modulation in the space charge layer and the other a direct spectral manifestation of surface states. Modulation frequency studies revealed that surface states could not keep up with modulation greater than 200 Hz; above this frequency, the direct surface state contribution to the ER spectrum disappeared. To some degree, the broad surface state feature they observe sloping upward at ~2.0 eV resembles the broad feature in the TiO_2 spectra of Fig. 5.9. For the case of TiO_2 examined with the present PR configuration, it may not be possible to deconvolve surface state features from bulk features.

5.5 Conclusion

The present work provides the first insights into time-dependent electric fields at polycrystalline TiO_2 surfaces and interfaces using photoreflectance, a type of contactless modulation spectroscopy. The implications of these electric fields are discussed as they pertain to TiO_2-based electronic devices. The lack of PR signal from TiO_2 on glass suggests adsorbates present in the atmosphere may passivate dangling bonds at the free surface. UHV experiments could be employed to examine the influence of absorbate coverage on electric fields at the TiO_2 surface. For TiO_2 on Si, PR confirms the existence of a built-in electric field at the interface, albeit one that exhibits temporal variations that depend, in some cases,

on film microstructure. Further studies should be undertaken to unravel the correlation between bulk electrical properties and electric field at the buried TiO_2-Si interface.

5.6 Figures

Fig. 5.1 Schematic representation of the photoreflectance effect for a n-type sample. When the laser is off, Fermi level pinning to surface states induces a built-in electric field. When the laser is turned on, photogenerated charge carriers recombine in the space charge region and neutralize charge in surfaces states. Figure after [39].

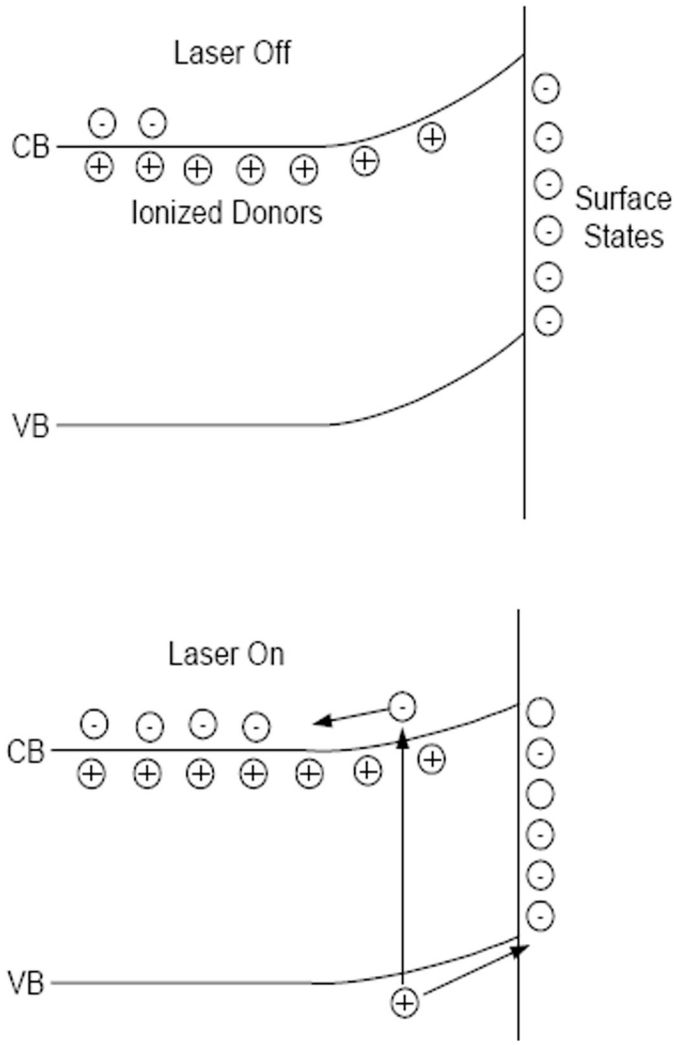

Fig. 5.2 Series of raw PR spectra from Ar-implanted Si(100)-SiO_2 annealed at 250°C for varying amounts of time [40].

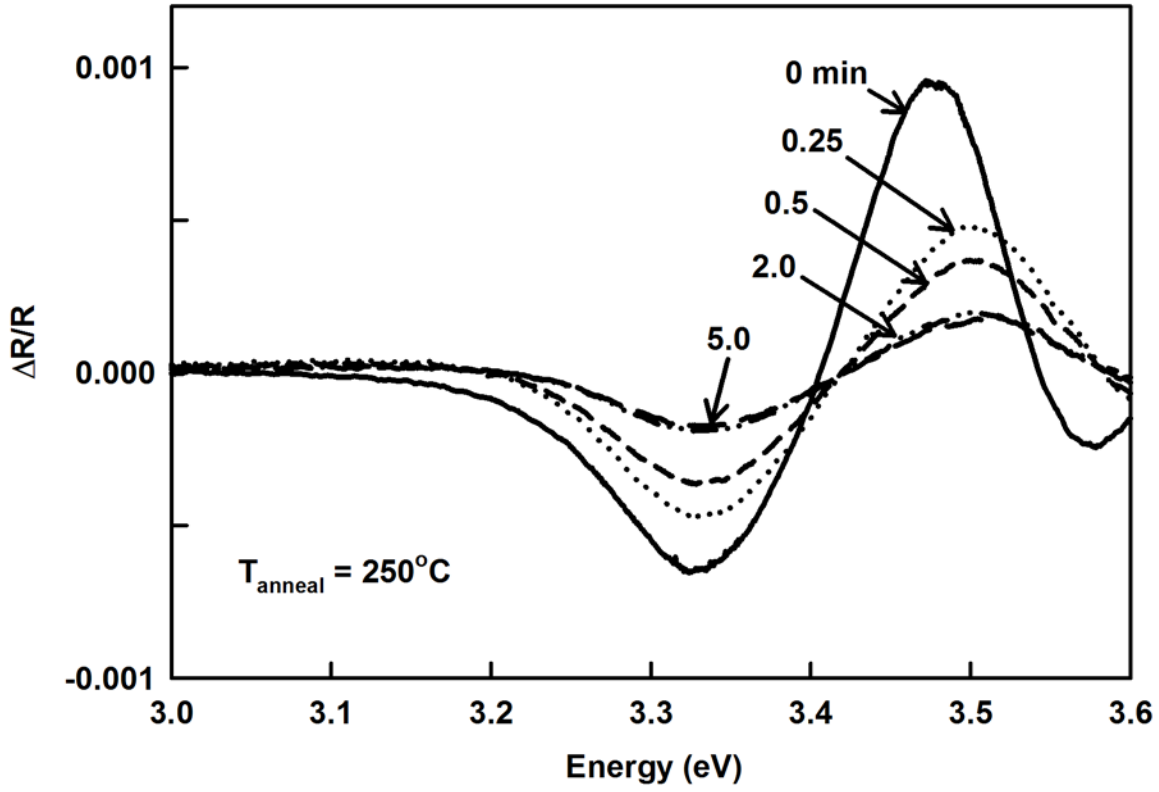

Fig. 5.3 Schematic diagram of TiO_2 photoreflectance apparatus.

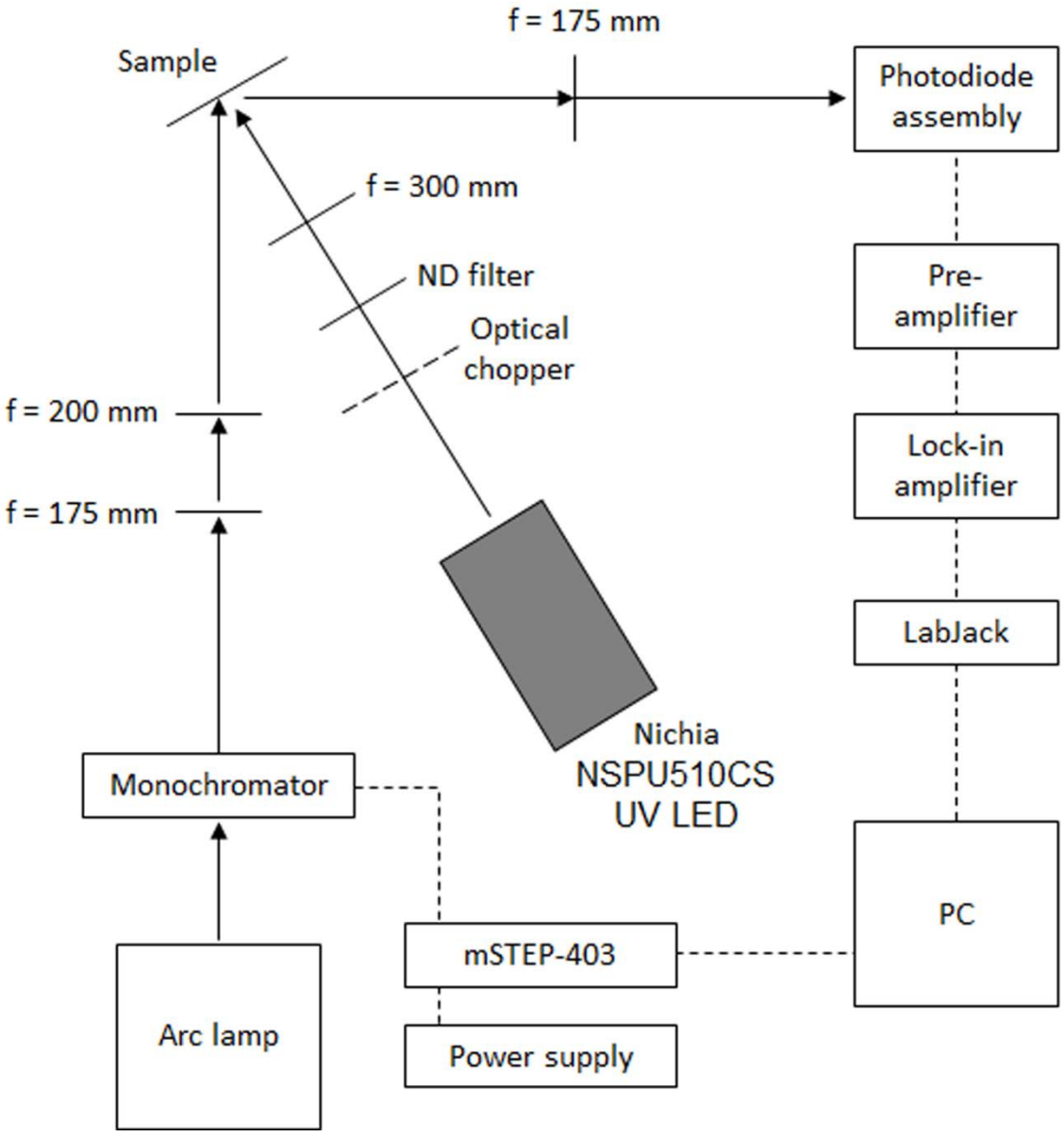

Fig. 5.4 Circuit schematics for (a) Hamamatsu S1336-44BK photodiode and (b) NSPU510CS UV LED from Nichia Corporation showing method of integration into photoreflectance apparatus.

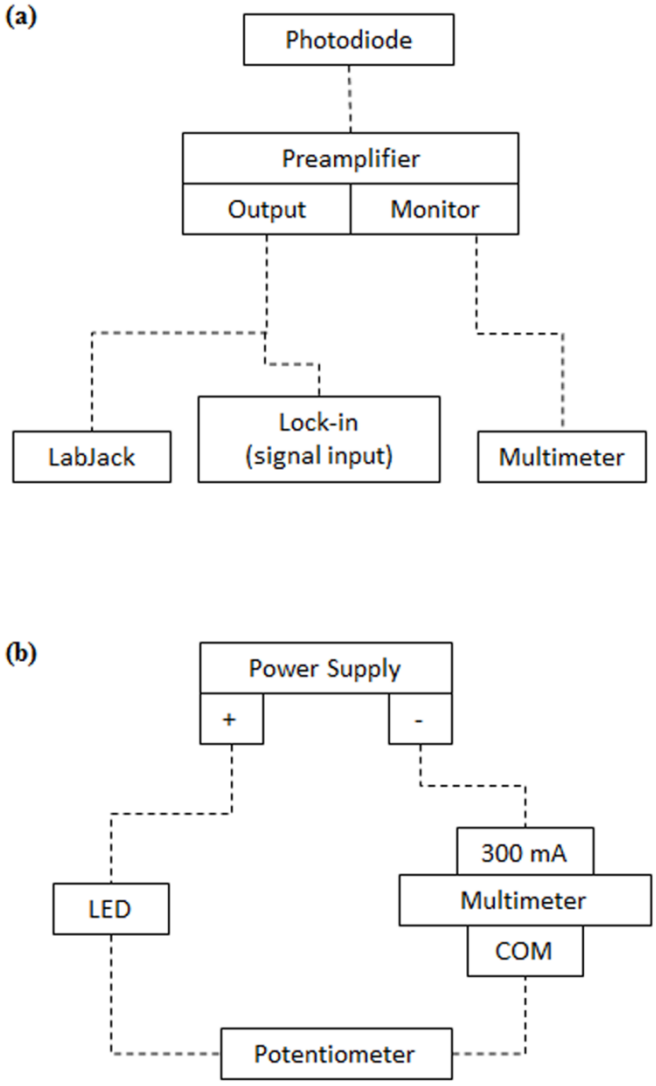

Fig. 5.5 User interface of the LabVIEW photoreflectance data collection VI.

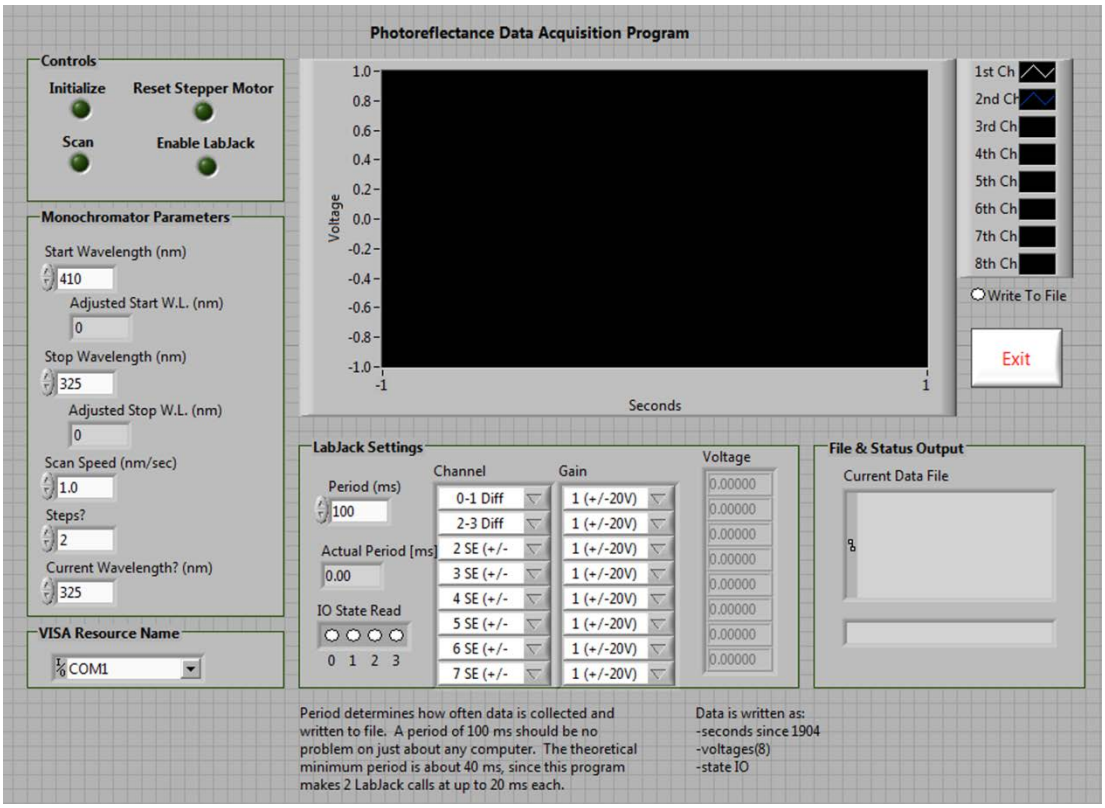

Fig. 5.6 User interface of the LabVIEW photoreflectance data analysis VI.

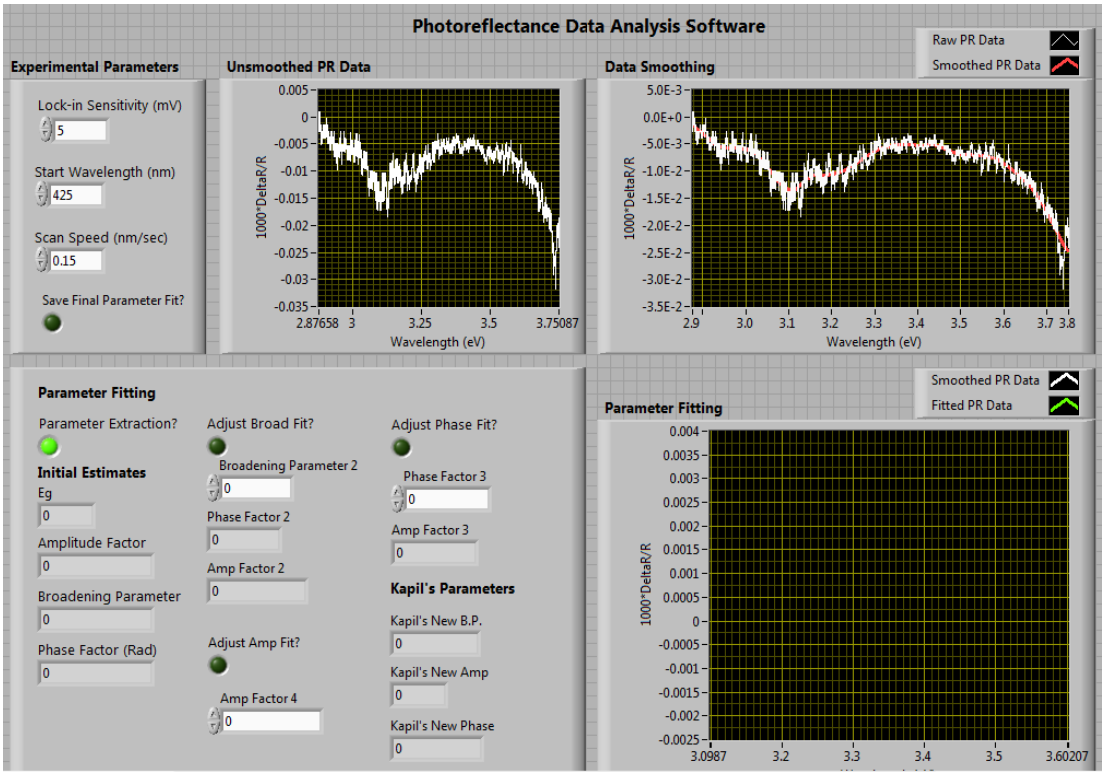

Fig. 5.7 Cross-sectional SEM images of 100 nm TiO_2 deposited at (a) 200°C with subsequent 24 hr, 550°C anneal and (b) 400°C as well as (c) XRD data for the same 200°C and 400°C films.

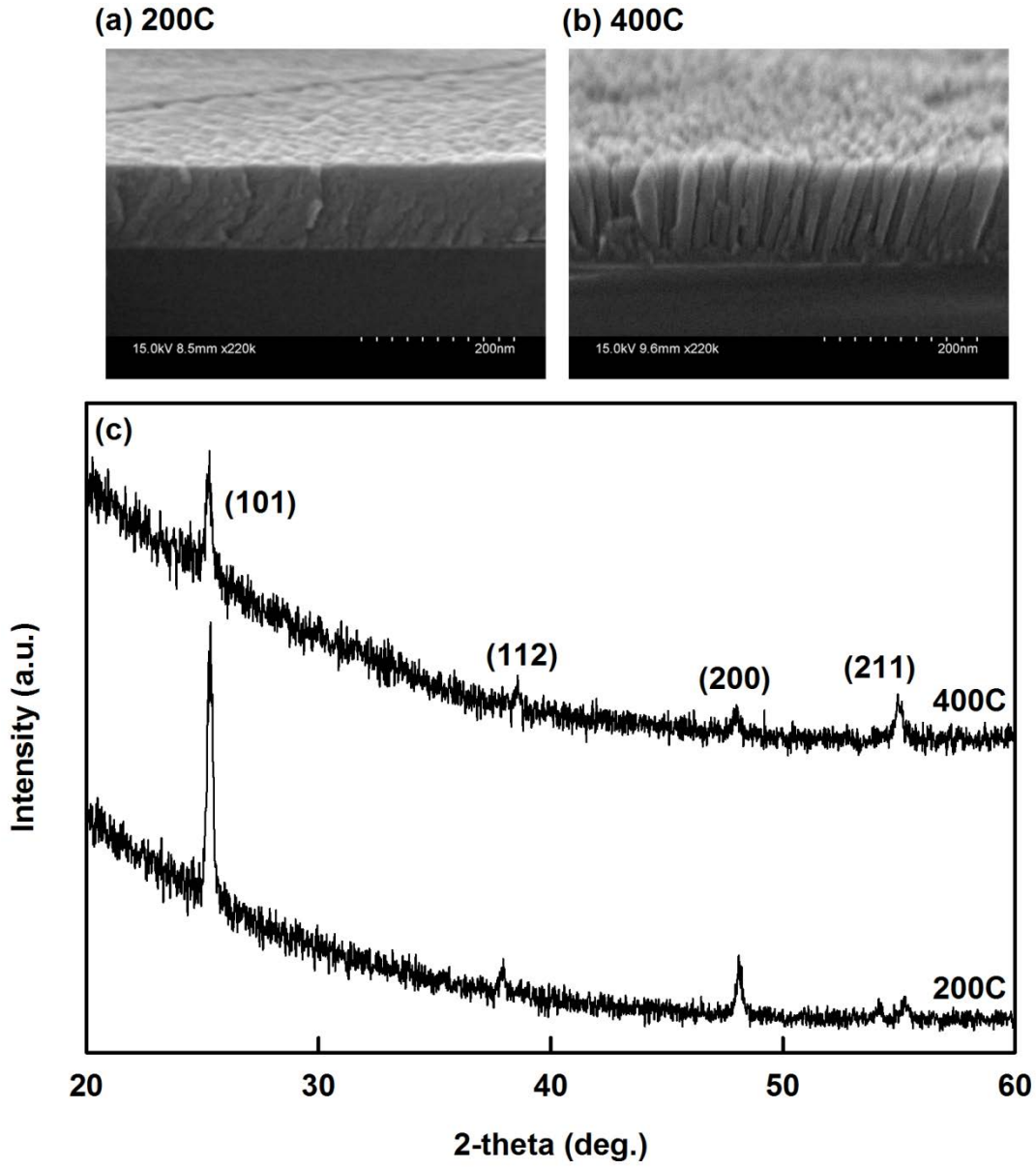

Fig. 5.8 Averaged PR spectra for ~200 nm polycrystalline anatase TiO_2 on glass deposited at (a) 200°C with subsequent 24 hr anneal at 550°C (Sample 102309.1, 5 mV) and (b) 400°C (Sample 102309.2, 2 mV).

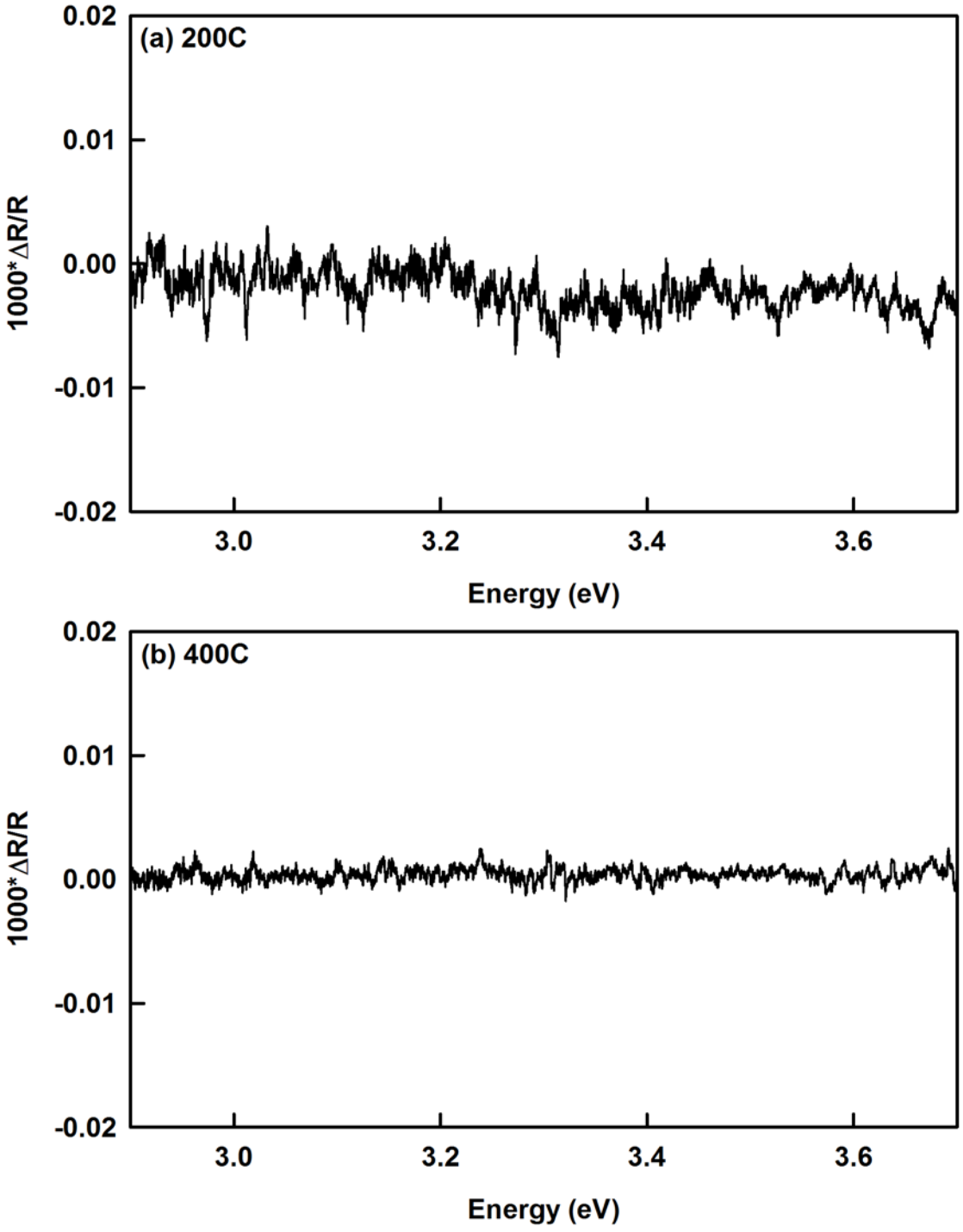

Fig. 5.9 Averaged PR spectra for ~500 nm polycrystalline anatase TiO_2 on Si(100) deposited at (a) 200°C with subsequent 24 hr anneal at 550°C (Sample 120409.6, 2 mV) and (b) 400°C (Sample 120709.5, 2 mV).

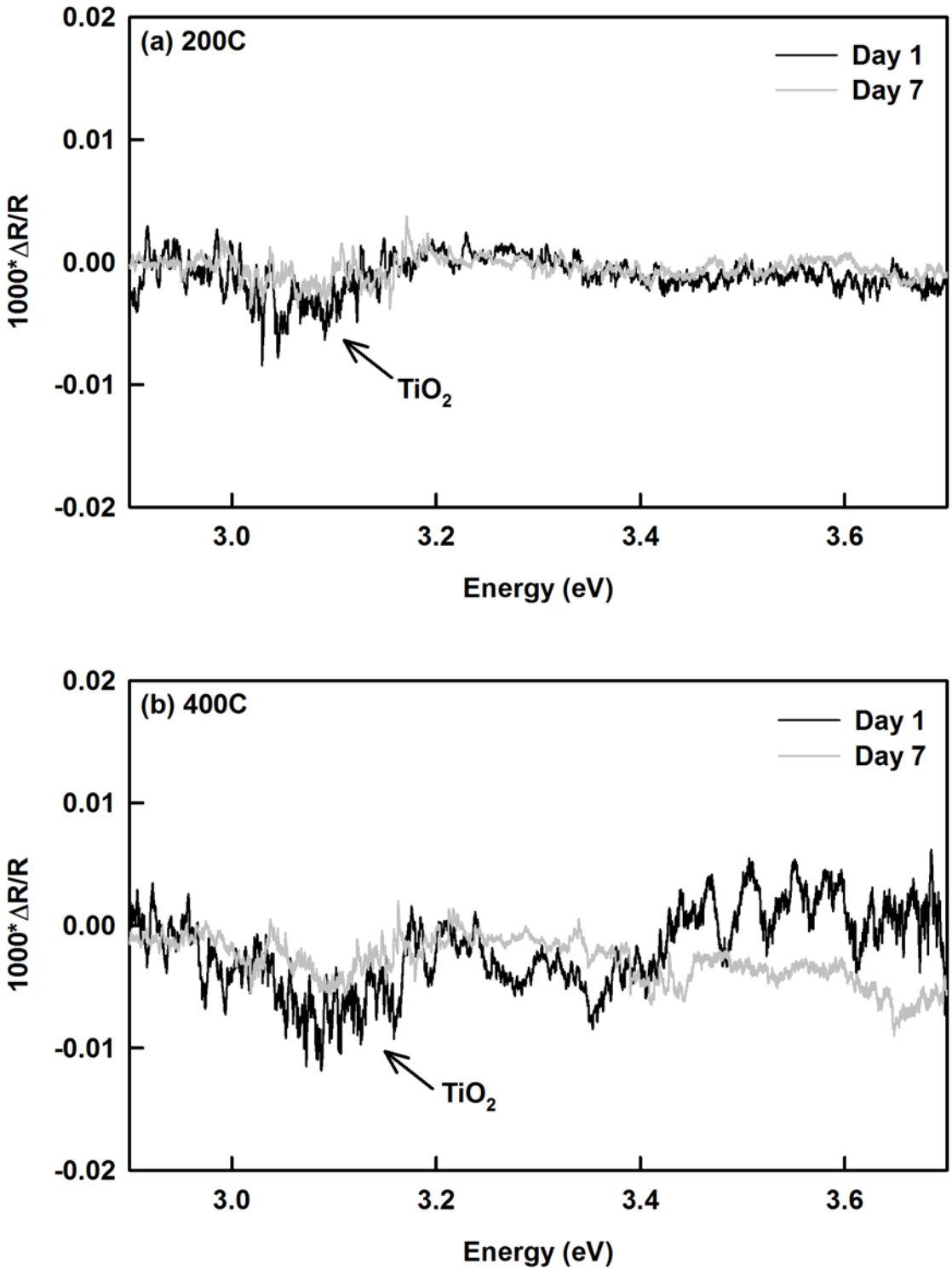

Fig. 5.10 Averaged PR spectra for ~100 nm polycrystalline anatase TiO_2 on Si(100) deposited at 200°C with subsequent 24 hr anneal at 550°C many days after synthesis (Sample 022310.2, 0.5 mV).

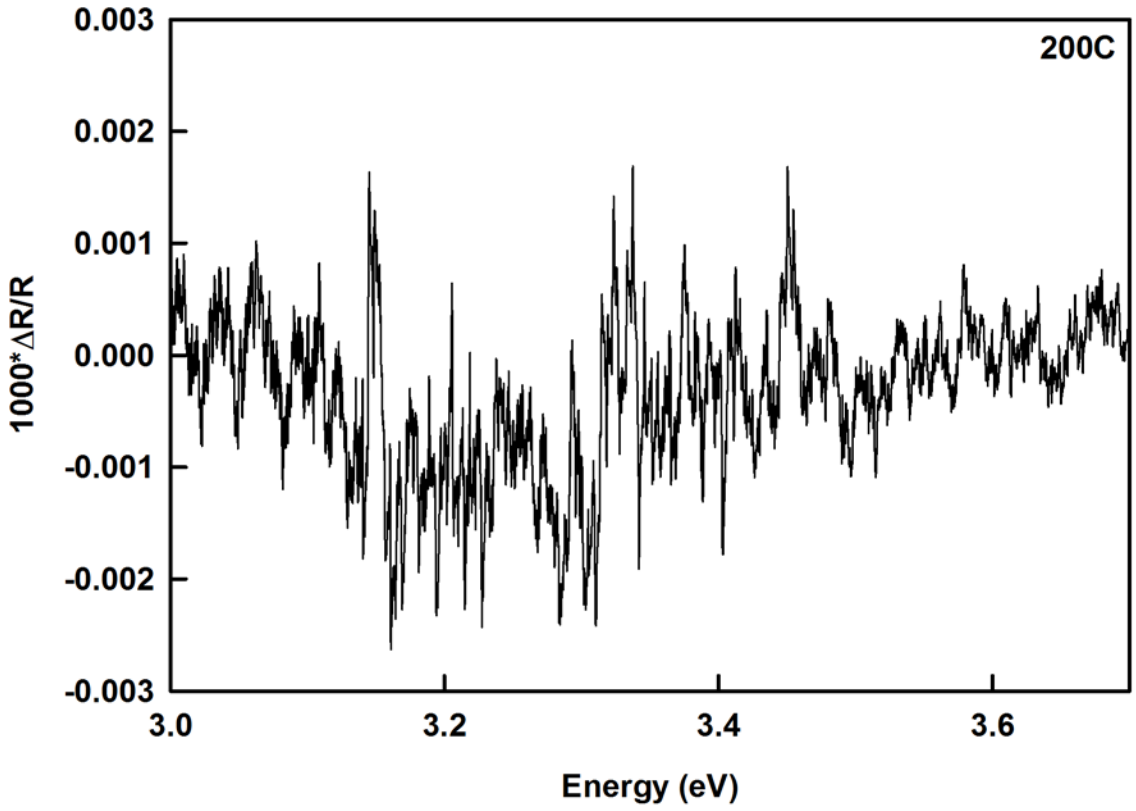

Fig. 5.11 Averaged PR spectra for (a) ~175 nm polycrystalline anatase TiO_2 on Si(100) deposited at 200°C with subsequent 20 min anneal at 550°C (Sample 092310.3, 0.5 mV, no HF etching prior to deposition) and (b) ~450 nm amorphous TiO_2 on Si(100) deposited at 200°C with no subsequent annealing (Sample K147, 1 mV, no HF etching prior to deposition).

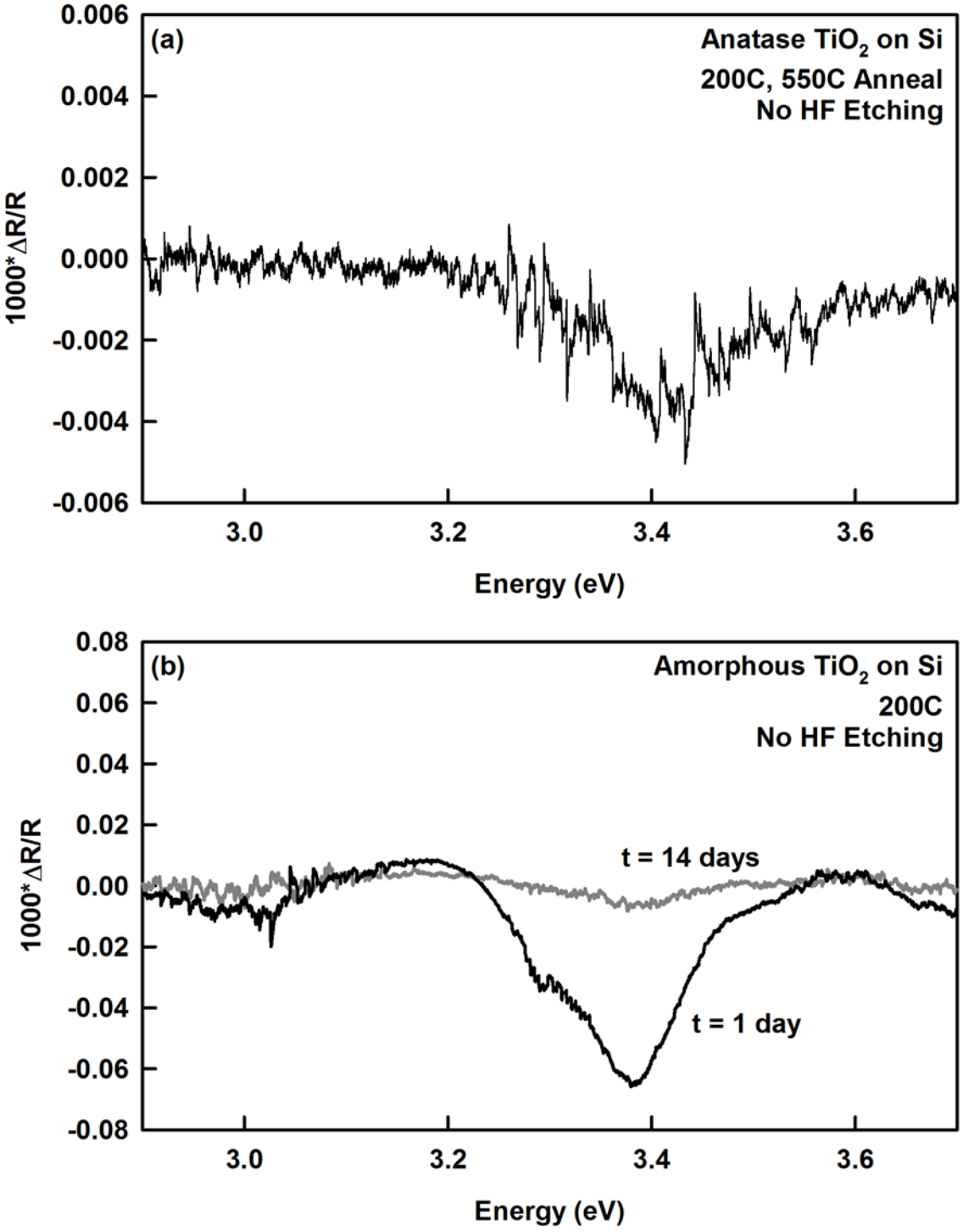

Fig. 5.12 Raw PR spectra for ~500 nm polycrystalline anatase TiO_2 on Si(100) deposited at 400°C (Sample 120709.5, 2 mV). Runs were collected sequentially over the course of about one hour.

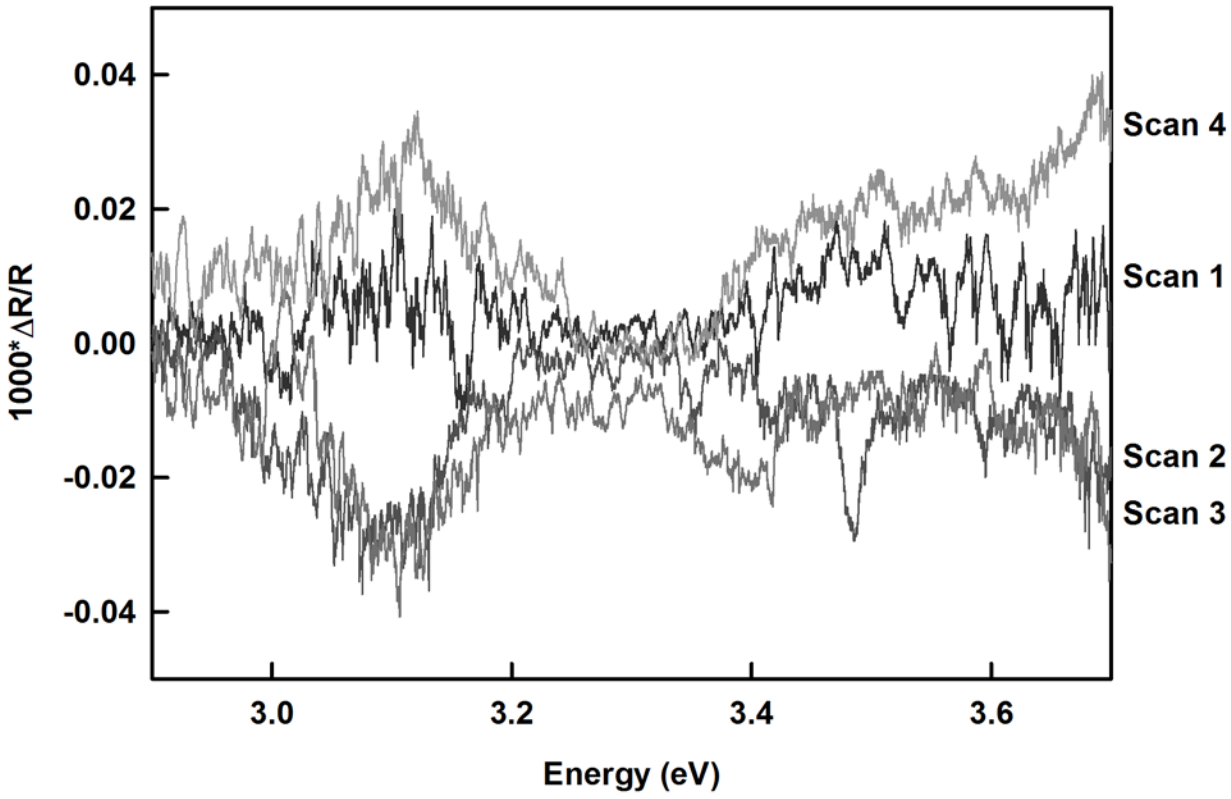

5.7 References

[1] S. Williams, *"How we found the missing memristor,"* IEEE Spectrum 29-35 (2008).

[2] F.-T. Kong, S.-Y. Dai, and K.-J. Wang, *"Review of recent progress in dye-sensitized solar cells,"* Adv. Optoelectron. **2007,** 75384 (2007).

[3] D. B. Strukov, G. S. Snider, D. R. Stewart, and R. S. Williams, *"The missing memristor found,"* Nature **453,** 80-83 (2008).

[4] D.-H. Kwon, K. M. Kim, J. H. Jang, J. M. Jeon, M. H. Lee, G. H. Kim, X.-S. Li, G.-S. Park, B. Lee, S. Han, M. J. Kim, and C. S. Huang, *"Atomic structure of conducting nanofilaments in TiO_2 resistive switching memory,"* Nature Nanotech. **5,** 148-153 (2010).

[5] S.-G. Park, B. Magyari-Kope, and Y. Nishi, *"Impact of oxygen vacancy ordering on the formation of a conductive filament in TiO_2 for resistive switching memory,"* IEEE Electron. Device Lett. **32,** 197-199 (2011).

[6] M. Gratzel, *"Dye-sensitized solar cells,"* J. Photoch. Photobio. C **4,** 145-153 (2003).

[7] S. Ruhle and D. Cahen, *"Electron Tunneling at the TiO_2/Substrate Interface Can Determine Dye-Sensitized Solar Cell Performance,"* J. Phys. Chem. B **108,** 17946-17951 (2004).

[8] M. Kittler and W. Seifert, *"EBIC defect characterisation: state of understanding and problems of interpretation,"* Mater. Sci. Eng., B **42,** 8-13 (1996).

[9] A. Pugatschow, R. Heiderhoff, and L. J. Balk, *"Time resolved determination of electrical field distributions within dynamically biased power devices by spectral EBIC investigations,"* Microelectron. Reliab. **47,** 1529-1533 (2007).

[10] B. Jun, R. D. Schrimpf, D. M. Fleetwood, Y. V. White, R. Pasternak, S. N. Rashkeev, F. Brunier, N. Bresson, M. Fouillat, S. Cristoloveanu, and N. H. Tolk, *"Charge trapping in irradiated SOI wafers measured by second harmonic generation,"* IEEE Trans. Nucl. Sci. **51,** 3231-3237 (2004).

[11] N. H. Tolk, M. L. Alles, R. Pasternak, X. Lu, R. D. Schrimpf, D. M. Fleetwood, R. P. Dolan, and R. W. Standley, *"Oxide interface studies using second harmonic generation,"* Microelectron. Eng. **84,** 2089-2092 (2007).

[12] P. Hofmann (2010). "Optical properties of surfaces." Retrieved Jan 28, 2011, from http://philiphofmann.net/surflec3/surflec016.html.

[13] M. Cardona, K. L. Shaklee, and F. H. Pollak, *"Electroreflectance at a semiconductor-electrolyte interface,"* Phys. Rev. **154,** 696-720 (1967).

[14] E. Y. Wang, W. A. Albers Jr., and C. E. Bleil (1967). II-VI Semiconducting Compounds. D. G. Thomas. New York, Benjamin.

[15] J. E. Fischer and D. E. Aspnes, *"Electroreflectance: A Status Report,"* Phys. Status Solidi B **55,** 9-32 (1973).

[16] C. R. Carlson, MS Thesis, University of Illinois at Urbana-Champaign, Urbana, 1993.

[17] R. Kudrawiec, P. Sitarek, J. Misiewicz, S. R. Bank, H. B. Yuen, M. A. Wistey, and J. S. Harris, *"Interference effects in electromodulation spectroscopy applied to GaAs-based structures: a comparison of photoreflectance and contactless electroreflectance,"* Appl. Phys. Lett. **86,** 091115 (2005).

[18] M. Motyka, R. Kudrawiec, M. Syperek, J. Misiewicz, M. Rudzinski, P. R. Hageman, and P. K. Larsen, *"Screening effect in contactless electroreflectance spectroscopy observed for AlGaN/GaN heterostructures with two dimensional electron gas,"* Thin Solid Films **515,** 4662-4665 (2007).

[19] D. O. Dumcenco, Y. S. Huang, H. P. Hsu, K. K. Tiong, F. Firszt, K. Strzalkowski, S. Legowski, and H. Meczynska, *"Temperature dependence of energies and broadening parameters of near band edge interband excitonic transitions in wurtzite ZnCdMgSe,"* J. Appl. Phys. **108,** 053502 (2010).

[20] R. Ditchfield, D. Llera-Rodriguez, and E. G. Seebauer, *"Semiconductor surface diffusion: Nonthermal effects of photon illumination,"* Phys. Rev. B: Condens. Matter **61,** 13710-13720 (2000).

[21] D. E. Aspnes and J. E. Rowe, *"High-resolution interband-energy measurements from electroreflectance spectra,"* Phys. Rev. Lett. **27,** 188-190 (1971).

[22] S. F. Chichibu, A. Tsukazaki, M. Kawasaki, K. Tamura, Y. Segawa, T. Sota, and H. Koinuma, *"Photoreflectance spectra of a ZnO heteroepitaxial film on the nearly lattice-matched $ScAlMgO_4$ (0001) substrate grown by laser molecular-beam epitaxy,"* Appl. Phys. Lett. **80,** 2860-2862 (2002).

[23] S. Ozaki, T. Mishima, and S. Adachi, *"Photoreflectance spectroscopy of ZnO for ordinary and extraordinary rays,"* Jpn. J. Appl. Phys. 1 **42,** 5465-5471 (2003).

[24] S. K. Han, S. K. Hong, J. W. Lee, J. Y. Lee, J. H. Song, Y. S. Nam, S. K. Chang, T. Minegishi, and T. Yao, *"Structural and optical properties of non-polar A-plane ZnO films grown on R-plane sapphire substrates by plasma-assisted molecular-beam epitaxy,"* J. Cryst. Growth **309,** 121-127 (2007).

[25] D. Tafalla, M. Pujadas, and P. Salvador, *"Direct measurements of flat-band potential shifts under illumination of the semiconductor-electrolyte interface by electrolyte electroreflectance,"* Surf. Sci. **215,** 190-200 (1989).

[26] G. K. Boschloo, A. Goossens, and J. Schoonman, *"Photoelectrochemical Study of Thin Anatase TiO_2 Films Prepared by Metallorganic Chemical Vapor Deposition,"* J. Electrochem. Soc. **144,** 1311-1317 (1997).

[27] B. Karunagaran, R. T. Rajendra Kumar, C. Viswanathan, D. Mangalaraj, S. K. Narayandass, and G. Mohan Rao, *"Optical constants of DC magnetron sputtered titanium dioxide thin films measured by spectroscopic ellipsometry,"* Cryst. Res. Technol. **38,** 773-778 (2003).

[28] A. I. Kulak, A. I. Kokorin, and D. V. Sviridov, *"Electrolyte electroreflectance study of TiO_2 films modified with metal nanoparticles,"* J. Mater. Res. **16,** 2357-2361 (2001).

[29] M. C. Kratzer, MS Thesis, University of Illinois at Urbana-Champaign, Urbana, 2008.

[30] R. Ditchfield, PhD Thesis, University of Illinois at Urbana-Champaign, Urbana, IL, 1998.

[31] K. Dev, PhD Thesis, University of Illinois at Urbana-Champaign, Urbana, 2005.

[32] M. Takeuchi, G. Martra, S. Coluccia, and M. Anpo, *"Investigations of the Structure of H_2O Clusters Adsorbed on TiO_2 Surfaces by Near-Infrared Absorption Spectroscopy,"* J. Phys. Chem. B **109,** 7387-7391 (2005).

[33] W. Gopel, G. Rocker, and R. Feierabend, *"Intrinsic defects of TiO_2(110): Interaction with chemisorbed O_2, H_2, CO, and CO_2,"* Phys. Rev. B: Condens. Matter **28,** 3427-3438 (1983).

[34] X. Wei, T. Xie, D. Xu, Q. Zhao, S. Pang, and D. Wang, *"A study of the dynamic properties of photo-induced charge carriers at nanoporous TiO_2/conductive substrate interfaces by the transient photovoltage technique,"* Nanotechnology **19,** 275707 (2008).

[35] A. Rothschild, A. Levakov, Y. Shapira, N. Ashkenasy, and Y. Komem, *"Surface photovoltage spectroscopy study of reduced and oxidized nanocrytalline TiO_2 films,"* Surf. Sci. **532-535,** 456-460 (2003).

[36] Y. S. Cho, J. S. Heo, J. C. Kim, and S. H. Moon, *"Monitoring of an interlayer between Si(100) and a TiO_2 layer formed during cyclic CVD,"* Chem. Vap. Deposition **12,** 659-664 (2006).

[37] P. R. McCurdy, L. J. Sturgess, S. Kohli, and E. R. Fisher, *"Investigation of the PECVD TiO_2-Si(100) interface,"* Appl. Surf. Sci. **233,** 69-79 (2004).

[38] M. T. M. Koper, A. M. Chaparro, H. Tributsch, and D. Vanmaekelbergh, *"Electrolyte electroreflectance study of the oscillatory hydrogen peroxide reduction on n-GaAs,"* Langmuir **14,** 3926-3931 (1998).

[39] V. A. Stoica, MS Thesis, West Virginia University, 2000.

[40] K. Dev, M. Y. L. Jung, R. Gunawan, R. D. Braatz, and E. G. Seebauer, *"Mechanism for coupling between properties of interfaces and bulk semiconductors,"* Phys. Rev. B: Condens. Matter **68,** 195311 (2003).

Chapter 6: Magnetic Properties of Mn-doped Anatase TiO_2 Synthesized by Atomic Layer Deposition*

6.1 Abstract

Mn-doped anatase TiO_2 thin films were grown on Si(100) by atomic layer deposition (ALD). The synthesis utilized $Ti(OCH(CH_3)_2)_4$ and H_2O as ALD precursors and $Mn(DPM)_3$ as a dopant source. All ALD-synthesized films exhibited room temperature ferromagnetism (RTFM); the microstructure, density, and magnetic field-dependent magnetization of the TiO_2 varied with the concentration of Mn and the film deposition temperature. ALD permits precise composition and thickness control, and much higher process throughput, compared to alternative techniques for synthesis of RTFM thin films for spintronics applications.

6.2 Introduction

Metal oxide semiconductors exhibiting room temperature ferromagnetism (RTFM) have been investigated extensively for spintronics applications [1, 2]. Spintronics, or "spin transport electronics," is a solid-state device technology that exploits not only the fundamental electronic charge of an electron, but also its intrinsic spin and associated magnetic moment. Spin-based technologies are slated to have a profound impact on nanoelectronics, data storage, and computer architecture [3, 4]. The disadvantages associated with current computer chips are becoming more pronounced as transistor size decreases per Moore's Law. For instance, a fundamental minimum energy (and amount of time) is

* Part of this work has been published: M.C.K. Sellers and E.G. Seebauer, *"Structural and magnetic properties of Mn-doped anatase TiO_2 films synthesized by atomic layer deposition,"* Appl. Phys. A, doi: 10.1007/s00339-011-6308-1 (2011).

required to switch a charge-based device on and off. Also, as device length scales drop to a few nanometers, transistors will begin to leak electrons. Manipulation of both charge *and* spin will allow for the fabrication of highly energy-efficient spin-based transistors capable of doing more computation than traditional transistors in a smaller space.

A ferromagnetic material is one that exhibits parallel alignment of local magnetic moments resulting in a large net magnetization even in the absence of an applied magnetic field. The local magnetic moments arise due to unpaired electron spins on individual atoms. Full control over the injection, transport, and detection of these spins is critical to the development of robust spin field-effect transistors (FETs) and spin metal-oxide-semiconductor FETs [5]. Importantly, long-range ordering occurs below a critical temperature called the Curie temperature; the stronger the coupling between neighboring atoms, the higher the temperature. This explains the interest in engineering materials that exhibit ferromagnetism at *room temperature*; a ferromagnetic semiconductor like Mn-doped GaAs with a Curie temperature of negative 120°C [6] is impractical for wide-scale use.

Experimentally, magnetic behavior is investigated by applying a magnetic field H to a material and observing the corresponding change in magnetization M. A ferromagnet has a characteristic M-H response, a schematic of which is shown in Fig. 6.1 [7]. As a DC magnetic field is applied to the sample, the magnetization increases up until a saturation point, M_s, is reached. As the field is decreased again, the magnetization does not drop to its original value; this results in the hysteresis seen in the M-H data. When H returns to zero, the material still exhibits a magnetization, referred to as the remanent magnetization, M_r. In order to remove the remanent magnetization, a field has to be applied in the opposite direction to the initial applied field. This field is called the coercive field, H_c. The values of

M_s, M_r, and H_c are dependent upon the ferromagnet and the manner in which it is synthesized.

One of the key challenges in the field of spintronics is identifying and engineering suitable device materials. Of particular interest are diluted magnetic semiconductors (DMSs), which are nonmagnetic semiconductors such as TiO_2, ZnO, AlN, or GaN modified by the addition of small atomic percentages of open-shell transition metal (TM) dopants. Of these options, oxide semiconductors are particularly attractive from an industrial standpoint due to their wide bandgaps, relatively low cost of fabrication, and high carrier density [8]. Indeed, RTFM has been reported for TiO_2 doped with Cr [9], Mn [10], Fe [11], and Co [12].

The origin of RTFM in TM-doped oxide semiconductors such as TiO_2 has been an issue of contention for several years [13, 14]. Early studies understandably emphasized the correlation between the transition metal dopant and the observed ferromagnetic ordering [12]. Other trends soon became apparent, however. The magnetization of 2.5 at% Mn-doped TiO_2 synthesized via sol-gel method varies from anatase to rutile TiO_2 [15]. A correlation between magnetic moment and film "quality" has been identified [16] wherein negligible ferromagnetism is observed in slow-grown (0.08 Å/sec) Mn-doped TiO_2 synthesized via plasma-assisted molecular beam epitaxy (PAMBE). The turning point in this debate was the observation of a small magnetic moment in TiO_2 without extrinsic doping [13].

RTFM in intrinsic TiO_2 is presently attributed to native point defects [13, 16], grain boundaries [17], and dislocations [18]. Excess electrons associated with bulk oxygen vacancies convert Ti^{4+} atoms to Ti^{3+} atoms; a magnetic moment arises due to the unpaired *3d* electrons localized on Ti^{3+} atoms. Doping may enhance magnetism via the formation of charge-compensating oxygen vacancies or dopant-oxygen vacancy complexes.

Alternatively, doping may result in the creation of metal nano-inclusions or macro-scale segregation. In the case of the latter, magnetic hysteresis may not be indicative of true ferromagnetism but rather the formation of magnetic secondary phases [2]. Especially in the case of Mn doping, the close coupling between ferromagnetism, film preparation conditions, and microstructure suggests opportunity for further optimization and control of TiO_2 magnetic properties via a precision synthesis method.

Atomic layer deposition (ALD), a pulsed-precursor vapor phase deposition method related to chemical vapor deposition (CVD), is an attractive technique for the fabrication of thin films with precise thickness and compositional control on large-area substrates. ALD of DMS TiO_2 has never been demonstrated, although this method has been used to deposit Mn-doped ZnO with DMS properties [19]. ALD avoids complications with solvent and byproduct removal and with calcination-induced shrinkage that arise during sol-gel synthesis. Other deposition techniques such as pulsed laser deposition (PLD) and PAMBE have been used to deposit Mn-doped TiO_2 thin films [20, 21], but these methods are ill-suited to the high throughput requirements of commercial manufacturing. In addition, PLD can result in significant particulate composition and uneven coverage, while PAMBE films suffer from thickness-dependent morphologies. ALD avoids such problems.

6.3 Methods and procedures

6.3.1 Atomic layer deposition of Mn-doped TiO_2

Undoped and Mn-doped TiO_2 films were deposited on Si(100) 2 cm x 2 cm in size via ALD using a low-pressure vapor phase deposition system. $Ti(OCH(CH_3)_2)_4$ (TTIP, Strem Chemicals Inc., 98%), H_2O (deionized), and $Mn(DPM)_3$ (DPM = 2,2,6,6-tetramethyl-

3, 5-heptanedionato, Strem Chemicals Inc., 99%) were used as the source materials for Ti, O, and Mn, respectively. TTIP and H_2O were placed in glass bubbling vessels and heated to 65°C and 23°C, in that order. 60 SCCM of N_2 carrier gas (SJ Smith, 99.999%) was used to introduce each precursor into the reactor. The total pressure in the chamber was 400 mTorr. The temperature of the Si substrate during deposition was maintained at either 200°C or 400°C via resistive heating and was monitored with a chromel-alumel (type K) thermocouple. $Mn(DPM)_3$ was evaporated from a porous filter enclosure suspended from the TTIP/H_2O delivery tube within the vacuum chamber. The supply rate of the Mn source was controlled by changing the distance between the filter enclosure and the resistively heated substrate platform. A full ALD cycle consisted of a TTIP pulse (8 sec), N_2 purge (10 sec), H_2O pulse (8 sec), and another N_2 purge (10 sec). At 200°C, undoped and Mn-doped TiO_2 were deposited with a total of 27 and 39 cycles in order to obtain films 100 nm thick. At 400°C, only 12 cycles were required to deposit 200 nm thick films. Following deposition, films synthesized at 200°C were annealed under an ambient atmosphere at 550°C for 24 hrs. Those synthesized at 400°C were not annealed.

6.3.2 Physical characterization

As described previously, film thickness was measured using a Rudolph Technologies AutoEL III single wavelength ellipsometer. X-ray photoelectron spectroscopy (XPS) data were obtained with a Kratos AXIS Ultra utilizing a pass energy of 40 eV, with excitation by monochromatized Al Kα radiation. TiO_2 morphology was examined using a Hitachi Model S4800 scanning electron microscope (SEM). X-ray diffraction (XRD) and x-ray reflectivity (XRR) patterns were obtained at room temperature with a high-resolution Philips X'Pert

diffractometer (λ = 0.15406 nm) operated at 45 kV and 40 mA with a Cu Kα1 primary x-ray beam from a hybrid monochromator consisting of a parabolic x-ray mirror and a 2-reflection Ge(220) monochromator. The secondary optics consisted of a high-speed PIXcel line detector using 255 channels.

6.3.3 Magnetic characterization

The room temperature magnetic properties of the films were measured at Argonne National Laboratory Center for Nanoscale Materials using a Quantum Design Magnetic Property Measurement System Model MPMS-XL. The modular MPMS design integrates a 7T Superconducting Quantum Interference Device (SQUID) detection system, a precision temperature control unit residing in the bore of a high-field superconducting magnet, and a computer operating system. The MPMS-XL is equipped with a reciprocating sample measurement option (RSO) in addition to the standard DC measurement option. RSO measurements are performed using a servo motor that rapidly oscillates the sample within the SQUID pickup coils; DC measurements entail the sample moving through the coils in discrete steps. The RSO allows for faster data acquisition and enhanced sensitivity.

Undoped and Mn-doped TiO_2 on Si(100) samples were cleaved into small fragments approximately 0.25 cm^2 in area for insertion in the SQUID sample space. There are several methods for affixing samples to the sample rod (straw, gelatin capsule, thread). Here, a clear plastic drinking straw was used to attach each sample. This method was selected to minimize the background signal and keep the sample firmly in place throughout the measurement sequence. A 8” long clear plastic drinking straw was slit from end-to-end. The TiO_2 sample was placed in the middle of the unfurled straw and wrapped tightly. This straw-enshrouded

sample was then slid into an unaltered straw, taking care to ensure that the sample was centered in the middle of the straw assembly. The lower end of the straw was sealed with a small piece of kapton tape, while the upper end was securely attached to the sample rod spacer. Using this geometry, the magnetic field was applied parallel to the film plane.

The MPMS-XL is controlled with the MPMS MultiVu application distributed by Quantum Design. The interface is used for sample insertion/removal as well as data acquisition. After each sample was inserted into the sample space, it was centered in the SQUID pickup coils to ensure that all four coils sensed the magnetic moment of the sample. This was accomplished by ramping the field up to 500 Oe and initiating an AC centering scan. The sample position was adjusted based on the outcome of the centering scan and confirmed by performing a repeat scan.

MPMS MultiVu was used to write a program sequence for *M-H* data acquisition over the range of -10 kOe to 10 kOe. The program code is shown in Fig. 6.2. Important features include:

1) 5 sec pause at the beginning of the sequence to confirm that the sample temperature is stable at 300K
2) 6 sec pause after each change in the applied field to confirm that the applied field is stable before measurements are taken
3) Four measurements at each value of applied field with a measurement rejection criteria in place (reject measurements that are greater than two standard deviations from the mean)
4) Smaller field increments in the range -2000 Oe < H < 2000 Oe to obtain better definition in the key regions of the hysteresis curve

Voltage readings taken as a function of the sample's position in the coils comprise the raw measurement data. Scan averaging is performed to improve the measurement resolution and prevent erroneous contributions to the data.

6.4 Results and discussion

6.4.1 Film thickness

Fig. 6.3 shows an example of the dependence of average film thickness on the number of ALD growth cycles. For both undoped and Mn-doped TiO_2, film thickness increases linearly with number of cycles, with the slope yielding the growth rate. At 200°C deposition temperature, the growth rate is noticeably higher for undoped TiO_2 (3.7 nm/cycle) versus Mn-doped TiO_2 (2.4 nm/cycle). This is attributed to a change in the gas velocity profile when the porous filter enclosure is affixed to the delivery tube and a reduction in the number of sites available for Ti, O precursor adsorption due to adsorption of Mn species. At 400°C deposition temperature, the growth rate is comparable for undoped and Mn-doped TiO_2 (8.4 nm/cycle).

The error bars in Fig. 6.3 represent the standard deviation of the measurements at five points on each specimen, and indicate the uniformity of the film thickness. For points sampled at a radial distance of 0.5 cm from the specimen center, the standard deviation is typically less than 1.0 nm (where the accuracy limit of the ellipsometer is about ± 0.3 nm). The ALD method results in significantly more uniform TiO_2 films than comparable films synthesized by CVD with TTIP as a precursor [22].

6.4.2 Chemical composition

XPS confirmed introduction of Mn into the films and provided an estimate of surface elemental composition. Mn doping levels in the range 1 – 3 at% are obtained by varying the supply rate of the Mn source during film deposition. Ti *2p*, O *1s*, and Mn *2p* peak positions, as well as estimated chemical compositions, are summarized in Table 6.1.

As shown in Fig. 6.4(a), no Mn *2p* features are found in the 660 to 635 eV binding energy (BE) range for undoped TiO_2 films. In Figs. 6.4(b) and (c) for Mn-doped TiO_2 deposited at 200°C and 400°C, the peaks at ~641.5 eV and ~653.4 eV correspond to the Mn $2p_{3/2}$ and $2p_{1/2}$ core-levels, respectively. As with similar films synthesized via PAMBE [23], the satellite structure observed at a BE ~5 eV higher than the $2p_{3/2}$ peak suggests the presence of divalent Mn ions. The Mn $2p_{3/2}$ binding energy values themselves indicate that Mn may also be present as Mn^{3+}; a similar mixture of Mn^{2+} and Mn^{3+} ions has been proposed for Mn-doped TiO_2 fabricated via sol-gel processing [24].

Fig. 6.5 provides example XPS spectra for the Ti *2p* core-levels at both deposition temperatures. In Fig. 6.5(a), the Ti $2p_{3/2}$ and Ti $2p_{1/2}$ peaks are situated at 458.6 and 464.3 eV for the undoped film and 458.3 and 464.0 eV for the 2.4 at% Mn film, all respectively. For films deposited at 400°C (Fig. 6.5(b)), the Ti $2p_{3/2}$ and Ti $2p_{1/2}$ peaks also shift ~0.4 eV towards lower BE. A comparable shift in the Ti *2p* peaks occurs for all ~1 at% Mn samples (not shown). The change in BE of the Ti *2p* peaks relative to those of metallic Ti and 5.7 eV line separation between Ti $2p_{3/2}$ and Ti $2p_{1/2}$ indicates that Ti atoms are in the +4 oxidation state [25]. The shift towards lower BE and slight peak broadening in the Mn-doped films is caused by Ti^{4+} ions releasing extra electrons to reestablish charge equilibrium following dopant incorporation [26].

6.4.3 Morphology and crystallinity

Fig. 6.6 shows cross-sectional SEM micrographs of undoped and Mn-doped TiO_2 as deposited. The underlying Si substrate can be distinguished by slightly darker coloration. The micrographs show that the undoped TiO_2 film deposited at 200°C (Fig. 6.6(a)) is densely packed with extremely small granular features on the order of 5 nm and minimal spacing between cross-sectional texturing. In contrast, the Mn-doped TiO_2 film deposited at 200°C (Fig. 6.6(b)) is composed of easily identifiable, round crystallites with an average size of ~20 to 40 nm. Doping clearly increases the number of visible grain boundaries and induces slight surface roughening. The morphology of the undoped TiO_2 film deposited at 400°C (Fig. 6.6(c)) comprises high aspect ratio columnar rods ~20 nm in width with substantial spacing in between crystallites. At 400°C, Mn doping leads to degradation of the high aspect ratio rods (Fig. 6.6(d)). The crystallites still appear vaguely columnar, but increase in width to ~40 nm; the visible void fraction is reduced and the columns merge together in the lateral direction.

Undoped TiO_2 films synthesized by alternative methods vary widely in morphology. Sol-gel films annealed at 500°C possess ~50 to 150 nm diameter grains with nontrivial intergrain spacing and crystallite shapes that depend on the acidity/basicity of the precursor solution [27]. PAMBE and PLD result in crystallites having much higher aspect ratios and average diameters [28] as well as visible grain boundaries [29] that depend strongly on oxygen partial pressure during growth. Nb-doped TiO_2 films prepared by the sol-gel method [30] resemble the Mn-doped TiO_2 deposited at 200°C with respect to crystallite shape and size; there is no basis for comparison in the Mn-doped TiO_2 literature, as micrographs have not been reported.

Fig. 6.7 shows XRD patterns for undoped and Mn-doped TiO_2. Regardless of deposition temperature and doping level, the films are polycrystalline anatase with slight preferential (101) orientation (JCPDS card No. 21-1272). In this regard, they are similar in structure to those fabricated by sol-gel spin coating [31], as opposed to those grown by PLD [20] and PAMBE [23], which show a single anatase phase highly oriented toward the (004) plane. Average crystallite size in the film growth direction changes significantly with doping at 200°C: values of 39.2 ± 2.0, 27.6 ± 1.9, and 22.3 ± 0.7 nm are obtained for the 0, 1.2, and 2.4 at% Mn samples from analysis of XRD peak profiles using a size-only fitting model. In contrast, crystallite size remains fairly constant in Mn-doped films deposited at 400°C: values of 27.9 ± 1.5, 28.4 ± 1.7, and 26.4 ± 2.0 nm are determined for the 0, 1.4, and 2.7 at% Mn samples. The dependence of average crystallite size on deposition temperature and doping level is shown graphically in Fig. 6.8(a).

XRR data were collected to evaluate roughness and obtain values of film density (Fig. 6.9). The spectrum for the undoped film deposited at 200°C exhibits interference fringes as expected from a well-defined multilayer stack. The fringes diminish in amplitude with doping, confirming increased interface roughness. XRR fitting indicates the undoped, 1.2, and 2.4 at% 200°C Mn-doped films have densities of 3.99 ± 0.20 g/cm^3, 3.85 ± 0.19 g/cm^3, 4.09 ± 0.20 g/cm^3, in that order. In contrast, the spectrum of the undoped film deposited at 400°C exhibits minimal interference fringes. This is consistent with the SEM shown in Fig. 6.6(c); the columnar rods result in substantial surface roughness. At 400°C, the addition of Mn causes the XRR interference fringes to increase in amplitude. Indeed, the micrograph in Fig. 6.6(d) confirms that doping at 400°C results in a smoothening of the film surface. The undoped, 1.4, and 2.7 at% 400°C Mn-doped films have densities of 2.8 ± 0.14 g/cm^3, 3.34 ±

0.17 g/cm^3, 3.95 ± 0.20 g/cm^3, respectively. All bulk density values are presented in Fig. 6.8(b) as a function of deposition temperature and doping level. For comparison, the bulk density of single crystal anatase is 3.89 g/cm^3.

6.4.4 Magnetic properties

Fig. 6.10(a) shows raw magnetization data for undoped TiO_2 as a function of magnetic field at 300K. The data has a diamagnetic background due to the Si substrate, which is expressed as a negative slope superimposed on the signal arising from the TiO_2. The contribution of the Si can be subtracted to obtain the response of the TiO_2 film alone [7]. This was accomplished by fitting the high field (above 8 kOe) part of the curve to a straight line, calculating the slope, and then subtracting a line with this slope from the raw data. The corrected data are shown in Fig. 6.10(b).

Regardless of deposition temperature, the *M-H* loops exhibit clear hysteresis with coercive fields of 56 Oe (200°C) and 50 Oe (400°C). This confirms a room temperature ferromagnetic characteristic that has been noted previously for undoped TiO_2 [13]. The saturation magnetization is 3.1 emu/cm^3 for the 200°C TiO_2 and 3.8 emu/cm^3 for the 400°C TiO_2. Despite the substantial differences in TiO_2 morphology and crystallinity as a function of deposition temperature, there is little variation in the experimentally determined values of H_c and M_s. This is surprising, since the magnetic properties of many thin films, including ZnO [32], depend on the temperature at which they are deposited.

Corrected *M-H* loops for the Mn-doped TiO_2 samples are seen in Fig. 6.11(a). Mn-doping leads to a slight and substantial increase in the saturation magnetization of TiO_2

deposited at 200°C and 400°C, in that order. Table 6.2 summarizes the magnetic properties of Mn-doped TiO_2 as well as undoped TiO_2.

At 200°C, M_s grows to 3.0 emu/cm^3 (0.3 μ_B/Mn atom) and 5.7 emu/cm^3 (0.3 μ_B/Mn atom) for 1.2 and 2.4 at% Mn-doped TiO_2, respectively, suggesting that doping over ~2 at% Mn leads to a slight enhancement in RTFM. As seen in Fig. 6.11(b), H_c remains almost constant with doping: 48 Oe and 54 Oe for 1.2 at% and 2.4 at% Mn. These values of H_c and M_s agree closely with values obtained for Mn-doped TiO_2 films synthesized via both sol-gel processing [31] and PAMBE [23].

On the other hand, at 400°C, M_s increases by almost an order of magnitude to 21 emu/cm^3 (2.1 μ_B/Mn atom) and 14 emu/cm^3 (0.6 μ_B/Mn atom) for 1.4 and 2.7 at% Mn-doped TiO_2. Fig. 6.11(c) illustrates the corresponding increase in coercive field to ~100 Oe for both samples. Note the decrease of the magnetic moment at high Mn concentration. Similar behavior has been reported for $Mn_xTi_{1-x}O_2$ (x=0.02-0.2) rutile [10] and anatase [13] thin films grown on Al_2O_3 by PLD. In rutile, this trend is attributed to an increased antiferromagnetic superexchange interaction between Mn moments at high (x = 0.12) doping levels. In anatase, the negative influence of doping on ferromagnetic ordering for Mn content greater than 10 at% is assigned to the formation of secondary phases and/or precipitate clusters.

Considering the available explanations for RTFM in doped oxide semiconductors, a number of insights can be gleaned on the origin of magnetic hysteresis in undoped and Mn-doped TiO_2 synthesized by ALD. First, there is little evidence to suggest that “poor crystal quality” activates magnetic ordering [16]. Indeed, the claim that TiO_2 deposited via PAMBE at a rate of 0.08 Å/sec has a “perfect” crystal structure with “few defects” is unsupported. No

clear correlation is observed between the magnetic properties and crystallinity, bulk density, or roughness of the TiO_2 synthesized in this study. Second, is it unlikely that the saturation magnetization of the 400°C films is enhanced solely due to an increase in the concentration of grain boundaries [17]. In fact, average crystallite size remains fairly constant (~26 to 28 nm) for films deposited at 400°C. Lastly, it is important to point out that the enhanced magnetization is not temperature-induced, since the 200°C films are actually annealed at 550°C for 24 hours.

Consequently, enhanced magnetization in Mn-doped TiO_2 synthesized by ALD entails interplay between Mn ions and native defects such as charged oxygen vacancies. One potential mechanism involves the trapping of electrons by oxygen vacancies to form a ferromagnetic Mn^{3+}-V_O-Mn^{3+} group or magnetic polaron [33]. The concentration of native point defects and extended defects such as grain boundaries and dislocations is controlled by film synthesis parameters and post-treatment protocols. It is predicted that further post-treatment involving reduction or oxidation would shed additional light on the specific defects responsible for the observed enhancement in room temperature ferromagnetism.

6.5 Conclusion

In contrast to other thin film synthesis methods, ALD allows for precise tailoring of TiO_2 microstructure via deposition temperature (crystallite shape and size) and deposition rate (defect concentration). From a scientific perspective, such capabilities allow for further decoupling of defect- and dopant-induced contributions to ferromagnetism of DMS TiO_2. Additional correlation between grain boundaries and magnetic behavior of Mn-doped TiO_2 is necessary, with an aim towards optimization of DMS TiO_2 for spintronics applications.

6.6 Tables and figures

Table 6.1 Summary of XPS data for undoped and Mn-doped anatase TiO_2 synthesized by ALD.

Sample # →	**020310.9**	**030310.4**	**022510.4**	**033110.4**	**050710.2**	**043010.5**
Description	0 at%, 200°C	1.2 at%, 200°C	2.4 at%, 200°C	0 at%, 400°C	1.4 at%, 400°C	2.7 at%, 400°C
Ti *2p*$_{3/2}$	458.6	458.3	458.3	458.5	458.6	458.1
Ti *2p*$_{1/2}$	464.3	464	464	464.2	464.3	463.8
Δ Ti *2p*	5.7	5.7	5.7	5.7	5.7	5.7
O *1s* (Lattice)	529.5	529.4	529.4	529.6	529.8	529.5
O *1s* (OH)	531.5	531.2	531.8	531.2	531.5	531.6
Mn *2p*$_{3/2}$	-	641.2	641.3	-	641.4	641.6
Mn *2p*$_{1/2}$	-	653.3	653.4	-	653.3	653.4
Δ Mn *2p*	-	12.1	12.1	-	11.8	11.8
At % Mn	-	1.2	2.4	-	1.4	2.7

Table 6.2 Magnetic properties of undoped and Mn-doped anatase TiO_2 synthesized by ALD.

Sample #	**Description**	M_s **(emu/cm^3)**	M_r **(emu/cm^3)**	H_c **(Oe)**
020310.10	0 at%, 200°C	3.1	0.4	56
030310.4	1.2 at%, 200°C	3.0	0.4	48
022510.4	2.4 at%, 200°C	5.7	0.6	55
033110.1	0 at%, 400°C	3.8	0.1	50
050710.2	1.4 at%, 400°C	21	5.5	101
043010.5	2.7 at%, 400°C	13.8	3.4	102

Fig. 6.1 Example *M-H* hysteresis loop for a ferromagnetic material with saturation magnetization, remanent magnetization, and coercivity labeled as M_s, M_r, and H_c, respectively.

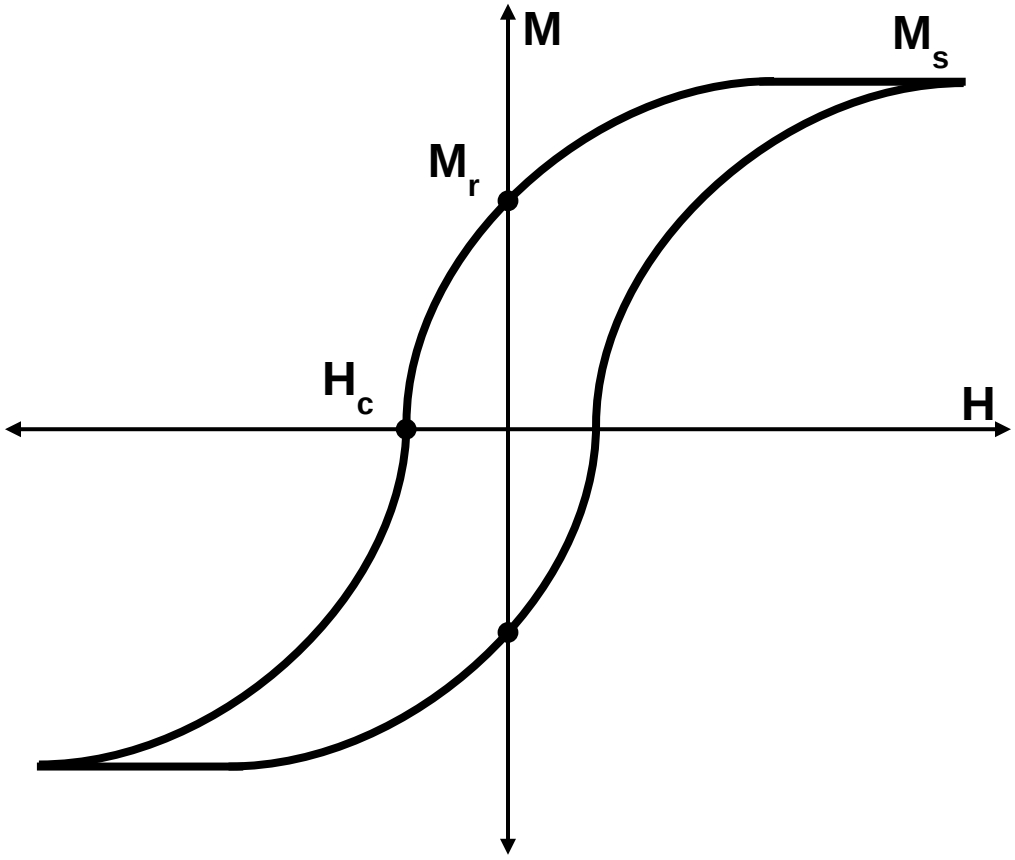

Fig. 6.2 MPMS MultiVu program sequence used for *M-H* data acquisition.

```
 1: Set Datafile: C:\users\Meredith\022510-2Run1
 2:
 3:
 4: Set Temperature 300.000K at 10.000K/min.
 5: Waitfor Temp:Stable Delay:5secs
 6:
 7: Scan Field from 0.00 Oe to 2000.00 Oe in 17 steps (125.00 Oe/step), No Overshoot, Hi Res Disabled
 8:    Waitfor Field:Stable Delay:6secs
 9:    Multi-Measure 4x Measure RSO: 5.00 cm, 3 cyc, 1 meas, 0.5 Hz, Center, AutoRng, Long, Iterative Reg., track:Yes, raw:Yes, diag:Yes
10: End Scan
11: Scan Field from 3000.00Oe to 10000.00 Oe in 1000.00 Oe increments (8 steps), No Overshoot, Hi Res Disabled
12:    Waitfor Field:Stable Delay:6secs
13:    Multi-Measure 4x Measure RSO: 5.00 cm, 3 cyc, 1 meas, 0.5 Hz, Center, AutoRng, Long, Iterative Reg., track:Yes, raw:Yes, diag:Yes
14: End Scan
15: Scan Field from 10000.00Oe to 3000.00 Oe in -1000.00 Oe increments (8 steps), No Overshoot, Hi Res Disabled
16:    Waitfor Field:Stable Delay:6secs
17:    Multi-Measure 4x Measure RSO: 5.00 cm, 3 cyc, 1 meas, 0.5 Hz, Center, AutoRng, Long, Iterative Reg., track:Yes, raw:Yes, diag:Yes
18: End Scan
19: Scan Field from 2000.00 Oe to -2000.00 Oe in 33 steps (-125.00 Oe/step), No Overshoot, Hi Res Disabled
20:    Waitfor Field:Stable Delay:6secs
21:    Multi-Measure 4x Measure RSO: 5.00 cm, 3 cyc, 1 meas, 0.5 Hz, Center, AutoRng, Long, Iterative Reg., track:Yes, raw:Yes, diag:Yes
22: End Scan
23: Scan Field from -3000.00Oe to -10000.00 Oe in -1000.00 Oe increments (8 steps), No Overshoot, Hi Res Disabled
24:    Waitfor Field:Stable Delay:6secs
25:    Multi-Measure 4x Measure RSO: 5.00 cm, 3 cyc, 1 meas, 0.5 Hz, Center, AutoRng, Long, Iterative Reg., track:Yes, raw:Yes, diag:Yes
26: End Scan
27: Scan Field from -10000.00Oe to -3000.00 Oe in 1000.00 Oe increments (8 steps), No Overshoot, Hi Res Disabled
28:    Waitfor Field:Stable Delay:6secs
29:    Multi-Measure 4x Measure RSO: 5.00 cm, 3 cyc, 1 meas, 0.5 Hz, Center, AutoRng, Long, Iterative Reg., track:Yes, raw:Yes, diag:Yes
30: End Scan
31: Scan Field from -2000.00 Oe to 0.00 Oe in 17 steps (125.00 Oe/step), No Overshoot, Hi Res Disabled
32:    Waitfor Field:Stable Delay:6secs
33:    Multi-Measure 4x Measure RSO: 5.00 cm, 3 cyc, 1 meas, 0.5 Hz, Center, AutoRng, Long, Iterative Reg., track:Yes, raw:Yes, diag:Yes
34: End Scan
35: Scan Field from 125.00Oe to 1000.00 Oe in 125.00 Oe increments (8 steps), No Overshoot, Hi Res Disabled
36:    Waitfor Field:Stable Delay:6secs
37:    Multi-Measure 4x Measure RSO: 5.00 cm, 3 cyc, 1 meas, 0.5 Hz, Center, AutoRng, Long, Iterative Reg., track:Yes, raw:Yes, diag:Yes
38: End Scan
```

Fig. 6.3 TiO_2 film thickness versus number of ALD cycles, where error bars represent the standard deviation of thickness at r = 0.5 cm from the center of each sample.

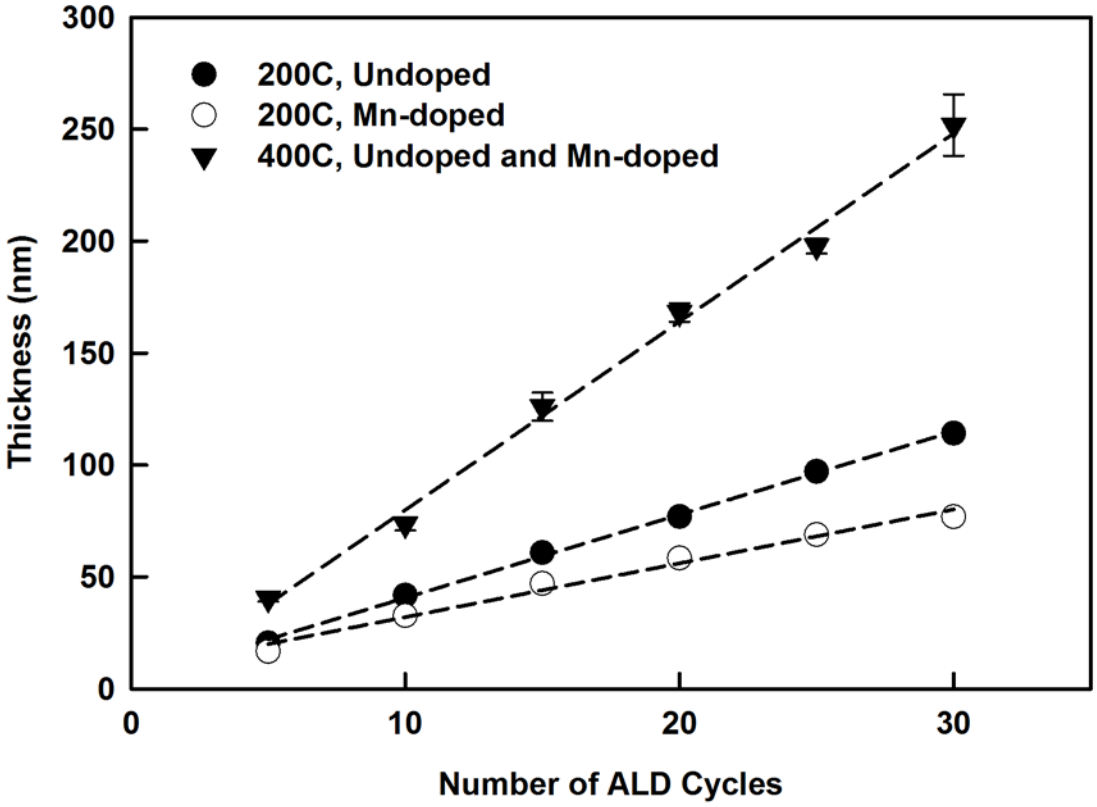

Fig. 6.4 XPS spectra of Mn *2p* core-levels for (a) undoped TiO_2, (b) 2.4 at% Mn-doped TiO_2 deposited at 200°C, and (c) 2.7 at% Mn-doped TiO_2 deposited at 400°C.

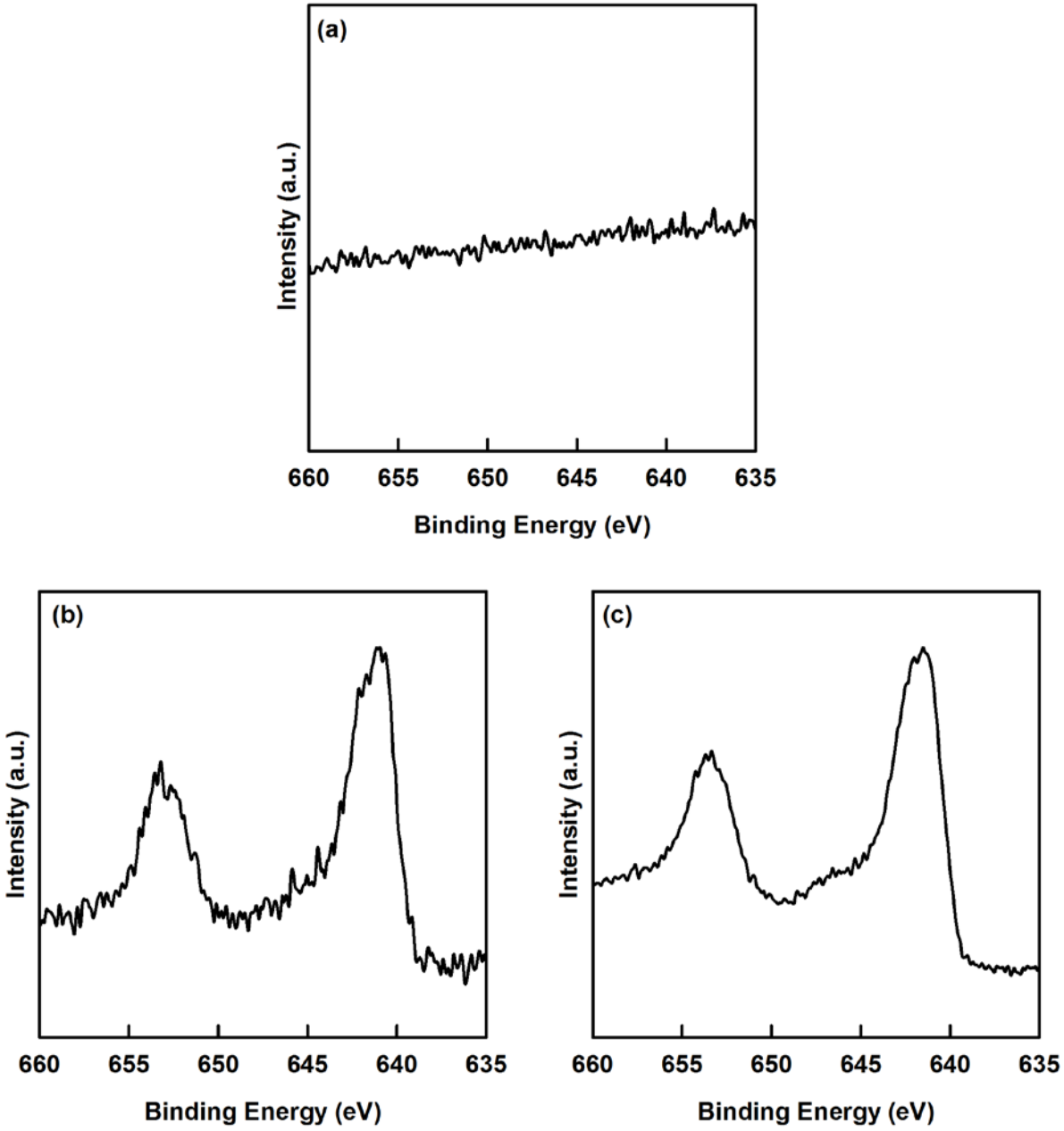

Fig. 6.5 XPS spectra of Ti *2p* core-levels for (a) undoped and Mn-doped TiO_2 deposited at 200°C and (b) undoped and Mn-doped TiO_2 deposited at 400°C. Both graphs illustrate the shift in the positions of the *2p* peaks with Mn incorporation.

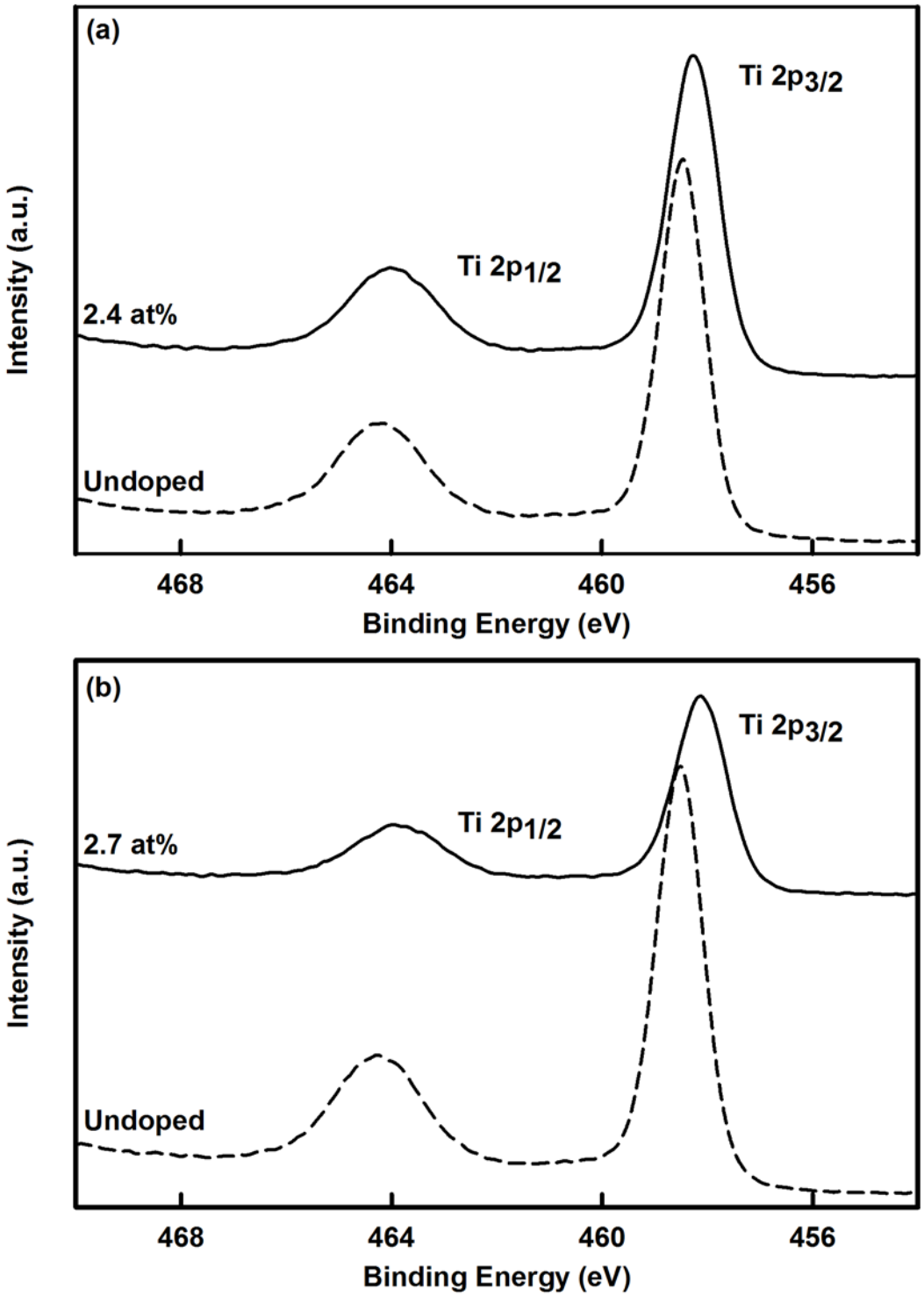

Fig. 6.6 SEM cross sections for ~100 nm thick (a) undoped and (b) Mn-doped TiO_2 deposited at 200°C and annealed at 550°C as well as (c) undoped and (d) Mn-doped TiO_2 deposited at 400°C.

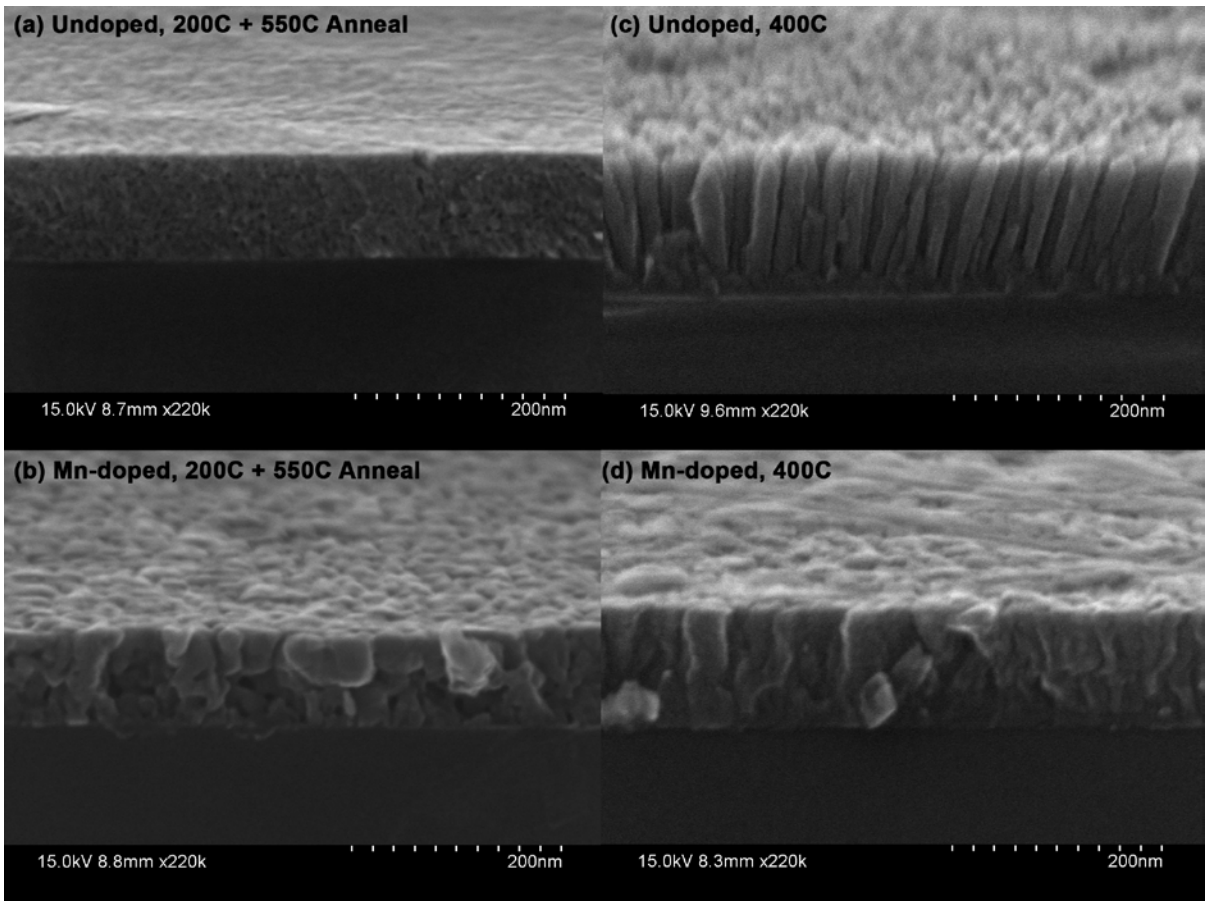

Fig. 6.7 XRD patterns of undoped, ~1 at%, and ~2 at% Mn-doped TiO_2 showing anatase structure and several crystalline orientations: (101), (112), (200), and (211).

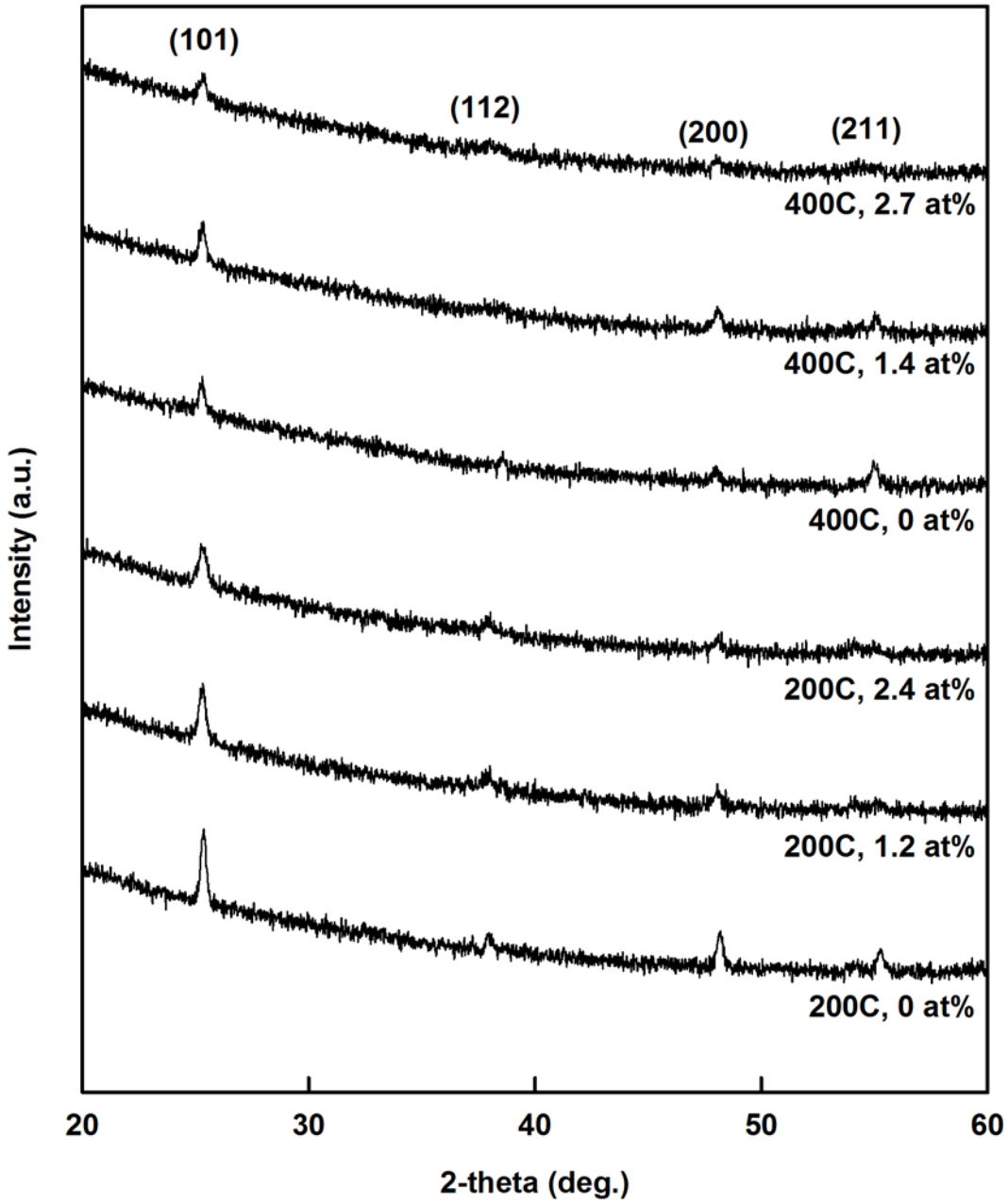

Fig. 6.8 (a) Average crystallite size obtained from fitting of XRD patterns and (b) bulk density obtained from analysis of XRR data.

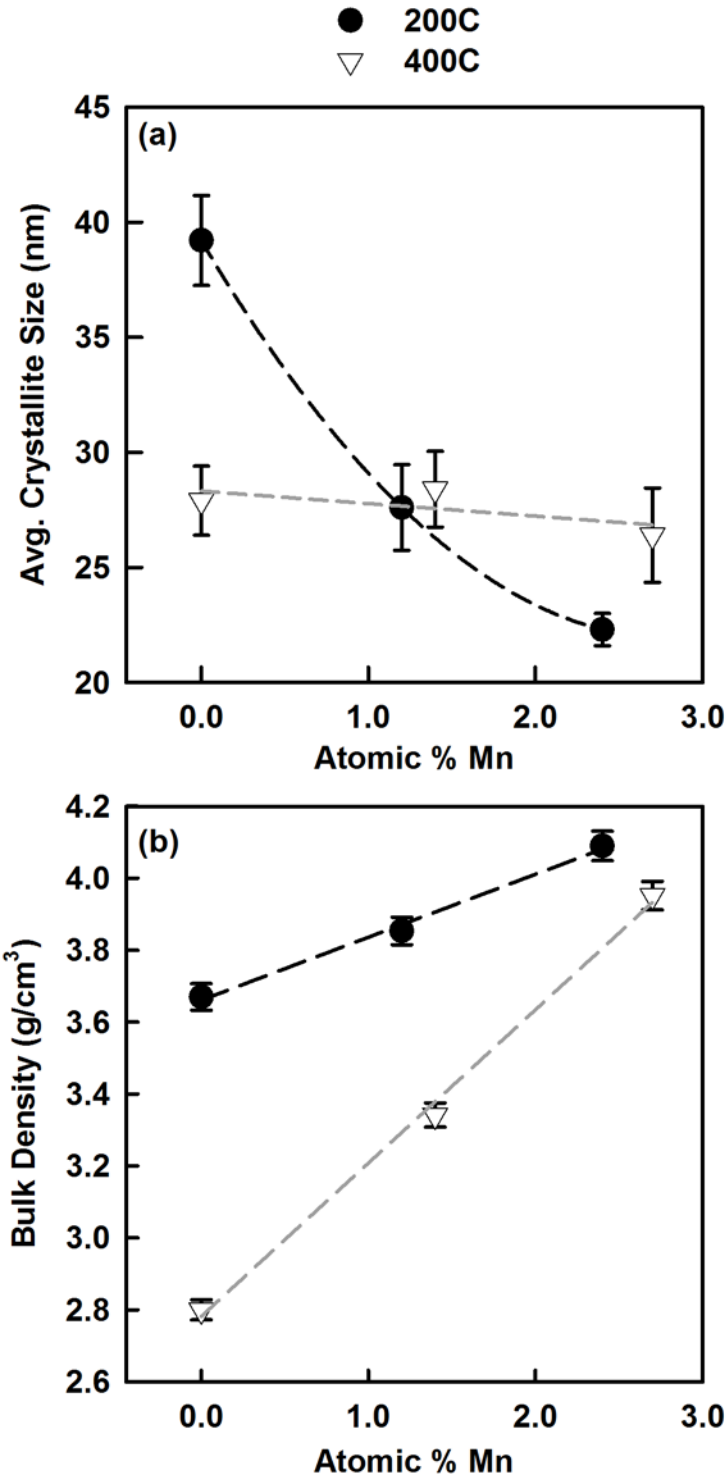

Fig. 6.9 XRR profiles for the same assortment of TiO_2 films used for determination of bulk density and estimation of surface roughness.

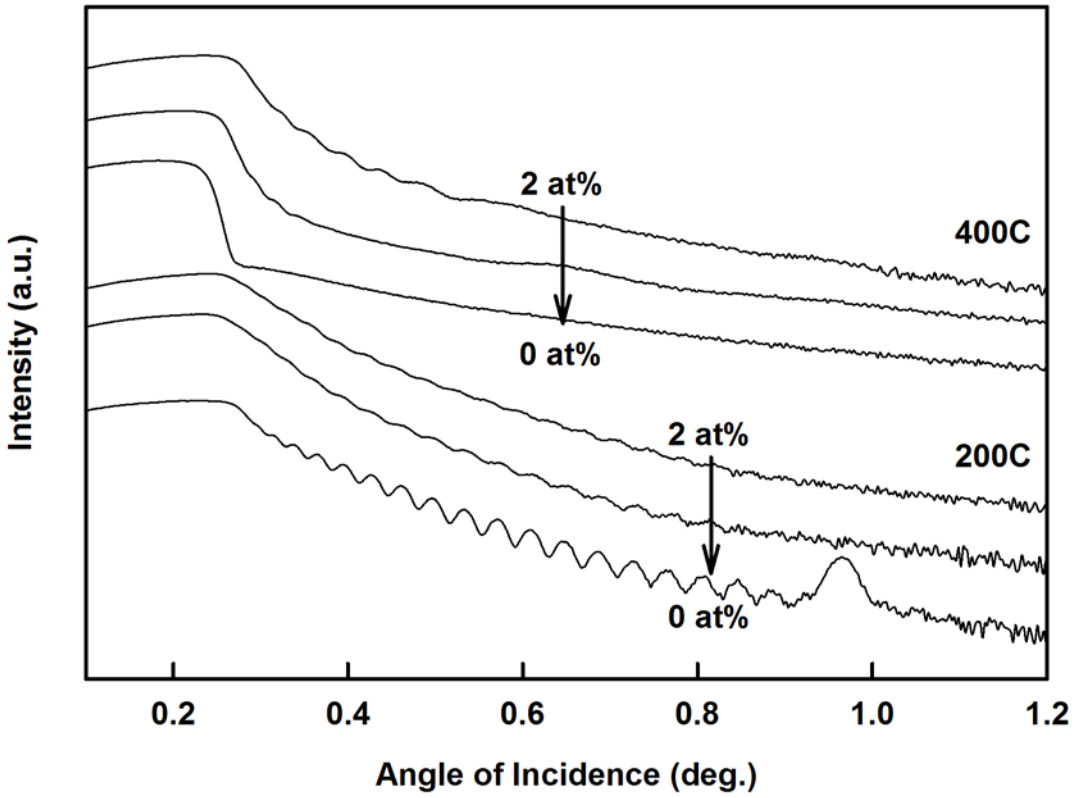

Fig. 6.10 (a) Room temperature *M-H* loops of undoped TiO_2 prior to background subtraction and (b) the same curves following background subtraction with inset showing region close to $H = 0$.

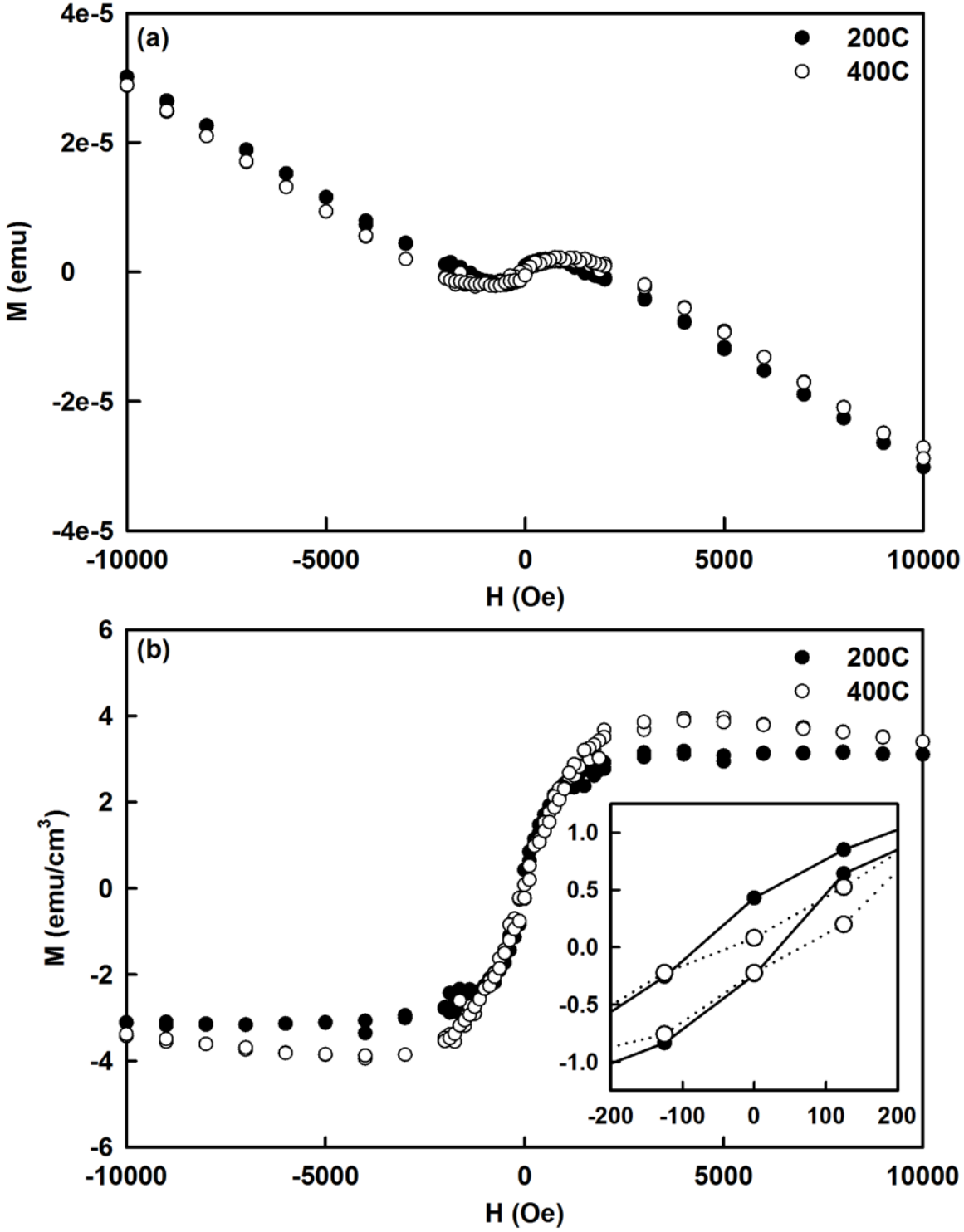

Fig. 6.11 (a) Room temperature *M-H* loops for ~1 at% and ~2 at% Mn-doped TiO_2 deposited at 200°C and 400°C along with close-up views of the (b) 200°C and (c) 400°C data near to $H = 0$.

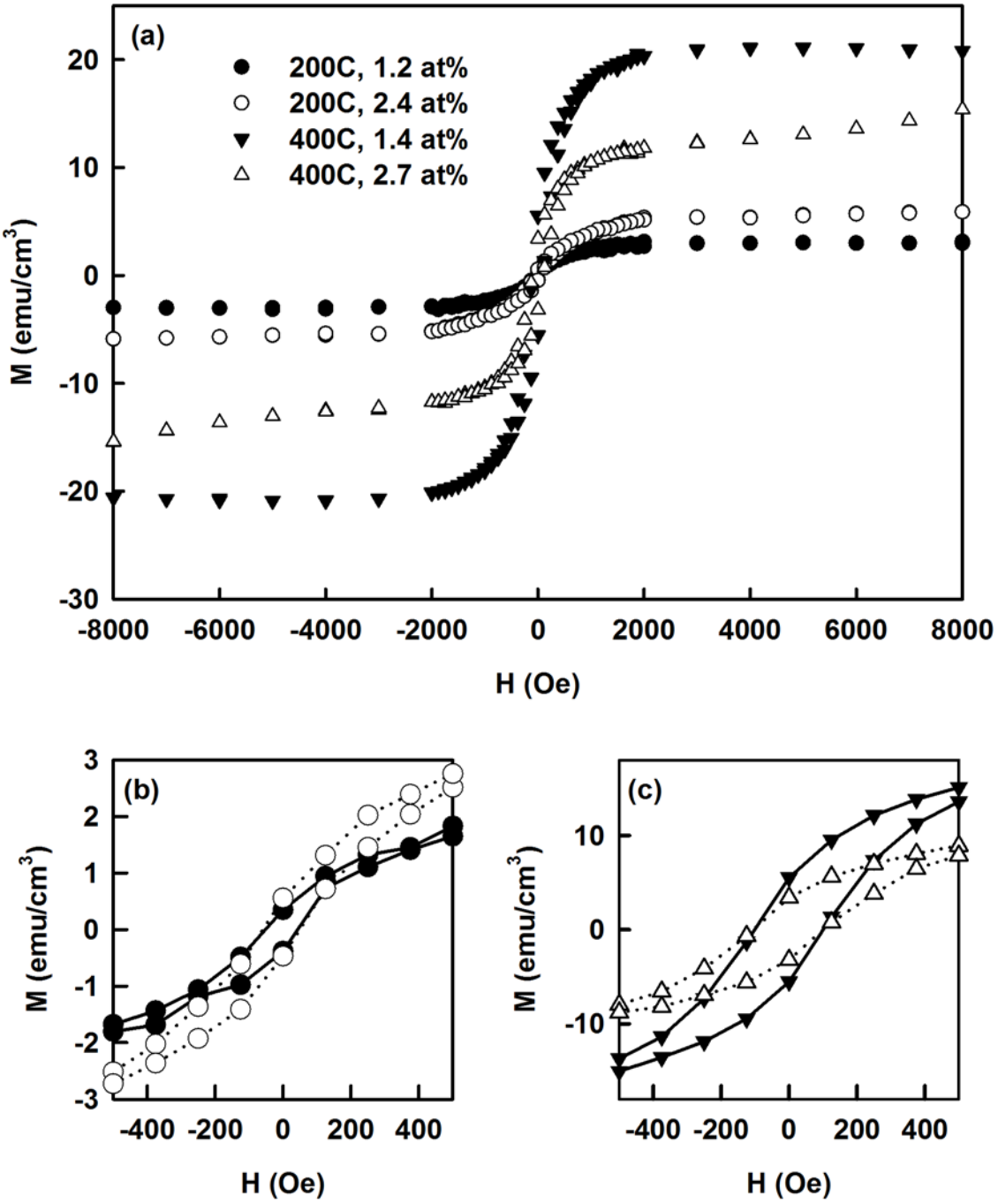

6.7 References

[1] S. A. Wolf, D. D. Awschalom, R. A. Buhrman, J. M. Daughton, S. von Molnar, M. L. Roukes, A. Y. Chtchelkanova, and D. M. Treger, *"Spintronics: A Spin-Based Electronics Vision for the Future,"* Science **294,** 1488-1495 (2001).

[2] S. A. Chambers, *"Ferromagnetism in doped thin-film oxide and nitride semiconductors and dielectrics,"* Surf. Sci. Rep. **61,** 345-381 (2006).

[3] S. P. Dash, S. Sharma, R. S. Patel, M. P. de Jong, and R. Jansen, *"Electrical creation of spin polarization in silicon at room temperature,"* Nature **462,** 491-494 (2009).

[4] M. E. Flatte, *"Solid-state physics: Silicon spintronics warms up,"* Nature **462,** 419-420 (2009).

[5] T. Dietl, D. D. Awschalom, M. Kaminska, and H. Ohno, *Spintronics* (Elsevier, Amsterdam, 2008).

[6] P. M. Krstajic, V. A. Ivanov, F. M. Peeters, V. Fleurov, and K. Kikoin, *"Ferromagnetism in Mn-Doped GaAs: The Kinematic Exchange,"* J. Supercond. **16,** 111-113 (2003).

[7] N. A. Frey, MS Thesis, University of South Florida, Tampa, 2004.

[8] T. Fukumura, H. Toyosaki, and Y. Yamada, *"Magnetic oxide semiconductors,"* Semicond. Sci. Technol. **20,** S103-S111 (2005).

[9] T. Droubay, S. M. Heald, V. Shutthanandan, S. Thevuthasan, S. A. Chambers, and J. Osterwalder, *"Cr-doped TiO_2 anatase: a ferromagnetic insulator,"* J. Appl. Phys. **97,** 046103 (2005).

[10] Z. Wang, J. Tang, Y. Chen, L. Spinu, W. Zhou, and L. D. Tung, *"Room-temperature ferromagnetism in manganese doped reduced rutile titanium dioxide thin films,"* J. Appl. Phys. **95,** 7384-7386 (2004).

[11] K. Y. S. Chan and G. K. L. Goh, *"Hydrothermal growth of ferromagnetic Fe-doped TiO_2 films,"* Thin Solid Films **516,** 5582-5585 (2008).

[12] Y. Matsumoto, M. Murakami, T. Shono, T. Hasegawa, T. Fukumura, M. Kawasaki, P. Ahmet, T. Chikyow, S. Koshihara, and H. Koinuma, *"Room-temperature ferromagnetism in transparent transition metal doped titanium-dioxide,"* Science **291,** 854-856 (2001).

[13] N. H. Hong, J. Sakai, A. Ruyter, and V. Brize, *"Does Mn doping play any key role in tailoring the ferromagnetic ordering of TiO_2 thin films?,"* Appl. Phys. Lett. **89,** 252504 (2006).

[14] N. H. Hong, J. Sakai, N. Poirot, and V. Brizé, *"Room-temperature ferromagnetism observed in undoped semiconducting and insulating oxide thin films,"* Phys. Rev. B: Condens. Matter **73,** 132404 (2006).

[15] J. P. Xu, Y. B. Lin, Z. H. Lu, X. C. Liu, Z. L. Lu, J. F. Wang, W. Q. Zou, L. Y. Lv, F. M. Zhang, and Y. W. Du, *"Enhanced ferromagnetism in Mn-doped TiO_2 films during the structural phase transition,"* Solid State Commun. **140,** 514-518 (2006).

[16] X. Y. Li, S. X. Wu, L. M. Xu, C. T. Li, Y. J. Liu, X. J. Xing, and S. W. Li, *"Effects of depositing rate on structure and magnetic properties of Mn:TiO_2 films grown by plasma-assisted molecular beam epitaxy,"* Mater. Sci. Eng., B **156,** 90-93 (2009).

[17] H. S. Hsu, J. C. A. Huang, S. F. Chen, and C. P. Liu, *"Role of grain boundary and grain defects on ferromagnetism in Co:ZnO films,"* Appl. Phys. Lett. **90,** 102506 (2007).

[18] S. Banerjee, K. Rajendran, N. Gayathri, M. Sardar, S. Senthilkumar, and V. Sengodan, *"Change in the room temperature magnetic property of ZnO upon Mn doping,"* e-print arXiv:0704.3541v3 (2008).

[19] A. Wojcik, M. Godlewski, E. Guziewicz, K. Kopalko, R. Jakiela, M. Kiecana, M. Sawicki, M. Guziewicz, M. Putkonen, L. Niinisto, Y. Dumont, and N. Keller, *"Low temperature growth of ZnMnO: A way to avoid inclusions of foreign phases and spinodal decomposition,"* Appl. Phys. Lett. **90,** 082502 (2007).

[20] S. Duhalde, C. E. R. Torres, M. F. Vignolo, F. Golmar, C. Chillote, A. F. Cabrera, and F. H. Sanchez, *"Ferromagnetism in doped TiO_2 thin films prepared by PLD,"* J. Phys., Conf. Ser. **59,** 479-482 (2007).

[21] X. Y. Li, S. X. Wu, L. M. Xu, Y. J. Liu, X. J. Xing, and S. W. Li, *"Room-temperature ferromagnetism in (Mn, N)-codoped TiO_2 films grown by plasma assisted molecular beam epitaxy,"* J. Appl. Phys. **104,** 093914 (2008).

[22] F. Hirose, M. Ito, and K. Kurita, *"Low-temperature chemical vapor deposition of anatase TiO_2 with titanium tetraisopropoxide and H_2O_2 vapor,"* Jpn. J. Appl. Phys. **47,** 5619-5622 (2008).

[23] X. Li, S. Wu, P. Hu, X. Xing, Y. Liu, Y. Yu, M. Yang, J. Lu, S. Li, and W. Liu, *"Structures and magnetic properties of p-type Mn:TiO_2 dilute magnetic semiconductor thin films,"* J. Appl. Phys. **106,** 043913 (2009).

[24] Y. Xu, B. Lei, L. Guo, W. Zhou, and Y. Liu, *"Preparation, characterization and photocatalytic activity of manganese doped TiO_2 immobilized on silica gel,"* J. Hazard. Mater. **160,** 78-82 (2008).

[25] J. T. Mayer, U. Diebold, T. E. Madey, and E. Garfunkel, *"Titanium and reduced titania overlayers on titanium dioxide(110),"* J. Electron. Spectrosc. Relat. Phenom. **73,** 1-11 (1995).

[26] J. Zhu, Z. Deng, F. Chen, J. Zhang, H. Chen, M. Anpo, J. Huang, and L. Zhang, *"Hydrothermal doping method for preparation of Cr^{3+}-TiO_2 photocatalysts with concentration gradient distribution of Cr^{3+},"* Appl. Catal. B **62,** 329-335 (2006).

[27] K. Jiang, A. Zakutayev, J. Stowers, M. D. Anderson, J. Tate, D. H. McIntyre, D. C. Johnson, and D. A. Keszler, *"Low-temperature, solution processing of TiO_2 thin films and fabrication of multilayer dielectric optical elements,"* Solid State Sci. **11,** 1692-1699 (2009).

[28] S. J. Wang, W.-T. Chang, J.-Y. Ciou, M.-K. Wei, and M. S. Wong, *"Preparation of TiO_2 thin films by laser ablation for photocatalytic applications,"* J. Vac. Sci. Technol. A **26,** 898-902 (2008).

[29] C. Sima and C. Grigoriu, *"Study on TiO_2 thin films grown by advanced pulsed laser deposition on ITO,"* Thin Solid Films **518,** 1314-1317 (2009).

[30] C. M. Wang, J. Meinhardt, and P. Löbmann, *"Growth mechanism of Nb-doped TiO_2 sol–gel multilayer films characterized by SEM and focus/defocus TEM,"* J. Sol-Gel Sci. Technol. **53,** 148-153 (2010).

[31] J. P. Xu, J. F. Wang, Y. B. Lin, X. C. Liu, Z. L. Lu, Z. H. Lu, L. Y. Lv, F. M. Zhang, and Y. W. Du, *"Effect of annealing ambient on the ferromagnetism of Mn-doped anatase TiO_2 films,"* J. Phys. D: Appl. Phys. **40,** 4757-4760 (2007).

[32] C.-F. Yu, S.-H. Chen, S.-J. Sun, and H. Chou, *"Influence of the substrate temperature on the electrical and magnetic properties of ZnO:N thin films grown by pulse laser deposition,"* J. Phys. D: Appl. Phys. **42,** 035001 (2009).

[33] J. M. D. Coey, A. P. Douvalis, C. B. Fitzgerald, and M. Venkatesan, *"Ferromagnetism in Fe-doped SnO_2 thin films,"* Appl. Phys. Lett. **84,** 1332-1334 (2004).

Appendix A: Supplementary *C-V* and Mott-Schottky Data for Undoped TiO_2

Table A.1 Summary of preparation and characterization parameters for undoped TiO_2 samples studied in Chapter 3.

Sample Batch #	Thickness (nm)	Annealing Time (hrs)	Exposure	*C-V* Date	Appendix Figure #
120910	62 - 259	0.33	Dark	12/13/10	A.2
120910b	62 - 259	0.33	Dark	12/20/10	A.3
120910c	62 - 259	0.33	Dark	12/27/10	A.4
120910d	62 - 259	0.33	Dark	1/12/11	A.5
120510	~ 100	0.33 - 24	Dark	12/8/10	A.6
121410	~ 100	0.33 - 24	Dark	12/17/10	A.7
122110	65 - 251	24	Ambient	1/4/11	A.8
122110D	65 - 251	24	Dark	1/6/11	A.9
120910L	62 - 259	0.33	Lamp	12/20/10	A.10
120910Lb	62 - 259	0.33	Lamp	12/27/10	A.11
120910Lc	62 - 259	0.33	Lamp	1/12/11	A.12

Fig. A.1 ICS measurement interface displaying example measurement parameters for *I-V* and *C-V* data collection.

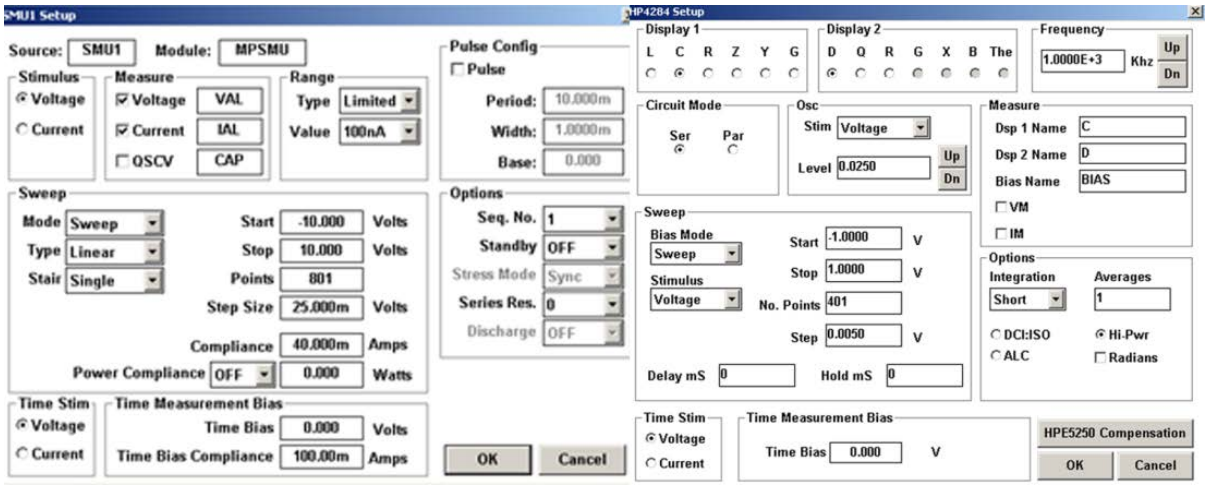

Fig. A.2 T_{dep} = 200°C, T_{anneal} = 550°C for 20 min, dark, 12/13/10, "120910."

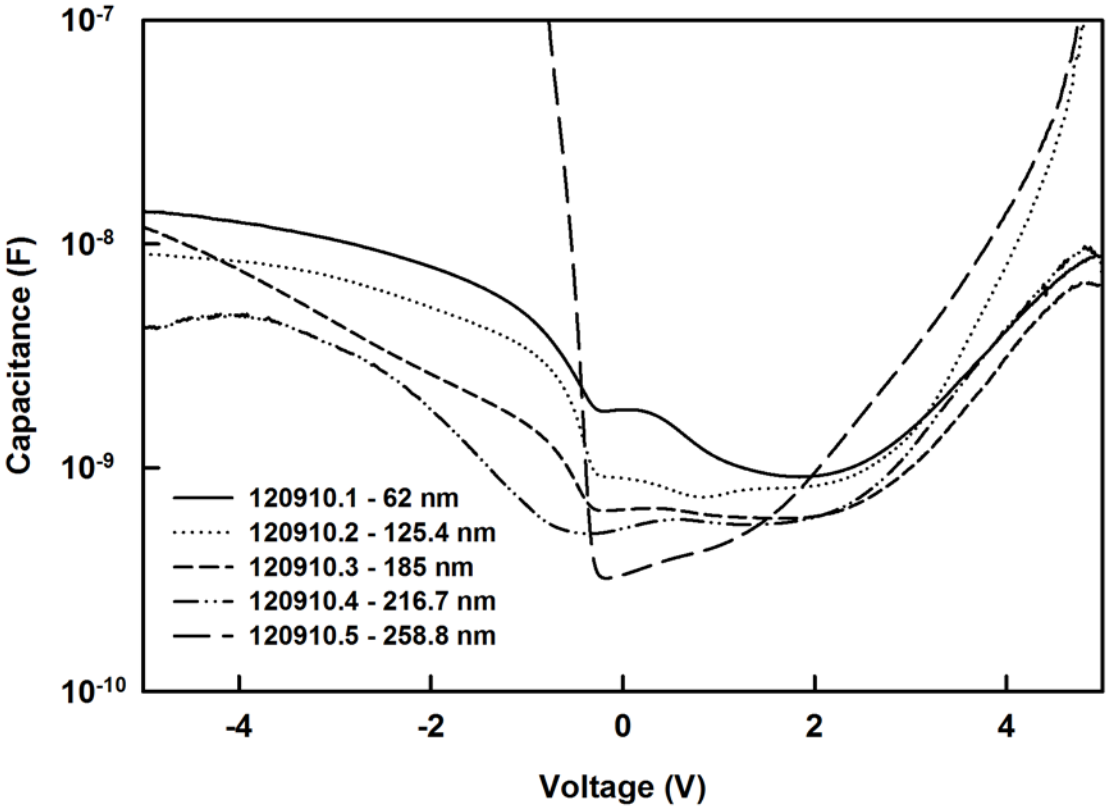

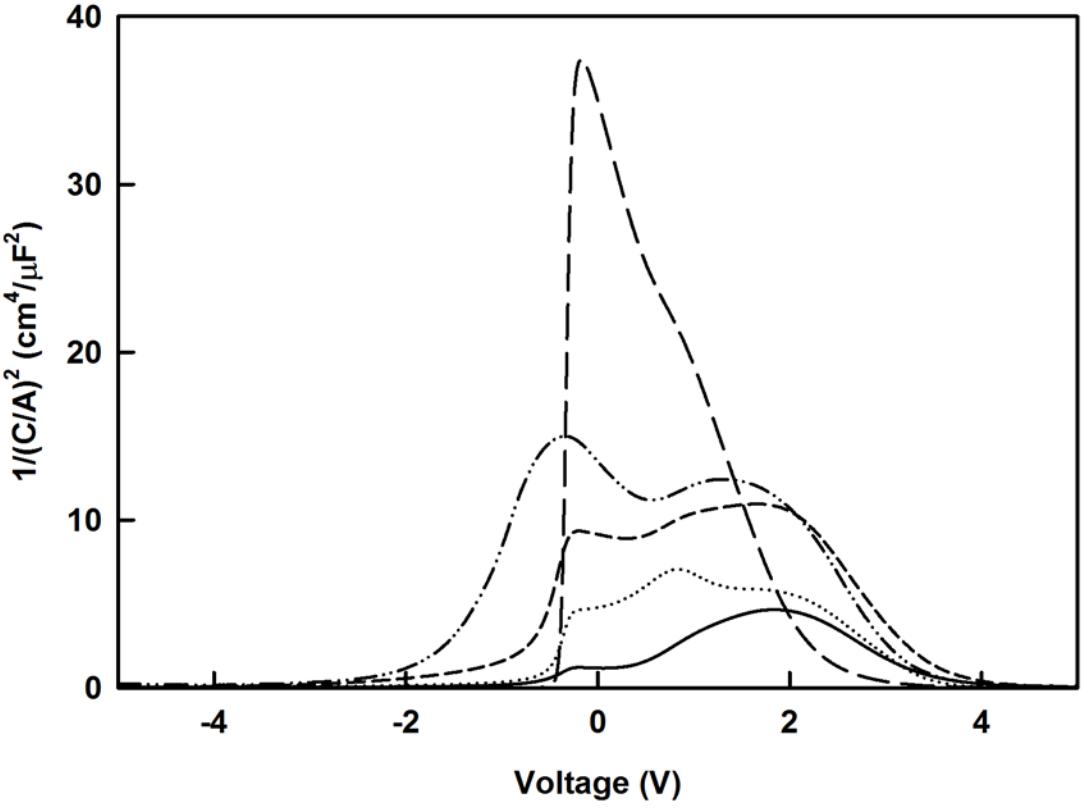

Fig. A.3 T_{dep} = 200°C, T_{anneal} = 550°C for 20 min, dark, 12/20/10, "120910b."

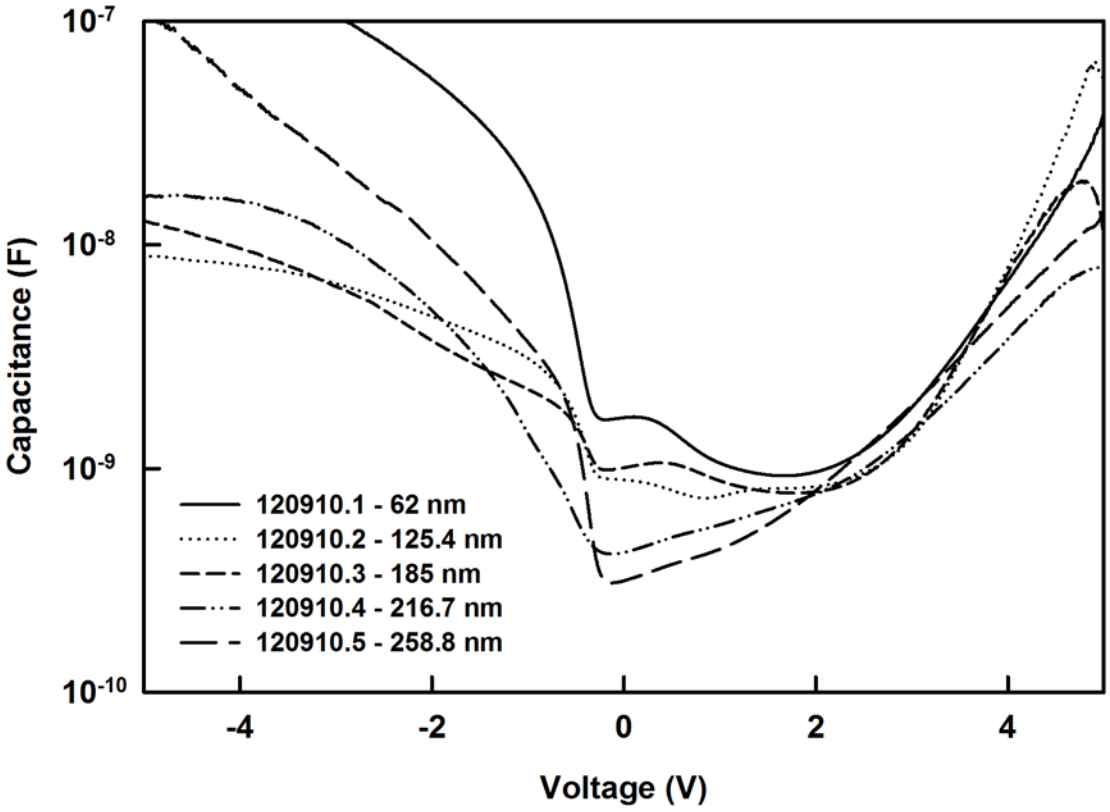

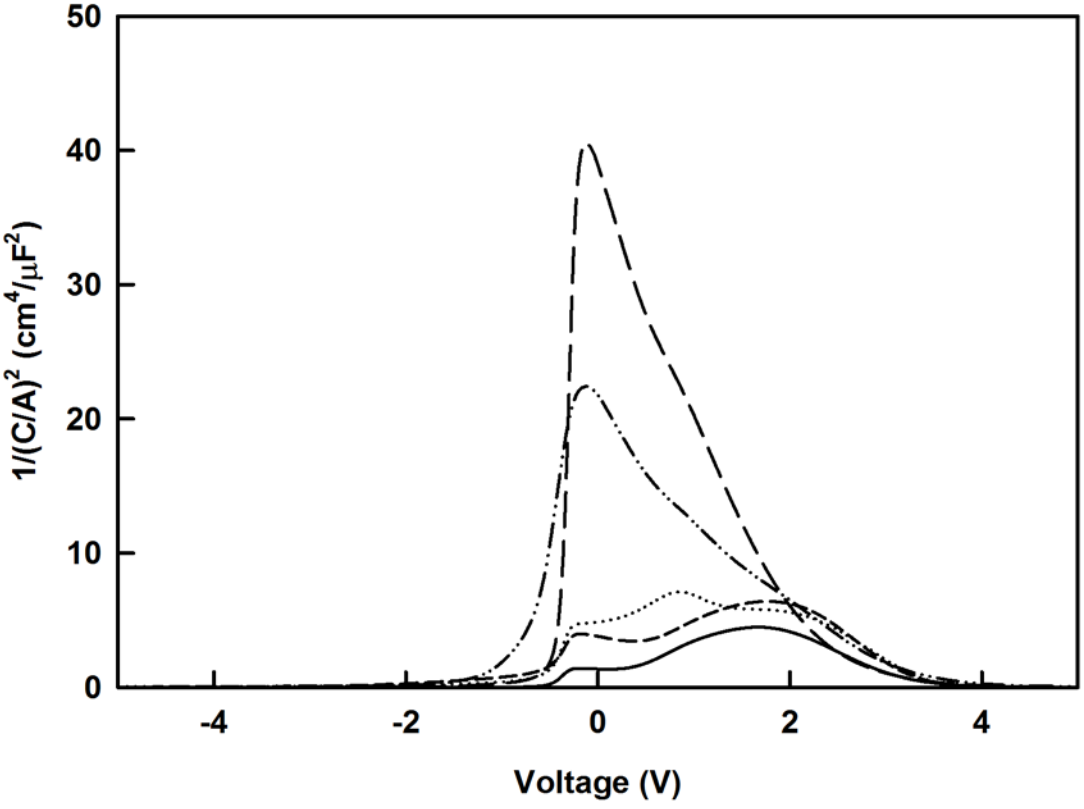

Fig. A.4 T_{dep} = 200°C, T_{anneal} = 550°C for 20 min, dark, 12/27/10, "120910c."

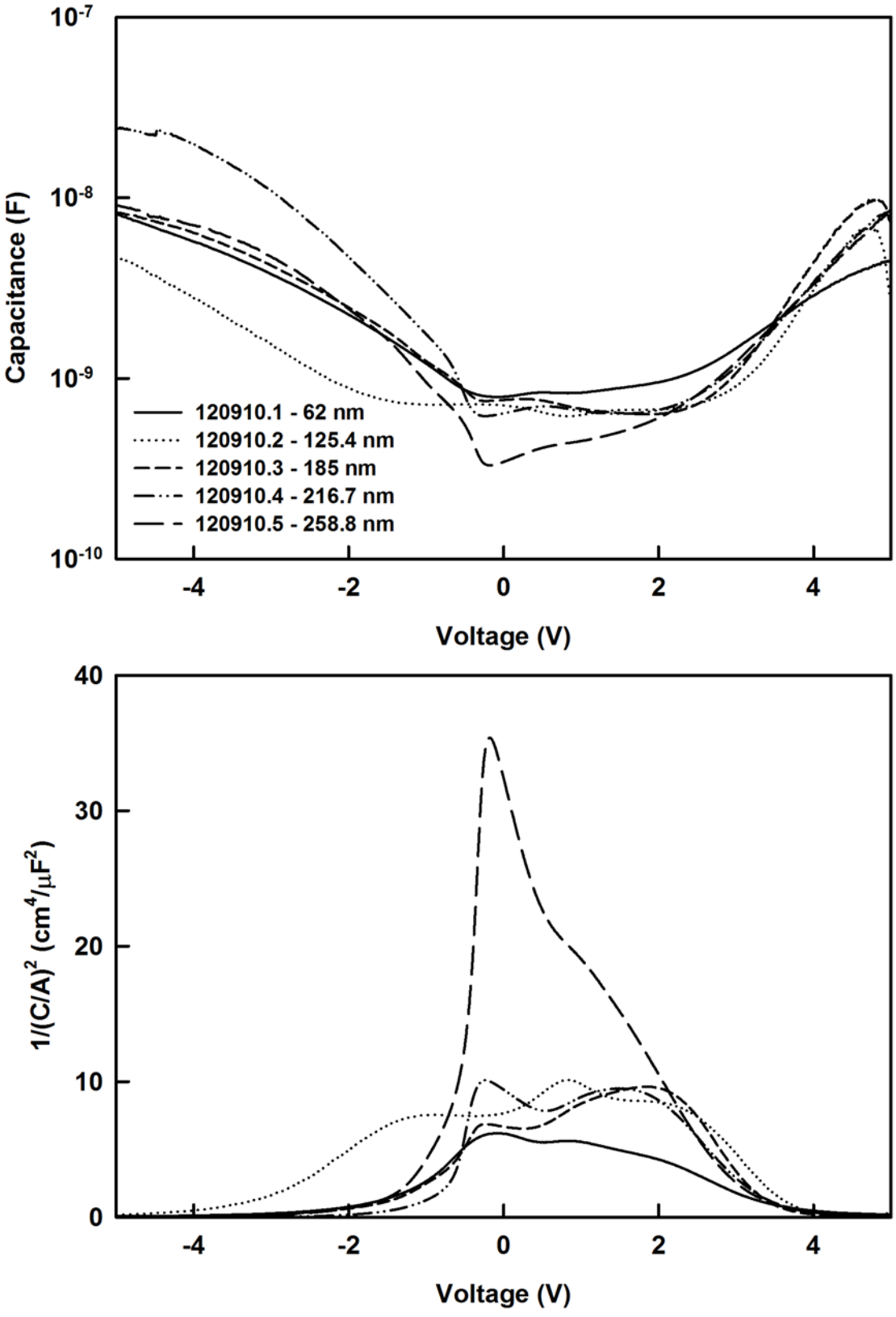

Fig. A.5 T_{dep} = 200°C, T_{anneal} = 550°C for 20 min, dark, 1/12/11, "120910d."

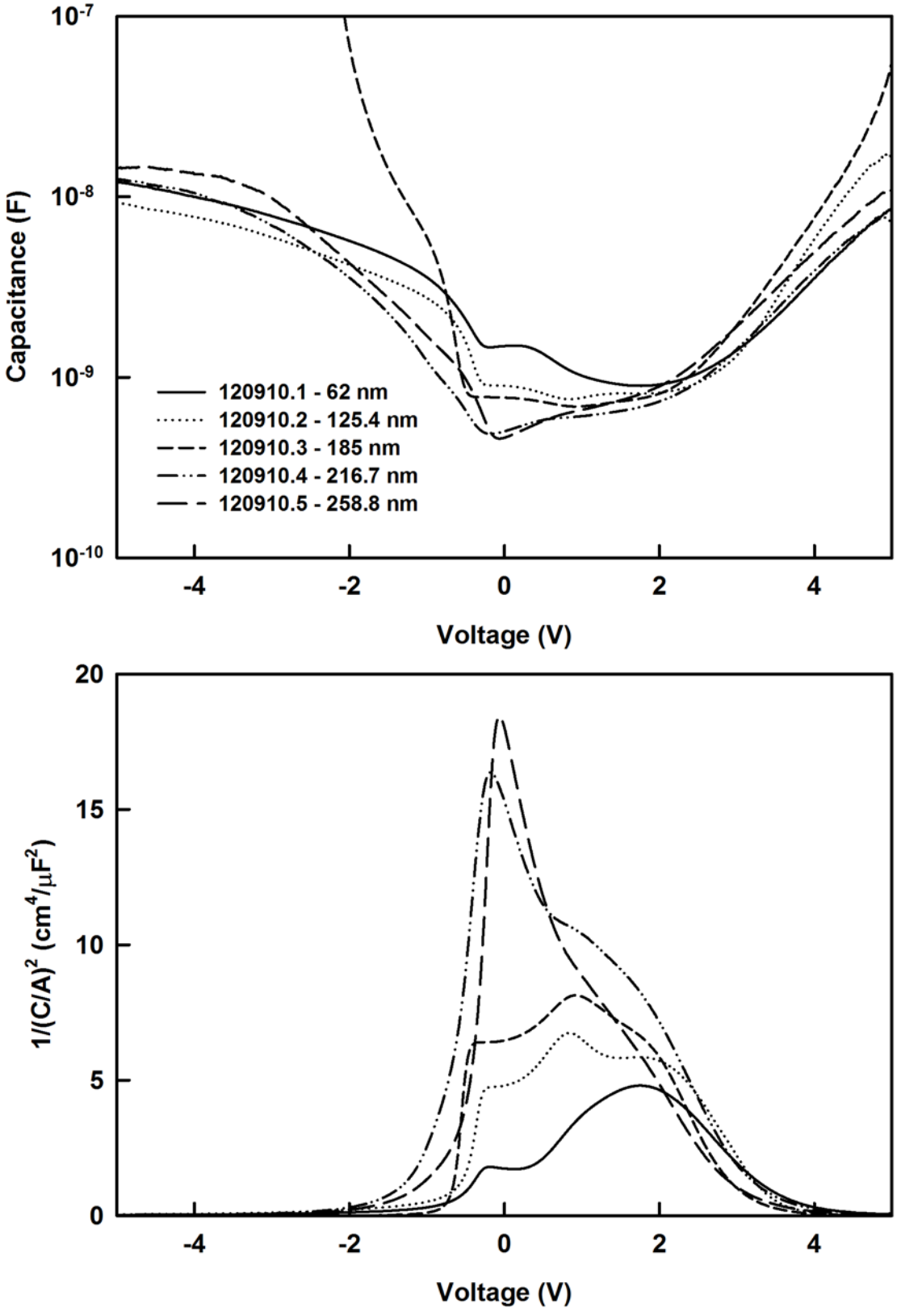

Fig. A.6 T_{dep} = 200°C, T_{anneal} = 550°C for 24 hours, ambient, 1/4/11, "122110."

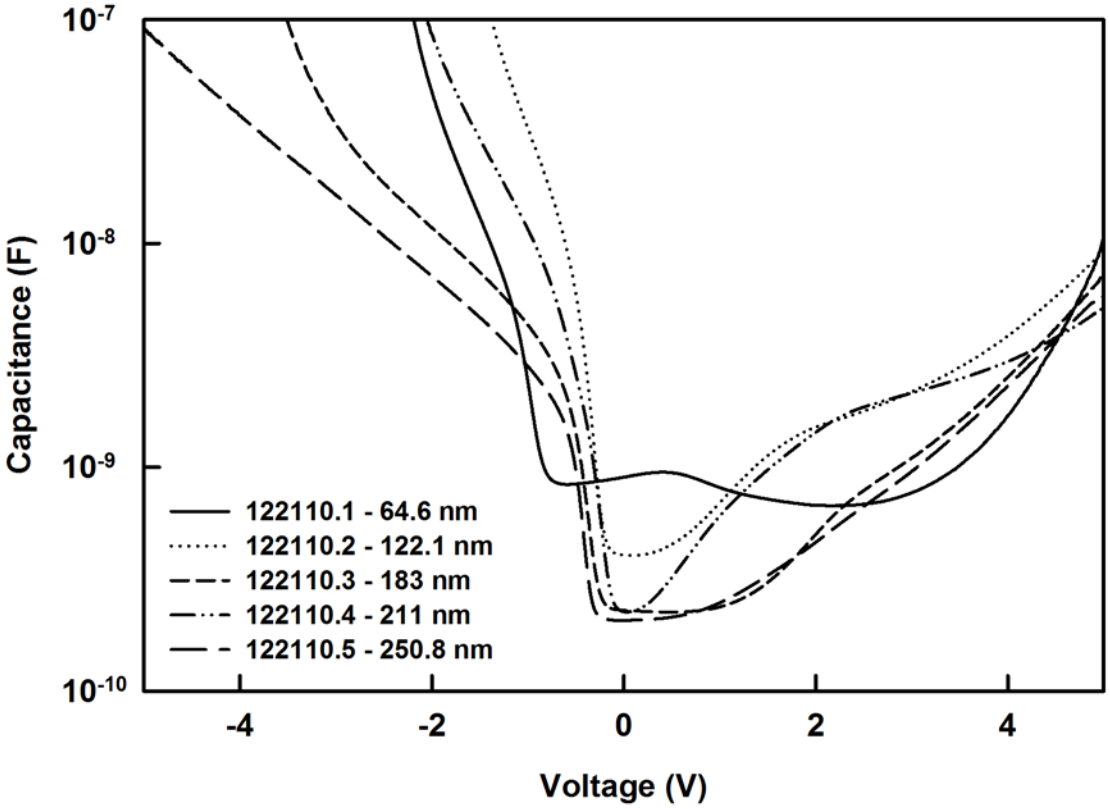

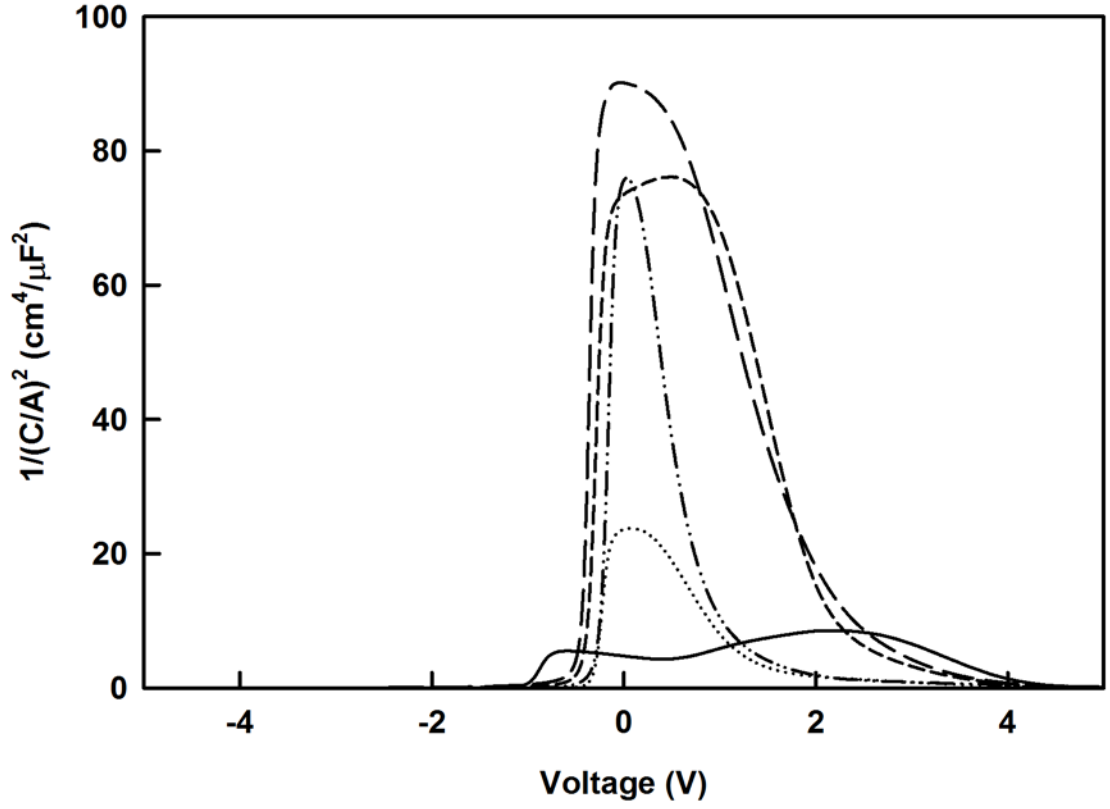

Fig. A.7 T_{dep} = 200°C, T_{anneal} = 550°C for 24 hours, dark, 1/6/11, "122110D."

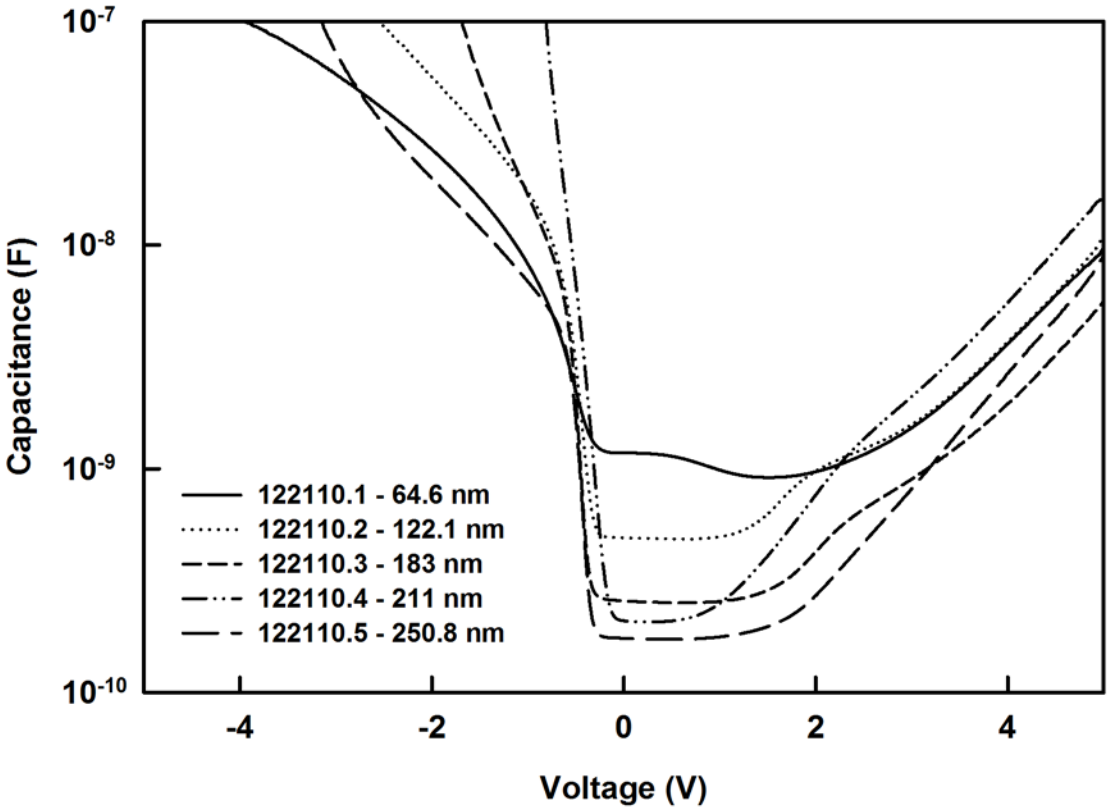

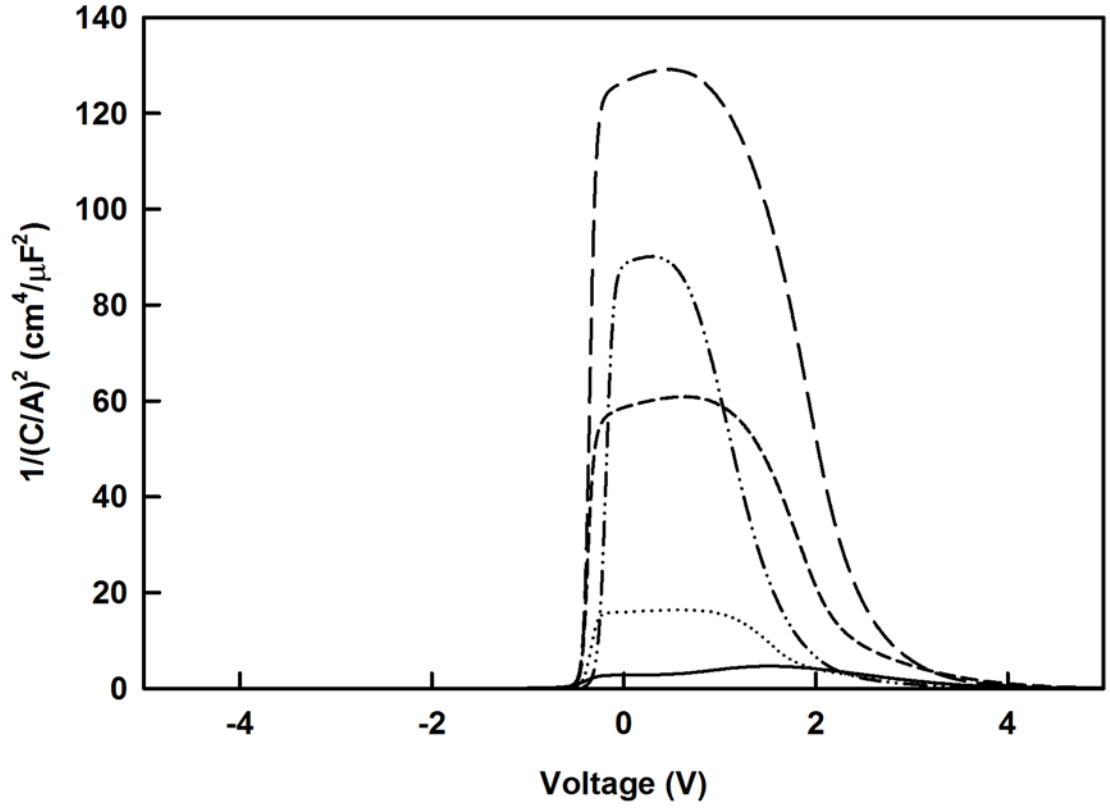

Fig. A.8 T_{dep} = 200°C, T_{anneal} = 550°C, t ~ 100 nm, dark, 12/8/10, "120510."

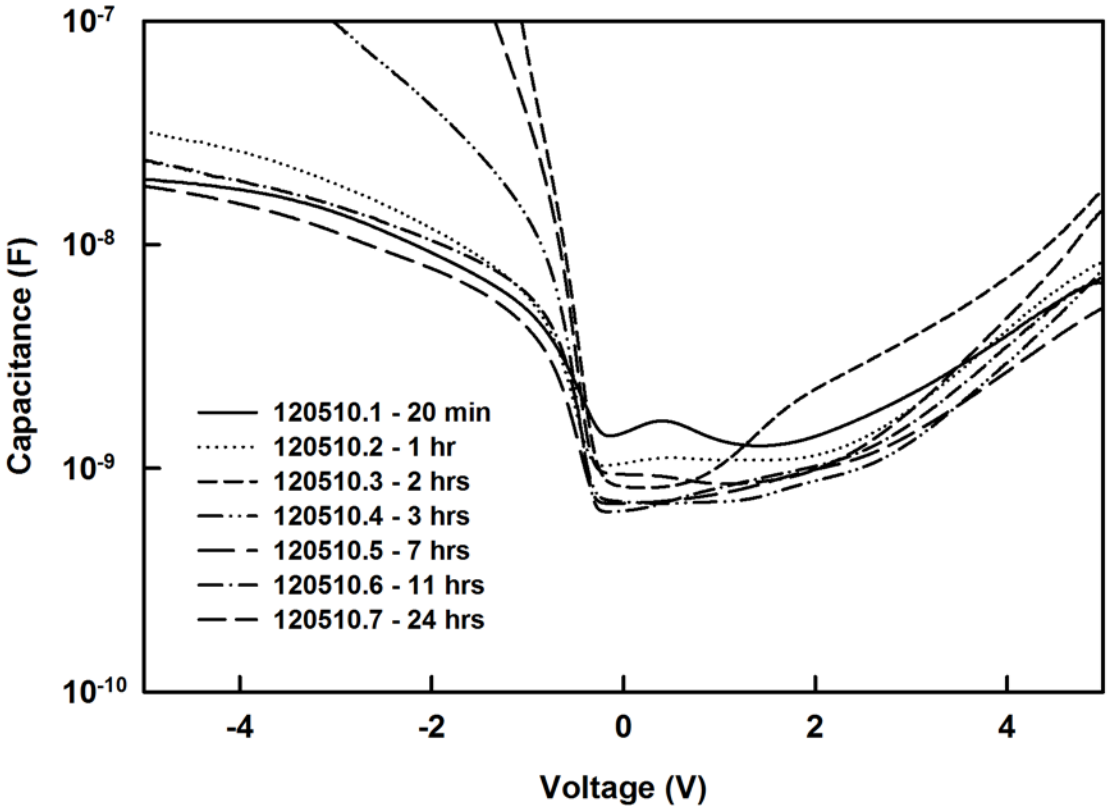

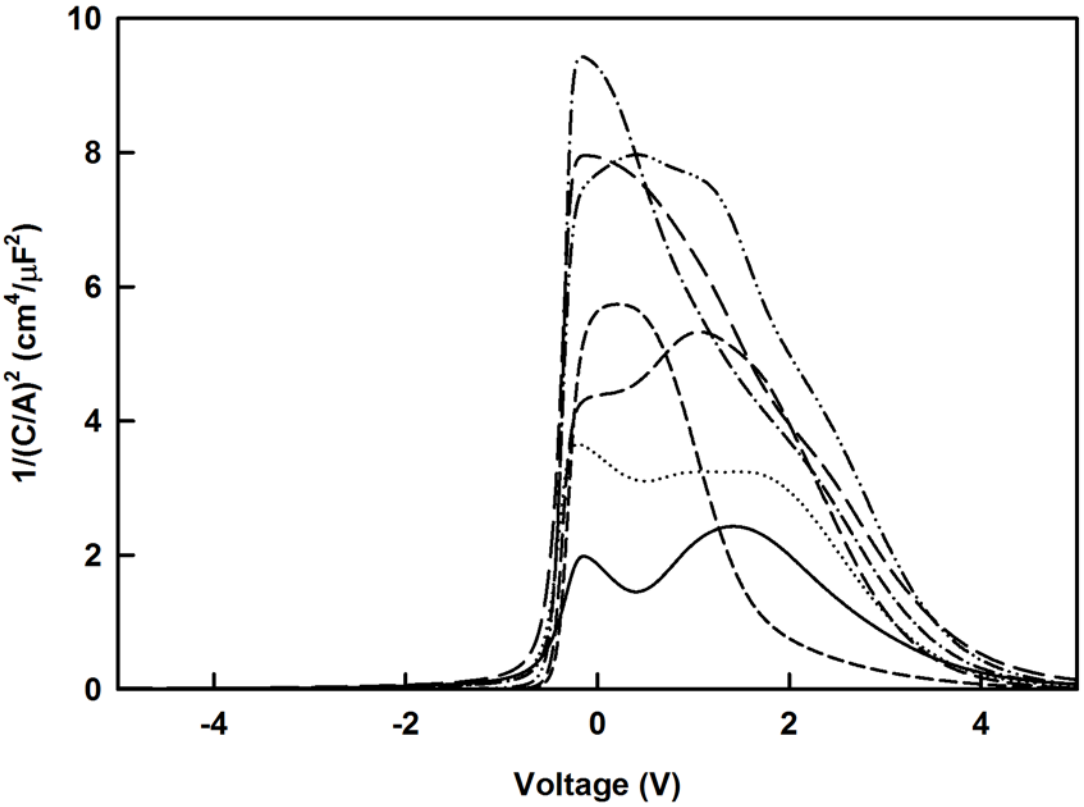

Fig. A.9 T_{dep} = 200°C, T_{anneal} = 550°C, t ~ 100 nm, dark, 12/17/10, "121410."

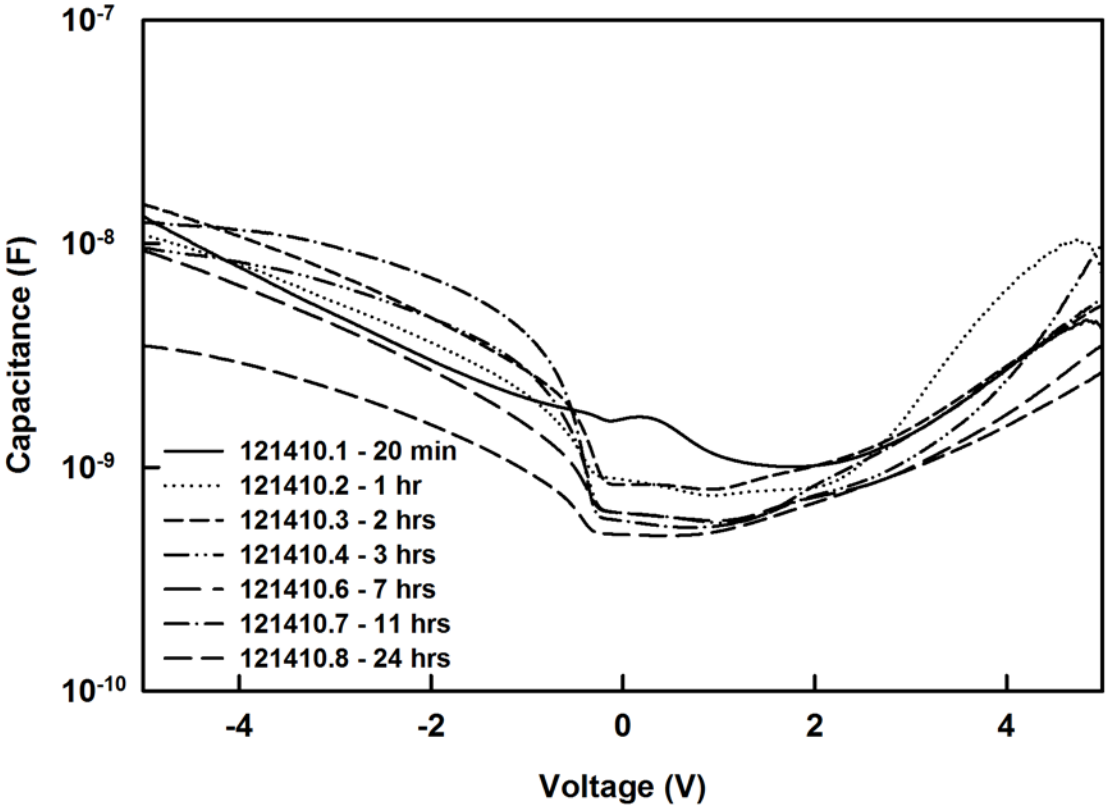

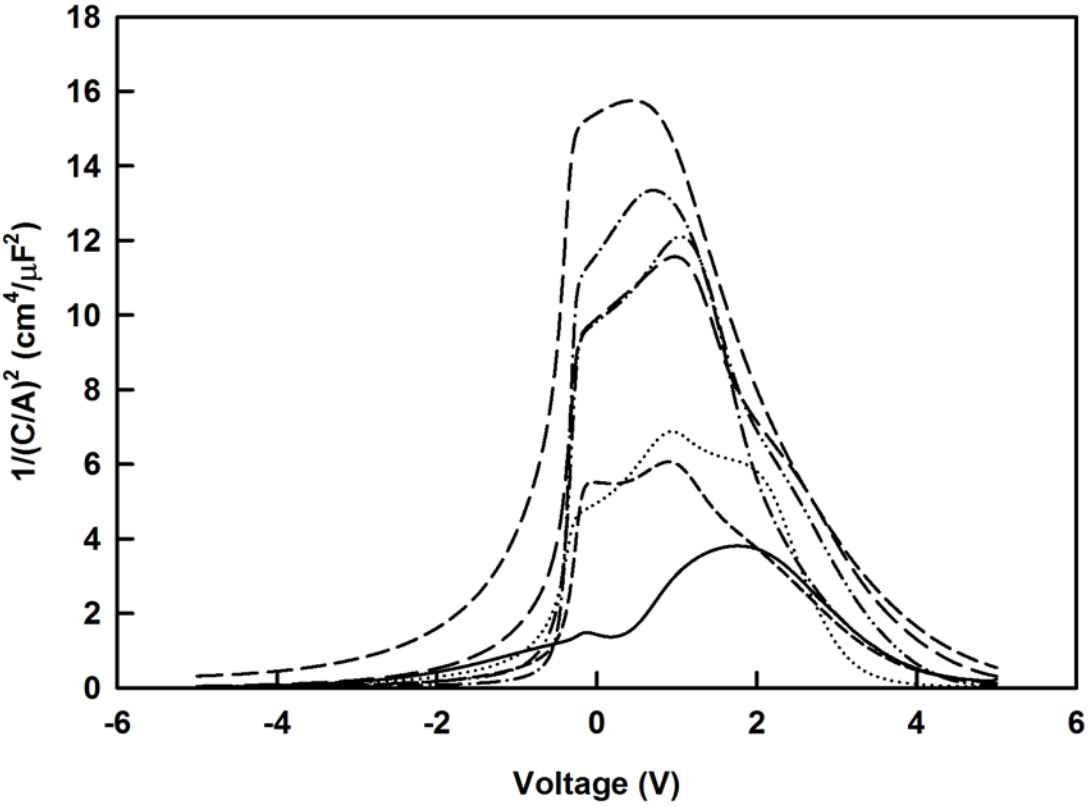

Fig. A.10 T_{dep} = 200°C, T_{anneal} = 550°C for 20 min, lamp, 12/20/10, "120910L."

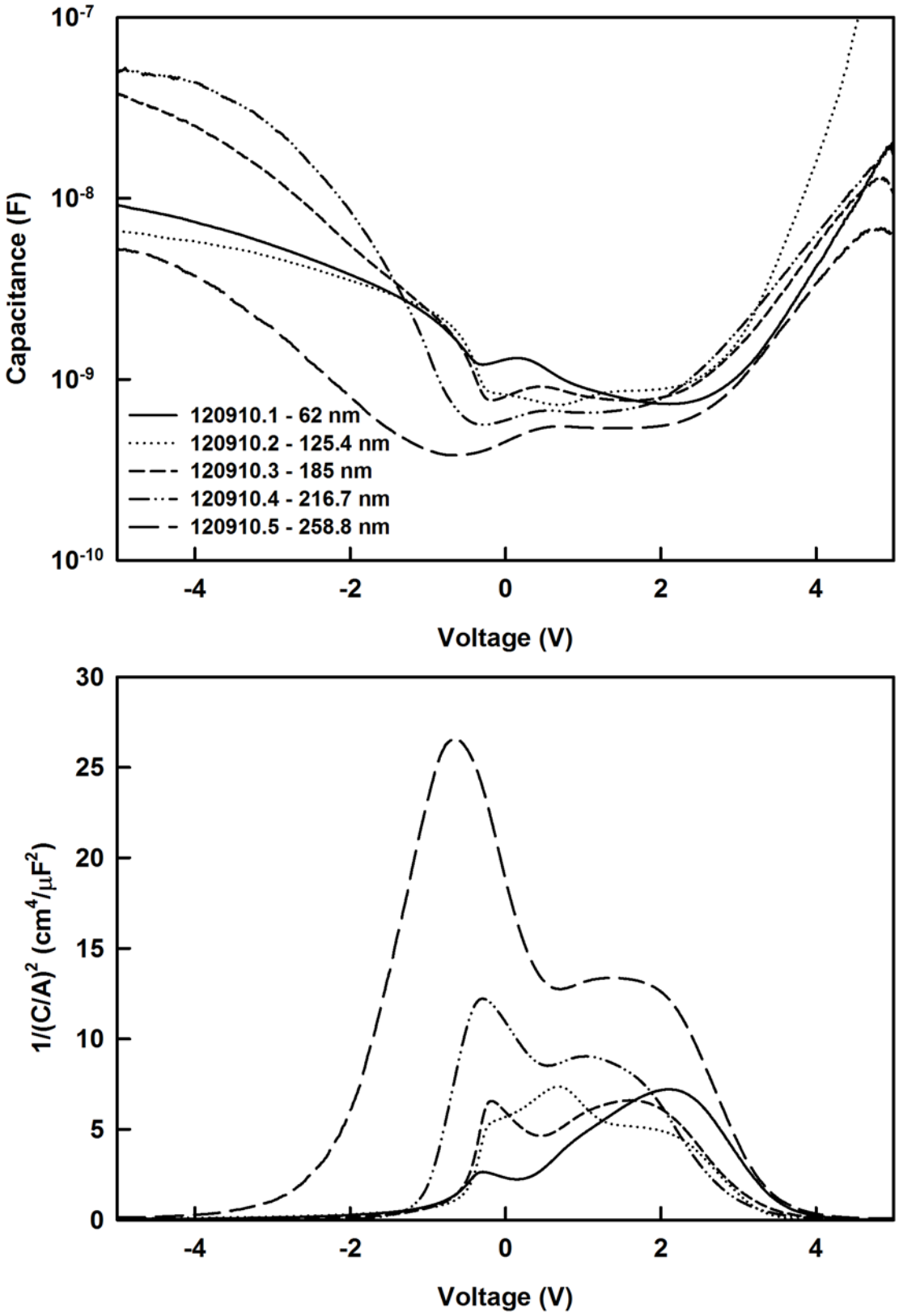

Fig. A.11 T_{dep} = 200°C, T_{anneal} = 550°C for 20 min, lamp, 12/27/10, "120910Lb."

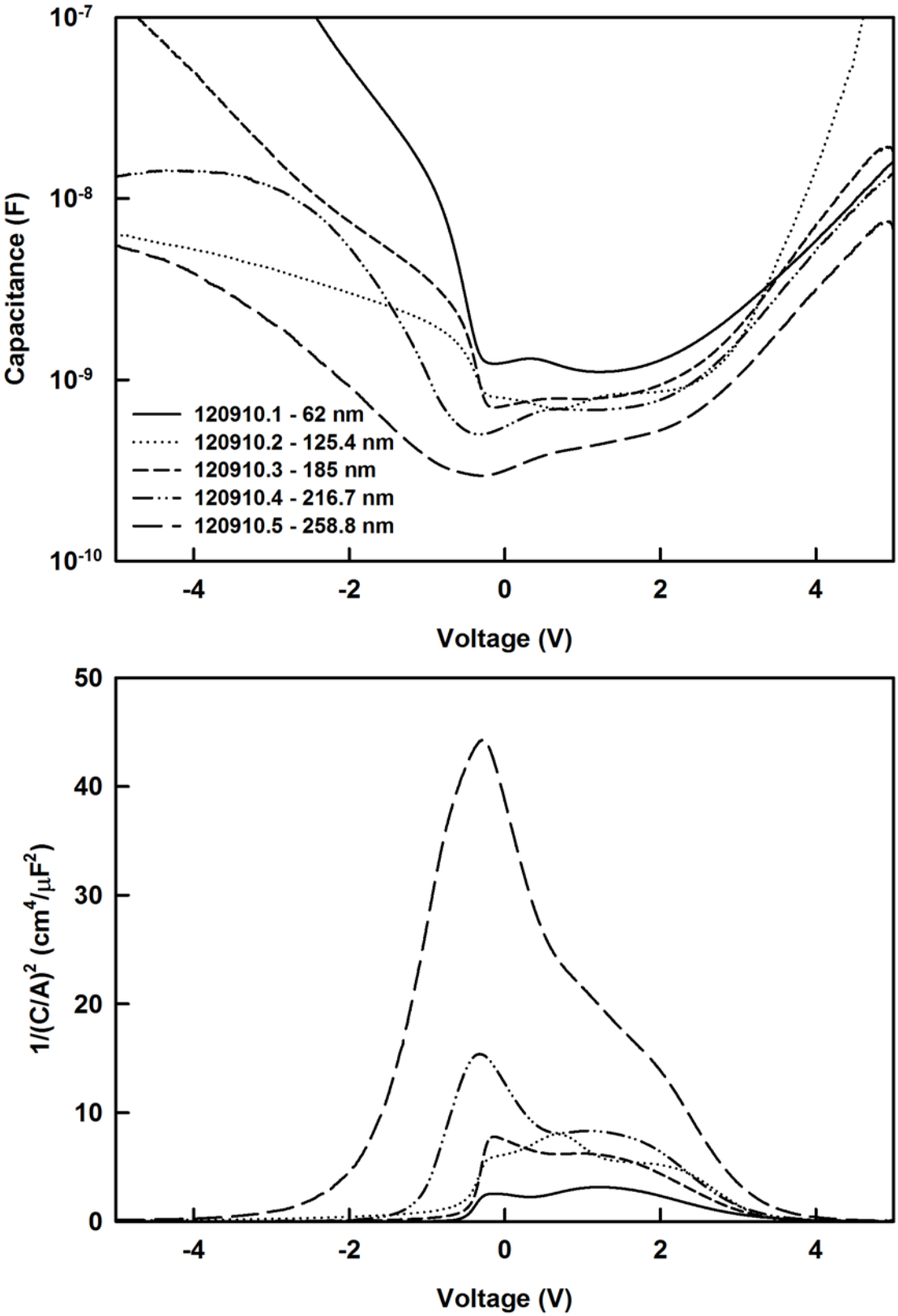

Fig. A.12 T_{dep} = 200°C, T_{anneal} = 550°C for 20 min, lamp, 1/11/11, "120910Lc."

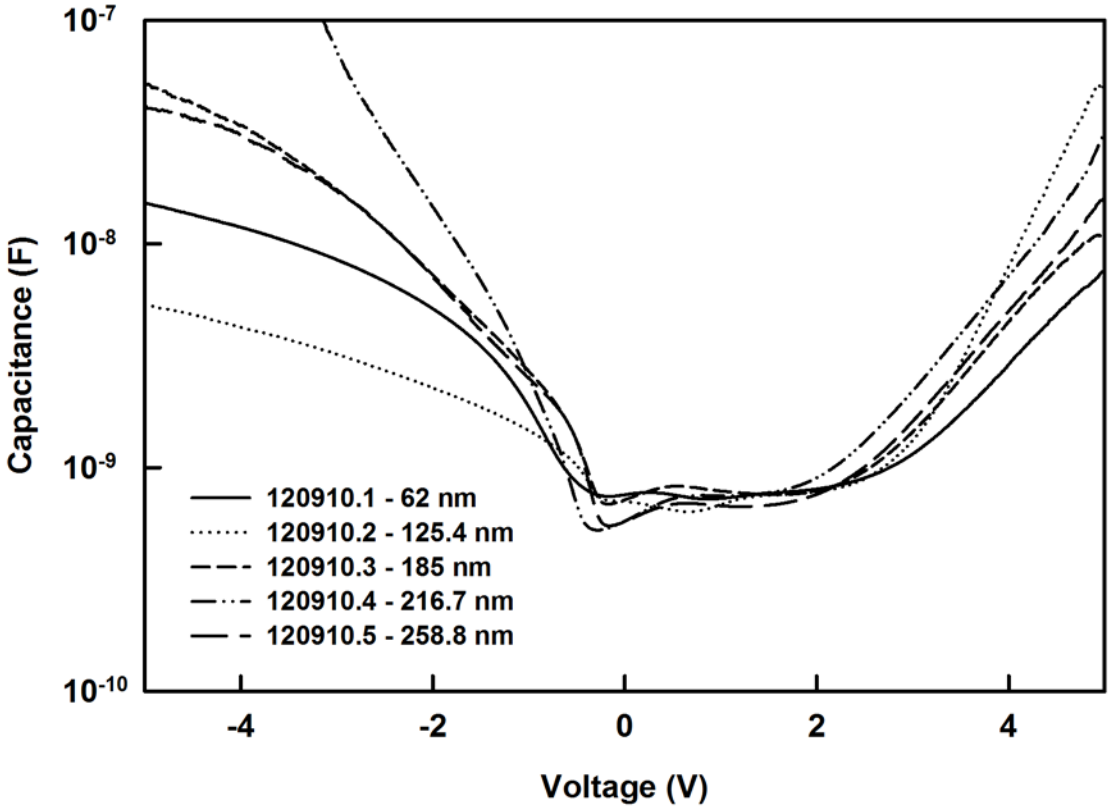

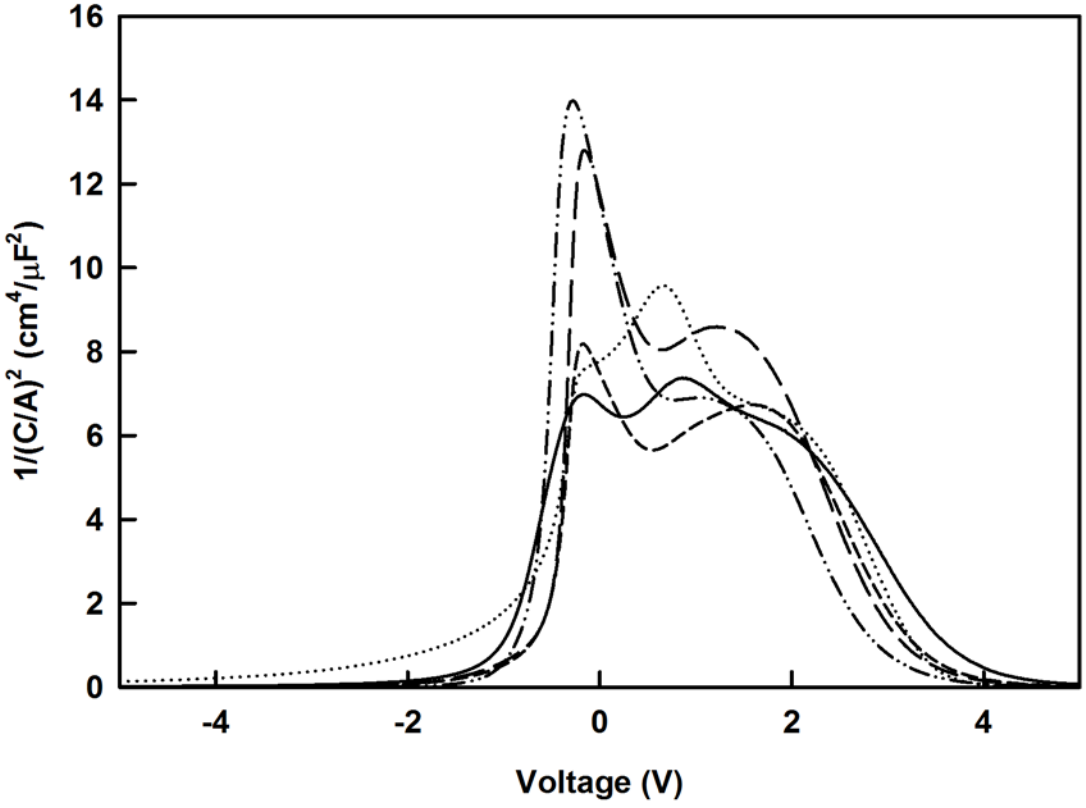

Appendix B: LabVIEW VIs for Photoreflectance

This section contains the details of the LabVIEW "virtual instruments" (VIs) written to automate the photoreflectance apparatus and analyze raw photoreflectance data.

Commands Written to Serial Port

\s ' Establish communication with card
P0\r 'Enter program mode <CR>
Dx\r 'Divide step rate <CR>
Iy\r 'Initial SPS <CR>
Vz\r 'Slew speed SPS <CR>
+ or - steps\r 'Increment or decrement by # of steps +20 or +0 depending on need to correct for hysteresis <CR>
W0\r 'Wait while move command is performed <CR>
- steps hysteresis\r 'Increment 20 steps if motor is originally stepped up from low wavelength to high wavelength or 0 steps if motor is originally stepped down from high wavelength to low wavelength <CR>
P0\r 'Exit program mode <CR>
G0\s1\r ' Execute program stored at location 0 <CR>
\03 'Terminate communication to card

- 0.25 second VISA delay command is inserted after every VISA write command in the stacked sequence structure.
- Must concatenate sign of StepsInit and StepsScan with an integer value before sending the string to the serial port. Sign value (i.e., positive or negative) depends on whether wavelength is being stepped up or down.
- \03 (terminate string) cannot be written immediately after G0\s1\r (run program string) otherwise no motion will occur.
- Write to file is achieved by calling VISA configure serial port outside of stepper motor control loop.

Monochromator Parameter Calculations

V = ScanStep
I = ScanStep
D = (15*I)/ScanSpeed + 3
WaveDiff = Start WL – Current WL
WaveDiffScan = Start WL – Stop WL
StepsInit = WaveDiff*ScanStep
StepsScan = WaveDiffScan*ScanStep
TimeScan = (Start WL – Stop WL)/ScanSpeed+4
TimeInit = abs[(Start WL – Stop WL)]/ScanSpeed

- V and I are 2 steps/sec for full steps and 4 steps/sec for half steps

Table B.1 Program commands for AMS mSTEP-403 stepper motor controller.

ASCII	Description	ASCII	Description
^C	Software reset	J	Jump
^N	Name controller	K	Ramp slope
^P	Party line mode	L	Loop on port
ESC	Abort/terminate	M	Move with ramping
+	CW Index	O	Set origin
-	CCW Index	P	Program mode
@	Soft stop	Q	Query program
[	Read NV memory	R	Index to position
]	Read limits	S	Store parameters
\	Write to NV memory	T	Trip point
^	Read moving bit	V	Slew speed
A	Read/write user ports	W	Wait
C	Erase memory	X	Examine parameters
D	Divide steps	Z	Display position
E	Settle display	g	Branch to location
F	Find home	h	Microstep count
G	Go	i	Special trip
H	Set resolution	j	Jump 1
I	Initial velocity	k	Special trip

Fig. B.1 First execution of LabVIEW PR data collection VI sequence structure.

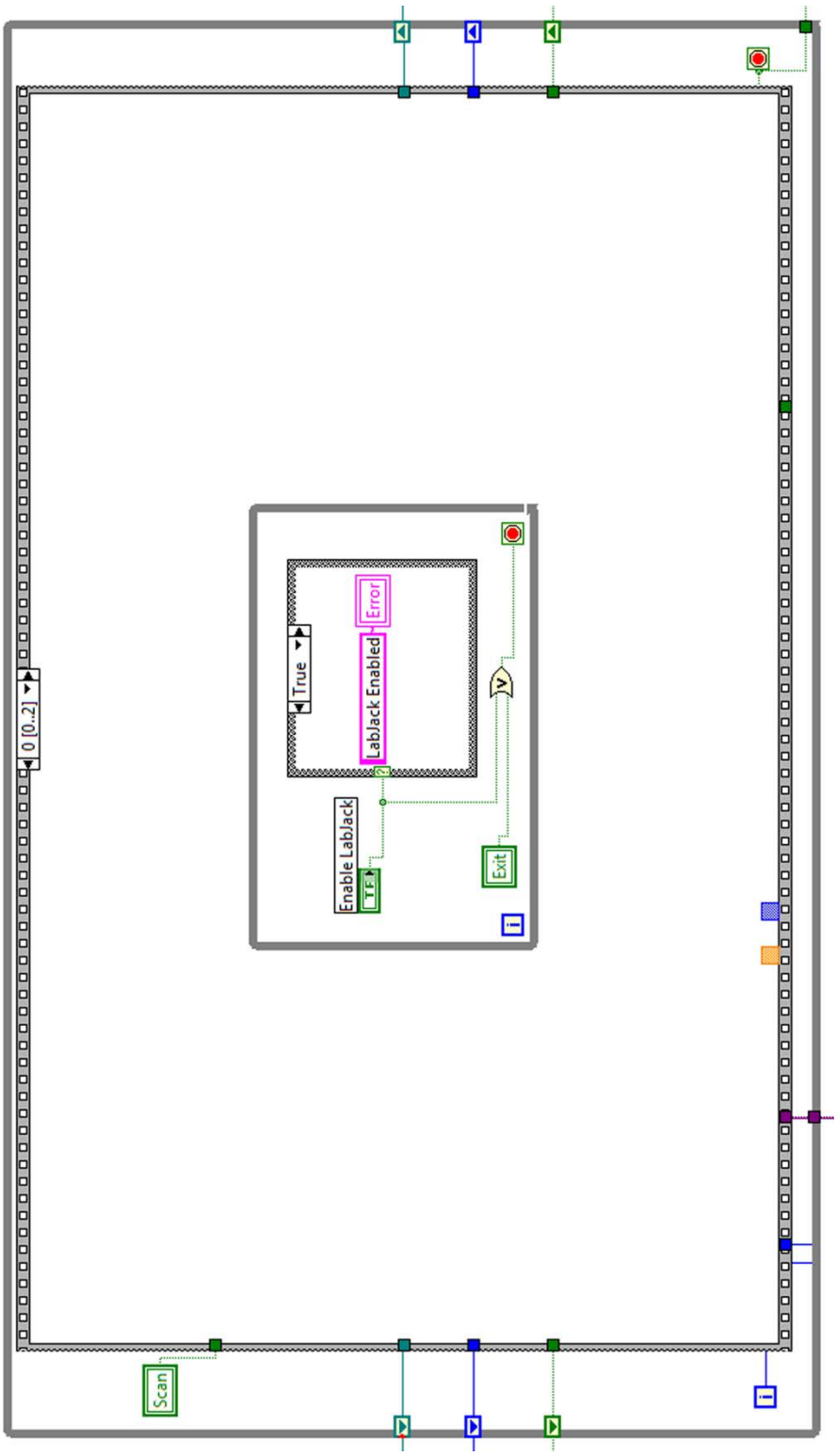

Fig. B.2 Second execution of LabVIEW PR data collection VI sequence structure.

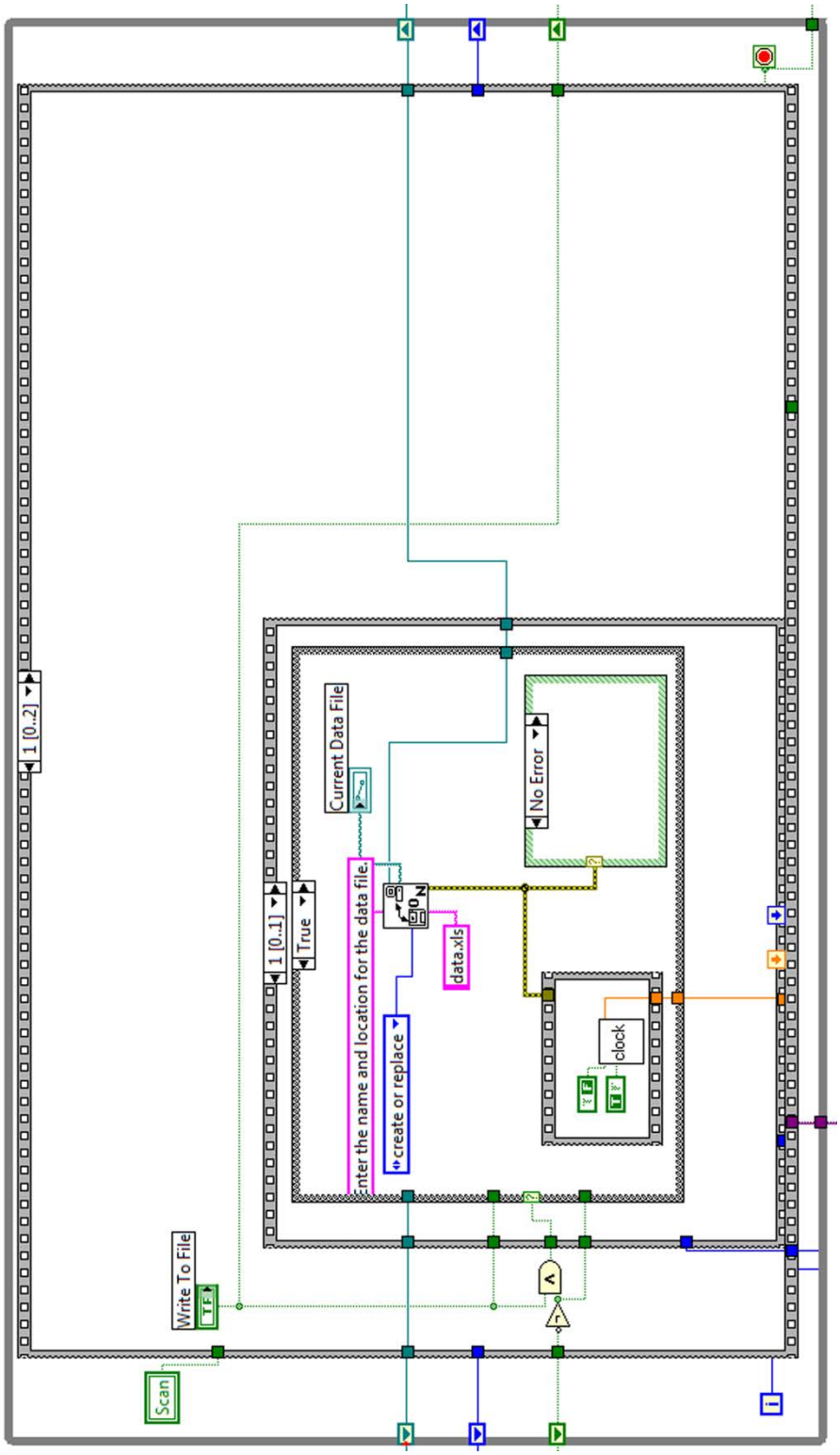

Fig. B.3 Third execution of LabVIEW PR data collection VI sequence structure.

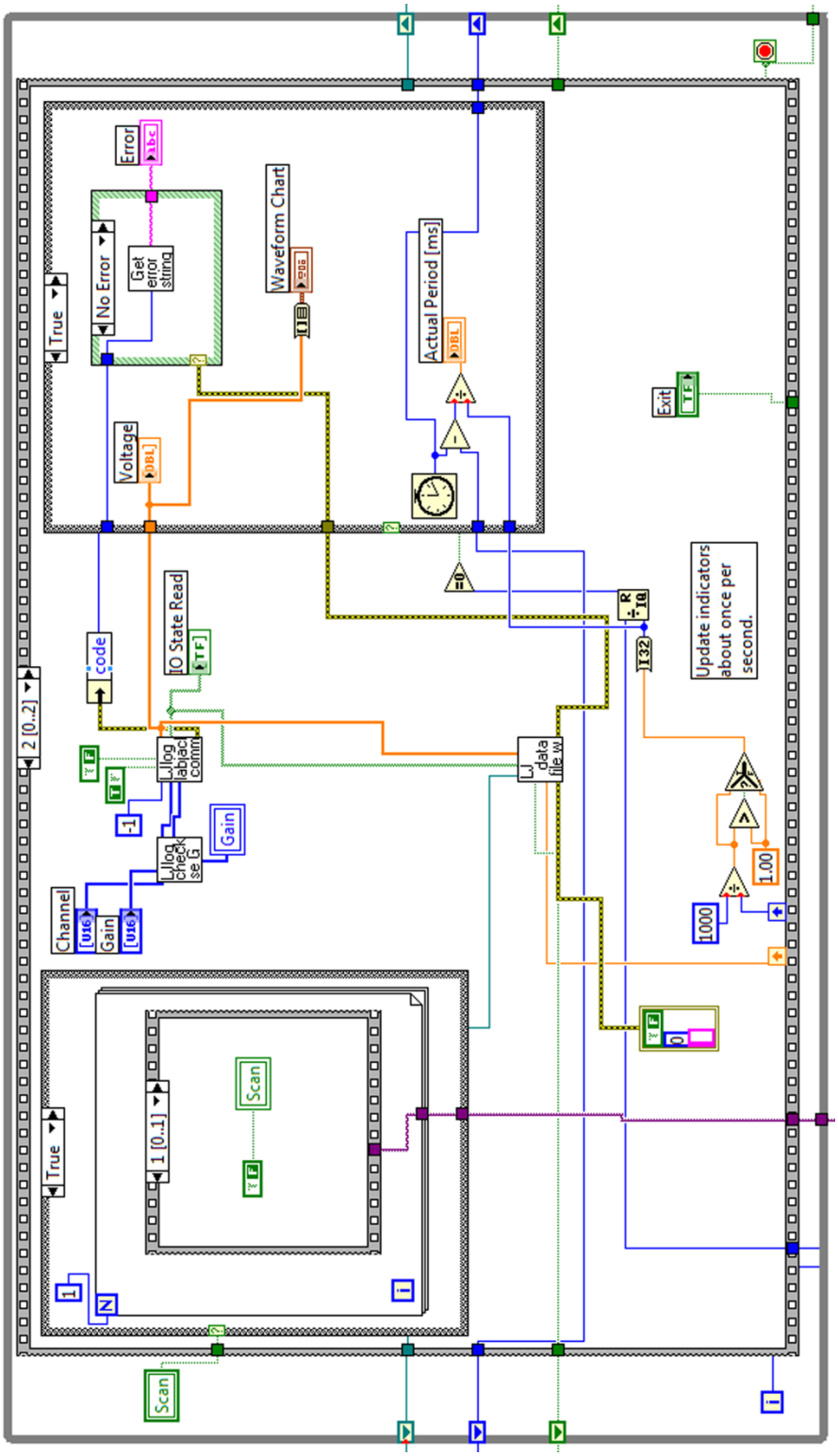

Fig. B.4 Left hand side of stepper motor control “for” loop containing “reset” and “inititialize” case structures as well as monochromator parameter calculations and variable assignments. Also, LabVIEW PR data collection VI.

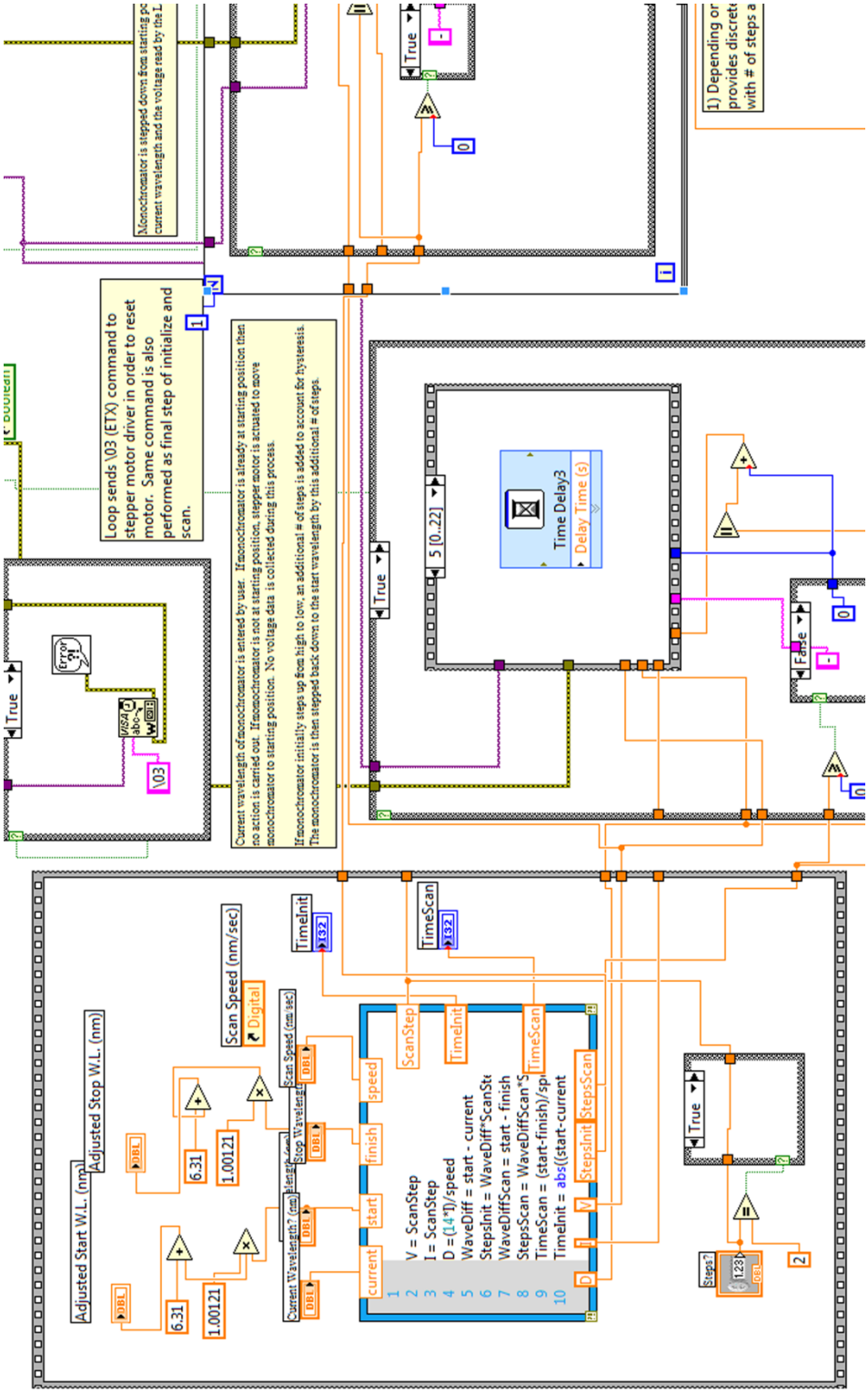

Fig. B.5 Right hand side of stepper motor control “for” loop containing “scan” case structure and “exit” sequence structure. Also, LabVIEW PR data collection VI.

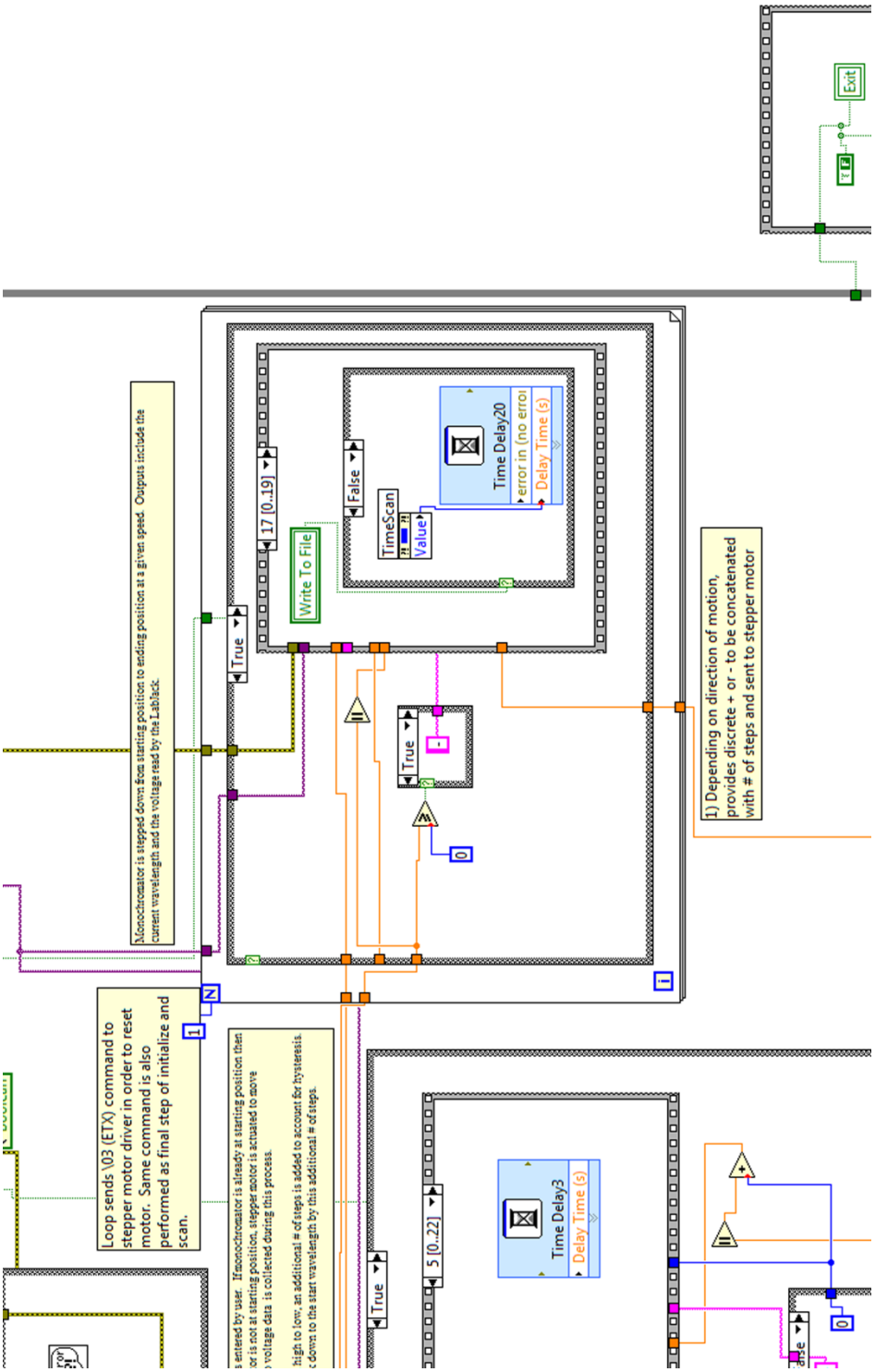

Fig. B.6 In LabVIEW VI for PR spectrum analysis, routine for conversion of raw PR data from seconds, ΔR, and R to wavelength (in eV) and $\Delta R/R$.

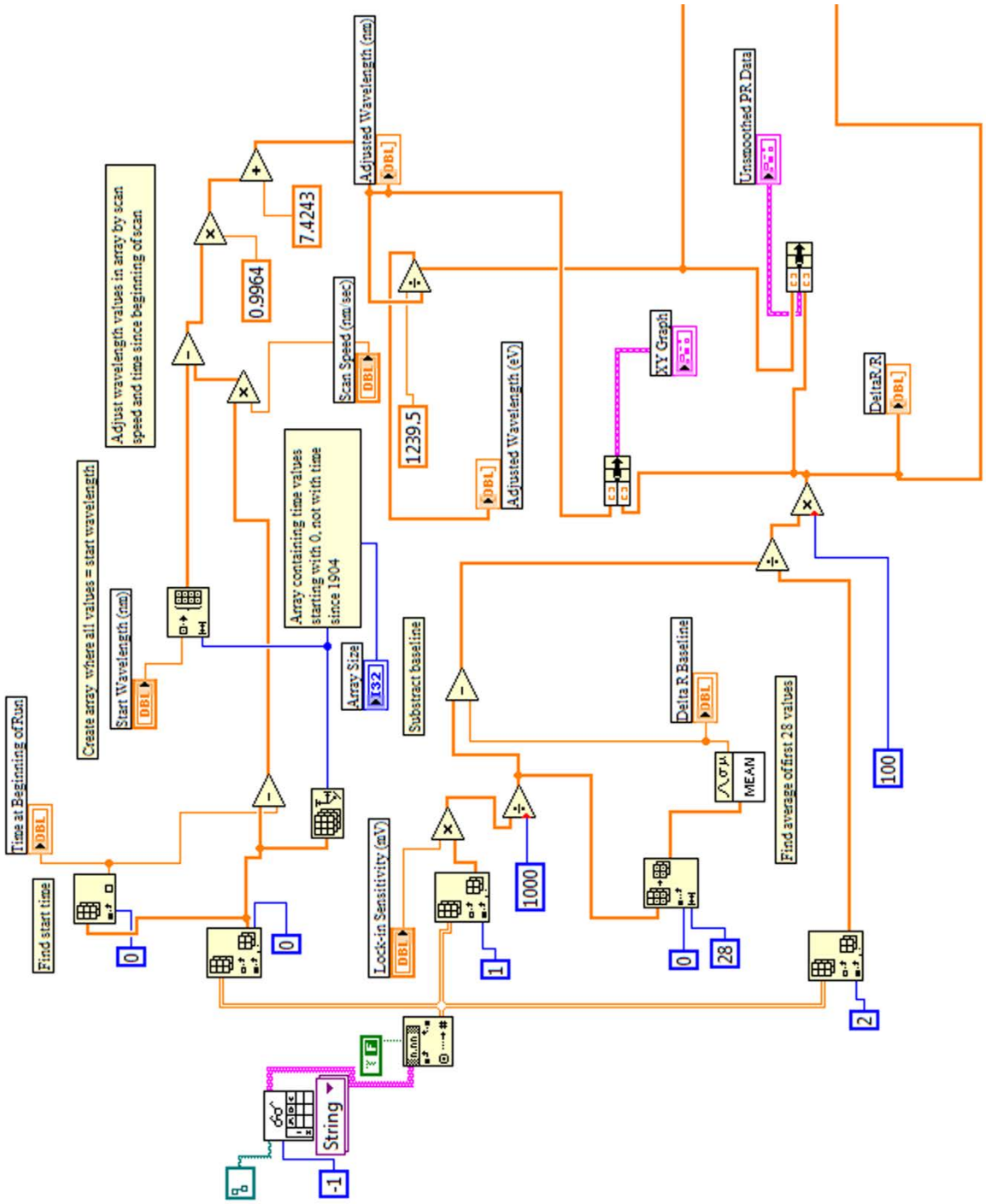

Fig. B.7 Data smoothing sequence structure in PR spectrum analysis VI.

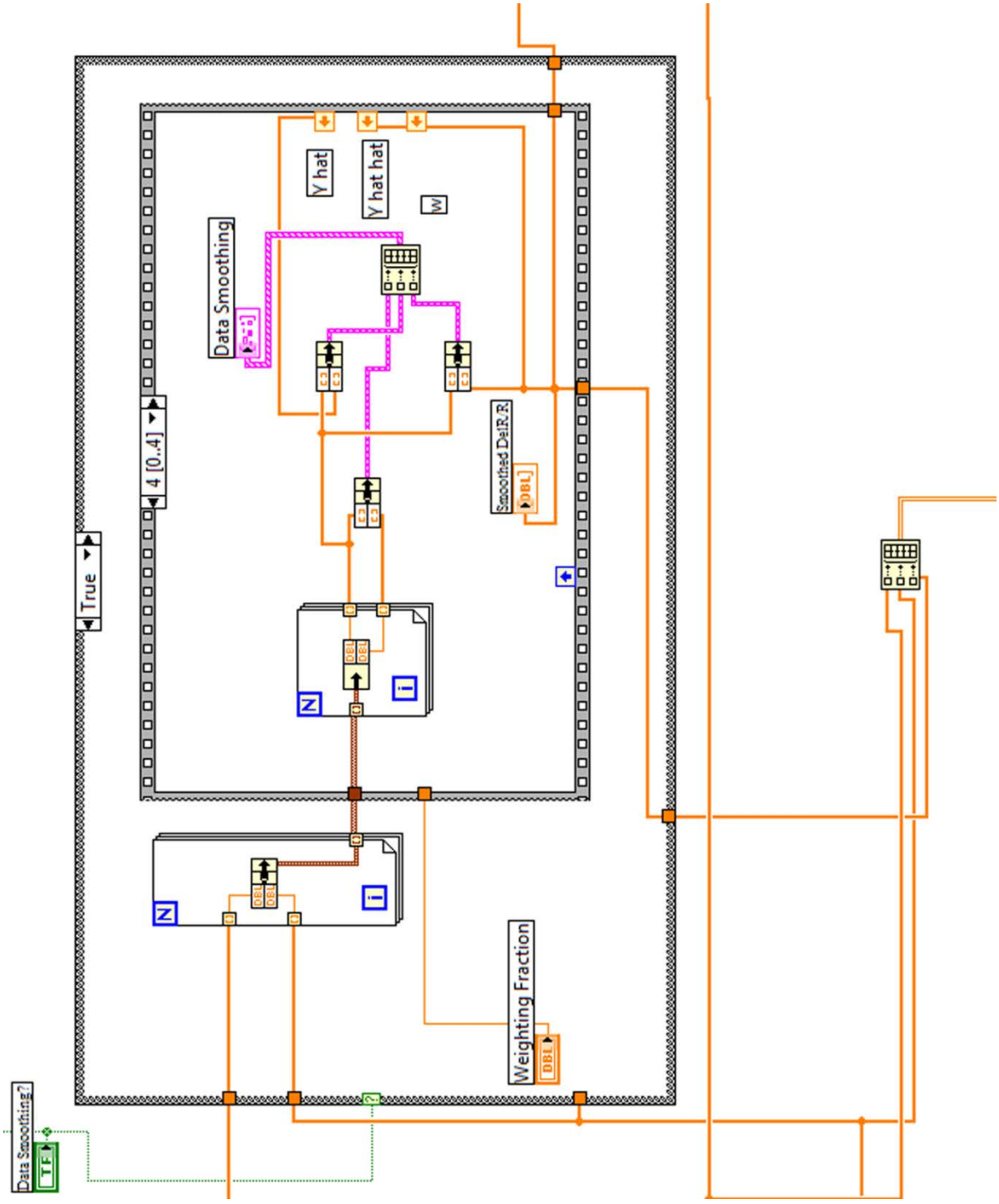

Fig. B.8 Top half of parameter estimation sequence structure in PR spectrum analysis VI.

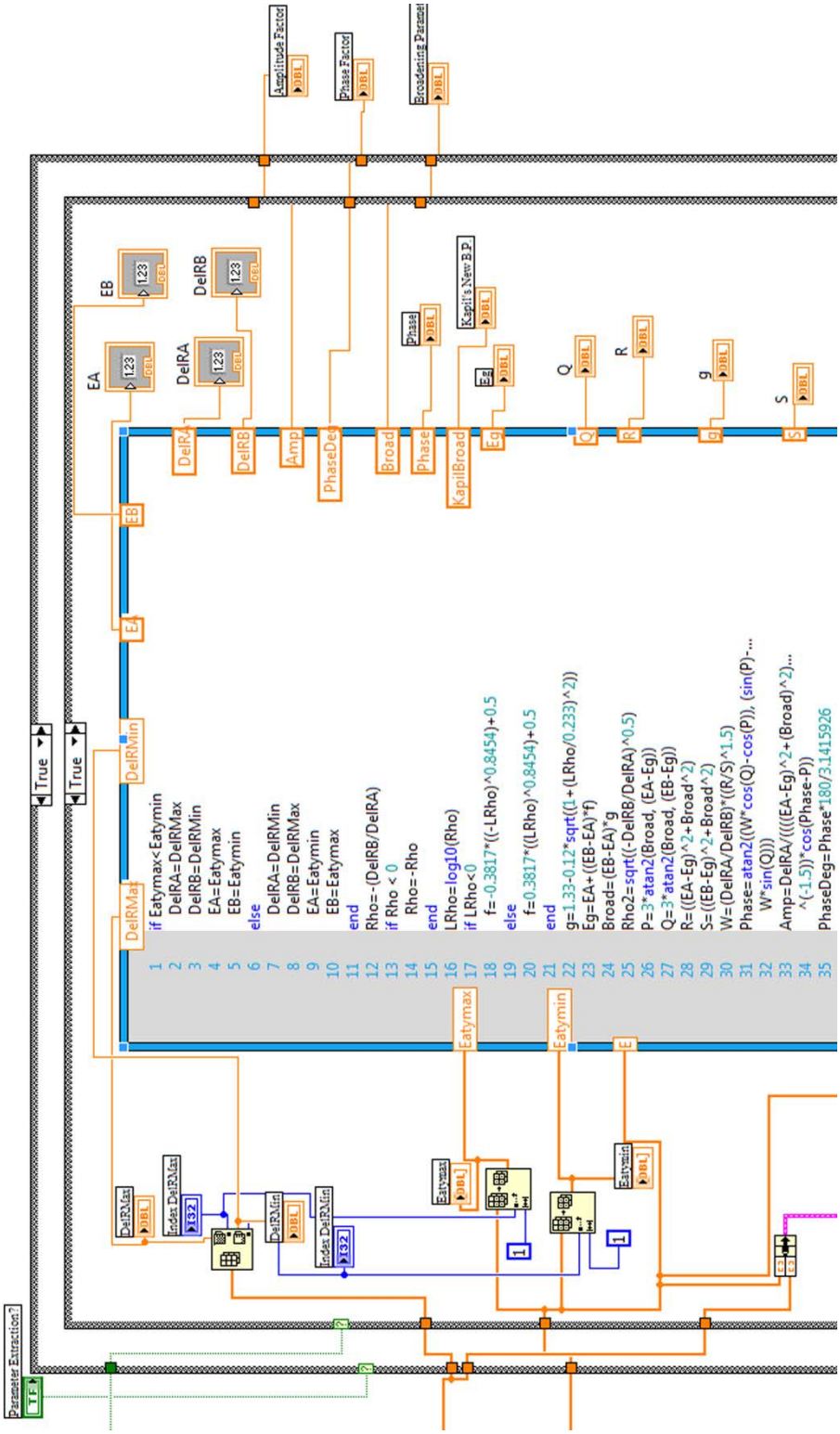

Fig. B.9 Bottom half of parameter estimation sequence structure in PR spectrum analysis VI.

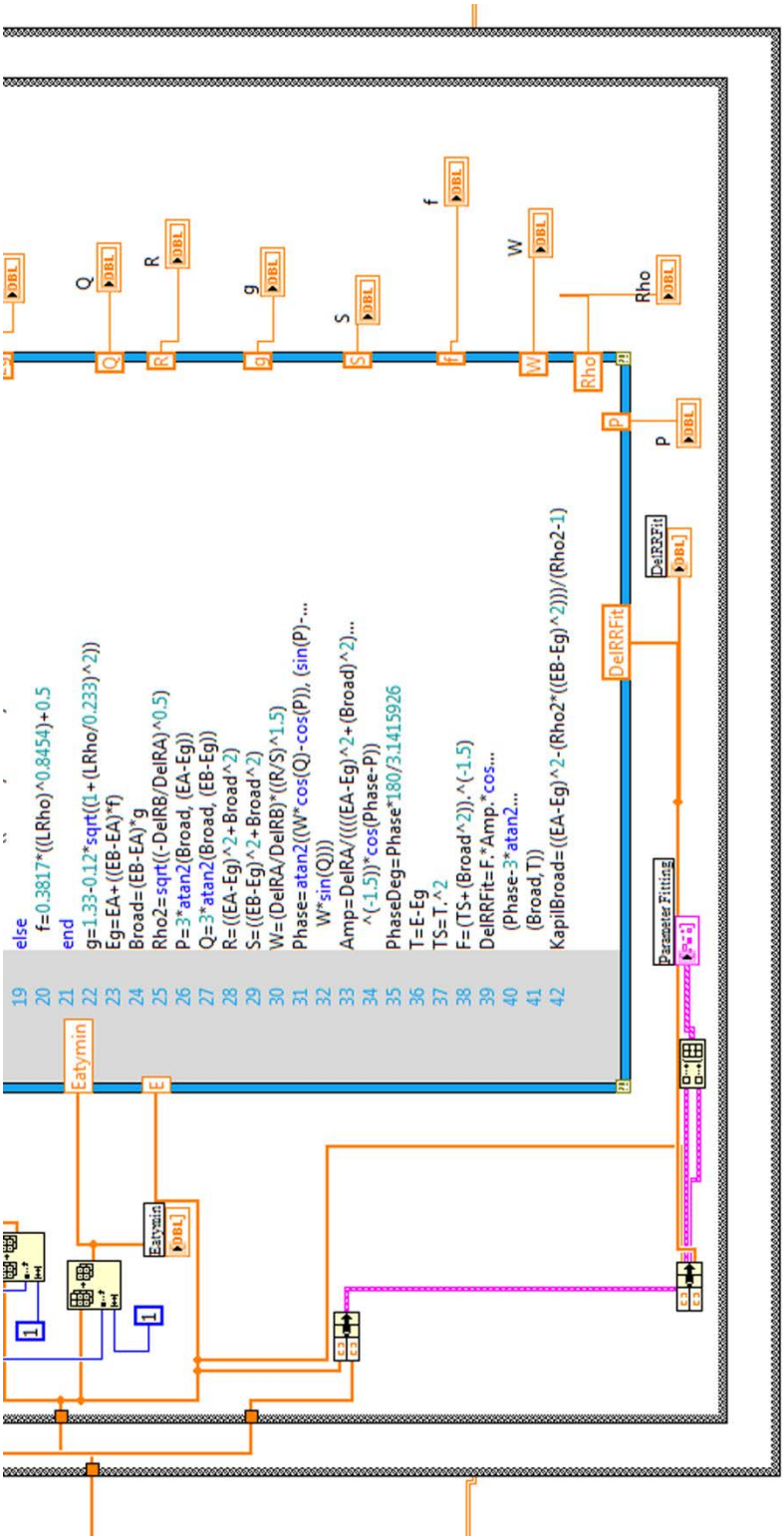

Fig. B.10 Sequence in PR spectrum analysis VI for generation and refinement of $\Delta R/R$ curve fit based on user inputs for broadening factor, amplitude factor, and phase factor.

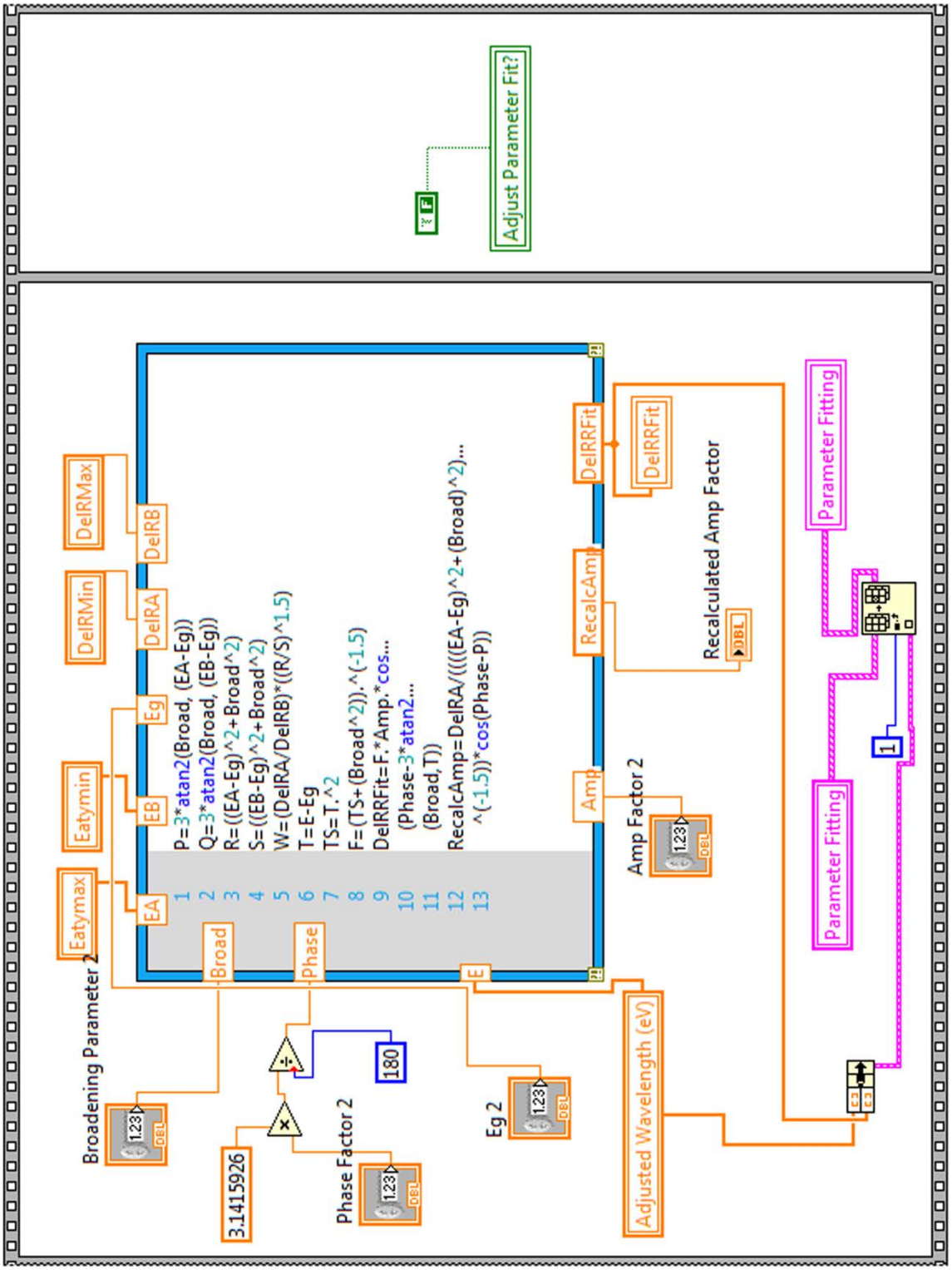

Fig. B.11 Final sequence structure in PR spectrum analysis VI comprising commands for collating and saving converted PR data, smoothed PR data, generated curve fit, and best-fit parameters, where applicable.

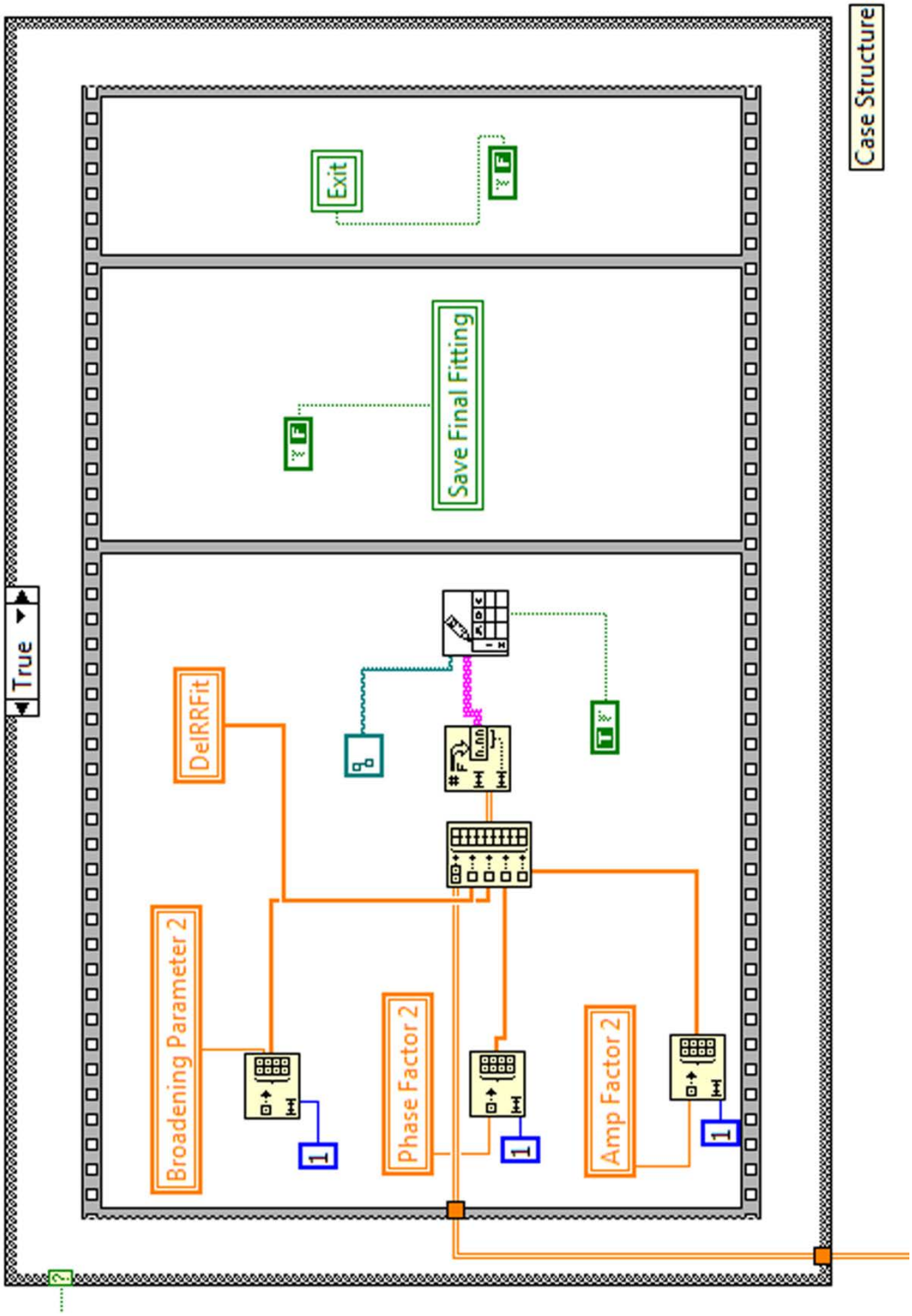

Fig. B.12 Alternative method for PR parameter estimation involving non-linear least-squares fitting routine based on a modified Marquardt-Levenberg algorithm. Fitting was performed using SigmaPlot.